8-2019

Oxidative Phosphorylation: A Critical Feature and Novel Therapeutic Target in Melanoma Brain Metastases

Grant Fischer

OXIDATIVE PHOSPHORYLATION: A CRITICAL FEATURE AND NOVEL THERAPEUTIC TARGET IN MELANOMA BRAIN METASTASES

By

Grant Matthew Fischer, B.S.

APPROVED:

_____
Michael A. Davies, M.D., Ph.D.
Advisory Professor

_____
Philip Lorenzi, Ph.D.

_____
John De Groot, M.D.

_____
Russell Broaddus, M.D., Ph.D.

_____
Dihua Yu, M.D., Ph.D.

APPROVED:

_____
Dean, The University of Texas
MD Anderson Cancer Center and UTHealth Graduate School of Biomedical Sciences

OXIDATIVE PHOSPHORYLATION: A CRITICAL FEATURE AND NOVEL THERAPEUTIC TARGET IN MELANOMA BRAIN METASTASES

Presented to the Faculty of the

The University of Texas

Graduate School of Biomedical Sciences

in Partial Fulfillment

of the Requirements

for the Degree of

Doctor of Philosophy

By

Grant Matthew Fischer, B.S.

Houston, Texas

Date of Graduation: August 2019

DEDICATION

I dedicate this work to the family members that I have gained (Sloane Josephine) and lost (John Cionko and Mary Ann Fischer) during this journey.

ACKNOWLEDGEMENTS

I would like to start by saying “thank you” to Michael Davies. As my advisor for the past 4 years, you have taught me how to conduct meaningful research and run an effective lab. I came to you when I found out that I couldn’t join the lab that I was originally planning on joining. You displayed a great deal of patience with me as I worked to create my project from scratch after completing an emergency tutorial with you. Taking on the amount of responsibility that I did as a graduate student wasn’t easy but you always believed in me. In the end, you helped me to accomplish everything that I set out to accomplish when I started graduate school. I hope that I have made you proud and continue to do so in the future.

I must also thank my committee members. You have played a vital role in getting me to this point. You have offered me meaningful guidance about my project and about my career. I am grateful for everything you have done to help me become the best researcher possible.

I would like to thank my colleagues and collaborators. Our *Cancer Discovery* paper was the result of effective team science. Thank you again for your input and assistance.

I am also grateful for the support of the MD/PhD program, Cancer Biology graduate program, and UT-GSBS. Numerous individuals from these programs have helped me in countless ways over the years, and I could not have succeeded without them.

I would like to thank my parents Gary and Rhonda Fischer. I could not have made it this far without you. You instilled in me the work ethic that I needed to complete such a rigorous program. More importantly, you have supported me in countless ways and made it possible to cross the finish line. To the rest of my family, thank you for all of your love and support. It has meant the world to me during my training.

Thank you to all of my friends. I appreciate your patience as there were many times I had to work instead of spending time with you. For what it's worth, the times we could do something together made these years tolerable.

Finally, thank you to my loving wife Darci. You are the light of my life. Your patience and belief in me have been unwavering. I could not have gotten to this point without you. Coming home to you has been the highlight of my day since I started on this path. We have come a long way since our first date at Olive Garden back in high school, and I can't wait to see what the future holds for us (hopefully more seasons of *Temptation Island*).

OXIDATIVE PHOSPHORYLATION: A CRITICAL FEATURE AND NOVEL THERAPEUTIC TARGET IN MELANOMA BRAIN METASTASES

Grant Matthew Fischer, B.S.

Advisory Professor: Michael A. Davies, M.D., Ph.D.

We recently showed via RNA-sequencing (RNA-seq) analysis of clinical samples that melanoma brain metastases (MBMs) have higher expression of oxidative phosphorylation (OXPHOS) genes (including *PPARGC1A* or *PGC1α*) than patient-matched extracranial metastases (ECMs). **Thus, the central hypothesis of this dissertation is that OXPHOS plays a critical role in the pathogenesis of MBMs.**

RNA-seq analysis identified increased expression of OXPHOS genes in intracranial (ICr) vs. subcutaneous (SQ) xenografts of 4 different human melanoma cell lines. Increased OXPHOS in the ICr xenografts was confirmed by direct metabolite analysis and [U-^{13}C]-glucose tracing analysis. Together, these studies indicate that the brain TME mediates OXPHOS enrichment in MBMs.

The functional significance of OXPHOS in MBM pathogenesis was tested using IACS-010759, a potent OXPHOS inhibitor currently in phase I clinical trials. IACS-010759 treatment of an RCAS-TVA mouse model of spontaneous MBM and lung metastasis significantly decreased the incidence of detectable MBMs but did not affect primary tumor growth or the incidence of lung metastases. To clarify if OXPHOS promotes the formation of MBMs or the outgrowth of micrometastases, we used an imageable experimental MBM model to demonstrate that IACS-

010759 treatment prevented the growth of MBMs but did not prevent their formation, and had no effect on the formation or growth of lung metastases. Likewise, knockdown of PGC1α significantly extended the survival of mice challenged by intracranial injection of melanoma cell lines but had no effect on subcutaneous tumor growth.

Hierarchical clustering analysis of surgically resected MBMs by OXPHOS genes identified subsets of MBMs particularly enriched (High-OXPHOS) and depleted (Low-OXPHOS) in OXPHOS. High-OXPHOS MBMs were characterized by mTORC1 pathway activation, immunosuppression, and enhanced glutamine metabolism. IACS-010759 treatment and treatment with the novel glutaminase inhibitor CB839 significantly improved the survival of mice bearing High-OXPHOS, MAPKi-resistant ICr xenografts.

Together these studies indicate that the brain TME mediates OXPHOS enrichment in MBMs. Further, while OXPHOS is not a critical determinant of brain metastasis formation, it plays a crucial role in intracranial tumor growth. These findings suggest that targeting this metabolic pathway and/or its dependencies may be an effective strategy for MBM treatment.

TABLE OF CONTENTS

LIST OF FIGURES

LIST OF TABLES

CHAPTER 1: INTRODUCTION

Copyright Disclosure:

This chapter is based upon:

1. **Fischer, G. M.**, Y. N. Vashisht Gopal, J. L. McQuade, W. Peng, R. J. DeBerardinis, and M. A. Davies. 2018. Metabolic strategies of melanoma cells: Mechanisms, interactions with the tumor microenvironment, and therapeutic implications. *Pigment Cell Melanoma Res* 31: 11-30.

2. **Fischer G.M.**, and M.A. Davies (2019) Melanoma Brain Metastasis: Insights, Progress, Challenges, and Opportunities. In: Fisher D., and B. Bastian (eds) Melanoma. Springer, New York, NY.

3. **Fischer, G. M.**, A. Jalali, D. A. Kircher, W. C. Lee, J. L. McQuade, L. E. Haydu, A. Y. Joon, A. Reuben, M. P. de Macedo, F. C. L. Carapeto, C. Yang, A. Srivastava, C. R. Ambati, A. Sreekumar, C. W. Hudgens, B. Knighton, W. Deng, S. D. Ferguson, H. A. Tawbi, I. C. Glitza, J. E. Gershenwald, Y. N. Vashisht Gopal, P. Hwu, J. T. Huse, J. A. Wargo, P. A. Futreal, N. Putluri, A. J. Lazar, R. J. DeBerardinis, J. R. Marszalek, J. Zhang, S. L. Holmen, M. T. Tetzlaff, and M. A. Davies. 2019. Molecular Profiling Reveals Unique Immune and Metabolic Features of Melanoma Brain Metastases. *Cancer Discov.* 9: 628-645.

1.1 - METABOLISM OF MELANOMAS

1.1.1 - Overview

Cutaneous melanoma is the most aggressive form of skin cancer, accounting for >80% of skin-cancer related deaths (1). Characteristically resistant to conventional chemotherapy and radiation, significant advances in metastatic melanoma treatments and outcomes have been made in the last several years due to improved understanding of the features and drivers of this disease. The Melanoma Cancer Genome Atlas (TCGA) effort and other studies have shown that the mitogen-activated protein kinase (MAPK) pathway is ubiquitously activated in cutaneous melanoma as a result of somatic mutations in multiple genes, including point mutations in the v-Raf murine sarcoma viral oncogene homolog *(BRAF)* (35%–50% of melanomas) and Neuroblastoma RAS viral oncogene homolog (*NRAS)* (10%–25%), and loss of function mutations affecting Neurofibromin 1 (*NF1*) (~15%). Efforts to target this pathway therapeutically culminated in the Food and Drug Administration (FDA) approval of the BRAF inhibitors vemurafenib and dabrafenib; the mitogen-activated protein kinase (MEK) inhibitor trametinib; and the combination regimens of dabrafenib + trametinib, vemurafenib + cobimetinib, and encorafenib + binimetinib (2). All of these agents were approved specifically for melanoma patients with mutations that cause substitution of the V600 residue of the BRAF protein (2). While the BRAF inhibitors, alone and in combination with MEK inhibitors, reduce tumor burden in almost all patients with a $BRAF^{V600}$ mutation, most patients will eventually develop resistance (3). In addition to these targeted therapies, several immune therapies have also been approved for patients with metastatic melanoma in recent years, including the checkpoint inhibitors ipilimumab, nivolumab, and pembrolizumab, and the combination of ipilimumab with nivolumab

(2). Clinical responses and benefit with these immunotherapies can last for several years, and may even be curative. However, the response rates with these immune therapies are lower than for the targeted therapies (i.e. 10-15% for ipilimumab; 35-45% for nivolumab and pembrolizumab; ~55% for ipilimumab + nivolumab) (2). Thus, while there has been tremendous progress, there remains a need for additional effective therapeutic strategies for this disease.

There is a growing appreciation and supporting data regarding the frequency and significance of metabolic reprogramming in cancer initiation, maintenance, and progression (4). However, tumor metabolism is complex, and metabolic phenotypes may reflect both intrinsic properties of tumor cells and interactions between tumor cells and the tumor microenvironment (TME). Efforts to improve our understanding of this hallmark of cancer have produced encouraging results that deserve further investigation.

1.1.2 - An Overview of Central Carbon Metabolic Pathways

Central carbon metabolism consists of glycolysis, the pentose phosphate pathway (PPP), and tricarboxylic acid (TCA) cycle (5, 6) (**Figure 1**). In normoxic, nonmalignant cells, a molecule of glucose undergoes the process of glycolysis in the cytosol to produce pyruvate, adenosine triphosphate (ATP), and reduced nicotinamide adenine dinucleotide (NADH) (7). Decarboxylation of pyruvate by mitochondrial pyruvate dehydrogenase (PDH) initiates the highly efficient process of mitochondrial oxidative phosphorylation (OXPHOS) by feeding acetyl coenzyme A (acetyl-CoA) into the TCA cycle (8). NADH and reduced flavin adenine dinucleotide (FADH2) molecules transfer electrons to the electron transport chain (ETC), which responds by transporting protons across the mitochondrial membrane (8). The resulting electrochemical gradient then drives ATP synthesis, with oxygen serving as the final electron acceptor, producing

water as a byproduct (8) (**Figure 1**). As oxygen is necessary for the coupling of glycolysis and OXPHOS to occur, hypoxic cells rely more on glycolysis to meet their energy needs (9). In a process known as lactic acid fermentation, lactate dehydrogenase (LDH) transfers electrons from NADH to pyruvate, producing lactate and replenishing the supply of NAD^+ in the cytosol to allow further glycolysis to continue (9). Melanoma cells take advantage of these available metabolic pathways, and others, by using them to meet their needs in a wide variety of contexts.

1.1.3 - Utilization and Regulation of Metabolic Pathways in Melanoma

1.1.3a - Glycolysis: An Essential Source of ATP and Molecular Precursors

Like many other cancer types, the majority of rapidly proliferating melanoma cells metabolize glucose into lactate regardless of oxygen levels, a process known as aerobic glycolysis, or the "Warburg effect," in honor of Otto Warburg, who first described the propensity of tumor cells to utilize glycolysis (10). When glycolysis is utilized at high rates in proliferating tumor cells, it can supply the ATP necessary for survival while also supplying materials required for proliferation. (11). Scott et al. found that in normoxic conditions, only 25% of pyruvate enters the mitochondria of melanoma cells exhibiting the Warburg phenotype, where it is converted to acetyl-CoA by PDH (10). Instead of fully circulating in the TCA cycle, the citrate is transported to the cytosol, where ATP citrate lyase (ACL) cleaves it into acetyl-CoA and oxaloacetate. Acetyl-CoA either enters the fatty acid synthesis pathway, which is critical for the proliferation of melanoma cells, or fuels acetylation of histones in epigenetic regulation reactions while oxaloacetate is converted to malate, which produces pyruvate via malic enzyme and subsequently lactate

via LDH (12, 13). The malic enzyme serves as a source of reduced nicotinamide adenine dinucleotide phosphate (NADPH), necessary for detoxifying melanoma cells of reactive

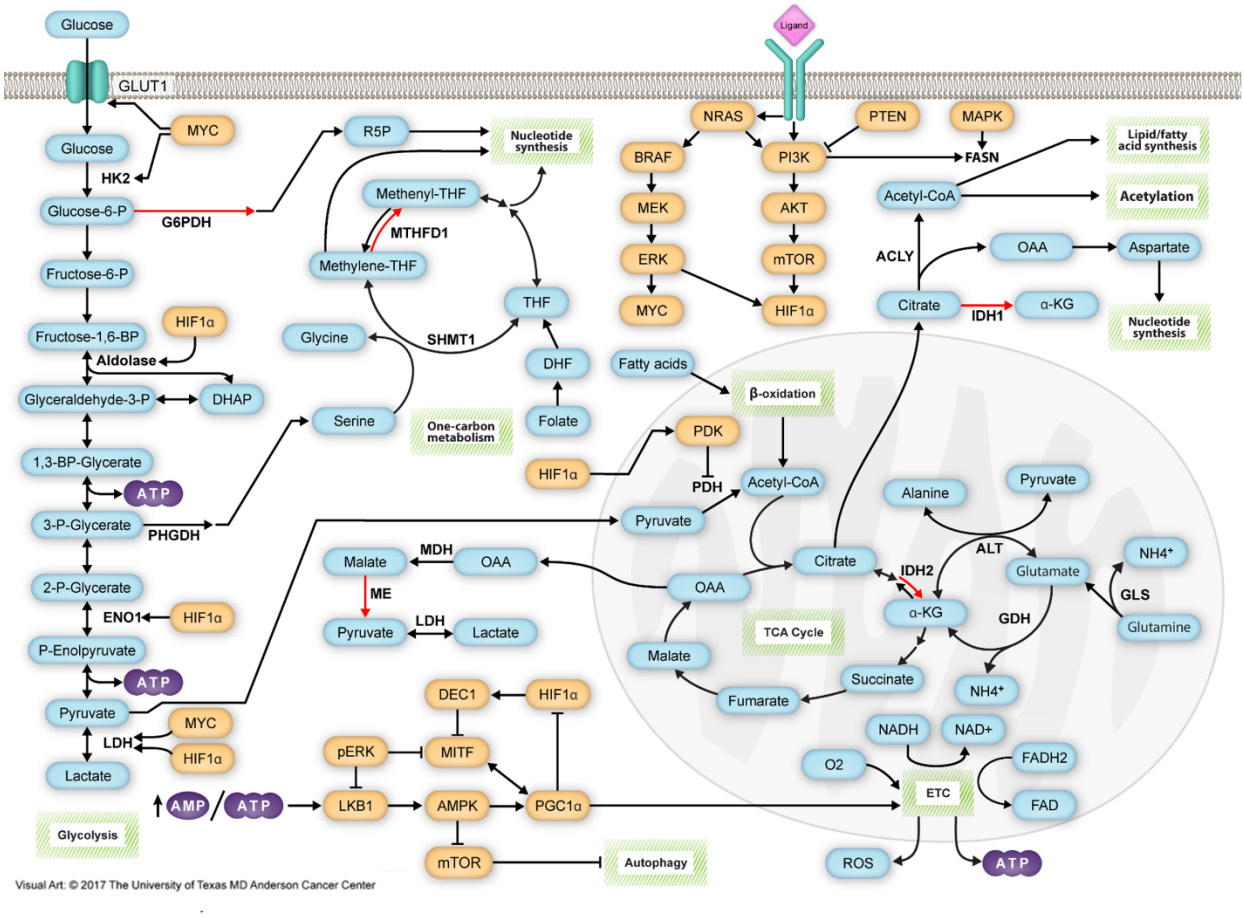

Figure 1: Signaling pathways promote melanoma progression by regulating critical metabolic reactions. Central carbon metabolism and one-carbon metabolism play critical roles in melanoma biology. Glycolysis produces ATP and intermediates that fuel the pentose-phosphate pathway (PPP) and serine-glycine/one-carbon metabolism pathways, which produce NADPH vital for maintaining the redox balance of the cell and for anabolic reactions. The TCA cycle uses acetyl-CoA derived from pyruvate or β-oxidation of fatty acids to produce NADH, which powers the ATP-generating electron-transport chain (ETC). The TCA cycle can also generate NADPH via isocitrate dehydrogenase 2 (IDH2). Like other tumor cells, the TCA cycle of melanoma cells can alternatively oxidize glutamine, which enters the TCA cycle as α-ketoglutarate (α-KG). In addition to its bioenergetic function, the TCA cycle produces critical biosynthetic precursors. Oxaloacetate (OAA) fuels reactions that generate NADPH via malic enzyme (ME) and also promotes nucleotide synthesis by supplying the cell with aspartate. Citrate provides the cell with acetyl-CoA necessary for fatty acid synthesis and acetylation reactions. Citrate also promotes NADPH production via isocitrate dehydrogenase 1 (IDH1). Signaling pathways play a critical role in determining which metabolic pathways are favored by melanoma cells. The MAPK and PI3K pathways promote glycolysis and the decoupling of glycolysis from the TCA cycle via HIF1α and MYC. However, through mechanisms currently unknown, a subset of melanomas highly expresses PGC1α, which promotes OXPHOS and makes the cells highly dependent on the oxidation of glutamine. GLUT1, glucose transporter 1; HK2, hexokinase 2; G6PD, glucose-6-phosphate dehydrogenase; PHGDH, phosphoglycerate dehydrogenase; ENO1, enolase 1; LDH, lactate dehydrogenase; SHMT1, serine hydroxymethyltransferase 1; MTHFD1, methylenetetrahydrofolate dehydrogenase 1; THF, tetrahydrofolate; DHF, dihydrofolate; MDH, malate dehydrogenase; FASN, fatty acid synthase; ACLY, ATP citrate lyase; PDH, pyruvate dehydrogenase; GLS, glutaminase; ALT, alanine aminotransferase; GDH, glutamate dehydrogenase. Red arrows indicate NADPH-producing reactions, blue bubbles indicate metabolites, orange bubbles indicate gene products known to regulate metabolic processes in melanomas, and green boxes indicate metabolic pathways. Used with permission from John Wiley & Sons Ltd. (Fischer, G. M., Y. N. Vashisht Gopal, J. L. McQuade, W. Peng, R. J. DeBerardinis, and M. A. Davies. 2018. Metabolic strategies of melanoma cells: Mechanisms, interactions with the tumor microenvironment, and therapeutic implications. *Pigment Cell Melanoma Res* 31: 11-30).

oxygen species (ROS), and LDH mitigates the surplus of NADH present from high glycolytic rates. Consistent with the role of glycolysis as a source of citrate, treatment of glycolytic B16-F10 melanoma cells with the PDH cofactor α-lipoic acid and the ACL competitive inhibitor hydroxycitrate results in significant growth inhibition (14, 15).

Glycolysis also supports the PPP and serine/glycine synthetic pathway in melanoma cells. Glucose-6-phosphate dehydrogenase (G6PD) oxidizes glucose-6-phosphate (G6P), a glycolytic intermediate, in the rate-limiting step of the PPP (7). After numerous additional reactions, the PPP produces a net gain of the reducing equivalent NADPH and 5-carbon sugars used in nucleotide synthesis. G6PD is highly expressed in melanomas, and inhibition of G6PD in A375 cells results in G1/S phase cell cycle arrest due to ROS-mediated inhibition of signal transducer and activator of transcription 3 (STAT3) (16). Phosphoglycerate dehydrogenase (PHGDH) catalyzes the initial step of the serine/glycine synthesis pathway, oxidizing the glycolytic intermediate 3-phosphoglycerate (3-PG). Serine plays a critical role in the biosynthesis of purines and pyrimidines, and it is the precursor of glycine. A bioinformatics analysis of 3131 human cancer samples found recurring copy number gains in *PHGDH* at a frequency of 40% in melanomas, and melanomas with *PHGDH* copy number gains were particularly sensitive to PHGDH inhibition (17, 18).

The utilization of the Warburg phenotype by melanomas is driven in part by activation of intrinsic signaling pathways, particularly the MAPK pathway (**Figure 1** and **Table 1**). Activation of the MAPK pathway increases the transcription of the hypoxia inducible factor 1α (*HIF1α*) and v-MYC avian myelocytomatosis viral oncogene homolog (*MYC*) (19, 20). Additionally, the MAPK pathway stabilizes HIF1α, allowing it to partner

with HIF1β to become active and promote glycolysis via transcription of *LDH*, aldolase (*ALDOA*), and enolase 1 (*ENO1*) (21). Furthermore, HIF1α activates pyruvate

Table 1: Impact of oncogenic signaling pathways on melanoma metabolism

Pathway	Alterations in Melanoma	Metabolic Effects
MAPK	• Constitutive activity due to point mutations in *BRAF* (35%–50%) and *NRAS* (10%–25%) and deletions in *NF1* (~15%)	• Suppresses MITF and PGC1α signaling to inhibit OXPHOS • Stimulates MYC and HIF1α signaling to promote glycolysis • Also promotes fatty acid synthesis
PI3K-AKT	• Loss of function of PTEN (30%–50%) • Point mutations in *PI3K* (<3%) • Point mutations in *AKT* (<3%) • Point mutations in *NRAS* (10%–25%)	• Stimulates MYC and HIF1α signaling to promote aerobic glycolysis • Promotes aerobic glycolysis and fatty acid synthesis • Stimulates mTOR to promote OXPHOS in a subset of melanomas
mTOR	• mTORC1 and 2 activated by PI3K/AKT pathway • mTORC1 stimulated in response to amino acids • mTORC1 suppressed by AMPK in response to ↑AMP/ATP	• Drives transcription of *HIF1α* and *MYC*, promoting aerobic glycolysis • Promotes fatty acid synthesis, protein synthesis, and nucleotide synthesis • Promotes translocation of MITF to the nucleus, promoting *PGC1α* expression and OXPHOS in a subset of melanomas
HIF1α	• Degradation inhibited by hypoxia and ROS • Transcription/translation promoted by MAPK pathway signaling, and translation promoted by PI3K pathway signaling	• Stimulates aldolase, ENO1, and LDH, which directly promote glycolytic flux • Activates PDK, preventing the flow of pyruvate into the TCA cycle • Promotes DEC1 activity, indirectly inhibiting OXPHOS
MYC	• Activated by P-ERK • Copy number gains (~30% of metastatic melanomas)	• Drives *GLUT1*, *HK2*, and *LDH* transcription, promoting aerobic glycolysis • Promotes glutaminase transcription, stimulating glutamine metabolism
MITF	• MITF inhibited by P-ERK • *MITF* transcription suppressed by HIF1α and DEC1 • *MITF* transcription promoted by PGC1α • *PGC1α* transcription promoted by LKB1-AMPK axis	• Promotes OXPHOS
LKB1-AMPK	• LKB1 responds to ↑AMP/ATP ratio by activating AMPK	• AMPK inhibits mTOR activity and biosynthetic reactions • Promotes *PGC1α* transcription and OXPHOS

dehydrogenase kinase (PDK), which inhibits PDH, preventing pyruvate from entering the TCA cycle for use in OXPHOS (22). Besides HIF1α, MYC also promotes increased glycolytic activity, either as a downstream effector of a constitutively active MAPK pathway or due to copy number gains, which Kraehn et al. identified in 4/8 primary melanomas and 11/33 metastatic melanomas (23). The MYC transcription factor activates LDH, glucose transporter 1 (GLUT1), and hexokinase 2 (HK2), thereby promoting glucose uptake and glycolytic activity (24, 25). The MAPK pathway also promotes the Warburg phenotype through its inhibition of the microphthalmia-associated transcription factor (MITF), a critical regulator and promoter of OXPHOS in tumor cells (26).

The phosphoinositide 3-kinase/protein kinase B/mechanistic target of rapamycin (PI3K/AKT/mTOR) signaling pathway is activated multiple ways in melanoma, including by loss of function of the PTEN tumor suppressor, activating mutations in *AKT* and *PIK3CA*, and compensatory signaling through growth factor receptors (27-31). Activation of this pathway promotes glycolytic metabolism in melanoma (**Figure 1** and **Table 1**). Phosphorylation and activation of AKT drives mTOR signaling, which can promote *HIF1α* transcription and activity, thereby driving the synthesis of glycolytic machinery (32, 33). Additionally, Zundel et al. demonstrated that restoring wild-type PTEN expression in glioblastoma cells lacking functional PTEN corrected the deregulation of cellular AKT and suppressed the transcription of numerous HIF1α-regulated genes, highlighting the interplay between the PI3K/AKT/mTOR pathway and HIF1α signaling (34).

1.1.3b - Oxidative Phosphorylation (OXPHOS): A Driver of Growth and Progression in a Subset of Human Melanomas

While many melanomas are characterized by the Warburg phenotype, OXPHOS also plays a critical role in melanoma. OXPHOS is significantly more efficient at generating ATP than glycolysis. While only 7% of pyruvate accesses the TCA cycle in hypoxic cells, OXPHOS still contributes a significant portion of ATP to these cells as large quantities of ATP are produced from a few molecules of pyruvate (10). Furthermore, a subset of melanomas rely extensively on OXPHOS to meet their bioenergetic needs. Our lab and others have identified that between 35-50% of BRAF-mutant and wild-type cell lines and patient samples can be characterized as "High-OXPHOS" (3, 26, 35). This phenotype is predominantly driven by peroxisome proliferator-activated receptor γ 1-α (PPARGC1A or PGC1α), a transcriptional co-factor that regulates multiple mitochondrial genes. Examination of *PGC1α* gene expression in the Broad Cancer Cell Line Encyclopedia (CCLE) database revealed that melanomas have the highest expression of *PGC1α* among >900 cell lines representing 23 cancer types (3). Melanomas highly expressing *PGC1α* also express numerous nuclear respiratory factors, mitochondrial transcriptional factors, mitochondrial DNA replication factors, mitochondrial fission mediators, and mitochondrial fusion mediators (35).

PGC1α expression is regulated by MITF in melanoma cells (26). HIF1α prevents the transcription of *MITF* in glycolytic melanomas through deleted in esophageal cancer 1 (DEC1) (36, 37). In High-OXPHOS melanomas, however, this regulation fails to occur (**Figure 1**). Instead, mTOR promotes the nuclear translocation of MITF, which drives the transcription of *PGC1α* and, subsequently, OXPHOS genes (**Table 1** and **Figure 2**) (3,

38). mTOR is the core component of two distinct complexes: mTOR complex 1 (mTORC1) and mTOR complex 2 (mTORC2) (39). The PI3K-AKT pathway activates both complexes by suppressing inhibitory inputs from tuberous sclerosis complexes 1/2 (TSC1/2) (39). mTORC1 also becomes active in the presence of amino acids. Once active, mTORC1 phosphorylates ribosomal protein S6 kinase (p70S6K) and eukaryotic translation initiation factor 4E-binding protein 1 (4EBP1), promoting protein synthesis, including the translation of MYC and HIF1α (39). Active mTORC2 primarily functions

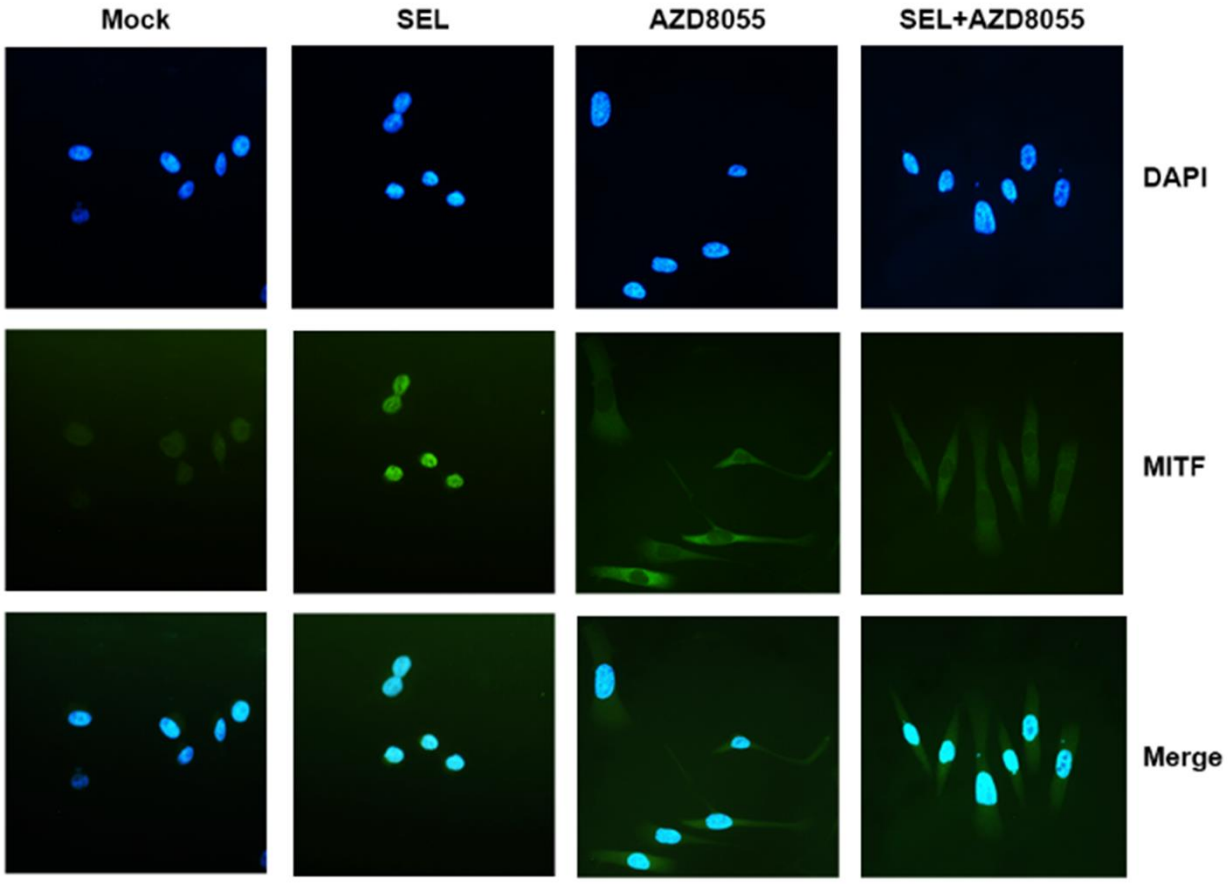

Figure 2: mTOR regulates the subcellular localization of MITF. In prior studies, High-OXPHOS MEL624 cells underwent 24-hour treatments with DMSO (Mock), the MEKi selumetinib (SEL), the mTORC1/2 inhibitor AZD8055, and selumetinib + AZD8055 (SEL + AZD8055). To identify the subcellular localization of MITF following each treatment, cells were fixed and probed with MITF antibody and stained with a FITC-labeled secondary antibody. Nuclei were stained with DAPI. Images were evaluated via immunofluorescent microscopy. AZD8055 caused a significant increase in cytoplasmic MITF staining and significant decrease in nuclear MITF staining, compared to mock treatments. In contrast, nuclear staining of MITF increased in MEL624 cells treated with selumetinib, relative to mock treatments. Gene expression profiling experiments demonstrated that 24-hour selumetinib treatments markedly increased MITF and PGC1α transcript levels in MEL624 cells, while AZD8055 inhibited basal and selumetinib-induced PGC1α expression. Used with permission from John Wiley & Sons Ltd. (Fischer, G. M., Y. N. Vashisht Gopal, J. L. McQuade, W. Peng, R. J. DeBerardinis, and M. A. Davies. 2018. Metabolic strategies of melanoma cells: Mechanisms, interactions with the tumor microenvironment, and therapeutic implications. *Pigment Cell Melanoma Res* 31: 11-30).

to phosphorylate AKT at serine 473, resulting in further activation of AKT (39). These interactions have been shown to promote protein synthesis, lipid synthesis, nucleotide synthesis, and glycolysis (39). mTOR is also known to increase mitochondrial activity and

OXPHOS via activation of YYI-PGC1α transcriptional complex (40). How mTORC1/2 signaling selects between promoting glycolysis or OXPHOS remains unclear.

AMP-activated protein kinase (AMPK) expression also positively correlates with *PGC1α* expression (41). In low cellular energy states, designated by a high ratio of AMP/ATP, liver kinase B1 (LKB1) activates AMPK, which inhibits anabolic reactions by suppressing mTORC1 and promotes mitochondrial gene expression, likely through PGC1α (41, 42). While the mechanism by which AMPK acts through PGC1α remains unclear, one possibility is that AMPK directly drives *PGC1α* expression (42). Alternatively, AMPK could promote PGC1α activation by either direct phosphorylation or indirectly through sirtuin-1 (SIRT1)-mediated deacetylation (42, 43). In glycolytic tumors, phosphorylated ERK (P-ERK) suppresses the activation of LKB1, inhibiting the typical response to energy deficiency (44). These cells are less responsive to high AMP/ATP ratios and less dependent on OXPHOS to meet their bioenergetic needs. It is likely that suppression of LKB1 also inhibits *PGC1α* expression, though this has not been tested.

1.1.3c - TCA Cycle Metabolism: A Supplier of Cellular Building Blocks

While mitochondria serve as the primary bioenergetic source for a subset of melanomas, functional mitochondria are critical for all melanoma cells by providing intermediates utilized by biosynthetic and redox reactions (45). In addition to producing the fatty acid precursor citrate via condensation with acetyl-CoA, oxaloacetate produced from the TCA cycle is converted to aspartate via transamination reactions involving glutamate. This aspartate cooperates with malate, another TCA intermediate, to power the

malate-aspartate shuttle, which moves NADH from glycolysis to the mitochondria (7). Furthermore, aspartate transported into the cytosol by the shuttle contributes to the synthesis of nucleic acids (12) (**Figure 1**). Rabinovich et al. demonstrated the role of cytoplasmic aspartate in promoting melanoma progression by suppressing arginosuccinate synthetase 1 (ASS1), which utilizes aspartate to produce arginosuccinate in the urea cycle. As a result, cytoplasmic levels of aspartate increased, activating carbamoyl phosphate synthetase II (CAD), the rate-limiting enzyme in pyrimidine synthesis, thereby facilitating the synthesis of nucleotides and promoting melanoma cell proliferation (46).

To continue utilizing citrate and oxaloacetate as biosynthetic precursors, melanoma cells must replenish TCA intermediates in a process called anaplerosis (47). While some cancers replenish oxaloacetate from pyruvate via pyruvate carboxylase, the contribution of pyruvate carboxylase to the TCA cycle is minimal in cultured melanoma cells characterized by the Warburg phenotype (10, 48, 49). Instead, these cells utilize glutamine as the primary source of carbon entering the TCA cycle (10). Upon transport into the cell via the glutamine receptor SLC1A5, glutamine is converted to glutamate via cytosolic glutaminase (50). Glutamate enters the TCA cycle as α-ketoglutarate via reactions catalyzed by either glutamate dehydrogenase 1 (GDH) or mitochondrial alanine and aspartate aminotransferase (GOT2 and GPT2, respectively) (50). Reactions catalyzed by GDH generate free ammonia, which can promote autophagy, while the aminotransferases transfer nitrogen to α-keto acids to form α-ketoglutarate and amino acids. Ratkinov et al. labeled Lu1205 melanoma cells with ^{13}C-glutamine to demonstrate that GDH and aminotransferases interchangeably catalyze this anaplerotic reaction and can maintain anaplerosis upon suppression of the alternative route (50). However, *in vitro* studies of SF188 glioblastoma cells demonstrated induction of GDH upon deprivation of

glucose and that GDH mediated survival in glucose-deprived conditions (51). In glioblastoma cells cultured in glucose-rich conditions, transamination reactions play a greater role in converting the glutamate to α-ketoglutarate (51, 52). Additional studies are required to further determine the contexts in which GDH and aminotransferase-catalyzed reactions predominate in melanoma cells and whether or not these findings can be verified *in vivo*.

Like other cancers, melanoma cells can reverse the flow of the TCA cycle via reductive carboxylation of α-ketoglutarate. This process increases the mitochondrial supply of citrate for use in fatty acid synthesis. For hypoxic melanoma cells, reductive carboxylation of glutamine-derived α-ketoglutarate provides over one-third of citrate necessary for fatty acid synthesis (10). In hypoxic WM35 and LU1205 melanoma cells, cytosolic isocitrate dehydrogenase 1 (IDH1) and mitochondrial isocitrate 2 (IDH2), 2 of 3 isoforms of IDH, are necessary and sufficient for the production of reductive carboxylation in hypoxic conditions (53) (**Figure 1**). Likewise, Mullen et al. demonstrated that IDH1 and IDH2 mediate reductive carboxylation in 143B human osteosarcoma cells with mitochondrial defects (54). In contrast, Metallo et al. utilized cells from multiple cancer types to demonstrate that IDH1 predominates in hypoxic conditions (55). Furthermore, IDH1 also predominates in monolayer detachment of multiple lung adenocarcinoma cell lines (56). With melanoma-specific findings limited to work performed on only two cell lines, additional work remains to fully understand the relative contributions of IDH1 and IDH2 to reductive carboxylation in melanoma and if these findings can be replicated in *in vivo* experiments.

A great deal of attention has been placed on IDH1 and IDH2 in recent years as heterozygous mutations have been identified at R132 in the cytosolic IDH1 and at R172

in mitochondrial IDH2 in glioblastoma and acute myeloid leukemia (53, 57-59). These mutated enzymes produce 2-hydroxyglutarate (2-HG) from alpha-ketoglutarate. 2-HG acts as an oncometabolite by inducing a variety of epigenetic changes in the tumor cells (60, 61). Mutations in IDH1/2 are rare in melanoma and typically affect IDH1 (53, 62). These mutations have shown to provide a growth advantage to melanoma cell lines with concurrent BRAF mutations (63). While succinate dehydrogenase and fumarate hydratase mutations have also been identified in a variety of cancers, they have not been identified in melanomas (12).

1.1.3d - Protein/Amino Acid Metabolism: Arginine, Proline, and Proteasomal Degradation in Human Melanomas

In addition to glutamine and aspartate, a considerable amount of amino acid research in melanoma has focused on arginine and proline. Interestingly, melanomas cannot synthesize their own arginine, as they lack expression of arginine synthetase (64). Thus, they are solely dependent on external sources of arginine in the TME for protein synthesis (65). While efforts have been made to starve melanoma cells by depleting them of arginine, this strategy has been complicated by resistance mechanisms in which arginine synthetase is stimulated following arginine depletion (66).

The limited supply of arginine directly impacts the synthesis of proline in melanoma cells, as it makes the cells largely dependent on glutamine for the synthesis of proline as opposed to using both arginine and glutamine to synthesize proline (60). Melanoma cells synthesize proline to a significantly greater extent than melanocytes (10, 67). Three isoforms of pyrroline-5-carboxylate reductase (PYCR) catalyze the rate-

limiting reaction of proline synthesis (67). PYCR1 and 2 are localized to the mitochondria and utilize glutamate and NADH to produce proline, while PYCRL is localized to the cytoplasm and utilizes NADPH and arginine-derived ornithine to produce proline (67). Only *PYCR1* and *2* are overexpressed in melanoma cells compared to melanocytes, suggesting that only glutamate-derived proline synthesis provides melanoma cells with a survival advantage (67). Given NADPH's critical role in maintaining redox balance in melanoma cells, it has been proposed that cells select against *PYCRL* expression in order to preserve NADPH levels, though this explanation remains to be explored further (13, 60). The potential role of proline in redox balance is further supported by the fact that melanoma cells synthesize proline regardless of the concentration of proline in the surrounding environment, suggesting that the act of synthesizing proline is significantly more important than proline itself (13). It is possible that melanoma cells synthesize proline via PYCR1 and PYCR2 to replenish the cellular supply of NAD^+ for use in glycolysis while preserving NADPH necessary for anabolic reactions and for managing oxidative stress.

While physiological proteasomal degradation of proteins is essential for the health of normal cells, melanoma cells take advantage of this existing machinery to rid themselves of various tumor suppressor proteins. For example, Healey et al. utilized Tyr/Tet-Ras $INK4a^{-/-}$ transgenic mice, and R545 melanoma cells isolated from their tumors, to demonstrate that Ras-mediated melanomas target the Inducible cAMP early repressor (ICER) for proteasomal degradation (68). Without functional ICER protein, the tumor cells upregulated the transcription of *cyclin D1*, an essential mediator of cell cycle progression (68). Likewise, *p53* mutations are relatively uncommon (~20%) in melanoma (69-73). However, Mouse double minute 2 homolog (MDM2) can still freely suppress the

transcriptional activity of p53 and target p53 for proteasomal degradation (74). Anwar et al. derived 8B20 cells from a genetically engineered mouse model (GEMM) of melanoma to demonstrate that low levels of p53 protein in the cells resulted from increased ubiquitin-mediated proteasomal degradation (75). Their attempts at disrupting this uncontrolled degradation of p53 protein triggered G1 cell cycle arrest in the 8B20 cells (75). Similarly, nutlins are a class of compounds that disrupt the interactions between MDM2 and p53. By preventing the unregulated degradation of p53, nutlin-3 restores p53 levels in human melanoma cell lines, regardless of p53 mutational status (76, 77). However, nutlin-3 selectively decreases the viability of cells with wild-type p53 (76, 77). Interestingly, nutlin-3 treatment increases cellular levels of MDM2, resulting in ubiquination and degradation of Insulin-like growth factor type 1 receptor (IGF-1R) (77). The disruption of the IGF-1R signaling axis causes an initial increase in melanoma cell proliferation but ultimately suppresses proliferation and inhibits migration (77). These examples demonstrate the tendency of melanoma cells to hijack common cellular machinery to promote their own survival and how doing so makes them vulnerable to novel classes of therapeutics.

1.1.3e - Lipid Metabolism: Synthesis and Degradation of Fatty Acids Promotes Melanoma Progression

Fatty acid synthase (FASN) catalyzes the rate-limiting step of the endogenous synthesis of fatty acids (78). FASN is positively regulated in normal tissue by insulin and hormones such as estrogen and progesterone and negatively regulated by leptin, which in turn is stimulated by free fatty acids (FFAs) (78-80). Insulin, estrogen, and progesterone

activate the transcription factor sterol regulatory element-binding protein 1c (SREBPC1c), which is responsible for driving *FASN* transcription (78-80). In many tumor types, including melanoma, SREBPC1c is constitutively driven by the MAPK and PI3K/AKT pathways, which causes significant upregulation of FASN (78-80) (**Figure 1** and **Table 1**). These signaling pathways promote the maturation of SREBP1c from its precursors and its nuclear localization from the Golgi apparatus following its maturation (78). The increased FASN is believed to provide a survival benefit to tumor cells by promoting a "lipogenic phenotype." Fatty acids form the structural foundation of cellular and organelle membranes. Proliferating cells require a large supply of fatty acids to form these structures. Constitutively active FASN ensures an adequate concentration of phospholipids necessary for this rapid proliferation (78). Saab et al. demonstrated that patient-derived metastatic melanomas test positive for FASN staining, as opposed to benign intracapsular nodal nevi (81).

Additionally, melanomas overexpress numerous genes involved in synthesis of sialylated glycosphingolipids known as gangliosides. For example, microarray analysis performed by Sumantran et al. determined that UDP-glucose ceramide glucosyltransferase (*UGCG*), hexosaminidase A (*HEXA*), ST3 β-galactoside α-2,3-sialyltransferase 5 (*ST3GAL5*), and ST8 α-N-acetyl-neuramide-α-2,8-sialyltransferaase 1 (*ST8SIA1*), all of which are involved in ganglioside synthesis, are upregulated in melanomas between 3 and 9-fold, relative to benign nevi (82). Subclones of M4BE melanoma cells enriched in gangliosides survive radiation treatment significantly better than parental cells (83). Furthermore, ganglioside $GD3^-$ SK-MEL-28-N1 melanoma cells became significantly more proliferative and invasive following transfection with GD3 via stimulation of p130Cas and paxillin signaling (84). siRNA-mediated knockdown of p130Cas and

paxillin subsequently inhibited ganglioside GD3 signaling in these cells, though the effects remain to be validated *in vivo* (84).

In addition to the synthesis of fatty acids, fatty acid oxidation (FAO) appears to play an important role in promoting melanoma progression. For example, carnitine palmitoyltransferase 2 (*CPT2*), the enzyme critical for translocation of long-chain fatty acids (LCFAs) in preparation for β-oxidation, is one of the most significantly upregulated genes in melanomas, relative to benign nevi (82). Furthermore, Rodrigues et al. derived metastatic $4C11^+$ cells from melan-a melanocytes after sequential detachment-re-adhesion cycles, and FAO contributed significantly to the energy reserves of these $4C11^+$ cells, relative to nonmetastatic controls (85). How FAO promotes melanoma progression remains unclear. Studies in other tumor types have demonstrated that fatty acids can provide an ATP boost for tumor cells when necessary under nutrient-depleted conditions (86-88). Indeed, the process of metastasis is a highly demanding process. Highly efficient β-oxidation could provide a survival advantage for cells away from the primary tumor site. Furthermore, fatty acids can serve as a valuable source of acetyl-CoA that contributes to citrate formation after entering the TCA cycle (87). As detailed earlier, this citrate can enter metabolic reactions that produce NADPH via IDH1, thereby contributing to redox balance in the tumor cells.

Numerous lipid-derived second messengers such as phospholipase D3 (*PLD3*), inositol triphosphate protein kinase B (*ITPKB*), and inositol triphosphate receptor 3 (*ITPR3*) are significantly upregulated in melanomas, relative to benign nevi (82). Furthermore, *ITPKB* is significantly upregulated in MALME_3M and UACC_257 melanoma cell lines of the National Cancer Institute (NCI) Cell Miner database (82).

1.2 - MOLECULAR BIOLOGY AND IMMUNOLOGY OF MELANOMA BRAIN METASTASES

1.2.1 - Signaling Pathways Implicated in Melanoma Brain Metastases

Focused studies have identified numerous signaling pathways that likely contribute to melanoma brain metastasis (MBM) pathogenesis, including the MAPK, PI3K-AKT, Janus kinase-signal transducer and activator of transcription (JAK-STAT), vascular endothelial growth factor (VEGF), and endothelin pathways. Additional molecules and pathways have been implicated in many of the steps that are critical to the establishment and maintenance of MBMs (**Table 2**).

1.2.1a - MAPK Pathway

Point mutation analysis of patient-matched MBMs and extracranial metastases (ECMs) demonstrated no significant differences in the prevalence of *BRAF* mutations between anatomical sites (89). Data regarding *NRAS* mutation concordance between anatomical sites differs depending on if the comparison occurs between MBMs and ECMs or between MBMs and primary tumors. Analysis of patient-matched MBMs and ECMs identified 100% concordance in *NRAS* mutations while significantly lower concordance (80%) was observed between patient-matched MBMs and primary tumors (89, 90). While no concordance data exist for *NF1* mutations, it is clear that MAPK pathway hyperactivation is highly prevalent in MBMs, which is consistent with the fact that

activating *BRAF* and *NRAS* mutations occur early in melanoma progression and are likely not selected against during the brain metastasis cascade (91, 92).

Table 2: Signaling pathways implicated in melanoma brain metastasis pathogenesis

Pathway	Alterations in Melanoma Brain Metastases	Significance
MAPK	• High concordance in *BRAF*/*NRAS* mutation status in MBMs and patient-matched ECMs and primary tumors • No information known about *NF1* concordance between MBMs and patient-matched ECMs and primary tumors	• Constitutive activation that parallels ECMs • Fundamental driver of melanoma pathogenesis • No evidence of selection against MAPK pathway hyperactivation during metastasis to the brain
PI3K-AKT	• Higher expression of numerous markers of PI3K-AKT activation ± lower expression of PTEN in MBM specimens compared to lung and liver metastases	• Pathway hyperactivity is selected for during the process of metastasis and/or the product of interactions with the brain TME • Precise mechanism by which pathway activation promotes MBM pathogenesis remains unclear
JAK-STAT	• Significantly higher levels of P-STAT3 in MBMs vs. primary tumor specimens • Significantly lower levels of SOCS1 (negative regulator of P-STAT3) in MBMs vs. primary tumor specimens	• Drives transcription of pro-invasive and angiogenic genes
VEGF	• Expression correlates with brain-metastatic capacity in melanoma cells *in vivo* • Forced expression promotes melanoma cell metastasis to the brain *in vivo*	• Stimulates formation of new blood vessels • Promotes co-option of existing blood vessels • Facilitates MBM growth
Endothelin	• *EDNRB* expression correlates with brain-metastatic capacity in melanoma cells	• EDNRB promotes a general metastatic phenotype • Targeting EDNRB prevents visceral metastasis and growth of brain metastases
BBB Penetration Factors	• *VLA-4* expression present in 90% of MBMs • *HPSE* is expressed at higher levels in brain-metastatic melanoma cells • *PLEKHA5* expression is significantly higher in brain-metastatic melanoma cells and in melanoma ECMs from patients that developed MBMs vs. those that did not • *S100A4 o*verexpression correlates with increased brain metastatic capacity of melanoma cells *in vivo* • *MMP2* expression is significantly higher in cells able to cross *in vitro* BBB models	• Promote invasion across the BBB for access to the brain parenchyma
Brain-Tropic Factors	• Melanoma cells that establish parenchymal metastases express significantly more *TGF-β* than those that establish leptomeningeal metastases • Brain-metastatic melanoma subclones express significantly less *CLDN1* than parental cells	• Promote the development of parenchymal metastases exclusively, as opposed to a general metastatic phenotype

1.2.1b - PI3K-AKT Pathway

PI3K-AKT pathway activation occurs frequently during tumorigenesis in multiple cancer types and promotes the malignant phenotype through multiple effectors (93, 94). The pathway can be activated via receptor tyrosine kinases (RTKs) following stimulation by extracellular ligands [e.g. hepatocyte growth factor (HGF) activating tyrosinase kinase protein Met (c-MET)], point mutations in RTKs [e.g. epidermal growth factor receptor (*EGFR*) in non-small-cell lung cancers], and/or gene amplifications in RTKs [e.g. receptor tyrosine-protein kinase erbB-2 (*HER2/neu*) in breast cancer]. The pathway can also be activated by mutations in key effectors, including point mutations in *PIK3CA* (encodes the catalytic subunit of PI3K), *AKT1*, and *AKT3*. Constitutive activation of the pathway also results from loss of function of the tumor suppressor PTEN, which dephosphorylates lipids to counteract the activity of PI3K.

In melanoma, point mutations rarely activate the pathway, affecting *AKT1* and *AKT3* in 1-2% of cases and *PIK3CA* in 3% (70, 95, 96). Mutations more commonly affect the *NRAS* gene, primarily at codons Q60/61 and G12/13, which results in constitutive activation of both the MAPK and PI3K-AKT pathways. Additionally, complete loss of PTEN has been detected in 10-30% of melanomas, generally in tumors with concurrent *BRAF* mutations, and thus mutually exclusive with *NRAS* mutations (97, 98). Missense mutations that inhibit the tumor suppressor function of PTEN have been recorded and typically occur in exon 5 of the *PTEN* gene, which encodes the phosphatase domain of the protein. Nonsense mutations are more common genetic causes of loss of PTEN function in melanomas (99). Interestingly, genetic aberrations might not explain all instances of loss of *PTEN* expression in melanomas. Epigenetic events including miRNA signaling

and promoter methylation can silence *PTEN* expression and may facilitate PI3K-AKT pathway hyperactivation in melanomas (100, 101). However, more recent genomic studies of the melanoma TCGA database that employed optimized criteria for identifying copy number alterations demonstrated that only point mutations or high-medium amplitude focal deletions corresponded with complete loss of *PTEN* expression and significant increases in P-AKT levels (102).

Unlike the MAPK pathway, a significant difference in PI3K-AKT pathway activation has been observed in MBMs compared to metastases at other sites. Reverse phase protein arrays (RPPA) analysis demonstrated significantly higher expression of numerous markers of PI3K-AKT activation and lower expression of PTEN in MBM specimens compared to lung and liver metastases (98). Subsequent RPPA analysis of patient-matched MBMs and ECMs confirmed PI3K-AKT pathway hyperactivation in MBMs, yet failed to demonstrate significant differences in PTEN protein levels (89). Immunohistochemistry (IHC) of an independent cohort of patient-matched samples also demonstrated PI3K-AKT pathway hyperactivation in MBMs, with some (but not all) of the brain lesions demonstrating decreased PTEN expression compared to the patient-matched ECMs (103). Together, these findings suggest that PI3K-AKT pathway hyperactivation plays an important role in MBM pathogenesis and that pathway activation can occur independently of loss of PTEN expression.

PI3K-AKT hyperactivation plays multiple roles in MBM pathogenesis by facilitating cell adhesion, extravasation, and angiogenesis. One study of patients with stage III melanoma determined that loss of PTEN protein levels correlated with significantly increased risk of MBM formation (97). Similarly, experiments by Cho et al. using a genetically engineered mouse model showed that PI3K-AKT pathway activation

promoted MBM formation. Loss of *Pten* in melanocytes with concurrent $Braf^{V600E}$ mutations and cyclin-dependent kinase inhibitor 2A (*Cdkn2a*) deletions formed primary melanomas in 100% of mice but infrequently caused distant metastases. However, introduction of a constitutively active Akt1 protein promoted MBM formation in 80% of mice (104). Together, these findings suggest that PI3K-AKT pathway hyperactivation promotes MBM formation, and primary tumors and ECMs enriched in this pathway may metastasize to the brain more frequently.

The TME also appears to play a critical role in mediating PI3K-AKT pathway hyperactivation. Zhang et al. demonstrated that loss of *PTEN* expression occurred following intracarotid injection of PTEN-intact cell lines from multiple tumor types, including B16-F10 melanoma cells (101). Astrocytes in contact with the tumor cells transferred miRNAs that suppressed expression of *PTEN* via exosomes. Interestingly, loss of *PTEN* expression promoted secretion of the cytokine C-C motif chemokine ligand 2 (CCL2), which recruited Iba1+ myeloid cells that promoted growth of the tumor cells. In contrast, the authors failed to observe differences in metastatic incidence between B16-F10 cells expressing *PTEN* and those in which *PTEN* was silenced. Further, Seifert et al. provided additional evidence that cerebrospinal fluid (CSF), which bathes the brain, can promote PI3K-AKT pathway activation (105). Culturing melanoma cells in the presence of CSF caused significant activation of the PI3K-AKT pathway and mediated resistance to targeted therapies without causing a loss of *PTEN* expression.

1.2.1c - JAK-STAT Pathway

The JAK-STAT pathway transduces signals from a variety of ligands – often cytokines such as interleukins and interferons - from the cell surface to the nucleus of tumor cells. Unlike RTKs, cytokine receptors typically lack intrinsic kinase activity. Instead, ligand binding triggers dimerization of receptors, which recruits and activates JAKs in the cytoplasm. In turn, JAKs phosphorylate the receptor, which facilitates binding of STAT proteins to the receptor. JAKs then phosphorylate and activate the STATs, which dimerize and move into the nucleus to drive transcription of genes (106).

STAT3 activity facilitates transcription of tumor cell survival, growth, angiogenesis, and immunosuppressive genes such as B-cell lymphoma 2 (*BCL2), c-MYC*, *Cyclin D1 (CCND1), VEGF-A*, and interleukin-10 (*IL-10*) (107). STAT3 has also been implicated in MBM pathogenesis. Xie at al.'s analysis of MBMs demonstrated significantly stronger staining for phosphorylated STAT3 (P-STAT3) in MBMs compared to primary tumors. In addition, the introduction of a constitutively active form of P-STAT3 transformed nonmetastatic A375P cells into highly brain-metastatic cells but did not alter the growth rates of cells implanted subcutaneously. Likewise, brain-metastatic TXM-18 melanoma cells lost their brain-metastatic capacity following suppression of P-STAT3 (108). Huang et al. demonstrated that overexpression of suppressor of cytokine signaling 1 (*SOCS1*), a negative regulator of JAK-STAT signaling, prevented brain-metastatic melanoma cell lines from forming MBMs following intracarotid injections (109). Mechanistic studies determined that JAK-STAT signaling promoted beneficial angiogenesis and invasion signaling cascades by increasing transcription of *VEGF-A* and matrix metalloprotease-2 (*MMP-2*) (108, 109). While these findings implicate JAK-STAT signaling in MBM pathogenesis, enforced expression of P-STAT3 also promoted melanoma cell metastasis to the lungs of mice, while suppression of P-STAT3 prevented

lung metastasis formation (108). Together, these findings suggest that JAK-STAT signaling may promote the general process of melanoma metastasis instead of metastasis specifically to the brain.

1.2.1d - VEGF

The VEGF signaling cascade is mostly mediated through the binding of the VEGF-A (VEGF) ligand to the VEGFR2 receptor on endothelial cells (110). Binding of the ligand to the receptor triggers activation of the PI3K-AKT, phospholipase Cγ, and Src family kinase signaling pathway to promote angiogenesis and vascular permeability (111, 112). Yano et al. used a panel of cell lines from multiple tumor types – including melanoma – to demonstrate that *VEGF* expression correlates with brain metastatic capacity *in vivo*. Cells expressing high levels of *VEGF* formed large, rapidly growing metastases while cells lacking *VEGF* expression formed small, poorly growing metastases (113). Additionally, forced overexpression of *VEGF* facilitated growth of MBMs formed by MEL57 cells following intracarotid injection. Interestingly, *VEGF* expression did not induce the formation of new vessels but rather caused beneficial co-option of existing blood vessels (114). This propensity for vascular co-option agrees with pathological assessments of human brain metastases that determined vascular co-option occurs more often in MBMs relative to metastases of other tumor types (115).

1.2.1e - Endothelins

Endothelin signaling appears to facilitate spread of melanomas to the brain. Cruz-Munoz et al. established a mouse model of spontaneous melanoma metastasis and determined via microarray analysis that brain-metastatic WM239 variants significantly overexpressed endothelin receptor B (*EDNRB)* compared to visceral metastatic variants. However, the visceral variants did not overexpress *EDNRB* compared to nonmetastatic variants. Forced overexpression of *EDNRB* in the visceral metastatic variants increased overall metastatic incidence and promoted metastasis to the brain. Pharmacological inhibition of EDNRB inhibited lung metastasis formation and brain metastasis growth. Together, these findings suggest that EDNRB promotes a general metastatic phenotype but plays a critical role in the formation of MBMs (116).

1.2.2 - Factors That Promote Penetration of the Blood Brain Barrier (BBB)

The BBB is a network designed to protect the brain by restricting free access of blood products to the brain parenchyma. Brain capillary walls are composed of endothelial cells connected via tight junctions, end-foot process of astrocytes surrounding the capillaries, and pericytes embedded in the basement membrane of the capillaries (117). Together, this BBB limits free passage into the brain to small (<400 Da) lipophilic molecules (118). Circulating melanoma cells must cross this BBB to access the brain parenchyma during a process known as *extravasation*. As described below, a variety of factors appear capable of contributing to this process (119, 120).Very late antigen 4 (VLA-4) mediates adhesion of melanoma cells to vascular cell adhesion molecule 1 (VCAM-1) on the surface of endothelial cells, which facilitates arrest in capillaries and successful extravasation. *VLA-4* expression promoted melanoma cell migration across several immortalized endothelial cell lines, and *VLA-4* inhibition prevented the formation

of melanoma lung metastases *in vivo* (121, 122). To assess the role of VLA-4 in MBM pathogenesis, Garcia-Martin et al. utilized a tissue microarray and determined that over 90% of MBMs express VLA-4. They subsequently constructed a mouse *in vitro* BBB model and observed that inhibition of VLA-4 prevented melanoma cells from adhering to the endothelial cells and migrating across the BBB (121). The exact route by which melanoma cells transverse the BBB remains unclear. Melanoma cells might utilize the paracellular route by degrading tight junction proteins via serine proteases such as seprase. Analyses of A2058 and B16-F10 melanoma cells demonstrated that secretion of seprase allowed these cells to migrate across an *in vitro* model of the BBB. Pharmacological and siRNA-mediated inhibition of seprase effectively prevented their transmigration across the BBB (123). However, the role of seprase in mediating extravasation has not been confirmed *in vivo*. Heparanase (HPSE) is an enzyme that degrades heparan sulfate chains in endothelial cell layers and appears to mediate extravasation. Murine (B16B15b) and human (70W) cells selected for their brain-metastatic capacity displayed significantly higher HPSE production and activity compared to their parental cell lines (B16F1 and MEWO) (124). Additionally, *in vitro* treatment of B16B15b cells with HPSE increased their ability to invade a brain slide model. Pharmacological inhibition of HPSE mitigated this effect (125). Interestingly, co-culturing brain-metastatic melanoma cells with syngeneic astrocytes or nerve growth factor (NGF) – a growth factor secreted in the brain - significantly enhanced their secretion of HPSE and invasiveness, indicating that normal brain tissue plays a role in facilitating the entrance of metastatic melanoma cells into the parenchyma (126, 127). To date, *in vivo* studies assessing HPSE's role in BM pathogenesis have been limited to breast cancer. Zhang et al. determined that breast cancer brain metastases lose expression of *miRNA-1258*, which is a key suppressor HPSE production. Further, *microRNA-1258* expression levels negatively correlated with the brain metastatic capacity of breast cancer cells. Transfection of *miRNA-1258* in breast cancer cells

significantly inhibited brain metastasis formation in an experimental model of metastasis (128). Interest in the role of pleckstrin homology domain containing A5 (PLEKHA5) in MBMs arose following Jilaveanu et al.'s integrative comparative analysis of a brain metastatic A375P subclone (A375Br) and the parental line and between ECMs from patients that did and did not develop MBMs (129). Gene expression profiling determined that *PLEKHA5* expression was significantly higher in A375Br cells, and in ECMs from patients that developed MBMs. Interestingly, *PLEKHA5* expression correlated only with formation of metastases in the brain. *PLEKHA5* suppression inhibited survival of A375Br cells and their ability to invade an *in vitro* BBB model. However, these findings have not been confirmed *in vivo*.

Studies of the A375 cell line's interactions with an *in vitro* BBB demonstrated that secretion of S100A4 calcium-binding protein A4 (S100A4) mediated BBB invasion by facilitating a loss of tight junction integrity (130). Binding of S100A4 to its receptor [receptor for advanced glycation end products (RAGE)] suppressed expression of the tight junction proteins occludin and VE-cadherin. These findings were confirmed *in vivo* where forced overexpression of *S100A4* increased brain metastasis formation of A375 cells following intracardiac injection. However, *S100A4* overexpression also stimulated metastasis to other anatomical sites, suggesting that S100A4 promotes a generic pro-metastatic phenotype as opposed to a brain-metastatic phenotype.

Studies across multiple tumor types have also implicated MMPs in tumor cell invasion and metastasis through their ability to proteolytically degrade components of the extracellular matrix (131). MMP-2 appears to mediate extravasation across the BBB. MMP-2 catalyzes the breakdown of type IV collagen, which forms a critical component of the basement membrane of endothelial cells in the BBB (131). Correlation studies determined that tumor *MMP-2* expression levels predict worse survival in patients (132). Gene expression studies established that *MMP-2*

is expressed significantly higher in primary melanoma cultures able to invade an *in vitro* model of the BBB compared to poorly invasive primary melanoma cultures (133). Interestingly, astrocytes facilitate expression of *MMP-2* in melanoma cells by secreting interleukin-23 (IL-23) (134). Tang et al. determined that IL-23 stimulates secretion of IL-17 by γδ T cells. The IL-17 drives increased levels of P-STAT3 through interleukin-6 (IL-6) and is likely the means by which this signaling axis promotes *MMP-2* transcription (135).

1.2.3 - Homing to the Brain

Circulating melanoma cells arrest in brain capillaries once they exceed the capillary in size (136). Additionally, they express numerous adhesion factors including integrins (including VLA-4, as previously described) and selectins that promote the arrest of the cells within the capillaries. Thus, mechanical factors promote the spread of melanoma cells to the brain. Consistent with Stephen Paget's "seed and soil" hypothesis, however, numerous additional factors (including the PI3K-AKT pathway, as previously described) appear to promote metastasis specifically to the brain.

Using miRNA expression profiling and three cohorts of clinical primary melanomas, Hanniford et al. derived a miRNA signature (*miR-150–5p, miR-15b-5p, miR-16–5p,* and *miR-374b-3p)* that predicted the likelihood of brain metastasis formation (137). Further, their signature distinguished primary melanomas that initially metastasized to the brain from those that metastasized to the brain along with other extracranial sites, suggesting that their signature might predict brain tropism. Zhang et al. demonstrated that TGF-β signaling is necessary for metastasis to the brain parenchyma (138). K1735 cells exclusively formed metastases in the brains of mice following intracarotid injections while B16F10 cells formed metastases in the ventricles. K1735

cells expressed high levels of *TGF-β2* while B16F10 cells lacked expressed of *TGF-β2*. Forced overexpression of *TGF-β2* in B16F10 cells promoted metastasis to the parenchyma while suppression of *TGF-β2* in K1735 cells inhibited metastasis to the brain parenchyma. Gene expression studies identified significantly higher levels of C-C chemokine receptor 4 (*CCR4*) in cell lines from MBMs compared to cell lines from cutaneous tumors (139). Klein et al. confirmed these findings by comparing flow cytometry results between YDFR.CB4, M12.CB3, and M16.CB2 brain-metastatic variants and their parental cell lines (YDFR.C, M12.C, and M16.C). They also determined that astrocytes and microglia secrete known CCR4 ligands and that incubation of these glial cells in brain metastasizing melanoma cell-conditioned media upregulates their secretion of CCR4 ligands. Further, incubation of YDFR.C cells overexpressing *CCR4* with CCR4 ligands facilitated transmigration across an *in vitro* BBB model, and pharmacological inhibition of CCR4 prevented metastasis of these cells to the brain *in vivo*. Together, these studies strongly implicate CCR4 in MBM pathogenesis (139). However, analysis of clinical specimens determined that both MBMs and lymph node metastases expressed *CCR4* at significantly higher levels than primary tumors, but *CCR4* expression did not differ between MBMs and lymph node metastases, suggesting that CCR4 might not mediate metastasis exclusively to the brain (140). In contrast, brain-metastatic YDFR cells express significantly less claudin-1 (*CLDN1*) than their parental cells (141). Forced overexpression of *CLDN1* in brain-metastatic YDFR cells significantly inhibited the formation of MBMs *in vivo* but had no effect on the formation of lung metastases, indicating that CLDN1 promotes melanoma metastasis exclusively to the brain (142).

1.2.4 - Comprehensive Molecular Analyses of Melanoma Brain Metastases

Global molecular characterization of MBMs was once quite limited. The studies that had been performed demonstrated that MBMs possess unique molecular features compared to metastases that form at other anatomical sites. Gene expression microarray studies identified numerous differentially expressed genes between MBMs and ECMs (89, 143). However, the microarray studies featured a relatively small number of samples, including very few patient-matched metastases, and overall failed to identify significantly enriched pathways. Whole exome sequencing (WES) analysis of multiple tumor types has identified significant differences between BMs and primary tumors, including three tumors from three melanoma patients (144). The analyses demonstrated significantly divergent evolution of BMs following metastasis from the primary tumors, yet minimal divergent evolution between multiple BMs from the same patient.

Gene expression microarray analyses of breast, lung, colorectal, and melanoma cell lines suggest that the brain TME can trigger a fundamental reprogramming of cell lines grown in mouse brains compared to those grown in subcutaneous tissue or orthotopic sites (145). Cells grown in the brain overexpressed thousands of genes and acquired neuronal cell characteristics following epigenetic changes induced by interactions with surrounding astrocytes. Interestingly, co-culturing tumor cells with astrocytes replicated this reprogramming. These studies highlighted the importance of the TME in regulating tumor cell biology.

Recently, we performed RNA-sequencing (RNA-seq) on the largest cohort of MBMs to date, and the largest cohort of patient-matched brain metastases and ECMs from any tumor type, and provided new insights into the pathogenesis of these tumors. Similar to melanoma regional (70) and distant metastases (146), our analysis demonstrated significant heterogeneity of the expression of immune related gene sets between MBMs from different patients. Immune infiltration correlated with prolonged overall survival (OS), which corroborates findings from previous studies (143, 147).

Our analysis of MBMs and patient-matched ECMs identified suppression of multiple components of the anti-tumor immune response in MBMs. Unsupervised hierarchical clustering of RNA-seq data for the 500 most variable genes (those with the greatest variance across samples) from 35 MBMs and 42 patient-matched ECMs (from 29 patients) showed that nearly all samples clustered by patient ID rather than by tissue site, suggesting overall similar gene expression patterns between MBMs and ECMs from individual patients (**Figure 3A**). However, further analysis of patient-matched MBMs and ECMs identified 494 differentially expressed genes (DEGs). Pathway analysis of numerous gene sets repeatedly indicated that MBMs are characterized by (1) suppression of immune cell networks and (2) upregulation of nervous system pathways. ImmuneScores – a 142 gene signature able to predict the extent of intratumoral immune cell infiltration – were significantly lower in the MBMs compared to the patient-matched ECMs, even after omitting lymph node (LN) ECMs from the analysis (**Figure 3B**). IHC staining confirmed significantly lower $CD3^+$ and $CD8^+$ T cell infiltration in the MBMs vs. patient-matched non-LN ECMs (**Figure 3C-D**), but no significant difference in $PAX5^+$ B cells was detected (**Figure 3E**). MCP-Counter analysis – a cell type quantification algorithm used to estimate immune cell populations from gene expression data – of other immune cell classes identified significantly fewer monocytic lineage cells and myeloid dendritic cells in MBMs; no significant difference in natural killer (NK) cells; and significantly more neutrophils in MBMs. We examined molecular features associated with immunosuppression and did not identify significant differences in membranous or cytoplasmic β-catenin expression or PTEN loss between MBMs and patient-matched ECMs. We also did not detect a significant difference in PD-L1 expression between the MBMs and ECMs overall, but discordant PD-L1 expression (MBM^+/ECM^- or MBM^-/ECM^+) was detected in 40% of patient-matched samples (**Figure 3F**). In addition, comparative analysis of RNA-seq data from a cohort of unmatched primary melanomas (148) identified

decreased ImmuneScores, myeloid dendritic cells, T cells, B lineage cells, and neutrophils in MBMs.

To supplement our transcriptomic profiling, we performed WES on patient-matched MBMs (n=21) and ECMs (n=23) from patients (n=17) with germline DNA and sufficient tissue available. We observed no significant difference between the overall number of genes with nonsynonymous somatic mutations between the patient-matched MBMs and ECMs, nor in the mutation rate of 74 therapeutically targetable genes (149). TCR-seq was performed on patient-matched MBMs (n=11) and ECMs (n=16) with sufficient DNA from 10 patients. Mean clonality did not differ between matched pairs (**Figure 3G**). Observed richness, however, was significantly lower in the MBMs (**Figure 3H**). Together the results indicate that while T cells present in MBMs are equally reactive as T cells in the ECMs, there is a significantly less diverse repertoire of T cell clones in MBMs. To evaluate T cell repertoire heterogeneity, we calculated the Morisita Overlap Index (MOI) (150), which identified minimal similarity in the T cell repertoires between MBMs and patient-matched ECMs (**Figure 3I**). This suggests divergent tumor immunogenicity associated with metastasis to the brain.

As previous studies have shown that $CD8^+$ T cell and other immune cell infiltrates correlate positively with responsiveness to anti-PD-1 immunotherapy in melanoma (151, 152), this result provides a potential explanation for the relatively disappointing intracranial response rates (ICRR) observed with pembrolizumab (18%) (153) and nivolumab (20%) (154). Notably, the ICRR for combined immunotherapy with ipilimumab and nivolumab appears to be more promising (154, 155), perhaps consistent with studies suggesting that the baseline T cell infiltrate is less critical to the efficacy of this regimen (156).

The cause for MBM immunosuppression remains unclear. While it might be tempting to blame the BBB for physically impeding immune cells from accessing MBMs, several lines of

evidence challenge this conclusion. BBB disruption occurs in numerous neurological diseases such as multiple sclerosis, stroke, and epilepsy. In each case, the BBB is unable to restrict the entry of immune cells into the brain parenchyma and prevent an inflammatory state as it typically does in a normal, healthy brain (157). MBMs induce significant leakage in the BBB during the processes of extravasation and angiogenesis. The previously described factors HPSE, MMP-2, and S100A4 damage the integrity of the BBB to promote extravasation into the parenchyma, and VEGF causes vessels to leak as it stimulates angiogenesis. Clinical imaging findings confirm MBM-induced BBB leakage. For example, MBMs take up gadolinium contrast agent during MRI imaging while normal brain parenchyma fails to do so. Additionally, immunotherapy with anti-CTLA4 and anti-PD1 antibodies achieve clinical responses in patients with MBMs (158, 159). Both of these treatments depend on T cells crossing the BBB and accessing the tumor. Clinical responses to these agents indicate that the BBB is not able to prevent the entry of T cells into the brain parenchyma. Together, these findings indicate that physical barriers cannot explain the immunosuppression observed in MBMs.

Several key signaling pathways mediate immunosuppression in melanoma ECMs and play critical roles in MBM pathogenesis. For example, Peng et al. observed that loss of PTEN stimulates PI3K-AKT pathway activation and secretion of VEGF in melanomas (160). Expression levels of VEGF inversely correlated with intratumoral T cell infiltrate and response to adoptive T cell therapy. Further, treatment of PTEN-null melanomas with the selective PI3KB inhibitor GSK2636771 overcame the immunosuppression and promoted response to immunotherapy. However, we did not detect differences in PTEN expression between the matched MBMs and ECMs, although this does not preclude the possibility that PI3K-AKT pathway activation in the MBMs by other mechanisms could contribute to the differences in immune cell infiltrate. We also

did not detect significant differences in either β-catenin expression or nonsynonymous somatic mutation frequency that would explain the observed immune suppression in MBMs (161, 162).

The immunosuppressive effects of TGF-β signaling have been extensively characterized (163, 164). Additionally, Walentynowicz et al. demonstrated that TGF-β2 polarizes glioma-associated macrophages into tumor-supporting cells (165). It is possible that the TGF-β2 signaling axis which is necessary for formation of parenchymal brain metastases also mediates MBM immunosuppression. Further studies would be necessary to confirm this possibility and to elucidate whether or not the mechanisms of TGF-β2-mediated immunosuppression are the same in MBMs as in ECMs. It is also possible that stromal cells may cause immunosuppression in MBMs via STAT3 signaling. Priego et al. performed IHC on 91 BMs, including 2 MBMs, and identified positive P-STAT3 staining in the peritumoral reactive astrocytes of 89% of the BMs.

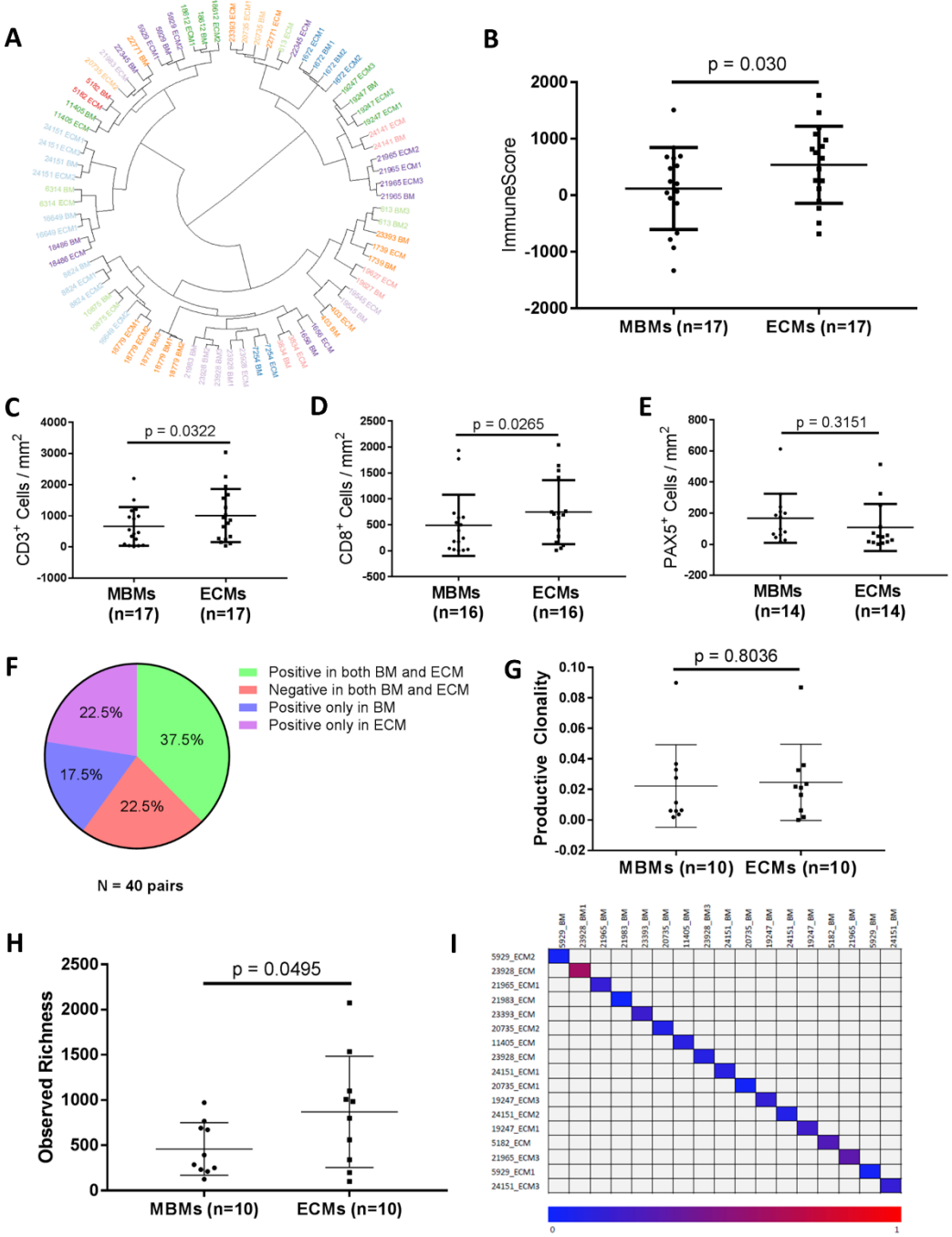

Figure 3: Melanoma brain metastases are immunosuppressed compared to patient-matched extracranial metastases
(**A**) Unsupervised hierarchical clustering of the 500 most variable genes from 35 MBMs and 42 ECMs from 29 melanoma patients. Samples are labeled according to the patient identifier and site. Multiple MBMs or ECMs from the same patient are labeled accordingly. (**B**) ESTIMATE ImmuneScores of MBMs and patient-matched ECMs (lymph nodes excluded). Lines represent mean ± S.D., and each dot represents the average of all MBM or ECM samples from a single patient. Significance determined by two-sided paired Student's *t*-test. (**C-E**) IHC analysis (CD3, CD8, and PAX5) of patient-matched MBMs and non-LN ECMs. Lines represent mean ± S.D., and each dot represents the average of all MBM or ECM samples from a single patient. Significance determined via one-sided paired Student's *t*-test. (**F**) Pie chart showing concordance and discordance for PD-L1 IHC positivity in patient-matched MBMs and ECMs. Each MBM from a single patient was compared against each ECM from the same patient. (**G-H**) Mean clonality and observed richness of patient-matched MBMs and ECMs by TCR-seq. Lines represent mean ± S.D., and each dot represents the average of all MBM or ECM samples from a single patient. Significance determined via two-sided paired Student's *t*-test. (**I**) Quantification of T cell clone repertoire overlap between patient-matched MBMs and ECMs with available TCR-seq data. The color scale indicates the Morisita Overlap Index (MOI) between two tumor samples. Used with permission from the American Association for Cancer Research (AACR). (Fischer, G. M., Y. N. Vashisht Gopal, J. L. McQuade, et al. 2019. Molecular Profiling Reveals Unique Immune and Metabolic Features of Melanoma Brain Metastases. *Cancer Discov.* 9: 628-645).

Further, strong P-STAT3 staining in reactive astrocytes significantly correlated with patient survival. Mechanistic studies determined that the BMs induced P-STAT3 signaling in the astrocytes, which in turn inhibited the activation of $CD8^+$ T cells and promoted the activity of pro-tumor macrophages/microglia expressing cluster of differentiation 74 (CD74). Importantly, inhibition of P-STAT3 signaling in reactive astrocytes inhibited the intracranial growth of the B16/F10-BrM melanoma cell line *in vivo*, suggesting that targeting this signaling axis in reactive astrocytes could be beneficial for patients with MBMs (166).

1.3 - METABOLISM OF MELANOMA BRAIN METASTASES

While there is a growing appreciation for the metabolism of melanomas and molecular features of MBMs, little is known about the metabolism of MBMs. As a first step towards addressing this gap in knowledge, we selected 70 MSigDB KEGG metabolism-specific gene sets and performed a preranked Gene Set Enrichment Analysis (GSEA-P) on the RNA-seq data from our patient-matched MBMs and ECMs. This analysis demonstrated greater enrichment of the KEGG OXPHOS gene set than any other metabolism gene set in the MBMs (**Figure 4A-B**). We used a panel of 15 melanoma cell lines with gene expression and Seahorse Extracellular Flux (XF) Assay data to derive an OXPHOS-Index (OP-Index), a transcriptional signature that correlates with OXPHOS *in vitro*. We found that the majority of MBMs had a higher OP-Index than their patient-matched ECMs, and the average OP-Index of MBMs was significantly higher than the OP-Index of patient-matched ECMs (**Figure 4C**). We confirmed OXPHOS enrichment in unmatched treatment-naïve MBMs (n=29) vs. ECMs (n=33), as well as in the patient-matched treatment-naïve MBMs (n=10) vs. ECMs (n=12) in that subset, excluding the possibility that enrichment of OXPHOS in MBMs was due to differences in prior treatments. The KEGG

OXPHOS gene set was also enriched in treatment-naïve MBMs (n=29) vs. a cohort of primary melanomas with available RNA-seq data (n=54) (**Figure 4D**).

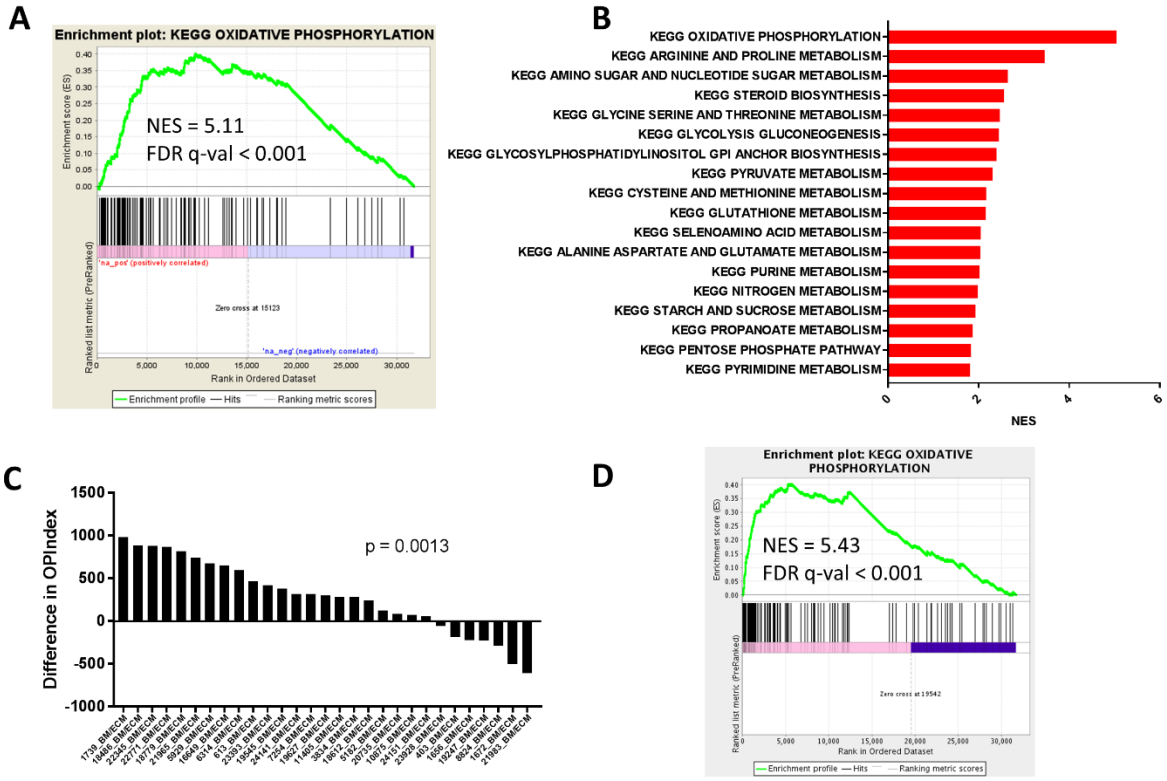

Figure 4: Oxidative phosphorylation is enriched in surgically resected melanoma brain metastases compared to patient-matched extracranial metastases. (**A**) GSEA-P analysis enrichment plot demonstrating significant enrichment of the KEGG OXPHOS gene set in 35 MBMs vs. 42 patient-matched ECMs. Normalized enrichment score (NES) and FDR q-val are listed on the enrichment plot. (**B**) GSEA-P analysis demonstrating all KEGG metabolism pathways significantly altered (FDR q-val<0.05) in MBMs (n=35) vs. patient-matched ECMs (n=42). Up-regulated gene sets are shown in red. The NES forms the x-axis. No down-regulated gene sets met the criteria for statistical significance. (**C**) Differences of OXPHOS-Index (OP-Index) in MBMs vs. patient-matched ECMs. For patients with multiple tumors, the difference was calculated using the average of all MBMs and the average of all ECMs. Significance determined via two-sided paired Student's *t*-test. (**D**) GSEA-P analysis enrichment plot demonstrating significant enrichment of the KEGG OXPHOS gene set in 29 treatment-naive MBMs vs. 54 primary tumors. NES and FDR q-val are listed on the enrichment plot. Used and modified with permission from the American Association for Cancer Research (AACR). (Fischer, G. M., Y. N. Vashisht Gopal, J. L. McQuade, et al. 2019. Molecular Profiling Reveals Unique Immune and Metabolic Features of Melanoma Brain Metastases. *Cancer Discov.* 9: 628-645).

1.4 - CENTRAL HYPOTHESIS

1.4.1 - Rationale and Significance

Melanoma is the deadliest type of skin cancer, accounting for over 80% of skin cancer-related deaths (1). Many of these deaths result from brain metastases, a devastating complication of melanoma diagnosed in up to 60% of patients with distant metastases (167). Surgery and radiation are the predominant therapeutic modalities used to treat MBMs, but they have minimal impact on the long-term survival of patients (167). As patients with MBMs traditionally have a median survival of ~4 months, there is a critical unmet need to develop new, more effective therapeutic strategies for this disease (167). Several phase II clinical trials meant to address this need have tested agents previously validated in the treatment of non-central nervous system (CNS) disease, though neither targeted therapies nor immunotherapies meet the pressing need for adequate therapies (154, 168-171). To address the shortcomings of available therapies for the treatment of MBMs, we must improve our understanding of the features, heterogeneity, and functional drivers of MBMs.

A metabolic phenotype defined by elevated OXPHOS (High-OXPHOS) has been identified in 30-50% of non-CNS melanomas and correlates with shorter patient survival (35, 172). Furthermore, OXPHOS mediates *de novo* and acquired resistance to FDA-approved MAPK pathway inhibitors and anti-PD1 immunotherapy (3, 26, 35, 173). Recently, we found that MBMs are significantly enriched in OXPHOS gene sets vs. ECMs from the same patients and that OXPHOS levels vary significantly between MBMs from different patients. While these findings represent the most comprehensive metabolic profiling of MBMs to date, they provided little insight into the functional role of OXPHOS in MBM pathogenesis nor which step in the metastatic cascade mediates the enrichment of OXPHOS in MBMs. Additionally, the molecular, immunological, and metabolic associations of OXPHOS in MBMs remain unknown.

The purpose of this study was to understand the role of OXPHOS in MBM pathogenesis to better prevent and treat this deadly disease complication. This dissertation demonstrates that

the brain TME is responsible for OXPHOS enrichment in MBMs compared to ECMs. Additionally, it provides new insight into the role of OXPHOS as a key mediator of MBM growth and validates direct OXPHOS inhibition as a feasible therapeutic approach for MAPKi-resistant MBMs. Finally, this work identifies multiple novel therapeutic targets that could improve the prognosis of MBMs most enriched in OXPHOS and thus at highest risk of developing therapeutic resistance to approved therapies.

1.4.2 - Hypothesis

The central hypothesis of this dissertation is that OXPHOS plays a critical role in the pathogenesis of MBMs.

CHAPTER 2: MATERIALS AND METHODS

Copyright Disclosure:

This chapter is based upon:

1. **Fischer, G. M.**, A. Jalali, D. A. Kircher, W. C. Lee, J. L. McQuade, L. E. Haydu, A. Y. Joon, A. Reuben, M. P. de Macedo, F. C. L. Carapeto, C. Yang, A. Srivastava, C. R. Ambati, A. Sreekumar, C. W. Hudgens, B. Knighton, W. Deng, S. D. Ferguson, H. A. Tawbi, I. C. Glitza, J. E. Gershenwald, Y. N. Vashisht Gopal, P. Hwu, J. T. Huse, J. A. Wargo, P. A. Futreal, N. Putluri, A. J. Lazar, R. J. DeBerardinis, J. R. Marszalek, J. Zhang, S. L. Holmen, M. T. Tetzlaff, and M. A. Davies. 2019. Molecular Profiling Reveals Unique Immune and Metabolic Features of Melanoma Brain Metastases. *Cancer Discov.* 9: 628-645.

2.1 - Patient Cohort/Sample Collection

For the MBM/ECM cohort, tumors resected from melanoma patients between 7/31/1991 and 10/15/2015 were obtained from the UT MD Anderson Cancer Center (MDACC) Central Nervous System Tissue Bank and the Melanoma Informatics, Tissue Resource, and Procurement Core facility (MelCore) under a protocol approved by the Institutional Review Board. Samples were formalin-fixed, paraffin embedded (FFPE) tissue blocks (stored at room temperature). Due to known differences in underlying biology between melanoma subtypes, only cutaneous melanomas were included. Full clinical information is freely available online in (174).

For the primary tumor cohort, sample selection and acquisition have been previously described (148). Briefly, patients between 1998 and 2010 were included if they had (1) a single, invasive, primary melanoma with Breslow thickness greater than 1.5 mm, (2) FFPE primary tumor tissue available for analysis, (3) no clinical evidence of regional metastasis at the time of primary tumor diagnosis, and (4) a sentinel lymph node biopsy conducted within 1 year of the primary tumor diagnosis. The pilot 35 patients were divided into two groups: (1) patients that relapsed with a non-CNS metastasis within 3-18 months after initial diagnosis (N=16) and (2) patients that did not recur with a minimum of 60 months of follow-up from initial diagnosis (N=19). Since this initial characterization, an additional 19 primary tumors that recurred with metastasis to the brain within 3-18 months after initial diagnosis were identified for molecular characterization and processed identically as the other tumors. Full clinical information is freely available online in (174).

2.2 - Cell Lines

All cell lines were grown at 37°C under 5% CO_2. Luciferase-tagged A375, MEWO, CHL1, MEL624, and WM1361A cells [provided by Guo Chen, MDACC], A375-R1 cells [developed by Y.N. Vashisht Gopal (3) and provided by Guo Chen, MDACC], and SKMEL5 cells [provided by the Center for Co-Clinical Trials, MDACC] were grown in RPMI-1640 media supplemented with glutamine and heat-inactivated 5% fetal bovine serum (FBS) (all from Gibco). Duel Luciferase and Green Fluorescent Protein (GFP)-tagged YUMM5.2 cell lines [developed by Marcus Bosenberg (175), Yale University, and provided by Guo Chen, MDACC] were grown in DMEM/F12 (50:50) media supplemented with 1% non-essential amino acids (NEAA) (both from Corning, Inc.) and 10% heat-inactivated FBS. Luciferase-tagged B16-F10 cells [developed and provided by Willem Overwijk, MDACC], A375Br3/A375P cells [developed and provided by Suyun Huang (108), MDACC], and YDFR.CB3/YDFR.C cells [developed and provided by Isaac Witz (176), Tel Aviv Institute] were grown in RPMI-1640 media supplemented with glutamine and 10% heat-inactivated FBS. A375P and G361 cells stably transfected with shRNA against PGC1α (shPGC1α) and a scrambled control vector (shScr) [developed and provided by Pere Puigserver (172), Dana-Farber Cancer Institute] were grown in high glucose DMEM (Gibco) containing 10% heat-inactivated FBS. Identity of the human cell lines was verified by short-tandem repeat (STR) fingerprinting at least every 6 months (177). All cell lines were confirmed negative for mycoplasma prior to the study using the MycoAlert Mycoplasma Detection Kit (Lonza) according to the manufacturer's specifications.

2.3 - Compounds

IACS-010759 is a proprietary compound of the Institute for Applied Cancer Science (IACS) at MDACC and synthesized as previously described (178). Compound used for *in vitro*

treatments was prepared in dimethylsulfoxide (DMSO; Sigma) and stored at -20°C until further use. For *in vivo* treatments, clear suspensions of the compound were prepared in 0.5% methylcellulose (0.5% MC) by IACS every 14 days. Compound was stored at 4°C in the absence of light and constantly stirred.

Metformin (Cayman Chemical) was prepared in phosphate buffered saline (PBS; Corning, Inc.) and filter-sterilized immediately before each *in vivo* treatment.

Isotype rat IgG control antibody (BioXCell, Clone: 2A3, #BE0089) and anti-mouse PD1 antibody (BioXCell, Clone: RMP1-14, #BE0146) were prepared in filter-sterilized PBS under sterile conditions immediately before each *in vivo* treatment.

Pimonidazole hydrochloride (Hypoxyprobe, Inc.) was prepared in normal saline (VWR International) and filter-sterilized. Compound was stored at 4°C in the absence of light and constantly stirred for up to 3 months for *in vivo* injections.

AZD2014 (Selleck Chemical) was formulated as a suspension in sterilized 0.5% hydroxypropyl methylcellulose (HPMC; Sigma)/0.1% Tween 80 (Sigma) under sterile conditions. Compound was stored at 4°C in the absence of light and constantly stirred for up to 14 days for *in vivo* treatments.

CB839 (Selleck Chemical) used for *in vitro* treatments was prepared in DMSO and stored at -20°C until further use. For *in vivo* studies, CB839 was prepared in 25% (w/v) hydroxypropyl-β-cyclodextrin (HPBCD; Roquette) in 10 mmol/L citrate, pH 2. Compound was stored at 4°C in the absence of light and constantly stirred for up to 14 days.

2.4 - Mice

All mouse experiments were approved by the Institutional Animal Care and Use Committees of MDACC and University of Utah Health Sciences Center. Female C57BL/6 and CD-1 nude mice were purchased from the Jackson Laboratory and Charles River Laboratories, respectively. C57BL/6 and CD-1 nude mice were used at 8 weeks of age, and experiments using these mice were performed at the MDACC South Campus Animal Vivarium and housed in specific pathogen-free conditions. All experiments using the RCAS-TVA model were conducted at the University of Utah Health Sciences Center.

2.5 - Stereotaxic Intracranial Injection

On the day of injection, cells between 80-90% confluent were trypsinized (Corning, Inc. 0.25% Trypsin, 0.1% EDTA in HBSS without Calcium, Magnesium and Sodium Bicarbonate) and resuspended in Hank's Balanced Salt Solution (HBSS; Corning, Inc.). Specifically, media was aspirated and tissue culture plates were rinsed with 10 ml of PBS per 100 mm plate. PBS was aspirated and 1 ml of trypsin was added to each 100 mm plate and incubated at 37°C for 1 minute. Trypsin was inactivated with addition of 5 ml of media (RPMI, DMEM/F12 50:50, or DMEM) + 5-10% FBS per 100 mm plate. Cells were pelleted via centrifugation at 500 x g for 3 minutes and resuspended in 5 ml ice-cold HBSS per 100 mm plate. Viable cells were counted using Trypan Blue (Gibco) and an automated cell counter. Only harvested cells with a mean viability of at least 90% were used in each injection. The live cell density was adjusted as necessary with ice-cold HBSS. The cell suspension was kept on ice until injection.

Mice were anesthetized with an intraperitoneal (i.p.) injection of ketamine/xylazine cocktail (80 mg/kg ketamine and 12 mg/kg xylazine). Once sufficiently deep anesthesia was confirmed via toe pinch, the scalp was sterilized via chlorhexidine scrub. Ophthalmic ointment

was applied. Using a sterile scalpel, a ~1 cm incision was made longitudinally along the midline of the scalp beginning at the level of the eyes and extending caudally. A sterile 23-gauge needle was used to pierce the bone at a position 1 mm posterior and 2 mm lateral to the bregma in the right hemisphere. The mouse was placed in a stereotaxic frame (World Precision Instruments) such that the head was in a level plane and immobilized to finger touch. 2.5 µl of the cell suspension was taken up into a 10 µl Hamilton syringe (Hamilton Co.) held by the stereotaxic frame. The Hamilton syringe needle was positioned at the entrance of the burr hole and then lowered perpendicularly to the skull through the burr hole to a depth of 4 mm. The needle was withdrawn slowly to a final depth of 3 mm. The cell suspension was delivered at a rate of 0.5 µl/min. After an additional 30 seconds, the needle was withdrawn over a period of 1 minute. A cotton swab was used to dry the surface of the skull around the burr hole. Sterile bone wax was applied to the burr hole. The incision was closed with sterile wound clips. This procedure was repeated until all mice were injected. Mice were monitored on a heating pad until alert and ambulatory and then transferred to a clean cage.

2.6 - Intracardiac Injection

On the day of injection, cells were prepared as described for intracranial injections. Live cell density was adjusted as necessary. Fur was removed from the ventral surface of C57BL/6 mice via hair removal cream. Each mouse was anesthetized (2.5% isoflurane in 100% O_2 in an induction chamber) and maintained with isoflurane (2.5% in 100% O_2) during the whole procedure via a nose cone. Anesthesia was confirmed when no withdrawal reflex was observed with toe pinch. The anesthetized mouse was taped to a heated imaging table in supine position. VisualSonics Vevo 770 ultrasound system was activated and the transducer 704 (40 MHz) was

initialized. Ultrasound gel was applied to the ventral surface of the mouse. The transducer was mounted securely in the holder of a stereotaxic frame. The transducer was lowered until the desired imaging depth was reached. The stage was then moved until the left ventricle was identified with the ascending aorta used as the landmark. The stage was then locked. 100 µl of cell mixture was drawn into a 1 ml syringe with a 27-gauge needle. The syringe was fixed on the syringe mount of the stereotaxic frame. The syringe was advanced towards the mouse's ventral surface and carefully moved until the needle tip was in the imaging field of view. The needle height and angle were adjusted to acquire direct access to the left ventricle upon penetration of the chest wall. The syringe needle was then pushed through the intercostal space and into the left ventricle under the guidance of ultrasound imaging. The needle was inspected for the reflux of fresh arterial blood into the syringe to confirm proper placement of the needle. The cell mixture was then injected over the course of 30 seconds. Upon completion, the needle was withdrawn and the mouse was thoroughly cleaned with dampened gauze and removed from the imaging stage. This procedure was repeated until all mice were injected. The mice were monitored on a heating pad until alert and ambulatory and then transferred to a clean cage.

2.7 - *In vivo* Bioluminescence Imaging (BLI)

At selected time points, D-luciferin sodium salt (BioVision) was injected at 150 mg/kg into the peritoneum of each mouse. After 10 minutes, the animal was placed into an IVIS100 *in vivo* imager and scanned on default settings with the exception that exposure time was automatically determined by the Living Image (v4.5.2) software. The bioluminescence image was overlaid onto a photographic image for anatomical location of the signal. Signal intensities were quantified using Living Image (v4.5.2) software. Briefly, regions of interest (ROIs) were

automatically determined by the software. The minimum % of peak pixel intensity for inclusion was set to 20%. Values were normalized against a black surface in the image and a non-luminescent surface of the animal. Total flux values were exported into Microsoft Excel 2013 and Prism 7.0 (Graphpad) for downstream analysis.

2.8 - Subcutaneous Injection

On the day of injection, cells were prepared as described for intracranial injections. Live cell density was adjusted as necessary. Each mouse was anesthetized (2.5% isoflurane in 100% O_2 in an induction chamber) and maintained with isoflurane (2.5% in 100% O_2) during the whole procedure via a nose cone. The injection site was cleaned with 70% ethanol. 100 µl of cell mixture was drawn into a 1 ml syringe with a 30-gauge needle. The needle was inserted superficially beneath the skin 5-10 mm into the subcutaneous tissue. The cell mixture was ejected from the syringe. A positive injection was indicated by the appearance of a "bleb." The needle was gently withdrawn and the mouse was placed in a cage once alert and ambulatory. The procedure was repeated until all mice were injected. Tumors were measured using a digital caliper (Fowler). The greatest longitudinal diameter (length or "L") and the greatest transverse diameter (width or "W") were recorded. Tumor volume was calculated as $[(LxW^2)/2]$.

2.9 - Intracranial (ICr) and Subcutaneous (SQ) Xenograft Implantation and Sample Collection for Tumor Microenvironment Gene Expression Studies

$3x10^3$ luciferase-tagged A375 and A375-R1 cells and $1x10^4$ MEWO and WM1361A cells suspended in HBSS were directly implanted in the brain parenchyma of CD-1 nude mice (female,

8-10 weeks of age). $3x10^6$ luciferase-tagged A375, A375-R1, MEWO, and WM1361A cells suspended in HBSS were subcutaneously implanted in the flanks of CD-1 nude mice of the same cohort. Mice with ICr tumors were euthanized if they lost > 20% body weight, if they became moribund, or if they displayed neurological symptoms (ataxia, seizures, circling behavior, paralysis, or cranial doming). Mice with SQ tumors were euthanized once tumors reached 250 mm^3. Tumors were harvested, rinsed briefly in ice-cold normal saline, embedded in optimal cutting temperature (OCT) compound (Fisher Scientific), and flash-frozen via liquid nitrogen.

2.10 - RCAS-TVA Model Tumor Induction and Sample Collection

FFPE specimens. Primary tumors were generated in *Dct::TVA;Braf*^{CA};*Cdkn2a*$^{lox/lox}$±*Pten*$^{lox/lox}$ mice using RCAS:*Cre* ± RCAS:myr*Akt1* retroviruses as previously described (179). A full necropsy was performed on all mice following euthanasia. Brain, lung, and primary tumor tissues were fixed in formalin overnight, dehydrated in 70% ethyl alcohol, and paraffin embedded. Sections were stained with hematoxylin & eosin (H&E) for review by a pathologist.

Frozen primary tumor specimens. RCAS-*myr*AKT1 was used as a template to generate *Akt1* mutant constructs. Mouse melanocyte cDNA and *Akt2*-specific primers (Dharmacon) were used to amplify *Akt2* via PCR reaction. The product was TOPO cloned into a gateway compatible pCR8 TOPO vector and then subcloned into the RCAS destination vector. RCAS-*myr*AKT2 was used as a template to generate *Akt2* mutant constructs. Mouse myr*Akt3* was amplified via PCR reaction from *Akt3* cDNA / ORF (Dharmacon) and *Akt3*-specific primers. The product was TOPO cloned into a gateway compatible pCR8 TOPO vector and then subcloned into the RCAS destination vector. RCAS-*myr*AKT3 used as a template to generate *Akt3* mutant constructs. All

mutants were engineered with an N-terminus HA-epitope tag. The E17K substitution was engineered into the forward primer of oligonucleotides of each paralog. All viral vectors were verified via Sanger Sequencing. Primer sequences and are available upon request. Viral production and spread were initiated and monitored as previously described (179). Primary tumors were generated in *Dct::TVA;Braf*^{CA}*;Cdkn2a*$^{lox/lox}$*;Pten*$^{lox/lox}$ mice using RCAS:*Cre* ± RCAS:*Akt1/2/3*-E17K mutant retroviruses as previously described (179).

2.11 - RNA-Sequencing and Analysis

cDNA library construction for clinical FFPE specimens, A375, A375-R1, MEWO, and WM1361A xenografts. Total RNA was assessed for quality using the Caliper LabChip GX2 at the Broad Institute (Cambridge, MA). The percentage of fragments with a size greater than 200 nucleotides (DV200) was calculated using software. An aliquot of 200 ng of RNA was used as the input for first strand cDNA synthesis using Illumina's TruSeq RNA Access Library Prep Kit. Synthesis of the second strand of cDNA was followed by indexed adapter ligation. Subsequent PCR amplification enriched for adapted fragments. The amplified libraries were quantified using an automated PicoGreen assay. 200 ng of each cDNA library, not including controls, were combined into 4-plex pools. Capture probes that target the exome were added, and hybridized for recommended time. Following hybridization, streptavidin magnetic beads were used to capture the library-bound probes from the previous step. Two wash steps effectively removed any non-specifically bound products. These same hybridization, capture, and wash steps were repeated to assure high specificity. A second round of amplification enriched the captured libraries. After enrichment, the libraries were quantified with qRT-PCR using the KAPA Library Quantification Kit for Illumina Sequencing Platforms and then pooled equimolarly. The entire

process was in 96-well format and all pipetting was done by either Agilent Bravo or Hamilton Starlet.

Illumina sequencing for clinical FFPE specimens, A375, A375-R1, MEWO, and WM1361A xenografts. Pooled libraries were normalized to 2 nM and denatured using 0.1 N NaOH prior to sequencing at the Broad Institute. Flowcell cluster amplification and sequencing were performed according to the manufacturer's protocols using HiSeq 2500. Each run was a 76-bp paired-end with an eight-base index barcode read. Data was analyzed using the Broad Picard Pipeline which includes de-multiplexing and data aggregation.

cDNA library construction for RCAS-TVA model specimens. Total RNA samples (100-500 ng) were hybridized with Ribo-Zero Gold at the University of Utah Health Sciences Center to substantially deplete cytoplasmic and mitochondrial rRNA from the samples. Stranded RNA sequencing libraries were prepared using the Illumina TruSeq Stranded Total RNA Kit with Ribo-Zero Gold (RS-122-2301 and RS-122-2302). Purified libraries were qualified on an Agilent Technologies 2200 TapeStation using a D1000 ScreenTape assay (cat# 5067-5582 and 5067-5583). The molarity of adapter-modified molecules was defined by qRT-PCR using the Kapa Biosystems Kapa Library Quant Kit (cat# KK4824). Individual libraries were normalized to 10 nM and equal volumes were pooled in preparation for Illumina sequencing and analysis.

Illumina sequencing for RCAS-TVA model specimens. Sequencing libraries (25 pM) were chemically denatured and applied to an Illumina HiSeq v4 single read flow cell using an Illumina cBot. Hybridized molecules were clonally amplified and annealed to sequencing primers with reagents from an Illumina HiSeq SR Cluster Kit v4-cBot (GD-401-4001). Following transfer of the flowcell to an Illumina HiSeq 2500 instrument (HCSv2.2.38 and RTA v1.18.61), a 50 cycle single-read sequence run was performed using HiSeq SBS Kit v4 sequencing reagents (FC-401-4002). The reference murine genome sequence (FASTA file) and annotation file (GTF file) were

downloaded from Ensembl release 92. A reference database was created using the *genomeGenerate* option of STAR aligner (v2.5.4a) (180). The *sjdbGTFfile* option was used to extract splice junctions from the GTF file with a maximum possible overhang of 49 bases (for the 50 bp read). The Illumina adapter sequences were trimmed using cutadapt (v1.16). The *-O option* trimmed after 6 matching bases and *-m option* discarded trimmed reads shorter than 20 bases. Following quality assessment via FastQC, the trimmed reads were aligned to the reference genome using STAR (v2.5.4a) in two pass mode with default parameters to generate an RNA-seq BAM file for each sequencing event. Picard *CollectRnaSeqMetrics* was used to calculate the post-alignment mapping statistics.

Count matrix generation. HTSeq-count (v0.9.1) tool (181) was applied with its default settings to aligned RNA-seq BAM files from the Broad Institute (except A375, A375-R1, MEWO, and WM1361A xenografts) to count uniquely aligned reads overlapping features in the GTF file, and featureCounts (v1.5.1) (182) was applied with its default settings to the aligned RNA-seq BAM files generated at the University of Utah Health Sciences Center. Samples with less than 10 million uniquely mapped reads were excluded from further analyses. Only Entrez genes were included in further analyses.

Xenome pipeline. RNA-seq data from A375, A375-R1, MEWO, and WM1361A ICr and SQ xenografts were processed on the Seven Bridges Cancer Genomics Cloud platform (https://cgc.sbgenomics.com/) with a workflow implemented using Common Workflow Language. After initial data upload (24 samples), starting BAM files were converted to FASTQs using the biobambam2 *bamtofastq* utility and processed with the Jackson Laboratory's RNA-Seq pipeline. Briefly, the transcriptome of hg38 and NOD (based on mm10 mouse genome) were used to construct the Xenome (v1.0.0) (183) indices (k=25) and then all reads from engrafted samples were classified into five types: human, mouse, both, neither and ambiguous at default parameters.

Reference indices for alignment were built by rsem-prepare-reference using ENSEMBL annotation (vGRCh38.91) for STAR aligner (v2.5.1b). Xenome-classified human-specific reads were further mapped to reference indices using STAR and expression estimates were performed using rsem-calculate-expression (v1.2.31) at default parameters (184). Picard *CollectRnaSeqMetrics* was used to calculate the post-alignment mapping statistics. Only Entrez genes were included in further analyses.

Identification of differentially expressed genes (DEGs). Counts were normalized using the TMM method and generalized linear models were used for differential expression analysis (185). Comparisons of interest were performed using functions from the edgeR and limma/voom Bioconductor packages in R (185). Blocking was performed to account for differences in cell line identity during xenograft studies. Clinical samples with median transcript counts of 0 were excluded from further analysis. Lowly expressed genes were filtered according to the following criteria in the preclinical models: genes with an average log2-(CPM+0.5) < 0 (A375, A375R1, MEWO, and WM1361A ICr and SQ xenografts) and genes with an average log2-(CPM+0.5) < 1 (RCAS-TVA model samples). DEGs were defined as those genes with a Benjamini-Hochberg corrected *p* value less than 0.05.

Pathway analyses. Preranked GSEA (GSEA-P) was implemented using the GenePattern module *GSEAPreranked* (v6.0.10). Gene sets were downloaded from the MSigDB database or featured the 70 KEGG metabolic pathways from **Table 3** included in a single .gmt file. Rank metric was calculated as the sign of log2-FCs multiplied by the inverse of *p*-values calculated using the EdgeR/limma/voom pipeline (186). Genes from murine samples were converted to their human orthologs via mapping from Ensembl BioMart version 77. GSEA-P was performed on the rank metric–sorted list of genes.

Single sample GSEA (ssGSEA) and OXPHOS-Index (OP-Index) derivation. ssGSEA was conducted on TMM-normalized, voom-transformed log2-(CPM+0.5) expression matrices using the GenePattern module *ssGSEAProjection* (v9.0.10) with default settings. To derive the OP-Index, we analyzed two datasets: 1) previously published gene expression data from MEL624 and SKMEL5 melanoma cells resistant to MEKi because of increased OXPHOS and MEKi-sensitive A375 and WM35 melanoma cells treated for 24 hours with 0.25 μM of the MEKi selumetinib (3) and 2) publicly available gene expression data from A375P cells transfected with two shRNAs targeting PGC1α and a scrambled control **(**GSE36879) (172). GSEA (v19.0.24) was performed as previously described (187) with default settings except that the rank metric was set to "log2 ratio of classes." The 8 OXPHOS-related MSigDB Hallmarks and c2 gene sets most enriched in both the MEKi-resistant cells and scrambled controls were identified as the basis of the index (**Figure 5**). We then acquired publicly available gene expression data from 15 melanoma cell lines (GSE101644**)** (188) with matching Seahorse Extracellular Flux (XF) Assay data.

Table 3 - KEGG metabolism gene sets used in metabolomics pathway analyses

Pathway Name	Pathway Name
GLYCOLYSIS GLUCONEOGENESIS	GLYCOSAMINOGLYCAN BIOSYNTHESIS CHONDROITIN SULFATE
CITRATE CYCLE TCA CYCLE	GLYCOSAMINOGLYCAN BIOSYNTHESIS KERATAN SULFATE
PENTOSE PHOSPHATE PATHWAY	GLYCOSAMINOGLYCAN BIOSYNTHESIS HEPARAN SULFATE
PENTOSE AND GLUCURONATE INTERCONVERSIONS	GLYCEROLIPID METABOLISM
FRUCTOSE AND MANNOSE METABOLISM	INOSITOL PHOSPHATE METABOLISM
GALACTOSE METABOLISM	GLYCOSYLPHOSPHATIDYLINOSITOL GPI ANCHOR BIOSYNTHESIS
ASCORBATE AND ALDARATE METABOLISM	GLYCEROPHOSPHOLIPID METABOLISM
FATTY ACID METABOLISM	ETHER LIPID METABOLISM
STEROID BIOSYNTHESIS	ARACHIDONIC ACID METABOLISM
PRIMARY BILE ACID BIOSYNTHESIS	LINOLEIC ACID METABOLISM
STEROID HORMONE BIOSYNTHESIS	ALPHA LINOLENIC ACID METABOLISM
OXIDATIVE PHOSPHORYLATION	SPHINGOLIPID METABOLISM
PURINE METABOLISM	GLYCOSPHINGOLIPID BIOSYNTHESIS LACTO/NEOLACTO SERIES
PYRIMIDINE METABOLISM	GLYCOSPHINGOLIPID BIOSYNTHESIS GLOBO SERIES
ALANINE ASPARTATE AND GLUTAMATE METABOLISM	GLYCOSPHINGOLIPID BIOSYNTHESIS GANGLIO SERIES
GLYCINE SERINE AND THREONINE METABOLISM	PYRUVATE METABOLISM
CYSTEINE AND METHIONINE METABOLISM	GLYOXYLATE AND DICARBOXYLATE METABOLISM
VALINE LEUCINE AND ISOLEUCINE DEGRADATION	PROPANOATE METABOLISM
VALINE LEUCINE AND ISOLEUCINE BIOSYNTHESIS	BUTANOATE METABOLISM
LYSINE DEGRADATION	ONE CARBON POOL BY FOLATE
ARGININE AND PROLINE METABOLISM	RIBOFLAVIN METABOLISM
HISTIDINE METABOLISM	NICOTINATE AND NICOTINAMIDE METABOLISM
TYROSINE METABOLISM	PANTOTHENATE AND COA BIOSYNTHESIS
PHENYLALANINE METABOLISM	FOLATE BIOSYNTHESIS
TRYPTOPHAN METABOLISM	RETINOL METABOLISM
BETA ALANINE METABOLISM	PORPHYRIN AND CHLOROPHYLL METABOLISM
TAURINE AND HYPOTAURINE METABOLISM	TERPENOID BACKBONE BIOSYNTHESIS
SELENOAMINO ACID METABOLISM	LIMONENE AND PINENE DEGRADATION
GLUTATHIONE METABOLISM	NITROGEN METABOLISM
STARCH AND SUCROSE METABOLISM	SULFUR METABOLISM
N GLYCAN BIOSYNTHESIS	AMINOACYL TRNA BIOSYNTHESIS
OTHER GLYCAN DEGRADATION	METABOLISM OF XENOBIOTICS BY CYTOCHROME P450
O GLYCAN BIOSYNTHESIS	DRUG METABOLISM CYTOCHROME P450
AMINO SUGAR AND NUCLEOTIDE SUGAR METABOLISM	DRUG METABOLISM OTHER ENZYMES
GLYCOSAMINOGLYCAN DEGRADATION	BIOSYNTHESIS OF UNSATURATED FATTY ACIDS

A

Gene Set	MSigDB Database
HALLMARK_OXIDATIVE_PHOSPHORYLATION	Hallmarks
KEGG_OXIDATIVE_PHOSPHORYLATION	C2: Curated Gene Sets
KEGG_CITRATE_CYCLE_TCA_CYCLE	C2: Curated Gene Sets
REACTOME_TCA_CYCLE_AND_RESPIRATORY_ELECTRON_TRANSPORT	C2: Curated Gene Sets
REACTOME_CITRIC_ACID_CYCLE_TCA_CYCLE	C2: Curated Gene Sets
REACTOME_RESPIRATORY_ELECTRON_TRANSPORT_ATP_SYNTHESIS_BY_CHEMIOSMOTIC_COUPLING_AND_HEAT_PRODUCTION_BY_UNCOUPLING_PROTEINS	C2: Curated Gene Sets
MOOTHA_TCA	C2: Curated Gene Sets
MOOTHA_VOXPHOS	C2: Curated Gene Sets
OPIndex → arithmetic mean of ssGSEA scores for listed gene sets	

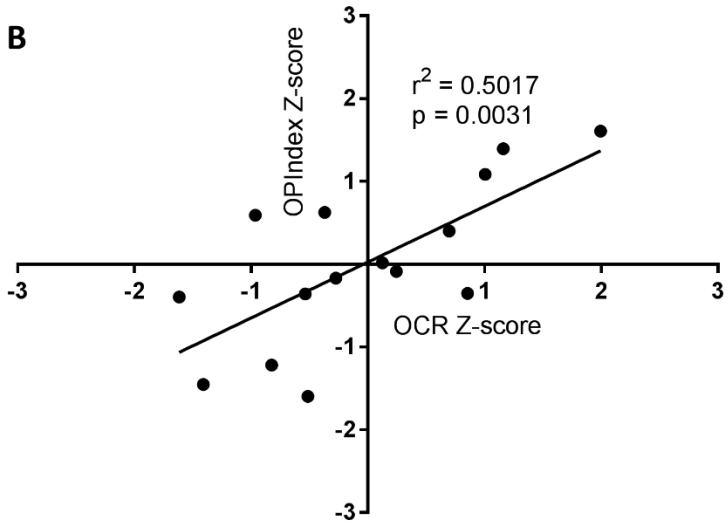

Figure 5: Derivation of the OXPHOS-Index. (**A**) List of gene sets included in the OXPHOS-Index (OP-Index). (**B**) Correlation analysis between the z-scores of oxygen consumption rates (OCR) (x-axis) and OP-Indices (y-axis) of 15 melanoma cell lines with publicly available gene expression data and Seahorse Extracellular Flux (XF) Assay data. Each dot is a single sample. Used with permission from the American Association for Cancer Research (AACR) (Fischer, G. M., Y. N. Vashisht Gopal, J. L. McQuade, et al. 2019. Molecular Profiling Reveals Unique Immune and Metabolic Features of Melanoma Brain Metastases. *Cancer Discov.* 9: 628-645).

ssGSEA was used to generate enrichment scores for each of the 8 OXPHOS-related gene sets in the 15 melanoma cell lines. The OP-Index was calculated by taking the arithmetic mean of these enrichment scores for each sample. The mean baseline oxygen consumption rate (OCR) of 3 readings was calculated from the XF Assay data. Z-scores were generated for the OP-Indices and mean OCR values across the 15 samples to determine the correlation between OP-Index and OCR.

Clustering analyses and principal components analysis (PCA) of clinical FFPE samples. Values from the 8 components of the OP-Indices of MBMs or primary tumors were median centered. Hierarchical clustering was conducted with distances calculated using Euclidean correlation metrics and clusters joined using complete linkage. PCA analysis was performed using "SVD with imputation." The heatmaps and PCA plots were generated via ClustVis (https://biit.cs.ut.ee/clustvis/).

ESTIMATE analyses. The R package software ESTIMATE was applied as previously described (189) to the TMM-normalized, voom-transformed log2(CPM+0.5) expression matrices to produce the ImmuneScores for comparison.

MCP-Counter analyses. The R package software MCP-counter was applied as previously described (190) to TMM-normalized, voom-transformed log2(CPM+0.5) expression matrices to produce the abundance scores for T-cells, $CD8^+$ T-cells, cytotoxic lymphocytes, NK cells, B lymphocytes, monocytic lineage cells, myeloid dendritic cells, and neutrophils.

2.12 – *In vivo* Metabolic Tracing Studies

Tumor implantation and infusions. $3x10^3$ luciferase-tagged A375 cells suspended in HBSS were directly implanted in the brain parenchyma of CD-1 nude mice (female, 8 weeks of age). $3x10^6$ cells suspended in HBSS were subcutaneously injected into the flanks of CD-1 nude

mice of the same cohort. Infusions occurred when mice bearing ICr xenografts lost 15% of body weight or when SQ tumors reached 250 mm^3 in size. Mice were fasted for 16 hours, and 27 gauge catheters were placed in the lateral tail vein under anesthesia. Isotope infusions started immediately after implantation of the catheter and continued for approximately 3 hours, also under anesthesia, as previously described (191). The total dose of [U-^{13}C]-glucose (Cambridge Isotope Laboratories) was 2.48 g/kg dissolved in 750 ml normal saline. The glucose solution was administered as a bolus of 125 mL/min (1 min) followed by a continuous rate of 2.5 mL/min for 3 hours. Animals were euthanized at the end of the infusion. Tumors were harvested, rinsed briefly in cold saline, and frozen in liquid nitrogen. Samples were stored at -80°C until analysis at the University of Texas Southwestern Metabolomics Facility.

Sample preparation and data acquisition. 15-25 mg of frozen tissue fragments were homogenized in 1 mL of 80% methanol on ice by a polytron electronic homogenizer and then centrifuged at 16,000xg for 15 min. to precipitate tissue debris. The supernatants were completely dried down under air flow, re-suspended in 40 uL of anhydrous pyridine with 10 mg/mL methoxyamine hydrochloride and subjected to a 70°C heatblock for 15 min. Samples were then transferred to gas chromatography-mass spectrometry (GC-MS) autoinjector vials containing 80 uL N-(tert-butyldimethylsilyl)-N-methyltrifluoroacetamide (MTBSTFA) derivatization reagent and incubated at 70°C for 1 hour. 1 uL of each this sample was injected into an Agilent 7890 Gas Chromatograph coupled with an Agilent 5975C Mass Selective Detector. The observed distributions of mass isotopologues were corrected for natural abundance. Steady-state metabolic fluxes were calculated by 13C mass isotopologue distributions (MIDs) for 3-phosphoglycerate, phosphoenolpyruvate, pyruvate, lactate, citrate, malate, and fumarate using the INCA software package with previously characterized assumptions (191).

2.13 - Targeted Metabolomics

***Tumor implantation and sample collection*.** $3x10^3$ luciferase-tagged A375 cells and $1x10^4$ luciferase-tagged CHL1 cells suspended in HBSS were directly implanted in the brain parenchyma of CD-1 nude mice (female, 8 weeks of age). $3x10^6$ luciferase-tagged A375 cells and CHL1 cells suspended in HBSS were subcutaneously implanted in the flanks of CD-1 nude mice of the same cohort. Mice with ICr tumors were euthanized once moribund. Mice with SQ tumors were euthanized once tumors reached 250 mm^3. Tumors were harvested, rinsed briefly in cold saline, and frozen in liquid nitrogen.

Reagents and internal standards. High-performance liquid chromatography (HPLC)-grade ammonium acetate, acetonitrile, methanol, chloroform, and water were procured from Burdick & Jackson. Mass spectrometry-grade formic acid was purchased from Sigma-Aldrich. Metabolites and internal standards were purchased from Sigma-Aldrich.

Sample preparation for mass spectrometry and metabolomics analysis. Tissues samples were stored at -80°C until the analysis at the Baylor College of Medicine Metabolomics Core. 25 mg of tissue was homogenized in 1:4 ice cold water:methanol mixture containing equimolar mixture of 2 standard compounds: Zeatine and [15N]-Tryptophan (mass difference from endogenous Tryptophan = 1 Da). Ice-cold chloroform and water were added in a 3:1 ratio for a final proportion of 1:4:3:1 water:methanol:chloroform:water. Both the organic and aqueous layers were transferred into a new tube, dried, and resuspended with 50:50 methanol:water. The resuspended sample was then deproteinized using a 3kDa molecular filter (Amicon ultracel-3K Membrane; Millipore Corporation) and the filtrate was dried under vacuum (Genevac EZ-2plus; Genevac). Prior to mass spectrometry, the dried extracts were re-suspended in 1:1 ratio of methanol and water and were subjected to liquid chromatography-mass spectrometry (LC-MS).

Separation of metabolites. Two different analytical methods were used for the separation of targeted metabolomics to measure 46 metabolites. ESI positive mode was used for Method 1. The HPLC column Waters X-bridge Amide 3.5 µm, 4.6 x 100 mm (PN: 186004868; Waters) was used. Mobile phase A and B were 0.1% formic acid in water and acetonitrile, respectively. Gradient: 0-3 min-85 % B; 3-12 min-30 % B, 12-15 min-2 % B, 16 min-95% B, followed by re-equilibration at the end of the gradient 23 min to the initial starting condition 85% B. Flow rate: 0.3 mL/min. ESI negative mode was used for Method 2. The HPLC column used was Waters X-bridge Amide 3.5 µm, 4.6 x 100 mm (PN: 186004868; Waters). Mobile phase A and B were 20 mM ammonium acetate in water with pH 9.0 and 100% acetonitrile, respectively. Gradient: 0-3 min-85% B, 3-12 min-30% B, 12-15 min-2% B, 15-16 min-85% B followed by re-equilibration at the end of the gradient 23 min to the initial starting condition of 85% B. Flow rate: 0.3 mL/min.

Data acquisition through LC-MS analysis. LC-MS was performed using a 6490 triple quadrupole mass spectrometer coupled to an Agilent 1290 series HPLC system (Agilent Technologies) with single reaction monitoring (SRM). This LC system is equipped with a degasser, binary pump, thermostatted auto sampler, and column oven. This SRM-based measurement of relative metabolite levels used normal phase chromatographic separation. 10 µL of suspended samples were injected and analyzed using source parameters as follows: Gas temperature - 250°C; Gas flow - 14 L/min; Nebulizer - 20 psi; Sheath gas temperature - 350°C; Sheath gas flow - 12 L/min; Capillary - 3000 V positive and 3000 V negative; Nozzle voltage - 1500 V positive and 1500 V negative. Approximately 8-11 data points were acquired per each detected metabolite.

Data analysis. Agilent MassHunter Workstation Software - Quantitative Analysis was used for manual review of chromatograms, and peak area integration was assessed based on the retention time. The normalization of each metabolite peak area was done by the peak area of the

spiked internal standard (L-zeatine for amino acids and L-tryptophan for fatty acids and TCA cycle metabolites) and then the data was log2-transformed. For every metabolite in the normalized dataset, paired Student's *t*-tests were conducted to compare expression levels between ICr and SQ tumors. Differential metabolites were identified by adjusting the *p*-values for multiple testing at a False Discovery Rate (FDR) threshold of <0.25. All metabolites significantly upregulated in ICr xenografts (log2FC>0 and FDR q-val<0.25) were uploaded into MetaboAnalyst 4.0 (http://www.metaboanalyst.ca/). The Pathway Analysis tool set to default settings was used to perform overrepresentation analysis (ORA) of the significantly upregulated metabolites, as previously described (192).

2.14 - Reverse Phase Protein Array (RPPA) Analysis

Protein extraction. Lysis buffer and 4x SDS sample buffer supplemented with β-mercaptoethanol (Sigma) were prepared according to protocols established by the MD Anderson Functional Proteomics Core. 15-25 mg of frozen tissue fragments were weighed and added to 2 ml tubes with ceramic beads in preparation for homogenization. Ice-cold lysis buffer was added to samples at a volume of 1 ml/40 mg of tissue. A Procellys homogenizer housed in a 4°C cold room was set to program 1 for sample homogenization. Lysates were centrifuged at 4°C for 15 minutes at 14,000 rpm. Supernatants were transferred to fresh microcentrifuge tubes kept on ice. Protein concentration was determined via BCA reaction according to the instructions from Pierce BCA Protein Assay Kit. Concentration was adjusted to 1.5 ug/ul with additional lysis buffer. Cell lysate was mixed with 4x SDS + β-mercaptoethanol sample buffer at 3 parts lysate + 1 part sample buffer. The samples were boiled at 95°C for 5 minutes and stored at -80°C until further processing.

A detailed description of the RPPA method (including antibodies available for xenograft tissues) and data normalization is available at the core facility's web page.

Analysis. Normalized data provided by the core was utilized for all downstream analysis. Generalized linear models were used for differential expression analysis (185). Blocking was performed to account for differences in cell line identity. Comparisons of interest were performed using functions from the *limma* Bioconductor packages in R (v3.3.3).

2.15 - Microarray Analyses

Datasets. Preprocessed and normalized Affymetrix Human Exon 1.0 ST Array (GSE34970 and GSE44660), Illumina HumanHT-12 WG-DASL Array V4.0 (GSE60464), and Agilent Human HEEBO 44K array (GSE23601) datasets were downloaded from GEO.

OP-Index calculations. OP-Indices were calculated as described for RNA-seq data using normalized expression matrices as the initial input.

***Pathway analysis*.** GSEA was performed on GSE34970, GSE44660, and GSE60464 using the GenePattern modules *GSEA* (v19.0.25) and normalized expression matrices as the initial input. Parameters used for the analyses were as follows. The MSigDB Hallmarks gene set collection and the aforementioned 70-member KEGG metabolism gene set collection were used for running GSEA. 1000 permutations were used to calculate statistical significance, and permutation type was set to "gene_set" in analyses with less than 7 samples per group. All basic and advanced fields were set to default for GSE44660 and GSE60464 samples while the "Metric for ranking genes" was set to "log2_Ratio_of_Classes" for GSE34970 samples. *GSEAPreranked* (v6.0.10) was used to perform pathway analysis for GSE23601. Rank metric was calculated as the average log2-FCs of replicates included in each analysis.

2.16 – Bioenergetics Stress Test

A Seahorse XFe96 Bioanalyzer (Agilent) was used according to the manufacturer's instructions. Briefly, cells were plated in a 96-well Seahorse XF Cell Culture Microplate at a density of 25,000/well in 100 ul of the appropriate cell culture growth media ± inhibitor and incubated for 12-16 hours at 37°C under 5% CO2. Media was then removed and replaced with minimal, unbuffered DMEM media supplemented with 5 mM glucose, 1 mM pyruvate, and 2 mM glutamine ± inhibitor for a 1-hour CO2-free incubation at 37°C. For Mito Stress Test, basal oxygen consumption rate (OCR) was recorded prior to stimulation with 1.5 µM oligomycin, 0.5 µM FCCP, and 0.5 µM rotenone/antimycin A. 3 cycles of 2-min mixes, 2-min wait times, and 3-min measure times were performed.

2.17 - *In vivo* Pharmacodynamics (PD) Studies

IACS-010759. CD-1 nude mice bearing human ICr xenograft tumors or RCAS-TVA model mice bearing *Braf*^{V600E}*;Cdkn2a*$^{-/-}$*;Pten*$^{-/-}$*;*myr*Akt1* primary tumors were treated with vehicle or IACS-010759 (5-7.5 mg/kg p.o. once daily). After 24 hours, 72 hours, or 7 days, the mice were intraperitoneal-injected with 60 mg/kg of pimonidazole and given one final treatment. Three hours after this treatment, tumors were harvested and fixed in 10% formalin. FFPE slides of these tumors were generated and probed with a combination of the following: anti-pimonidazole (marker of hypoxia), anti-P-S6 (marker of mTOR pathway activation), anti-ki67 (marker of proliferation), or anti-cleaved caspase 3 (marker of apoptosis) antibody, as described previously (178).

BRAFi and mTORC1/2i. CD-1 nude mice bearing human ICr xenograft tumors were treated with vehicle, dabrafenib (30 mg/kg p.o. once daily), or AZD2014 (20 mg/kg p.o. once daily). On day 3 (dabrafenib and vehicle) or day 7 (AZD2014 and vehicle), mice were given one final treatment. Three hours after this treatment, tumors were harvested and fixed in 10% formalin. FFPE slides of these tumors were generated and probed for P-ERK (marker of MAPK pathway activation) and P-S6 (marker of mTOR pathway activation), as previously described (3).

2.18 - Metastasis Studies

RCAS-TVA model studies. Primary tumors were generated in *Dct::TVA;Braf*^{CA}*;Cdkn2a*$^{lox/lox}$*;Pten*$^{lox/lox}$ mice using RCAS:myr*Akt1* and RCAS:*Cre* retroviruses as previously described (179). Upon detection of a primary tumor, mice were gavaged once daily with 0.5% methylcellulose vehicle control or IACS-010759 (7.5 mg/kg) until the experimental endpoint. Body weights and tumor volumes were recorded every 3 days. A full necropsy was performed on all mice following euthanasia. Brain, lung, and primary tumor tissues were fixed in formalin overnight, dehydrated in 70% ethyl alcohol, and paraffin embedded. Sections were stained with hematoxylin and eosin (H&E) for review by a pathologist. A rate-based tumor/control (T/C) metric was used to compare growth in primary tumors treated with IACS-010759 vs. those treated with vehicle control (193).

Experimental metastasis studies. $2.5x10^6$ duel luciferase/GFP-tagged YUMM5.2 cells were injected into the left cardiac ventricle of 5 C57BL/6 mice (female, 8 weeks of age). Brain metastasis was confirmed by BLI. Animals were sacrificed once the mice were moribund. The brain with the greatest BLI signal was dissociated with collagenase type I (200 units/ml) and DNase (270 units/ml) to form single cell suspensions, as previously described (194). A purified

population of cells was acquired via GFP^+ cell sorting (performed on the FACSAria Fusion Cell Sorter with assistance from the MDACC South Campus Flow Cytometry Facility). To increase the brain-seeking capacity of the brain-metastasizing variants, cells were passaged in the brain for three successive passages yielding brain metastasis variants (Br1, Br2, and Br3). All of these variants were established as cell lines but only the YUMM5.2-Br3 cell line was used for metastasis studies. To determine if inhibition of OXPHOS diminishes CNS metastatic potential, YUMM5.2-Br3 cells were treated *in vitro* with IACS-010759 (100 nM) or with vehicle control for 12 hours. $2.5x10^6$ cells were then injected into the left cardiac ventricles of C57BL/6 mice (female, 8 weeks of age). Mice injected with the cells treated *in vitro* with vehicle were randomized to receive either 0.5% methylcellulose vehicle control (once daily) or IACS-010759 (7.5 mg/kg once daily) via oral gavage. In parallel, mice injected with cells treated *in vitro* with IACS-010759 were randomized to receive either 0.5% methylcellulose vehicle control (once daily) or IACS-010759 (7.5 mg/kg once daily) via oral gavage. *In vivo* treatments began 3 hours after cardiac injections. After 14 days, mice were injected with 150 mg/kg D-luciferin salt and euthanized 10 min later for *ex vivo* BLI analysis to evaluate organ involvement in detail. Brains were fixed in formalin overnight, dehydrated in 70% ethyl alcohol, and paraffin embedded. Sections were stained with H&E for review by a pathologist.

Effect of pharmacological OXPHOS inhibition on intracranial tumor growth. $1x10^3$ luciferase-tagged A375-R1 cells suspended in HBSS were directly implanted in the brain parenchyma of CD-1 nude mice (female, 8 weeks of age). Mice were immediately randomized to receive either 0.5% methylcellulose vehicle control (once daily) or IACS-010759 (5 mg/kg once daily) via oral gavage. Mice were weighed every two days and underwent BLI every week. Mice that progressed to 20% weight loss were euthanized. Additionally, mice were euthanized once

moribund or upon displaying neurological symptoms (ataxia, seizures, circling behavior, paralysis, or cranial doming).

PGC1α knockdown studies. $1x10^4$ A375P cells and $2x10^4$ G361 cells stably transfected with shRNA against PGC1α (shPGC1α) and their scrambled controls (shScr) suspended in HBSS were directly implanted in the brain parenchyma of CD-1 nude mice (female, 8 weeks of age). Mice were weighed every two days. Mice that progressed to 20% weight loss were euthanized. Additionally, mice were euthanized once moribund or upon displaying neurological symptoms (ataxia, seizures, circling behavior, paralysis, or cranial doming). In parallel, $3x10^6$ shScr and shPGC1α A375P and G361 cells were injected subcutaneously into mice from the same cohort. Tumors were measured using a digital caliper every 3 days for a total of 28 days. The greatest longitudinal diameter (length or "L") and the greatest transverse diameter (width or "W") were recorded. Tumor volume was calculated as $[(LxW^2)/2]$.

2.19 - Efficacy Studies

IACS-010759 monotherapy. $1x10^3$ luciferase-tagged A375-R1 cells and $2x10^4$ SKMEL5 cells suspended in HBSS were directly implanted in the brain parenchyma of CD-1 nude mice (female, 8 weeks of age). After 3 days (A375-R1) and 14 days (SKMEL5), mice were randomized to receive either 0.5% methylcellulose vehicle control (once daily) or IACS-010759 (5 mg/kg once daily) via oral gavage. Mice were weighed every two days. Mice with 15% weight loss were provided with a single intraperitoneal injection of normal saline [mL = (0.06 x weight in g)/2] and placed on a drug holiday. Mice that recovered to less than 10% weight loss restarted their treatment regimen while those that progressed to 20% weight loss were euthanized. Additionally, mice were euthanized once moribund or upon displaying neurological symptoms (ataxia, seizures,

circling behavior, paralysis, or cranial doming). A375-R1 treatments were designed to end 42 days after randomization while SKMEL5 treatments ended 42 days or 80 days after randomization.

IACS-010759+BRAFi. $1x10^3$ luciferase-tagged A375 and A375-R1 cells and $2x10^4$ SKMEL5 cells suspended in HBSS were directly implanted in the brain parenchyma of CD-1 nude mice (female, 8 weeks of age). After 3 days (A375-R1) and 14 days (A375 and SKMEL5), mice were randomized into 4 treatment arms: vehicle, IACS-010759 (5 mg/kg p.o. once daily), dabrafenib (30 mg/kg p.o. once daily), and IACS-010759 (5 mg/kg p.o. once daily) + dabrafenib (30 mg/kg p.o. once daily). Mice were weighed every two days and were euthanized once progressing to 20% weight loss. Additionally, mice were euthanized once moribund or upon displaying neurological symptoms (ataxia, seizures, circling behavior, paralysis, or cranial doming). Treatments ended 60 days after randomization. Brains were harvested from two A375 ICr mice progressing on vehicle treatments and two A375 ICr mice progressing on dabrafenib treatments. Collagenase type I (200 units/ml) and DNase (270 units/ml) were used to form single cell suspensions, as previously described (194). A purified population of cells was acquired via treatment with 2 ug/ml puromycin (previously confirmed to kill all untransfected A375 cells after 72 hours).

Metformin+anti-PD1. $5x10^3$ luciferase-tagged B16-F10 cells suspended in HBSS were directly implanted in the brain parenchyma of C57BL/6 mice (female, 8 weeks of age). After 5 days, tumor uptake was confirmed via BLI and mice were randomized into 4 treatment arms: isotype control (200 ug i.p. 3x/week) + PBS (10 ul/g body weight i.p. every other day), anti-PD1 (200 ug i.p. 3x/week) + PBS (10 ul/g body weight i.p. every other day), isotype control (200 ug i.p. 3x/week) + metformin (50 mg/kg i.p. every other day), and anti-PD1 (200 ug i.p. 3x/week) + metformin (50 mg/kg i.p. every other day). Mice were weighed every 2 days and were euthanized

once progressing to 20% weight loss. Additionally, mice were euthanized once moribund or upon displaying neurological symptoms (ataxia, seizures, circling behavior, paralysis, or cranial doming). Treatments were designed to end 42 days after randomization.

CB839 monotherapy. Cell proliferation inhibition was determined using Cell Titer Blue (Promega), as previously described (3). Subsequently, $1x10^3$ luciferase-tagged A375-R1 and $1x10^4$ MEL624 cells suspended in HBSS were directly implanted in the brain parenchyma of CD-1 nude mice (female, 8 weeks of age). After 7 days, tumor uptake was confirmed via BLI, and mice were randomized into 2 treatment arms: vehicle and CB839 (200 mg/kg p.o. twice daily). Mice were weighed every 2 days and were euthanized once progressing to 20% weight loss. Additionally, mice were euthanized once moribund or upon displaying neurological symptoms (ataxia, seizures, circling behavior, paralysis, or cranial doming). Treatments were designed to end 42 days after randomization.

2.20 - qRT-PCR Analysis

cDNA synthesis. 1000 ng of RNA was used to synthesize the first strand of cDNA using the High Capacity cDNA Archive kit (Applied Biosystems) following standard ABI Protocol.

qRT-PCR. Inventoried TaqMan assays were purchased from Life Technologies [Mm00443258_m1 (*Tnf*), Mm00812512_m1 (*Prf1*), Mm01168134_m1 (*Ifng*), Mm00442837_m1 (*Gzmb*), Mm01182107_g1 (*Cd8a*), Mm00445235_m1 (*Cxcl10*), Mm00434946_m1 (*Cxcl9*), Mm00492586_m1 (*Ido1*), Mm00439531_m1 (*Stat1*), Mm01208835_m1 (*Ppargc1a*), Mm00499674_m1 (*Idh3a*), Mm01250094_m1 (*Cox4i1*), Mm05874166_g1 (*Ldhb*), and Mm01165335_m1 (*Ndufa5*)]. All qRT-PCR reactions were performed using the 7900HT Fast Real-Time PCR system and Taqman gene expression master mix (Applied Biosystems) with a standard cycling program of 40 cycles at 95 °C for 15 s and at 60 °C for 1 min. All reactions were run in duplicate and normalized to human *18S* (Hs99999901_s1). Data was analyzed using the $2^{-\Delta\Delta CT}$ method.

2.21 - Immunohistochemistry (IHC) of Clinical Samples

All IHC studies were performed on 5 µm FFPE sections using a Leica BOND RXm autostainer. Slides were stained with antibodies targeting human P-S6 (Cell Signaling #4858, 1:100) and P-PRAS40 (Cell Signaling #13175, 1:200) using a modified version of either the standard Leica Bond DAB "F" or red "J" IHC protocols. Slides were scored by a pathologist and given an H-score based on percentage and intensity of positivity.

2.22 - Statistical Analyses

Overall survival analyses. Overall survival (OS) was defined as the time interval from date of craniotomy (clinical samples) or treatment initiation (mouse studies) to date of death or censoring from any cause. Survival duration was analyzed by the Kaplan-Meier method. Survival

curves were drawn in Prism 7.0 (Graphpad). Hazard ratios and significance were calculated via the Mantel-Haenszel test and log-rank test, respectively, in Prism 7.0 (Graphpad).

Additional analyses. Data analyses and representations were performed either with the R (v3.3.3), Microsoft Excel 2013, or Prism 7.0 (GraphPad). Comparison of continuous variables between two groups was performed by unpaired or paired Student's *t*-test. The Perason correlation coefficient was calculated to assess correlation between continuous variables. To control for multiple hypothesis testing, we applied the Benjamini-Hochberg method. Lastly, all statistical significance testing was two-sided at Type-I error rate of 0.05 except where specifically noted in relevant figure legends.

CHAPTER 3: THE BRAIN TUMOR MICROENVIRONMENT MEDIATES ENRICHMENT OF OXIDATIVE PHOSPHORYLATION IN MELANOMA BRAIN METASTASES

Copyright Disclosure:

This chapter is based upon:

1. **Fischer, G. M.**, Y. N. Vashisht Gopal, J. L. McQuade, W. Peng, R. J. DeBerardinis, and M. A. Davies. 2018. Metabolic strategies of melanoma cells: Mechanisms, interactions with the tumor microenvironment, and therapeutic implications. *Pigment Cell Melanoma Res* 31: 11-30.

2. **Fischer, G. M.**, A. Jalali, D. A. Kircher, W. C. Lee, J. L. McQuade, L. E. Haydu, A. Y. Joon, A. Reuben, M. P. de Macedo, F. C. L. Carapeto, C. Yang, A. Srivastava, C. R. Ambati, A. Sreekumar, C. W. Hudgens, B. Knighton, W. Deng, S. D. Ferguson, H. A. Tawbi, I. C. Glitza, J. E. Gershenwald, Y. N. Vashisht Gopal, P. Hwu, J. T. Huse, J. A. Wargo, P. A. Futreal, N. Putluri, A. J. Lazar, R. J. DeBerardinis, J. R. Marszalek, J. Zhang, S. L. Holmen, M. T. Tetzlaff, and M. A. Davies. 2019. Molecular Profiling Reveals Unique Immune and Metabolic Features of Melanoma Brain Metastases. *Cancer Discov.* 9: 628-645.

3.1 - INTRODUCTION

3.1.1 - Impact of the Tumor Microenvironment on Tumor Metabolism

While it is most convenient to classify melanomas as either glycolytic or oxidative, an increasing body of evidence suggests that metabolic phenotypes of tumors are more accurately viewed as dynamic in nature (11). While key oncogenic pathways implicated in melanomas (RAS-RAF-MAPK and PI3K-AKT) typically promote glycolysis, this metabolic pathway requires an extensive supply of glucose to fuel reactions. Tumor cells are not equally supplied with oxygen and nutrients due to inadequate vascularization, and frequently they must adapt to hypoxia and to glucose deprivation (11). In the presence of adequate glucose, hypoxic melanoma cells almost completely decouple glycolysis from the tricarboxylic acid (TCA) cycle (10). Glutamine then fuels the TCA cycle and provides citrate for fatty acid synthesis. Despite the uncoupling of glycolysis and the TCA cycle, glutamine and glucose oxidation continue to produce significant ATP for the cell because of the efficiency of oxidative phosphorylation (OXPHOS) relative to glycolysis (10). Alternative pathways such as glutamine and fatty acid oxidation (FAO) are essential in glucose-depleted conditions. For example, adipocytes in the tumor microenvironment (TME) can communicate with melanoma cells via exosomes carrying proteins involved in FAO (195). Upon uptake by melanoma cells, via an uncharacterized mechanism, these exosomes force a metabolic reprogramming in melanoma cells characterized by high levels of FAO and aggressiveness (195).

In recent years, the role of autophagy and macropinocytosis in promoting survival of melanoma cells in hostile microenvironments has gained considerable interest. Autophagy is a highly regulated process that involves the degradation of macromolecules and organelles into

useful constituent components. In this manner, large proteins can be degraded to provide nitrogen and carbon for bioenergetic maintenance. MEK/ERK signaling in melanoma upregulates phorbol-12-myristate-13-acetate-induced protein 1 (NOXA), which promotes an increase in autophagy through cAMP responsive element binding protein (CREB) (196, 197). NOXA-driven autophagy delays the apoptosis of human melanoma cells in nutrient-depleted conditions (196). Furthermore, autophagy provides a survival advantage to melanoma cells cultured in harsh, acidic conditions (197, 198). In addition to autophagy, a variety of tumor types utilize macropinocytosis to scavenge extracellular nutrients when grown in harsh conditions (12). Macropinocytosis can supply tumor cells with necessary nitrogen and carbon (12, 199). In melanoma, hyperactive PI3K-AKT pathway signaling drives macropinocytosis so efficiently that the cells require activation of Ras-related protein Rab-7 (RAB7) to clear the vesicles taken into cells before a form of cell death called *methuosis* occurs (200). In scenarios of widespread nutrient starvation, the ratio of ATP to AMP declines, stimulating the LKB1-AMPK axis to suppress mTOR-mediated anabolic processes and to stimulate autophagy and macropinocytosis (12).

Directly in contrast with the Warburg effect, the reverse Warburg effect was originally proposed by Pavlides et al. in 2009. In this model, tumor cells and surrounding stromal cells engage in a symbiotic relationship where tumor cells corrupt caveolin-1-deficient cancer associated fibroblasts (CAFs) via secretion of hydrogen peroxide. Mitochondrial activity in the CAFs is inhibited, forcing the cells to depend exclusively on glycolysis. These cells secrete lactate into the TME via Monocarboxylate transporter 4 (MCT4), which tumor cells take up via Monocarboxylate transporter 1 (MCT1) to fuel oxidative metabolism (201-203). While this model originally was described in breast cancer, similar tumor-stroma interactions have been demonstrated in a variety of other cancers, including oral squamous cell carcinoma and osteosarcoma (204, 205). Though this model could offer novel therapeutic approaches via

disruption of lactate shuttling, it remains to be investigated in melanoma, as does the concept of metabolic symbiosis. Similar to the reverse Warburg effect, this version of lactate shuttling involves hypoxic glycolytic tumor cells secreting lactate into the TME via MCT4, which oxidative tumor cells uptake via MCT1 and utilize for energy. Interestingly, Ho et al. demonstrated that increased expression of MCT1 and MCT4 correlate with melanoma progression (206). This finding suggests that metabolic symbiosis could play a role in melanoma progression and represents a potential therapeutic opportunity. For example, inhibition of MCT1 in a mouse model of lung carcinoma resulted in oxygenated cells switching to glycolysis for ATP production. As a result, hypoxic tumor cells died secondary to glucose starvation (207).

Studies in other cancer types have provided numerous insights into the role of the TME in shaping tumor cell metabolism. For example, Smolkova et al. demonstrated that 4 days of glucose deprivation completely reprogrammed HTB-126 breast cancer cells, significantly elevating OXPHOS to compensate for aglycemia (208). Mitochondria are actually able to function at oxygen concentrations as low as 0.5%, allowing this flexibility to occur even under hypoxic conditions (12, 209, 210). The LKB1-AMPK-PGC1α signaling axis stimulates OXPHOS in these scenarios (208). Redox balance is maintained through one-carbon metabolism, cytoplasmic malic enzyme, and isocitrate dehydrogenase 1/2 (IDH1/2)-mediated production of NADPH (12). Metabolic flexibility allows tumor cells to survive inhibition of a single metabolic pathway and provides a survival advantage necessary for survival in harsh TMEs (211, 212). Furthermore, this metabolic flexibility has complicated attempts to target single metabolic pathways as a therapeutic strategy. However, targeting glycolysis and OXPHOS via simultaneous treatment with the electron transport chain complex I inhibitor metformin and the lactate dehydrogenase (LDH) inhibitor oxamate has produced promising results, significantly inhibiting B16-F10 tumor growth in C57BL/6 mice (213).

To date, no studies have attempted to understand the effect of the brain tumor microenvironment on melanoma cell metabolism. Interestingly, Chen et al.'s breast cancer metastasis study provides potential insights into this topic (211). The authors acquired circulating tumor cells from a metastatic breast cancer patient and derived brain-metastatic and bone-metastatic variants of these cells via *in vivo* selection in immunodeficient mice. The brain-metastatic cells underwent significant adaptations to survive in the brain TME. Specifically, they upregulated expression of enzymes involved in glycolysis, TCA cycle, and OXPHOS relative to both parental cells and the bone-metastatic cells. Importantly, these cells maintained this phenotype *in vitro*. These findings strongly suggest that the brain TME poses unique metabolic challenges and selects metastatic cells inherently enriched in OXPHOS.

3.1.2 - Hypothesis Tested

Our recent RNA-seq analysis of 35 MBMs and 42 patient-matched ECMs identified 494 genes that were differentially expressed between the MBMs and ECMs (174). Focused pathway analyses for the expression of 70 different metabolic gene networks demonstrated that OXPHOS was the most significantly enriched metabolic pathway in MBMs. This expression profile could be the result of the brain TME selecting cells inherently enriched in OXPHOS or from adaptation of tumor cells to the brain TME. A previously published analysis of experimental breast cancer brain metastasis indicated that the brain TME selects cells inherently enriched in OXPHOS for colonization and outgrowth compared to melanoma cells that metastasize to other distant sites (211). **Thus, we tested the hypothesis that OXPHOS enrichment in MBMs results from improved efficiency of melanoma cells with increased OXPHOS to form metastases at this site in the body.**

3.2 – RESULTS

3.2.1 – Oxidative Phosphorylation Levels Do Not Predict Brain Tropism in Metastatic Melanoma

We hypothesized that OXPHOS levels differ between primary melanomas that metastasize to the brain compared to primary melanomas that metastasize exclusively to other distant sites. To test this hypothesis, we performed RNA-seq analysis of primary melanomas from patients that developed an MBM within 3-18 months of initial diagnosis (n=19) and patients that developed metastases at sites other than the brain within 3-18 months of initial diagnosis (n=16). We calculated OXPHOS-Indices (OP-Indices) for all samples and performed hierarchical clustering to elucidate if samples would cluster by site of distant metastasis. However, we did not observe any identifiable clustering pattern (**Figure 6A**). Significant heterogeneity was observed in both groups of samples. To confirm these observations, we performed principal components analysis (PCA) of the samples. Samples failed to cluster by site of distant metastasis. Instead, groups significantly overlapped with each other (**Figure 6B**). Additionally, we again observed marked variability within groups. Subsequent preranked gene set enrichment (GSEA-P) analysis demonstrated no significant difference in KEGG OXPHOS gene set expression between these two groups of samples (FDR q-val=0.516) (**Figure 6C**), and direct comparison of OP-Indices failed to identify a significant difference between the groups (p=0.5513) (**Figure 6D**). Finally, we pooled samples and divided them into tertiles based on OP-Indices. Patients with high OP-Indices (highest tertile) had comparable brain metastasis-free survival as patients with low OP-Indices (lowest tertile) (**Figure 6E**). Together, these results

indicate that our observed OXPHOS enrichment in MBMs vs. ECMs was unlikely due to primary tumors highly enriched for this metabolic program metastasizing to the brain more efficiently than other primary tumors.

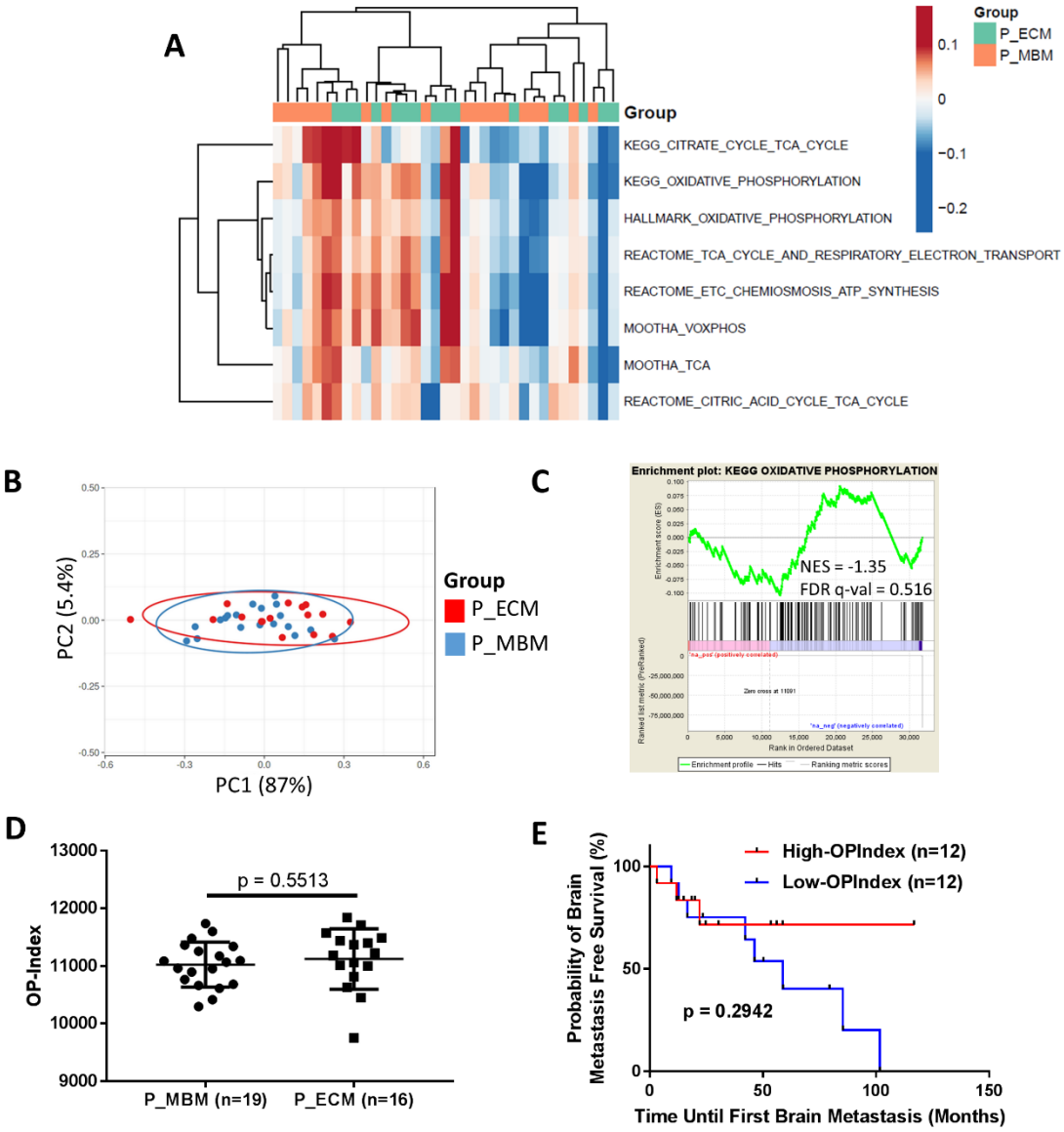

Figure 6: Oxidative phosphorylation is not enriched in surgically excised brain-metastatic primary melanoma tumors compared to primary melanoma tumors that metastasize to other anatomical sites. (**A**) Hierarchical clustering of the OXPHOS-Indices (OP-Indices) from brain-metastatic human primary melanomas (P_MBM; n=19) vs. metastatic human primary melanomas that failed to develop brain metastases (P_ECM; n=16). Results are represented as a heatmap of median-centered values from each of the 8 components of the OP-Index. (**B**) Principal components analysis (PCA) of the OP-Indices from brain-metastatic human primary melanomas (P_MBM; n=19) vs. metastatic human primary melanomas that failed to develop brain metastases (P_ECM; n=16). (**C**) GSEA-P analysis enrichment plot of the KEGG OXPHOS gene set in brain-metastatic human primary melanomas (P_MBM; n=19) vs. metastatic human primary melanomas that failed to develop brain metastases (P_ECM; n=16). Normalized enrichment score (NES) and FDR q-val are listed on the enrichment plot. Significance was set to FDR q-val < 0.05. (**D**) Comparison of OP-Indices from brain-metastatic human primary melanomas (P_MBM; n=19) and metastatic human primary melanomas that failed to develop brain metastases (P_ECM; n=16). Lines represent mean ± S.D., and each dot represents a single sample. Significance determined via two-sided Student's *t*-test. (**E**) All metastatic human primary tumor samples (n=35) were pooled and organized in descending order according to OP-Index. Kaplan–Meier survival analysis shows no significant difference in brain metastasis-free survival between primary tumors from the highest (n=12) and lowest (n=12) OP-Index tertiles.

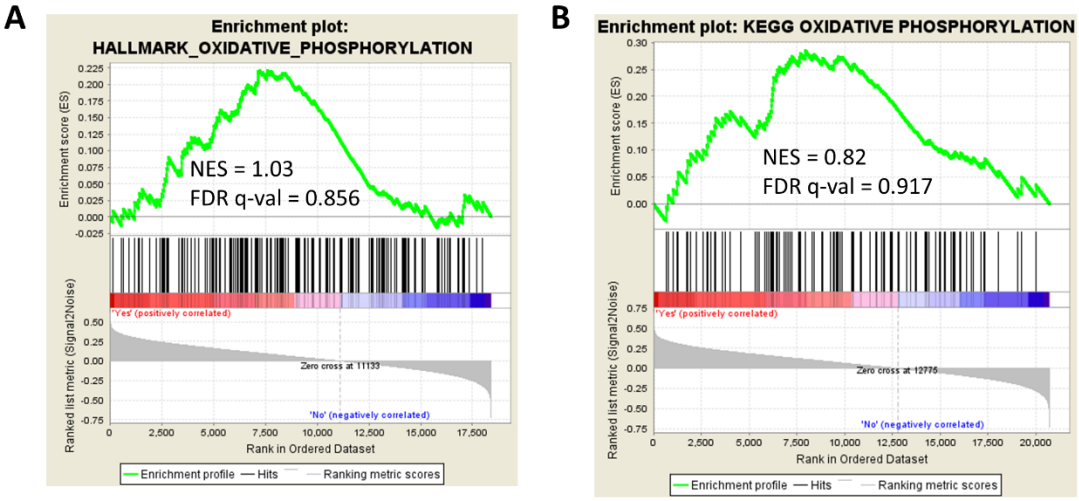

Figure 7: Oxidative phosphorylation does not correlate with cerebrotropism in melanoma extracranial metastases. GSEA enrichment plots of (**A**) MSigDB Hallmarks Oxidative Phosphorylation and (**B**) KEGG Oxidative Phosphorylation gene sets in extracranial metastases with cerebrotropism (development of brain metastasis within < 6 months of stage IV disease diagnosis) vs. extracranial metastases that failed to develop brain metastases for > 18 months from stage IV diagnosis. Normalized enrichment score (NES) and FDR q-val are listed on the enrichment plots. Significance was set to FDR q-val < 0.05.

Next, we evaluated publicly available Illumina microarray data (GSE60464) from extracranial metastases of stage IV patients with cerebrotropism (developed brain metastases within 6 months of initial stage IV disease diagnosis; n=17) and stage IV patients without cerebrotropism (did not develop brain metastases within 18 months of initial stage IV diagnosis; n=25) (129). GSEA determined that OXPHOS gene set expression was not significantly different between groups (**Figure 7A-B**).

However, we recognized the possibility that bulk gene expression studies of primary tumors and extracranial metastases might have failed to identify subclones highly enriched in OXPHOS that efficiently metastasize to the brain but do not comprise the majority of cells in the analyzed specimens. Thus, we downloaded publicly available Affymetrix microarray data (GSE44660) for cell lines generated from surgically resected melanoma lymph node metastases

(LNMs; n=12), and MBMs (n=7) (214). Lymph node specimens from patients with poor prognosis (n=3) were excluded from this analysis to avoid the interference of gene expression

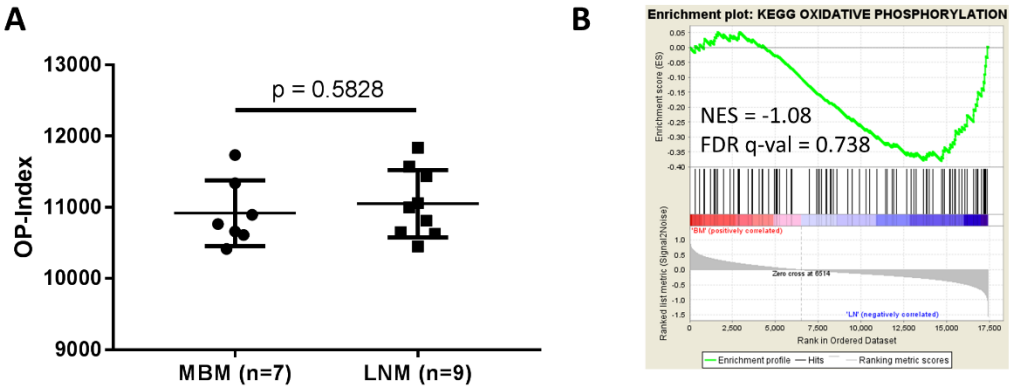

Figure 8: Oxidative phosphorylation does not differ between cell lines acquired from brain and lymph node metastases. (**A**) Comparison of OXPHOS-Indices (OP-Indices) of cell lines derived from surgically resected melanoma brain metastases (MBMs; n=7) and cell lines derived from lymph node metastases (LNMs) in patients with a good clinical prognosis (n=9). Lines represent mean ± S.D., and each dot represents a single sample. Significance determined via two-sided Student's *t*-test. (**B**) GSEA enrichment plots of the KEGG Oxidative Phosphorylation gene set in cell lines derived from surgically resected MBMs (n=7) vs. cell lines derived from LNMs in patients with a good clinical prognosis (n=9). Normalized enrichment score (NES) and FDR q-val are listed on the enrichment plots. Significance was set to FDR q-val < 0.05.

associated with distant organ metastasis – including undiagnosed MBMs - that may be present in LNMs from patients with poor prognosis. We reasoned that if the brain TME selects for rare subclones inherently more enriched in OXPHOS than cells that metastasize to other sites, cell lines derived from brain metastases should express OXPHOS genes at significantly higher levels than cell lines derived from LNMs. However, we observed no significant differences in OP-Indices between the groups (p=0.5828) (**Figure 8A**). Additionally, GSEA of the KEGG OXPHOS gene set demonstrated no significant enrichment of OXPHOS in MBM-derived cell lines vs. LNM-derived cell lines (FDR q-val=0.738) (**Figure 8B**).

To confirm our findings, we downloaded publicly available Agilent microarray data from a preclinical model of spontaneous melanoma brain metastasis (GSE23601) (116) and compared

gene expression profiles from two variants of the human melanoma cell line WM239 (named WM239_BM1 and WM239_BM2) which metastasize spontaneously to the brain after implantation into the subcutaneous tissue and a variant that spreads to sites other than the brain (WM239_ECM). GSEA-P demonstrated no significant enrichment of the KEGG OXPHOS gene set in the brain-metastatic variants vs. the variant that metastasizes to non-CNS sites (**Figure 9**).

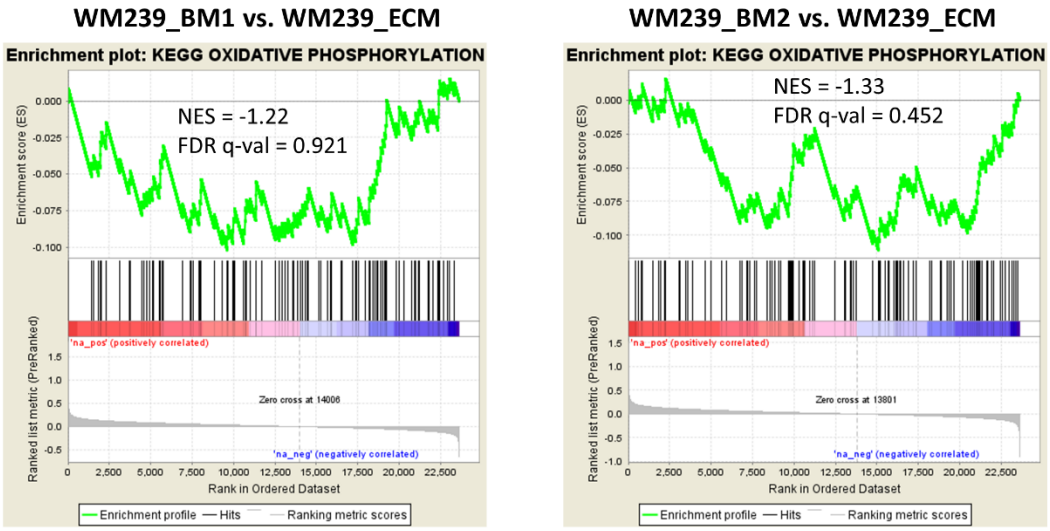

Figure 9: Oxidative phosphorylation does not differ between WM239 cell line variants that form brain metastases and variants that metastasize exclusively to other anatomical sites. GSEA-P enrichment plots of the KEGG Oxidative Phosphorylation gene set in two variants of the human melanoma cell line WM239 which can metastasize spontaneously to the brain parenchyma following implantation into subcutaneous tissue (named WM239_BM1 and WM239_BM2) vs. a variant that metastasizes exclusively to sites other than the brain (named WM239_ECM). Normalized enrichment score (NES) and FDR q-val are listed on the enrichment plots. Significance was set to FDR q-val < 0.05.

Cumulatively, these results disprove our initial hypothesis that OXPHOS enrichment in MBMs vs. ECMs can be explained via selection of cells inherently more enriched in OXPHOS genes than cells that metastasize to other sites. Instead, our findings suggest that the brain TME facilitates OXPHOS gene expression to a significantly greater extent than other organs.

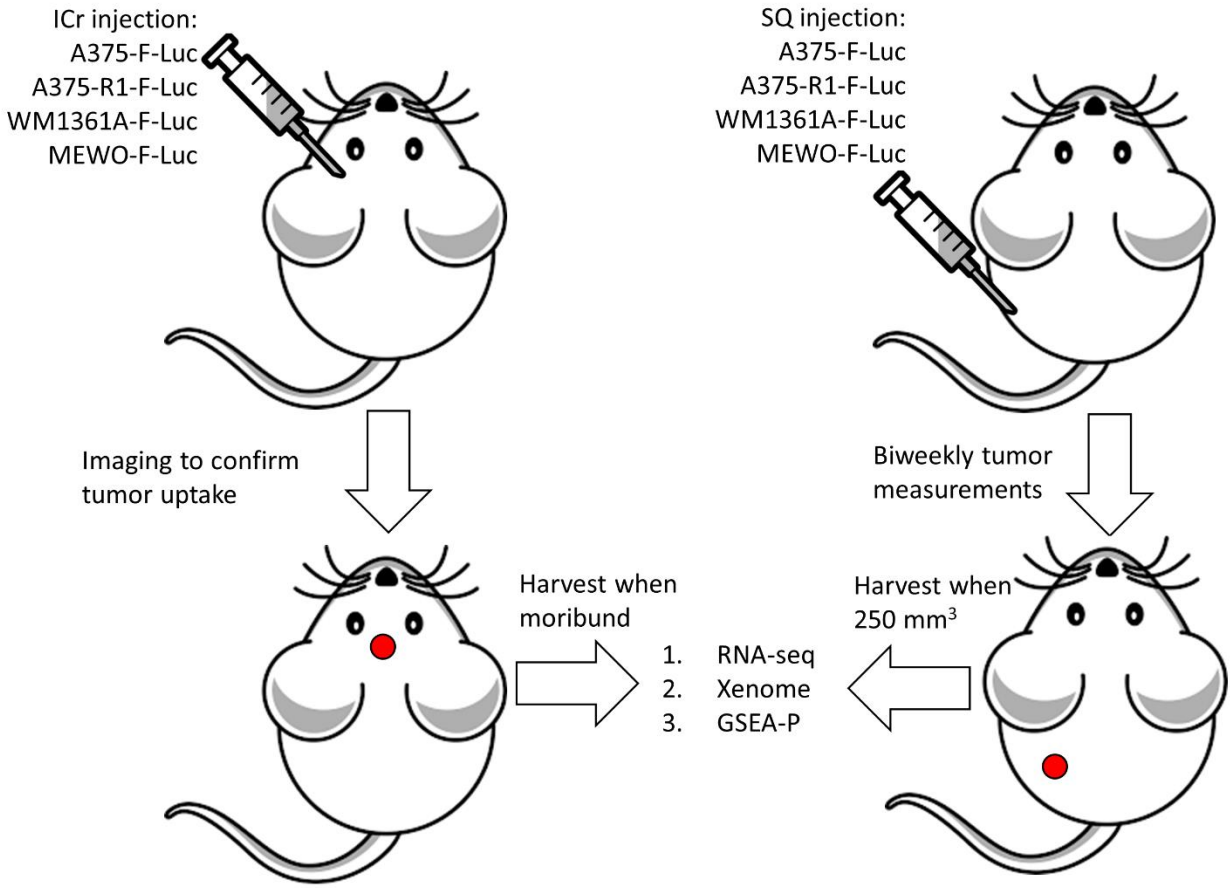

Figure 10: Injection scheme designed to assess the effect of tumor microenvironment on gene expression profiles. Luciferase-tagged A375, A375-R1, MEWO, and WM1361A cells were injected into the brain and subcutaneous (SQ) tissue of CD-1 nude mice from the same cohort. Mice with intracranial (ICr) tumors were euthanized if they lost > 20% body weight, if they became moribund, or if they displayed neurological symptoms (ataxia, seizures, circling behavior, paralysis, or cranial doming). Mice with SQ tumors were euthanized once tumors reached 250 mm^3. RNA-seq was performed on RNA isolated from dissected tumor tissue, and Xenome was used to further discern gene expression signatures from the tumor (human) RNA. Pathway analysis was performed to assess the effect of the brain tumor microenvironment on oxidative phosphorylation enrichment.

3.2.2 - The Brain Tumor Microenvironment Induces Oxidative Phosphorylation in Metastatic Melanomas

3.2.2a – Transcriptomics Studies Verify Increased Expression of Oxidative Phosphorylation Genes in Melanoma Cells Growing in the Brain Compared to Subcutaneous Tissue

To test the effect of the brain TME on OXPHOS gene expression, we implanted A375 ($BRAF^{V600E/wt}$), A375-R1 ($BRAF^{V600E/wt}$;$MEK^{F129L/wt}$) (3), WM1361A ($NRAS^{Q61R/Q61R}$), and MEWO ($BRAF^{wt/wt}$;$NRAS^{wt/wt}$) human melanoma cells intracranially (ICr) and subcutaneously (SQ) in CD-1 nude mice (**Figure 10**). Tumors were harvested when mice became moribund or SQ tumors reached 250 mm^3. RNA-seq was performed on RNA isolated from dissected tumor tissue, and Xenome (183) was used to further discern gene expression signatures from the tumor (human) RNA. Data was pooled following correction for cell line-intrinsic differences. GSEA-P of this dataset identified OXPHOS as the most enriched KEGG metabolic pathway in the ICr xenografts (**Figure 11A**). Additionally, anatomical locations were compared within each model, and GSEA-P analysis established OXPHOS as the KEGG metabolism gene network most enriched in the ICr xenografts from all of the models (**Figure 11B-E**). Together, these results confirm that the brain TME is sufficient to induce transcription of OXPHOS genes.

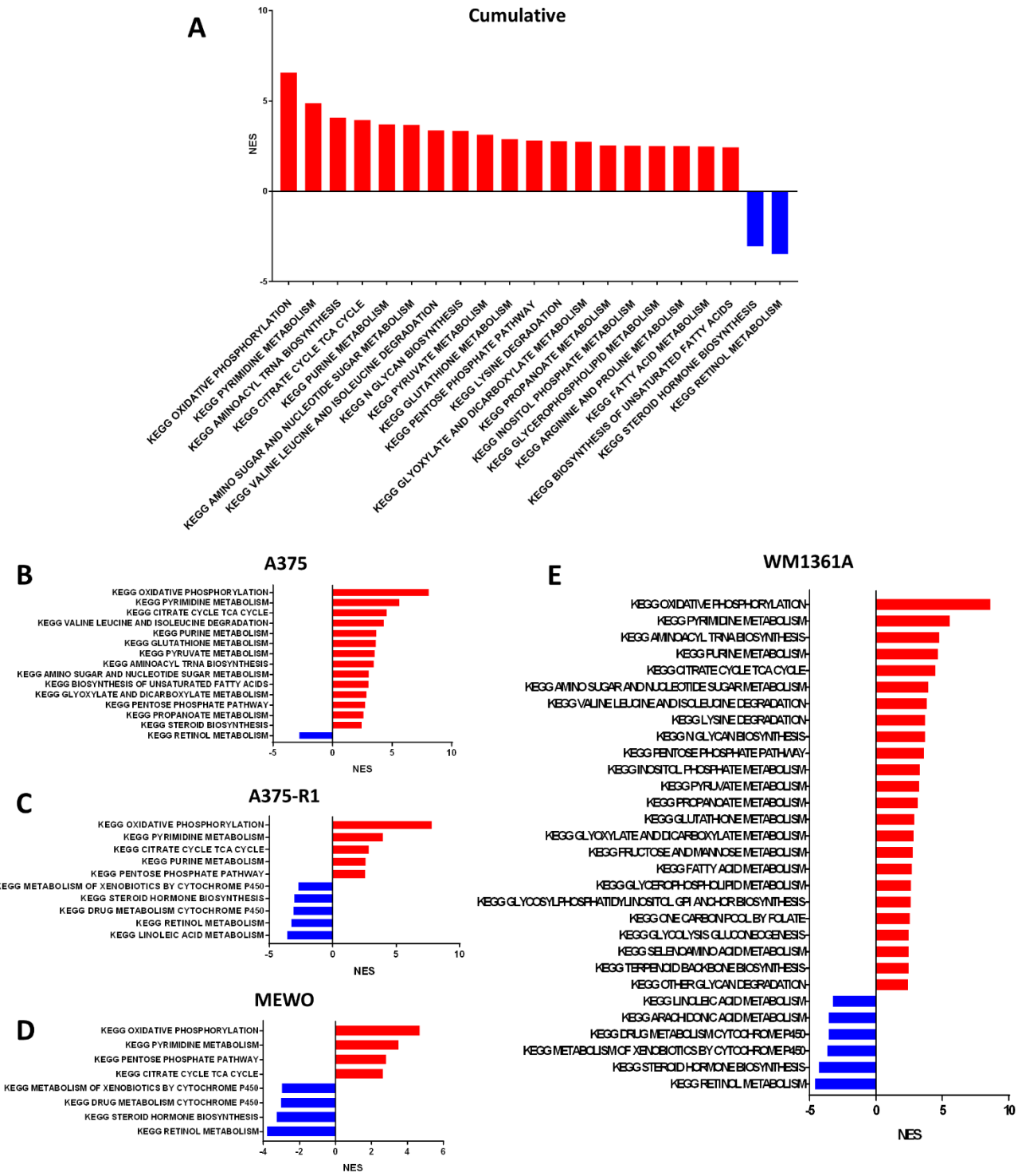

Figure 11: Oxidative phosphorylation is enriched in intracranial melanoma xenografts. GSEA-P analysis enrichment plots demonstrating that Oxidative Phosphorylation is the most enriched KEGG metabolism gene set in (**A**) A375, A375-R1, MEWO, and WM1361A ICr xenografts vs. A375, A375-R1, MEWO, and WM1361A SQ xenografts following correction for cell line differences, (**B**) A375 ICr vs. A375 SQ xenografts, (**C**) A375R1 ICr vs. A375R1 SQ xenografts, (**D**) MEWO ICr vs. MEWO SQ xenografts, and (**E**) WM1361A ICr vs. WM1361A SQ xenografts. Normalized enrichment score (NES) is listed on the enrichment plots. Red indicates enrichment in ICr xenografts while blue indicates depletion in ICr xenografts. Significance was set to FDR q-val < 0.0001.

3.2.2b - Metabolomics Analyses Confirm Increased Oxidative Phosphorylation in Melanoma Cells Growing in the Brain Compared to Subcutaneous Tissue

To directly assess the metabolism of MBMs, Low-OXPHOS A375 and CHL1 *($BRAF^{wt/wt}$;$NRAS^{wt/wt}$)* human melanoma cells were implanted into the brains and SQ tissue of CD-1 nude mice. Liquid chromatography-mass spectrometry (LC-MS) analysis of metabolites collected from the ICr and SQ xenografts demonstrated significantly higher concentrations of individual tricarboxylic acid (TCA) cycle metabolites in ICr vs. SQ xenografts for both cell lines (**Figure 12A-B**). Metabolite set enrichment analysis (MSEA) of differentially expressed metabolites (DEMs) (FDR q-val<0.25) demonstrated significant enrichment (FDR q-val<0.05) of the TCA cycle pathway in ICr vs. SQ xenografts for both lines (**Figure 12C-D**), supporting increased OXPHOS in MBMs. To further support this finding, we implanted Low-OXPHOS A375 cells into the brains and SQ tissue of CD-1 nude mice and performed *in vivo* [U-^{13}C]-glucose tracing studies (**Figure 13A**). Gas chromatography-mass spectrometry (GC-MS) analysis of the xenografts demonstrated greater labeling of the TCA cycle metabolites fumarate ($p<0.01$), malate ($p<0.01$), and citrate ($p<0.001$) in ICr vs. SQ tumors but no significant differences in labeling patterns in glycolytic intermediates, indicating a specific increase in glucose oxidation in ICr xenografts (**Figure 13B**).

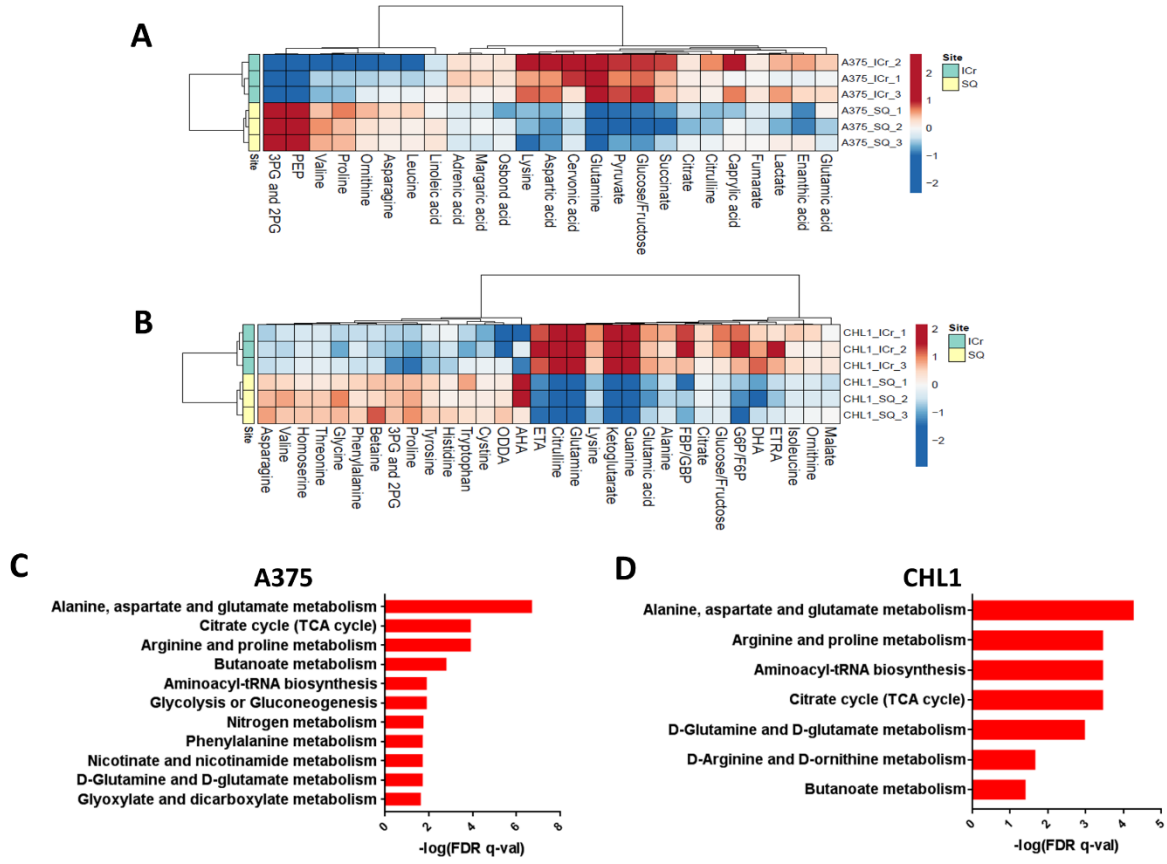

Figure 12: Direct metabolite analysis confirms that the brain microenvironment promotes oxidative phosphorylation in melanoma brain metastases. (**A-B**) Liquid chromatography-mass spectrometry (LC-MS) analysis was performed on A375 and CHL1 intracranial (ICr) and subcutaneous (SQ) xenografts to identify differentially expressed metabolites (DEMs) (FDR q-val<0.25). The tricarboxylic acid (TCA) cycle metabolites fumarate, citrate, and succinate were significantly upregulated (log2FC>0 and FDR q-val<0.25) in A375 ICr xenografts, and the TCA cycle metabolites malate, citrate, and α-ketoglutarate were significantly upregulated in CHL1 ICr xenografts. Data are presented as heatmaps of median-centered log2-tranformed concentrations of all DEMs. (**C-D**) Metabolite set enrichment analysis (MSEA) of individual metabolites significantly upregulated (log2FC>0 and FDR q-val<0.25) in A375 and CHL1 ICr vs. SQ xenografts. All pathways listed are significantly enriched in ICr vs. SQ xenografts (FDR q-val<0.05). X-axis indicates degree of significance. Values were generated from three biological replicates per condition. Used and modified with permission from the American Association for Cancer Research (AACR) (Fischer, G. M., Y. N. Vashisht Gopal, J. L. McQuade, et al. 2019. Molecular Profiling Reveals Unique Immune and Metabolic Features of Melanoma Brain Metastases. *Cancer Discov.* 9: 628-645).

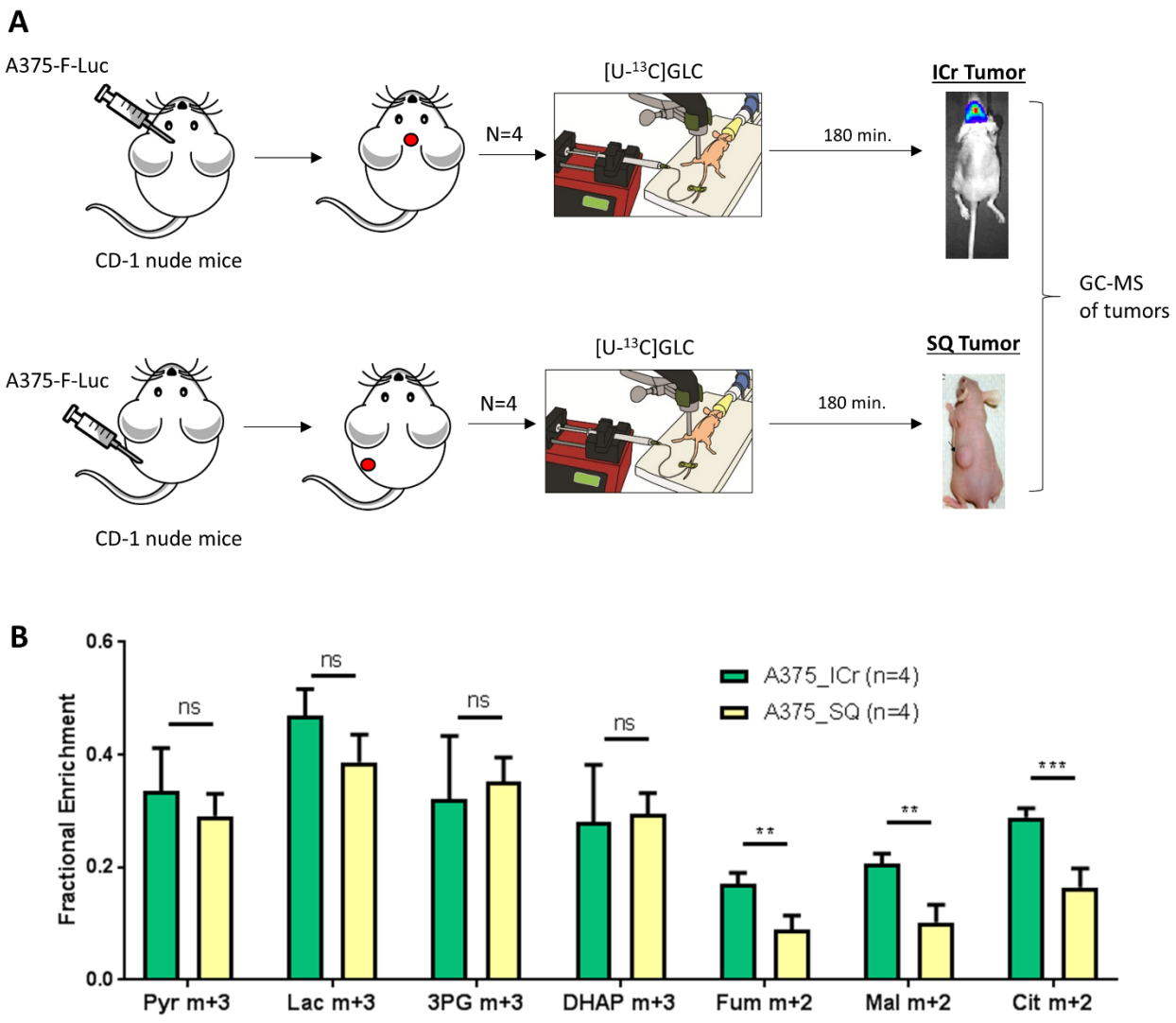

Figure 13: *In vivo* tracing studies confirm that the brain microenvironment promotes oxidative phosphorylation in melanoma brain metastases. (**A**) A375 cells were implanted into the brains and subcutaneous (SQ) tissue of CD-1 nude mice from the same cohort. Mice were infused with [U-^{13}C]-glucose for 180 minutes. Tumors were harvested for gas chromatography mass spectrometry (GC-MS) tracing studies analysis. (**B**) ^{13}C enrichment in metabolites from intracranial (ICr) and SQ xenografts of A375 cells following infusions with [U-^{13}C]-glucose. The fractional enrichment of metabolites is made relative to the enrichment of glucose in the tissue. Average values and S.D. for four biological replicates for each condition are displayed. Pyr, pyruvate; Lac, lactate; 3-PG, 3-phosphoglycerate; DHAP, dihydroxyacetone phosphate; Fum, fumarate; Mal, malate; Cit, citrate. ***P <0.001; **P <0.01; ns, not significant (P>0.05) by two-sided Student's t-test. Used and modified with permission from the American Association for Cancer Research (AACR) (Fischer, G. M., Y. N. Vashisht Gopal, J. L. McQuade, et al. 2019. Molecular Profiling Reveals Unique Immune and Metabolic Features of Melanoma Brain Metastases. *Cancer Discov.* 9: 628-645).

3.2.2c - Soluble Factors Secreted by the Brain Promote Oxidative Phosphorylation in Melanoma Cells

Klein et al. isolated soluble factors from normal mouse brains and acquired microarray data from cutaneous variants of YDFR melanoma cells (YDFR.C) grown *in vitro* in the presence and absence of these brain-derived soluble factors (176). We downloaded the microarray data (GSE34970) to further validate the role of the brain TME in facilitating OXPHOS enrichment. Cumulative GSEA analysis of the 70 KEGG metabolism gene sets determined that OXPHOS was the third most enriched pathway in the YDFR.C cells grown in the presence of brain-derived soluble factors (**Figure 14A**). Subsequent pathway analysis demonstrated that that the cells grown in the presence of brain-derived soluble factors were significantly enriched in both the KEGG and MSigDB Hallmarks OXPHOS gene set collections (FDR q-val = 0.005 and FDR q-val < 0.0001, respectively) (**Figure 14B-C**). Together, these results confirm that factors present in the brain TME are sufficient to induce significant upregulation of OXPHOS genes.

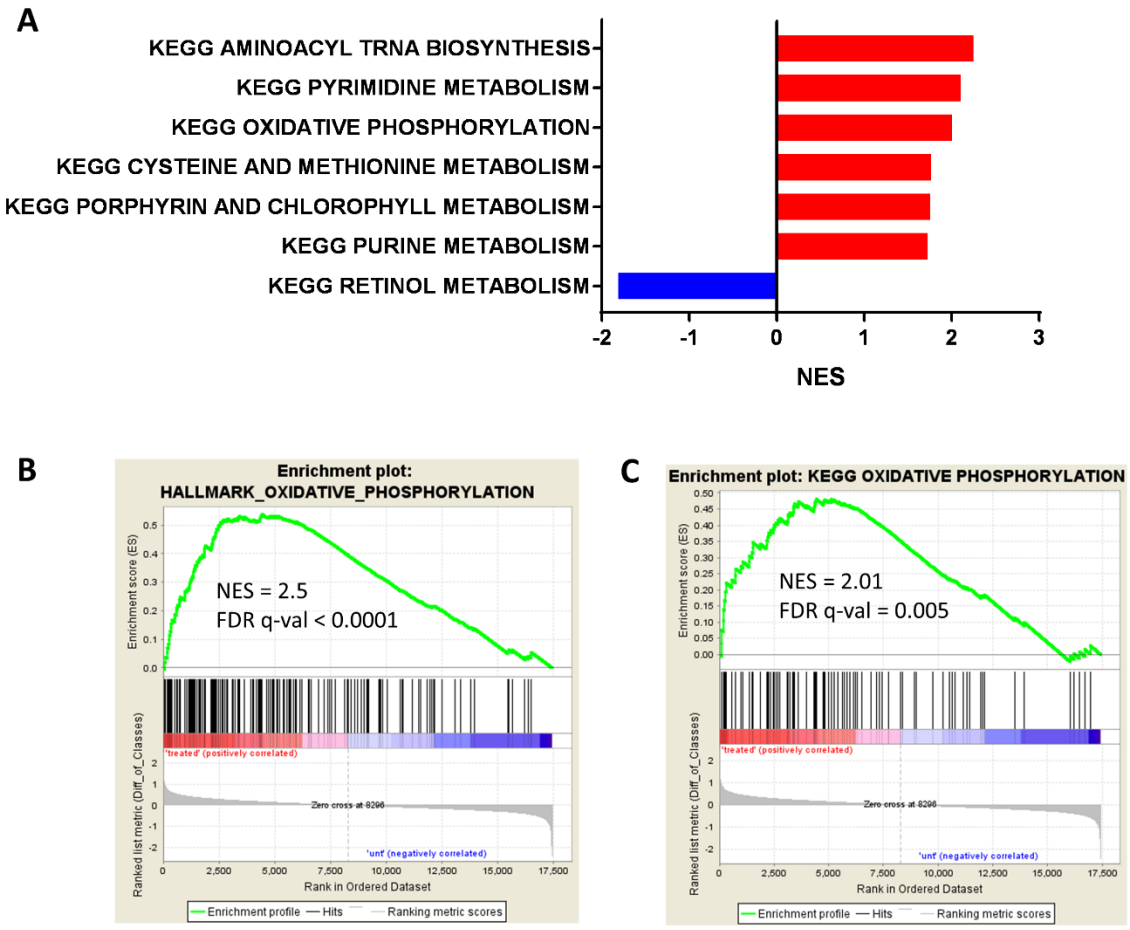

Figure 14: Brain-derived soluble factors induce oxidative phosphorylation in melanoma cells. (**A**) Cumulative GSEA analysis enrichment plot demonstrating significant enrichment or depletion of KEGG metabolism gene sets in YDFR.C cells treated *in vitro* for 48 hours with brain-derived soluble factors vs. untreated cells. Red indicates enrichment while blue indicates depletion. Normalized enrichment score (NES) forms the x-axis. Significance was set to FDR q-val < 0.05. Individual GSEA enrichment plots demonstrating significant enrichment of the (**B**) MSigDB Hallmarks Oxidative Phosphorylation and (**C**) KEGG Oxidative Phosphorylation gene sets in YDFR.C cells treated for 48 hours with brain-derived soluble factors vs. untreated cells. NES and FDR q-val are listed on the enrichment plots. Significance was set to FDR q-val < 0.05.

3.2.2d - The Brain Tumor Microenvironment Activates Signaling Pathways Known to Promote Oxidative Phosphorylation

Our lab and others have implicated mTOR signaling as a key mediator of tumor cell oxidative metabolism (3, 40). A pooled GSEA-P analysis of the A375, A375-R1, MEWO, and WM1361A ICr and SQ xenografts determined that OXPHOS was the most enriched MSigDB Hallmarks pathway in ICr xenografts (**Figure 15A**). Interestingly, genes regulated by mTORC1 signaling were identified as the third most enriched MSigDB Hallmarks gene set in ICr xenografts (**Figure 15A-B**). Additionally, genes induced by the PI3K-AKT-mTOR signaling axis were also significantly enriched in ICr xenografts (**Figure 15B**).

To confirm these findings at the protein level, A375, A375-R1, and WM1361A cells were implanted in the brains and SQ tissue of CD-1 nude mice. Tumors were harvested when mice became moribund or SQ tumors reached 250 mm^3. Following correction for intrinsic cell line differences, pooled analysis of reverse phase protein array (RPPA) data from the samples demonstrated significant activation of the PI3K-AKT and mTOR signaling pathways in ICr xenografts. Specifically, **Figure 16** depicts significant upregulation of insulin-like growth factor-1 receptor (IGF1R), P-AKT (S473 and T308), P-mTOR (S2448), P-4E-BP1 (S65), and P-70-S6K (T389).

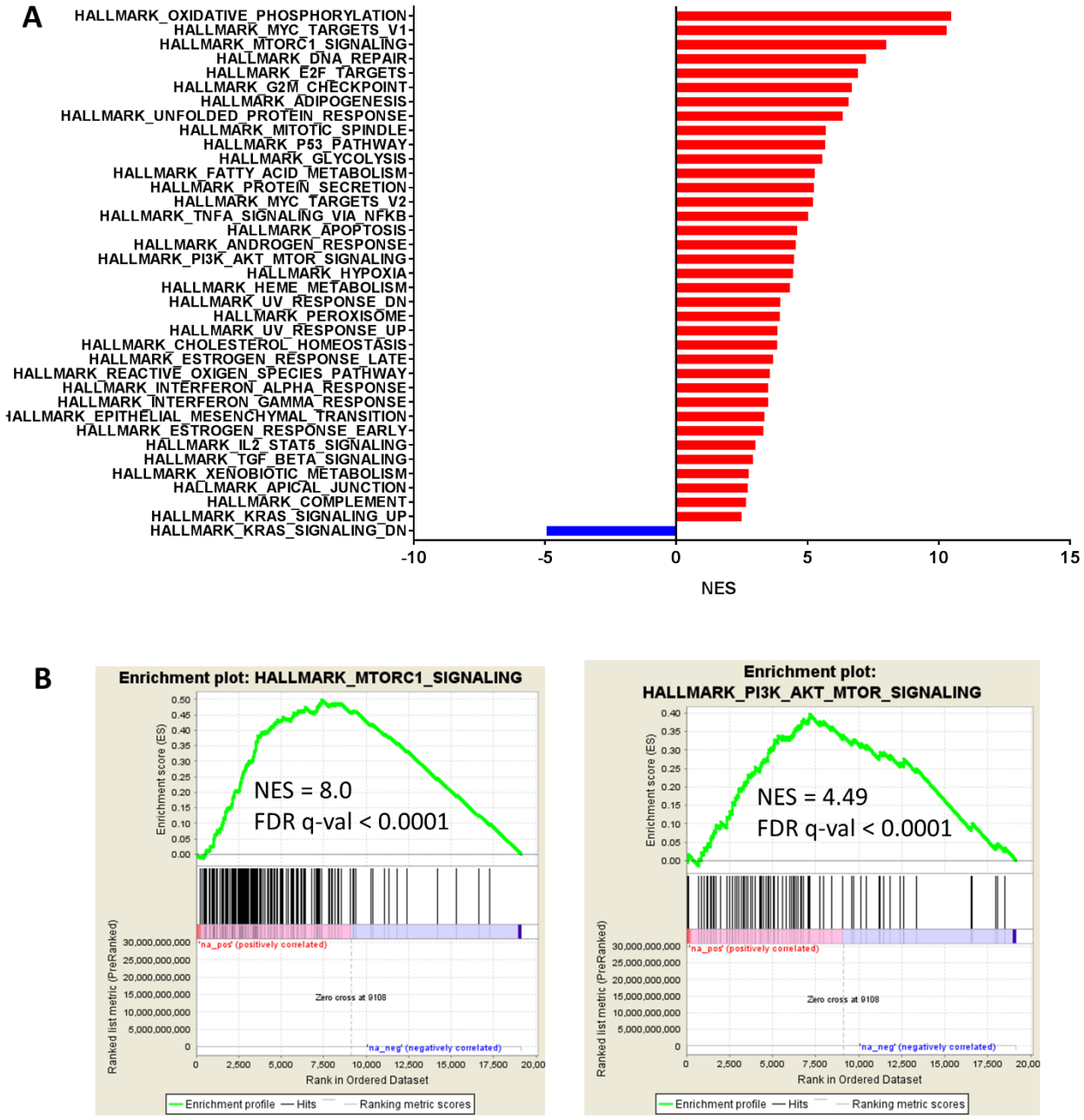

Figure 15: Gene expression studies indicate that the brain microenvironment facilitates PI3K-AKT-mTOR signaling. (**A**) GSEA-P analysis enrichment plot demonstrating significant enrichment or depletion of MSigDB Hallmarks gene sets in A375, A375-R1, MEWO, and WM1361A ICr xenografts vs. A375, A375-R1, MEWO, and WM1361A SQ xenografts following correction for cell line differences. Red indicates enrichment while blue indicates depletion. Significance was set to FDR q-val < 0.0001. (**B**) GSEA-P enrichment plots demonstrating significant enrichment of the MSigDB Hallmarks mTORC1 and PI3K-AKT-mTOR gene sets in A375, A375-R1, MEWO, and WM1361A ICr xenografts vs. A375, A375-R1, MEWO, and WM1361A SQ xenografts following correction for cell line differences. Significance was set to FDR q-val < 0.0001.

Additionally, compensatory upregulation of PTEN was observed. Interestingly, we observed that the brain TME mediated profound metabolic effects at the protein level. Significant upregulation of the succinate dehydrogenase complex flavoprotein subunit A (SDHA) and downregulation of the glycolytic enzyme lactate dehydrogenase A (LDHA) were observed in the ICr xenografts, indicating that these tumors increased their mitochondrial biogenesis *in lieu* of producing enzymes involved in glycolysis. These results suggest that the brain TME promotes OXPHOS in our ICr xenografts by activating the PI3K-AKT-mTOR signaling pathway through RTKs such as IGF1R.

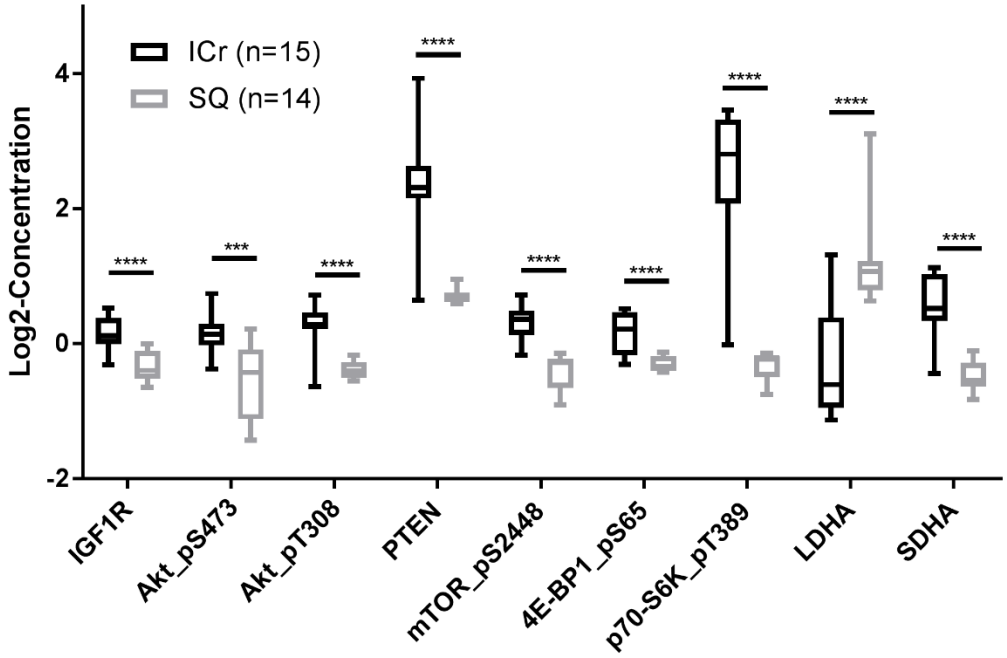

Figure 16: Proteomics studies indicate that the brain microenvironment facilitates PI3K-AKT-mTOR signaling. Reverse phase protein array (RPPA) analysis of PI3K-AKT-mTOR signaling proteins and metabolically relevant proteins from A375, A375-R1, and WM1361A ICr xenografts vs. A375, A375-R1, and WM1361A SQ xenografts, following correction for cell line differences. Each plot is a simple box and whisker plot. Median values (lines) and interquartile range (whiskers) are indicated. ****P<0.0001, ***P<0.001, via generalized linear model analysis.

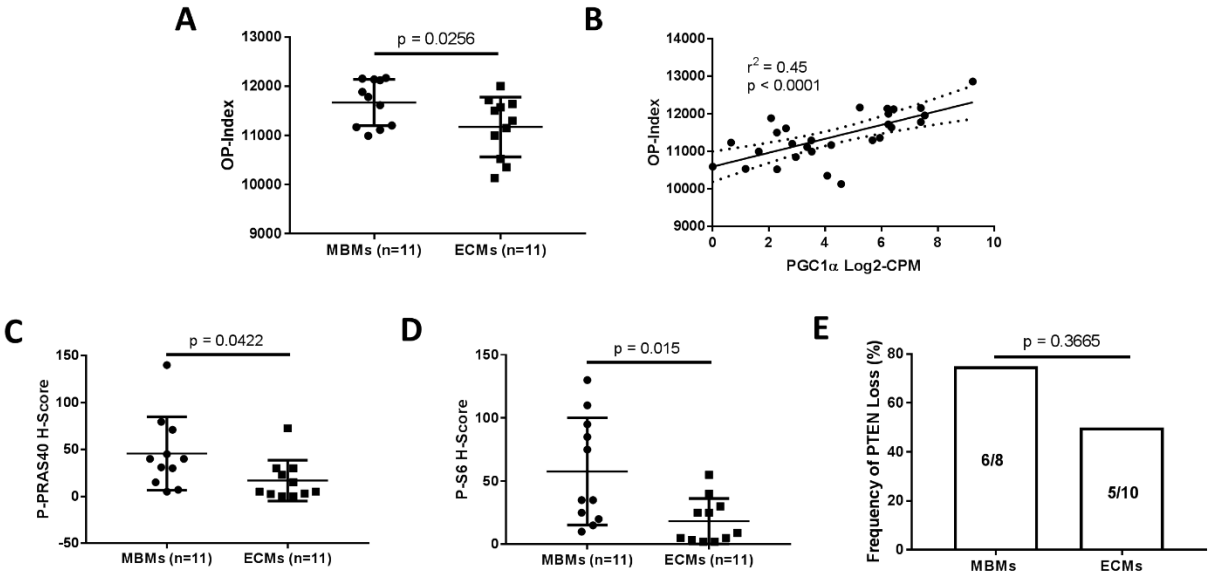

Figure 17: PI3K-AKT-mTOR signaling associates with oxidative phosphorylation in treatment-naïve, patient-matched melanoma brain and extracranial metastases. (**A**) OP-Index analysis of Tx-naïve, patient-matched MBMs and ECMs. Significance determined via two-sided Student's *t*-test. (**B**) Correlation analysis of PGC1α expression and OP-Indices in Tx-naïve, patient-matched MBMs and ECMs. Analysis of (**C**) P-PRAS40 and (**D**) P-S6 H-scores in Tx-naïve, patient-matched MBMs and ECMs. Significance determined via two-sided Student's *t*-test. (**E**) Comparison of prevalence of complete PTEN loss between Tx-naïve, patient-matched MBMs and ECMs with tissue available for staining. Significance determined via two-sided Fisher's exact test.

To determine if PI3K-AKT-mTOR signaling associated with OXPHOS discrepancy between surgically resected MBMs and ECMs, OP-Indices were first compared between patient-matched, treatment (Tx)-naïve MBMs and ECMs (n=11). As anticipated, mean OP-Index was significantly higher in the MBMs (p=0.0256) (**Figure 17A**). PGC1α expression correlated significantly with OP-Indices across the cohort of samples (r^2=0.45, p<0.0001) (**Figure 17B**). Together, these results established that PGC1α-mediated OXPHOS was significantly enriched in the Tx-naïve MBMs vs. patient-matched, Tx-naïve ECMs. Next, we performed immunohistochemistry to demonstrate that P-PRAS40 and P-S6 stained significantly higher in Tx-naïve MBMs

vs. patient-matched, Tx-naïve ECMs (p=0.0422 and p=0.015, respectively) (**Figure 17C-D**). However, we observed no significant difference in the incidence of complete PTEN loss between groups (p=0.3665) (**Figure 17E**). Cumulatively, these results establish a potentially meaningful association between hyperactive PI3K-AKT-mTOR signaling and PGC1α-mediated OXPHOS enrichment in Tx-naive MBMs vs. patient-matched, Tx-naïve ECMs.

3.3 - DISCUSSION

In this study, we investigated why we previously observed significant enrichment of OXPHOS genes in MBMs compared to patient-matched ECMs. This represents the first effort to provide an explanation for that novel insight into the metabolism of MBMs. Based on a previous study of experimental breast cancer brain metastasis (211), **we hypothesized that OXPHOS enrichment in MBMs resulted from improved efficiency of melanoma cells with increased OXPHOS to form metastases at this site in the body.**

Using bulk gene expression analysis methods, we compared primary tumors from patients that developed brain metastases to primary tumors from patients that developed metastases at other distant sites. We observed no significant differences in OXPHOS gene expression between these groups, which strongly argues against the possibility of explaining differences in the metabolism of MBMs and ECMs through differences in primary tumors. Likewise, OXPHOS levels of ECMs did not associate with cerebrotropism in stage IV patients. Our subsequent analysis of cell lines derived from surgically resected MBMs and lymph node metastases (LNMs) demonstrated no differences in OXPHOS between groups, which excludes the possibility that the brain TME selects subclones inherently enriched in OXPHOS compared to subclones that

metastasize to LNs. We confirmed this finding by observing no differences in OXPHOS between brain-metastatic WM239 variants and WM239 variants that metastasize exclusively to other anatomical locations. Cumulatively, these studies prompted us to reject our initial hypothesis and assess if differences between TMEs could sufficiently explain OXPHOS enrichment in MBMs.

Our initial preclinical studies sought to thoroughly characterize the effect of the TME on the transcriptome of melanoma cells. We identified OXPHOS as the most enriched metabolic pathway in brain xenografts from all 4 of our models and in our pooled analysis following corrections for intrinsic cell line differences. We confirmed these observations through direct metabolite analysis, which demonstrated significant enrichment of TCA cycle metabolites in brain xenografts vs. subcutaneous xenografts, and via *in vivo* [U-^{13}C]-glucose tracing studies, which demonstrated that brain xenografts preferentially oxidized glucose compared to their subcutaneous counterparts. Finally, we employed RPPA analysis to determine that the brain TME activates the PI3K-AKT-mTOR pathway and promotes synthesis of mitochondrial proteins *in lieu* of glycolytic enzymes. mTOR signaling has been implicated in mediating OXPHOS in non-CNS melanoma metastases (3, 40). Thus, this finding provides potential mechanistic insight into how the brain TME mediates OXPHOS enrichment compared to other anatomical sites. Of note, we did not observe significant differences in PTEN levels between brain and subcutaneous xenografts, despite previous studies demonstrating that the brain TME can activate the PI3K-AKT-mTOR pathway via epigenetic silencing of PTEN (101). However, we observed significantly increased levels of IGF1R in brain xenografts, which has been implicated in mediating metastatic melanoma resistance to targeted therapies via activation of the PI3K-AKT-mTOR pathway and OXPHOS (3, 215). We subsequently demonstrated PTEN-independent activation of the PI3K-AKT-mTOR pathway in Tx-naïve MBMs vs. Tx-naïve, patient-matched ECMs.

This study is highly novel as it employs analysis of clinical samples and preclinical models to provide the first detailed assessment of the brain TME's effect on melanoma metabolism. We ensured adequate representation of *BRAF* and *NRAS*-mutant and triple wild-type melanomas and corrected for potential stromal contamination in our gene expression studies through our use of the Xenome platform. Furthermore, we employed the highly novel technique of *in vivo* [U-^{13}C]-glucose tracing analysis to confirm our transcriptomic studies. Potential limitations of our study include the absence of syngeneic models, which could more accurately model tumor cell/TME interactions. Alternatively, patient-derived xenografts more accurately model tumor cell biology *in vivo* and would represent a potential improvement over standard cell lines in our immunodeficient models. Additionally, we did not analyze lesions grown in lungs and livers and instead relied exclusively on analysis of subcutaneous tumors.

Our findings are highly clinically relevant. Previous analyses found that the brain was the most common new site of disease progression in *BRAF*-mutant patients without CNS involvement at baseline that were treated with the FDA-approved combination of dabrafenib (BRAFi) and trametinib (MEKi) (216). Further, in the phase II COMBI-MB study of dabrafenib and trametinib in MBM patients, 47% of patients progressed in the brain before progressing extracranially, and the median duration of intracranial responses was ~50% shorter than that previously reported in patients without CNS involvement (171). As our group and others have previously shown that OXPHOS can mediate resistance to BRAFi and MEKi targeted therapies (3, 26), the finding of increased OXPHOS in MBMs provides a potential explanation for these clinical observations. This study provides insight into how OXPHOS becomes enriched in MBMs compared to other sites and represents a critical step in overcoming the negative effects mediated by this metabolic pathway.

CHAPTER 4: OXIDATIVE PHOSPHORYLATION PROMOTES THE GROWTH OF MELANOMA BRAIN METASTASES

Copyright Disclosure:

This chapter is based upon:

1. **Fischer, G. M.**, Y. N. Vashisht Gopal, J. L. McQuade, W. Peng, R. J. DeBerardinis, and M. A. Davies. 2018. Metabolic strategies of melanoma cells: Mechanisms, interactions with the tumor microenvironment, and therapeutic implications. *Pigment Cell Melanoma Res* 31: 11-30.

2. **Fischer G.M.**, and M.A. Davies (2019) Melanoma Brain Metastasis: Insights, Progress, Challenges, and Opportunities. In: Fisher D., and B. Bastian (eds) Melanoma. Springer, New York, NY.

3. **Fischer, G. M.**, A. Jalali, D. A. Kircher, W. C. Lee, J. L. McQuade, L. E. Haydu, A. Y. Joon, A. Reuben, M. P. de Macedo, F. C. L. Carapeto, C. Yang, A. Srivastava, C. R. Ambati, A. Sreekumar, C. W. Hudgens, B. Knighton, W. Deng, S. D. Ferguson, H. A. Tawbi, I. C. Glitza, J. E. Gershenwald, Y. N. Vashisht Gopal, P. Hwu, J. T. Huse, J. A. Wargo, P. A. Futreal, N. Putluri, A. J. Lazar, R. J. DeBerardinis, J. R. Marszalek, J. Zhang, S. L. Holmen, M. T. Tetzlaff, and M. A. Davies. 2019. Molecular Profiling Reveals Unique Immune and Metabolic Features of Melanoma Brain Metastases. *Cancer Discov.* 9: 628-645.

4.1 – INTRODUCTION

4.1.1 – Steps of the Brain Metastasis Cascade

Metastasis of cancer cells to the brain is a complex, multi-step process that involves invasion of tissues surrounding the primary tumor; access to and survival in the lymphatic system and bloodstream; arrest in brain capillaries and extravasation into the brain parenchyma; and growth and survival in the brain (**Table 4**). Understanding the features that are critical to each of these steps, and the drivers that support the maintenance and aggressive behavior of MBMs, will facilitate the development of rational, more effective treatments for patients. Notably, many of these studies suggest that MBMs have distinct characteristics that may contribute to the distinctly poor outcomes associated with these tumors.

Table 4 - Key steps in melanoma brain metastasis formation and maintenance

Stage	Description
Growth of primary tumor	Genetic aberrations drive unregulated growth of transformed melanocytes; accumulation of mutations results in creation of subclones with increased metastatic propensity
Migration/invasion of surrounding tissues	Loss of adherence to cells in primary tumors; increased communication with extracellular matrix and surrounding stroma; digestion of extracellular matrix; increased cellular motility
Intravasation/spread to regional lymph nodes	Acquisition of access to lymphatic vessels and growth in regional lymph nodes, where melanoma cells typically spread to initially
Survival in bloodstream	Survival in harsh environment and shear stress inherent to circulatory system; ability to form emboli increases survival
Arrest in brain capillary beds	Mechanical arrest in the capillary beds of brain; mediated by interactions between adhesion molecules expressed on blood vessels of brain capillaries and tumor cells
Extravasation	Exit from the circulatory system across the BBB; mediated by factors able to digest tight junctions of the BBB
Angiogenesis	Acquisition of vital nutrients via formation of new blood vessels or co-option of existing blood vessels in the brain
Evasion of immune system	Evasion of immune attack facilitates tumor growth

4.1.2 – Metabolic Pathways Implicated in Melanoma Metastasis

4.1.2a - Lactate/H^+ Metabolism: A Major Contributor to Melanoma Metastasis

Produced at the end of glycolysis in order to maintain NAD^+, lactate is subsequently secreted into the tumor microenvironment (TME) via monocarboxylate transporters (MCTs), with MCT4 as the most significant transporter (217). Pinheiro et al. demonstrated that glucose transporter 1 (GLUT1) and MCT4 overexpression significantly correlated with progression from primary tumor to lymph node metastasis in a cohort of patient-derived melanoma samples, indicating that the Warburg phenotype and lactate secretion cooperate to promote melanoma metastasis (218). In glycolytic tumor cells, HIF1α and MYC upregulate MCT4 to promote the secretion of lactate into the TME (219, 220). Lactate drastically alters the TME, facilitating angiogenesis, promoting metastasis, and suppressing the immune system (221). Once secreted, lactate is taken up by surrounding endothelial cells via MCT1, where it facilitates nuclear factor kappa-light-chain-enhancer of activated B cells (NFκB), HIF1α, and interleukin-8 (IL-8) signaling, resulting in upregulation of vascular endothelial growth factor receptor 2 (VEGFR2) and basic fibroblast growth factor (bFGF) signaling (219, 222, 223) (**Figure 18**). Intracellular protons produced via dissociation of lactic acid are secreted into the melanoma TME via sodium-proton exchanger 1 (NHE1), lowering the pH of extracellular space (219, 224, 225). Additional membrane protein complexes, including carbonic anhydrase IX (CAIX), sodium-bicarbonate transporter 1, and anion exchanger 2 (AE2) also contribute to extracellular acidosis (218, 219, 226-228) (**Figure 18**).

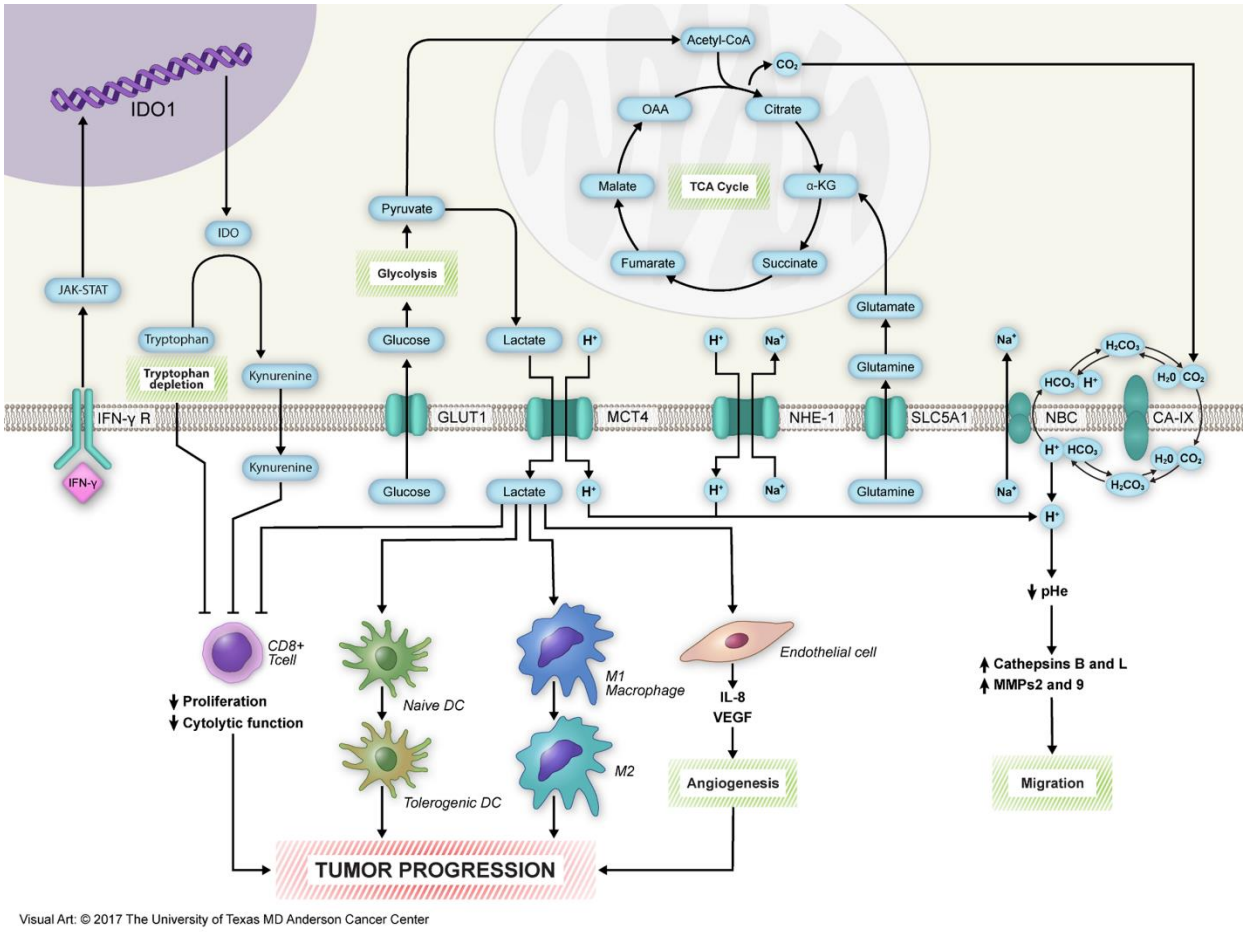

Figure 18: Melanoma cell metabolism promotes disease progression by shaping the tumor microenvironment. The secretion of lactate into the tumor microenvironment (TME) by monocarboxylate transporter 4 (MCT4) results in immunosuppression and angiogenesis, facilitating tumor progression. Lactate inhibits $CD8^+$ T cell proliferation and function, prevents the maturation of dendritic cells, and converts M1 macrophages to M2 macrophages. It also facilitates angiogenesis by increasing IL-8 and VEGF signaling in endothelial cells. Tryptophan metabolism further promotes immunosuppression via depletion of tryptophan and secretion of kynurenine into the TME. Acidification of the TME via proton transport activates cathepsins and matrix metalloproteases (MMPs), which promote migration and metastasis through degradation of the extracellular matrix. IFN-γ, interferon-gamma; IFN-γ R, interferon-gamma receptor; GLUT1, glucose transporter 1; NHE-1, sodium-hydrogen antiporter 1; SLC5A1, solute carrier family 5 member 1; NBC, sodium-coupled bicarbonate transporter; CA-IX, carbonic anhydrase 9; IDO, indoleamine 2,3-dioxygenase; OAA, oxaloacetate; α-KG, α-ketoglutarate. Used with permission from John Wiley & Sons Ltd. (Fischer, G. M., Y. N. Vashisht Gopal, J. L. McQuade, W. Peng, R. J. DeBerardinis, and M. A. Davies. 2018. Metabolic strategies of melanoma cells: Mechanisms, interactions with the tumor microenvironment, and therapeutic implications. *Pigment Cell Melanoma Res* 31: 11-30).

Acidification of the TME facilitates melanoma metastasis in several ways. First, a low extracellular pH promotes the formation of collagen–integrin interactions in the lamellipodia of melanoma cells, allowing focal adhesion complexes to form and increasing migration of melanoma cells (219, 229). In addition, extracellular acidosis disrupts cellular junctions through the induction of matrix metalloproteases (MMPs) 2 and 9 and cathepsins B and L, which are secreted into the TME as inactive zymogens and require a low pH to be activated (230) (**Figure 18**). Rofstad et al. demonstrated that melanoma cells grown in an acidic pH are significantly more metastatic than those grown in normal pH and that treatment with MMP and cathepsin inhibitors prevented the metastasis of the acid-treated cells following tail vein injection in immunodeficient mice (230). As further evidence, inhibition of NHE1 *in vitro* prevented the invasive behaviors of melanoma cells to a significantly greater extent than vehicle controls (224, 225). Additionally, inhibitors of AE2 and CAIX block invasiveness of a variety of other tumor cell types (219, 231-233).

4.1.2b - One-Carbon Metabolism: A Critical Deterrent of Oxidative Stress

Melanoma cells are subjected to oxidative stress, with reactive oxygen species (ROS) formed secondary to oncogenic mutations, aberrant signaling pathways, unregulated proliferation, and hypoxia (12). While minimal levels of ROS are actually beneficial to these cells by stimulating proliferation and inducing mutations, excessive ROS can induce damage and eventually apoptosis (12). As oxidative stress increases during tumorigenesis progression and metastasis, melanoma cells must adjust and strengthen their antioxidant defenses to survive (234). In addition to activating nuclear

factor (erythroid-derived 2)–related factor-2 (NRF2) to drive the transcription of antioxidant proteins, tumor cells increase their reliance on glutathione peroxidase to manage oxidative stress (235). This protein utilizes reduced glutathione (GSH) to convert peroxides to water. Glutathione reductase utilizes NADPH to restore GSH to its oxidized state (GSSG), making NADPH a critical component of redox balance in melanoma cells. Early in tumorigenesis, the PPP supplies the majority of the NADPH used by this enzyme. Together with NRF2-regulated genes, the PPP is sufficient to manage the oxidative stress secondary to intense proliferation. However, the role of one-carbon metabolism, mediated by the folate cofactor, becomes increasingly important as tumorigenesis progresses, glucose becomes scarce, and hypoxia becomes a more significant source of ROS (12). In this pathway, serine is converted to glycine via serine hydroxymethyltransferase (SHMT1) in a reaction that also converts tetrahydrofolate (THF) to 5,10-methylenetetrahydrofolate. Methylenetetrahydrofolate reductase dehydrogenase 1 (MTHFD1) subsequently catalyzes a series of three reactions, the first of which produces NADPH for use in redox reactions (7). One-carbon metabolism is critical in the management of deleterious ROS during metastasis. Piskounova et al. demonstrated that melanoma cells that successfully metastasized to distant sites in NSG mice increase their dependence on one-carbon metabolism. Inhibition of one-carbon metabolism prevented the formation of distant metastases without affecting subcutaneous tumor growth (236).

4.1.2c - Lipid Metabolism: Synthesis and Degradation of Fatty Acids Promotes Melanoma Metastasis

Fatty acid synthase (FASN) catalyzes the rate-limiting step of the endogenous synthesis of fatty acids (78). FASN expression levels correlate with tumor invasion and poor prognosis in cutaneous melanoma (237, 238). Targeting FASN prevents the proliferation of B16-F10 melanoma cells *in vitro* and activates the intrinsic apoptotic pathway in melanoma cells (238). Furthermore, inhibiting the thioesterase domain of FASN with orlistat, a drug originally approved by the FDA for the treatment of obesity, prevented the metastasis of B16-F10 mouse melanoma cells following implantation in the peritoneal cavity of C57BL/6 mice (239).

In addition to the synthesis of fatty acids, fatty acid oxidation (FAO) appears to play an important role in promoting melanoma progression and metastasis. Rodrigues et al. derived metastatic $4C11^+$ cells from melan-a melanocytes after sequential detachment-re-adhesion cycles, and FAO contributed significantly to the energy reserves of these $4C11^+$ cells, relative to nonmetastatic controls (85). How FAO promotes melanoma metastasis remains unclear. Studies in other tumor types have demonstrated that fatty acids can provide an ATP boost for tumor cells when necessary under nutrient-depleted conditions (86-88). Indeed, the process of metastasis is a highly demanding process. Highly efficient β-oxidation could provide a survival advantage for cells away from the primary tumor site. Furthermore, fatty acids can serve as a valuable source of acetyl-CoA that contributes to citrate formation after entering the tricarboxylic acid (TCA) cycle (87). This citrate can enter metabolic reactions that produce NADPH via isocitrate dehydrogenase 1 (IDH1), thereby contributing to redox balance in the tumor cells.

Additionally, fatty acid binding proteins, which are regulators of fatty acid uptake and lipid trafficking, appear to play important roles in melanoma progression. Slipicevic et al. demonstrated that fatty acid binding protein 7 (FABP7) is involved in proliferation

and invasion of melanoma cells *in vitro* (Slipicevic et al., 2008) (240). siRNA-mediated suppression of FABP7 inhibited invasion and proliferation of melanoma cells without affecting apoptosis (240). However, the relevance of FABP7 in *in vivo* models of metastasis remains to be validated.

Finally, Nath and Chan identified a crucial role for fatty acid metabolism in melanoma progression while deriving a gene signature to detect activation of epithelial-mesenchymal transition (EMT) programming across multiple cancers (241). TCGA melanoma patients enriched in the authors' 5-gene signature, which included the fatty acid uptake genes caveolin-1 (CAV1) and cluster of differentiation 36 (CD36) and the fatty acid oxidation gene carnitine palmitoyltransferase 1C (CPT1C), have significantly worse overall survival than those whose melanomas are not enriched for the signature (241). Additionally, CD36 amplifications significantly correlate with invasiveness in 501mel melanoma cells (241, 242). In contrast, melanoma cells lacking CD36 fail to metastasize in NOD scid gamma (NSG) mice following tail vein inoculation (242). These studies further implicate lipid metabolism in the metastasis of human melanoma.

4.1.2d - Oxidative Phosphorylation (OXPHOS) – A Potential Driver of Melanoma Metastasis

Peroxisome proliferator-activated receptor γ, coactivator 1α (PPARGC1A or PGC1α) is a transcriptional co-factor that regulates multiple mitochondrial genes. PGC1α overexpression promotes OXPHOS metabolism and significantly correlates with decreased overall survival in patients with stage III melanoma (172). Additionally, basal and compensatory upregulation of PGC1α expression also correlates with *de novo* and

acquired resistance to MAPK pathway inhibitors (3, 35). PGC1α-high melanoma cells tolerate oxidative stress to a significantly greater extent than PGC1α-low cells (172). As tumor cells experience a great deal of oxidative stress, particularly during metastasis, decreased sensitivity to ROS is beneficial for melanoma cells. Consistent with this notion, shRNA knockdown of PGC1α in PGC1α-high melanoma cells inhibited expression of numerous ROS-scavenging genes and sensitized these cells to ROS (172). Furthermore, LeBleu et al. demonstrated that inhibition of PGC1α-mediated OXPHOS prevented metastatic spread of B16-F10 melanoma cells in a murine model of melanoma metastasis (243).

4.1.3 - Hypothesis Tested

To date, few studies have functionally validated metabolic pathways as mediators of brain metastasis pathogenesis. Interestingly, reported analyses tend to indicate that the Warburg phenotype does not sufficiently describe the metabolic dependencies of these lesions. For example, MDA-MB-231 human breast cancer cells subjected to three rounds of *in vivo* selection for brain-metastatic capacity survive in glucose-depleted conditions characteristic of the brain microenvironment significantly better than parental cells by performing gluconeogenesis and oxidizing glutamine and branched-chain amino acids. Silencing the expression of gluconeogenesis enzymes inhibited development of breast cancer metastases within the brains of mice (244). Sondstrom et al. showed that melanoma metastasis to the brain does not require expression of lactate dehydrogenase A (LDHA), an enzyme implicated in aerobic glycolysis, and that LDHA expression does not influence MBM progression (14). However, the authors did not identify alternative metabolically active genes necessary for MBM formation and maintenance.

Our recent RNA-seq analysis of 35 MBMs and 42 patient-matched ECMs identified 494 genes that were differentially expressed between the MBMs and ECMs (174). Focused pathway analyses for the expression of 70 different metabolic gene networks demonstrated that OXPHOS was the most significantly enriched metabolic pathway in MBMs. **Thus, we hypothesized that OXPHOS plays a critical role in the formation and maintenance of MBMs.**

4.2 - RESULTS

4.2.1 - Molecular Profiling of Animal Models Implicates Oxidative Phosphorylation in Melanoma Brain Metastasis Pathogenesis

Activation of the PI3K-AKT pathway promotes spontaneous metastasis to the lungs and brain in an autochthonous RCAS-TVA mouse model of melanoma characterized by the *BRAF*^{V600E} mutation and loss of *Cdkn2a* (179). To determine if OXPHOS contributed to MBM formation in this model, exploratory RNA-seq was performed on primary tumors, lung metastases, and brain metastases. Enrichment of the KEGG OXPHOS gene set and OXPHOS-Index (OP-Index) was detected in the murine MBMs compared to both lung metastases (FDR q-val<0.001 and p=0.0049, respectively) and primary tumors (FDR q-val<0.001 and p=0.0479, respectively) (**Figure 19A-D**). Focused qRT-PCR on RNA from additional tumors confirmed increased expression (p<0.0001-p<0.01) of several OXPHOS-related genes in the MBMs (**Figure 19E**).

Preranked Gene Set Enrichment Analysis (GSEA-P) identified significant enrichment (FDR q-val=0.048) of KEGG OXPHOS gene set expression in primary melanomas of patients that developed MBMs (n=19) vs. patients that developed no metastases with at least 5 years of

follow-up (n=19) (**Figure 20A**) (148). Thus, we performed RNA-seq on 17 primary tumors from the RCAS-TVA model with various genotypes and incidences of lung and brain metastasis (**Figure 20B**). Consistent with our analysis of the clinical specimens, we observed enrichment of the KEGG OXPHOS gene set and OP-Index in brain-metastatic primary tumors vs. non-metastatic primary tumors, regardless of genotype (FDR q-val<0.001 and p<0.001, respectively) (**Figure 20C-F**).

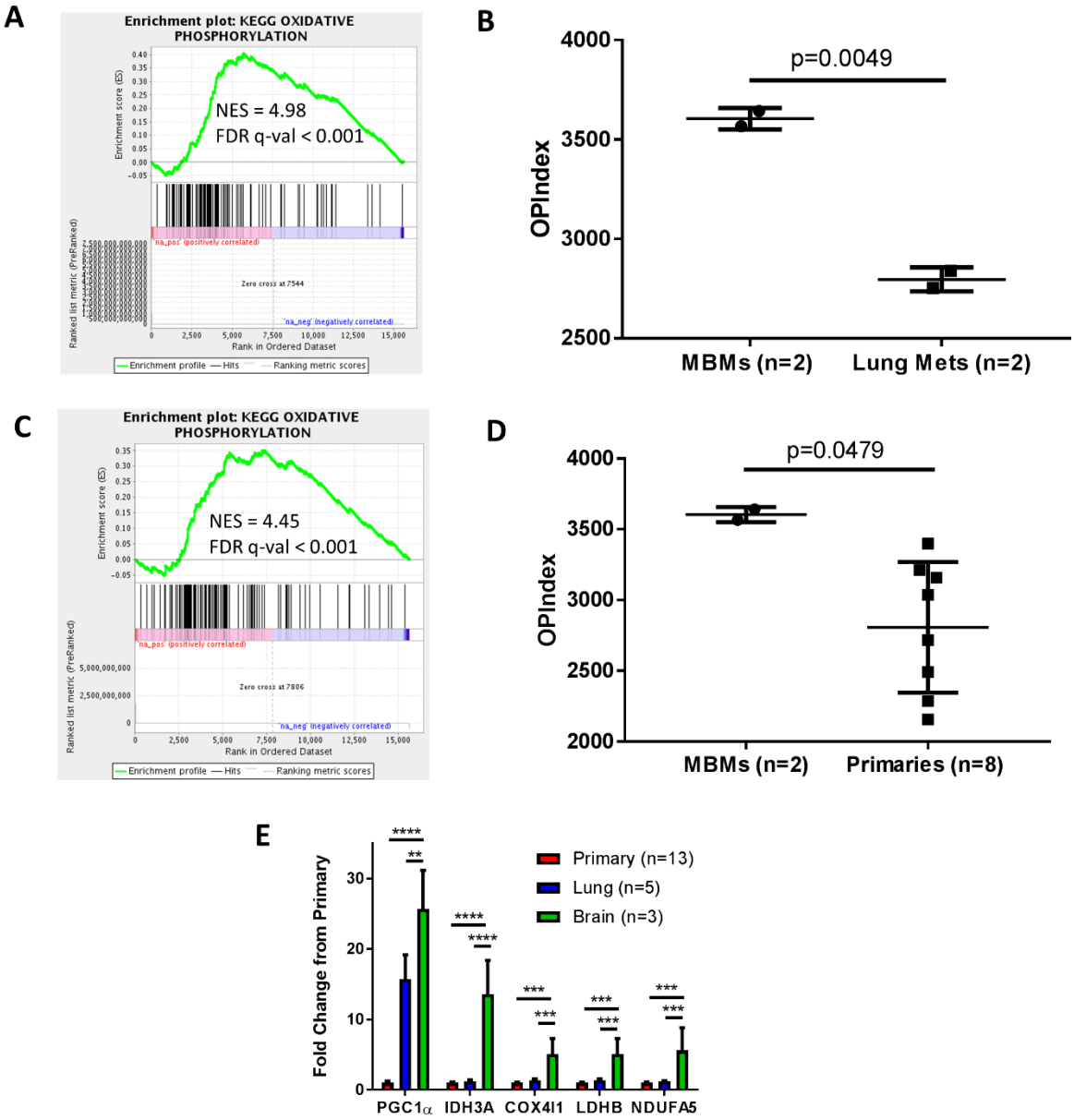

Figure 19: Oxidative phosphorylation is enriched in melanoma brain metastases acquired from an RCAS-TVA mouse model of spontaneous melanoma metastasis. (**A**) GSEA-P analysis enrichment plot demonstrating significant enrichment of the KEGG OXPHOS gene set in MBMs (n=2) vs. lung metastases (n=2) acquired from an RCAS-TVA model of spontaneous melanoma brain and lung metastasis. Normalized enrichment score (NES) and FDR q-val are listed on the enrichment plot. (**B**) OP-Indices of the murine MBMs (n=2) and lung metastases (n=2). Lines represent mean ± S.D., and each dot represents a single sample. Significance determined via two-sided Student's *t*-test. (**C**) GSEA-P analysis enrichment plot demonstrating significant enrichment of the KEGG OXPHOS gene set in MBMs (n=2) vs. primary tumors (n=8) acquired from an RCAS-TVA model of spontaneous melanoma brain and lung metastasis. NES and FDR q-val are listed on the enrichment plot. (**D**) OP-Indices of the murine MBMs (n=2) and primary tumors (n=8). Lines represent mean ± S.D., and each dot represents a single sample. Significance determined via two-sided Student's *t*-test. (**E**) mRNA levels of OXPHOS genes measured in RCAS-TVA model tumors from brain, lung, and primary sites by qRT-PCR. Values represent mean ± S.D. of indicated numbers of biological replicates analyzed as technical triplicates. ****$P < 0.0001$; ***$P < 0.001$; **$P < 0.01$ by two-sided Student's *t*-test.

A

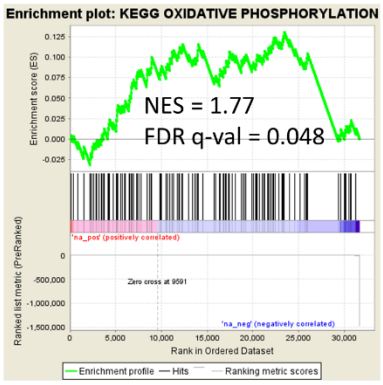

B

Sample ID	Cohort	Brain met	Lung met
4326	$BRAF^{V600E}$; $Cdkn2a^{-/-}$; $Pten^{-/-}$		
3143	$BRAF^{V600E}$; $Cdkn2a^{-/-}$; $Pten^{-/-}$		
3971	$BRAF^{V600E}$; $Cdkn2a^{-/-}$; $Pten^{-/-}$		
3125	$BRAF^{V600E}$; $Cdkn2a^{-/-}$; $Pten^{-/-}$		
4083	$BRAF^{V600E}$; $Cdkn2a^{-/-}$; $Pten^{-/-}$		
7873	$BRAF^{V600E}$; $Cdkn2a^{-/-}$; $Pten^{-/-}$; Akt1-E17K	+	
7788	$BRAF^{V600E}$; $Cdkn2a^{-/-}$; $Pten^{-/-}$; Akt1-E17K	+	+
9819	$BRAF^{V600E}$; $Cdkn2a^{-/-}$; $Pten^{-/-}$; Akt1-E17K	+	
8195	$BRAF^{V600E}$; $Cdkn2a^{-/-}$; $Pten^{-/-}$; Akt1-E17K	+	+
10932	$BRAF^{V600E}$; $Cdkn2a^{-/-}$; $Pten^{-/-}$; Akt2-E17K		
10995	$BRAF^{V600E}$; $Cdkn2a^{-/-}$; $Pten^{-/-}$; Akt2-E17K	+	+
10819	$BRAF^{V600E}$; $Cdkn2a^{-/-}$; $Pten^{-/-}$; Akt2-E17K		
10996	$BRAF^{V600E}$; $Cdkn2a^{-/-}$; $Pten^{-/-}$; Akt2-E17K	+	+
11358	$BRAF^{V600E}$; $Cdkn2a^{-/-}$; $Pten^{-/-}$; Akt3-E17K		+
11360	$BRAF^{V600E}$; $Cdkn2a^{-/-}$; $Pten^{-/-}$; Akt3-E17K		
11361	$BRAF^{V600E}$; $Cdkn2a^{-/-}$; $Pten^{-/-}$; Akt3-E17K		
11355	$BRAF^{V600E}$; $Cdkn2a^{-/-}$; $Pten^{-/-}$; Akt3-E17K		

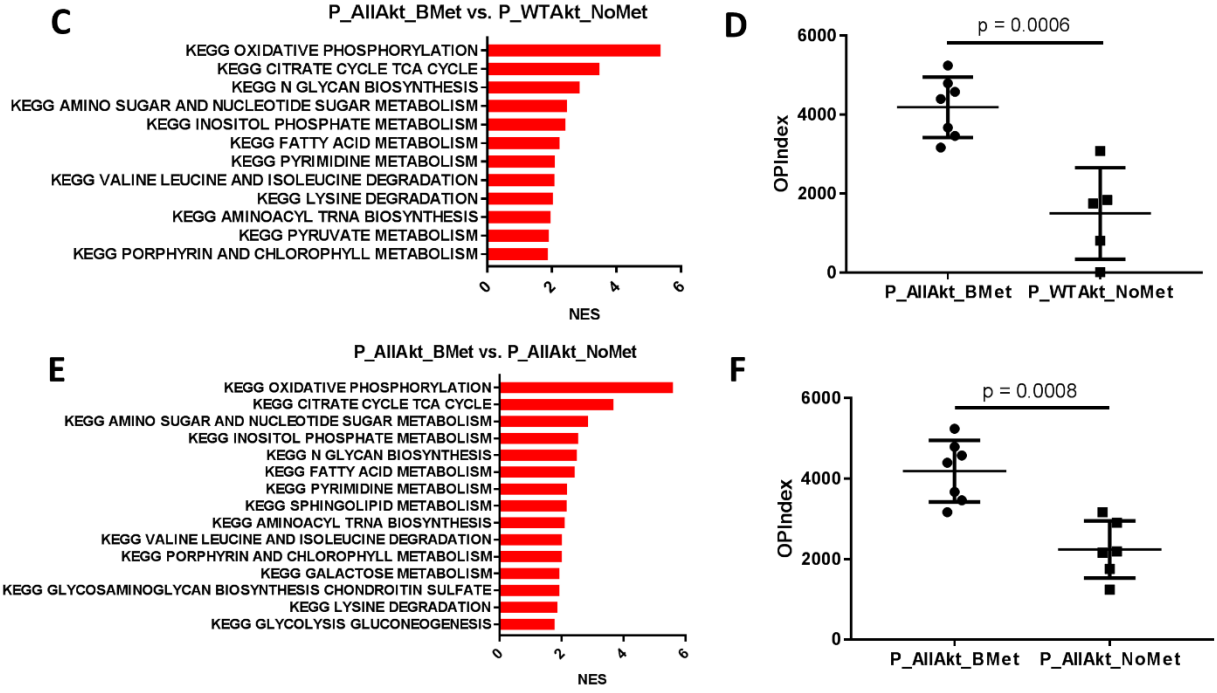

Figure 20: Oxidative phosphorylation associates with brain metastasis formation from human primary melanomas and primaries from an RCAS-TVA model of spontaneous melanoma metastasis. (A) GSEA-P analysis enrichment plot demonstrating significant enrichment of the KEGG OXPHOS gene set in brain-metastatic human primary melanomas (n=19) vs. non-metastatic human primary melanomas (n=19) from 38 unique patients. Normalized enrichment score (NES) and FDR q-val are listed on the enrichment plot. (**B**) Genotypes and metastasis incidence of primary tumors acquired from the RCAS-TVA model of spontaneous brain and lung metastasis. "Sample ID" is the ear tag of the mouse. "Cohort" is the genotype of each mouse's tumor. "Brain Met" and "Lung Met" indicate the presence (+) or absence (blank) of metastases at the designated anatomical site. (**C**) GSEA-P analysis demonstrates all KEGG metabolism pathways significantly enriched (FDR q-val<0.05) in $Braf^{V600E}$;$Cdkn2a^{-/-}$;$Pten^{-/-}$;$Akt1/2^{E17K}$ brain-metastatic primaries vs. $Braf^{V600E}$;$Cdkn2a^{-/-}$;$Pten^{-/-}$ non-metastatic primaries. NES forms the x-axis. (**D**) OP-Indices of $Braf^{V600E}$;$Cdkn2a^{-/-}$;$Pten^{-/-}$;$Akt1/2^{E17K}$ brain-metastatic primaries and $Braf^{V600E}$;$Cdkn2a^{-/-}$;$Pten^{-/-}$ non-metastatic primaries. Each dot represents a single sample and lines indicate mean ± S.D. Significance determined via two-sided Student's *t*-test. (**E**) GSEA-P analysis demonstrates all KEGG metabolism pathways significantly enriched (FDR q-val<0.05) in $Braf^{V600E}$;$Cdkn2a^{-/-}$;$Pten^{-/-}$;$Akt1/2^{E17K}$ brain-metastatic primaries vs. $Braf^{V600E}$;$Cdkn2a^{-/-}$;$Pten^{-/-}$;$Akt1/2/3^{E17K}$ non-metastatic primaries. NES forms the x-axis. (**F**) OP-Indices of $Braf^{V600E}$;$Cdkn2a^{-/-}$;$Pten^{-/-}$;$Akt1/2^{E17K}$ brain-metastatic primaries and $Braf^{V600E}$;$Cdkn2a^{-/-}$;$Pten^{-/-}$;$Akt1/2/3^{E17K}$ non-metastatic primaries. Each dot represents a single sample and lines indicate mean ± S.D. Significance determined via two-sided Student's *t*-test.

Next, we acquired previously characterized brain-metastatic variants of A375P and YDFR.C cells (A375-Br3 and YDFR.CB3, respectively) (109, 141). Bioenergetics stress testing by Seahorse analyzer showed that the brain-metastatic variants were characterized by significantly higher basal and maximum oxygen consumption rates (OCRs) (**Figure 21A-D**). We then accessed publicly available Affymetrix microarray data (GSE34970) from YDFR.CB3 and YDFR.C cells (176). GSEA analysis identified the KEGG OXPHOS gene set as the only KEGG metabolism pathway enriched in the YDFR.CB3 cells (**Figure 21E**). Together, these analyses strongly implicate OXPHOS in the pathogenesis of melanoma brain metastasis.

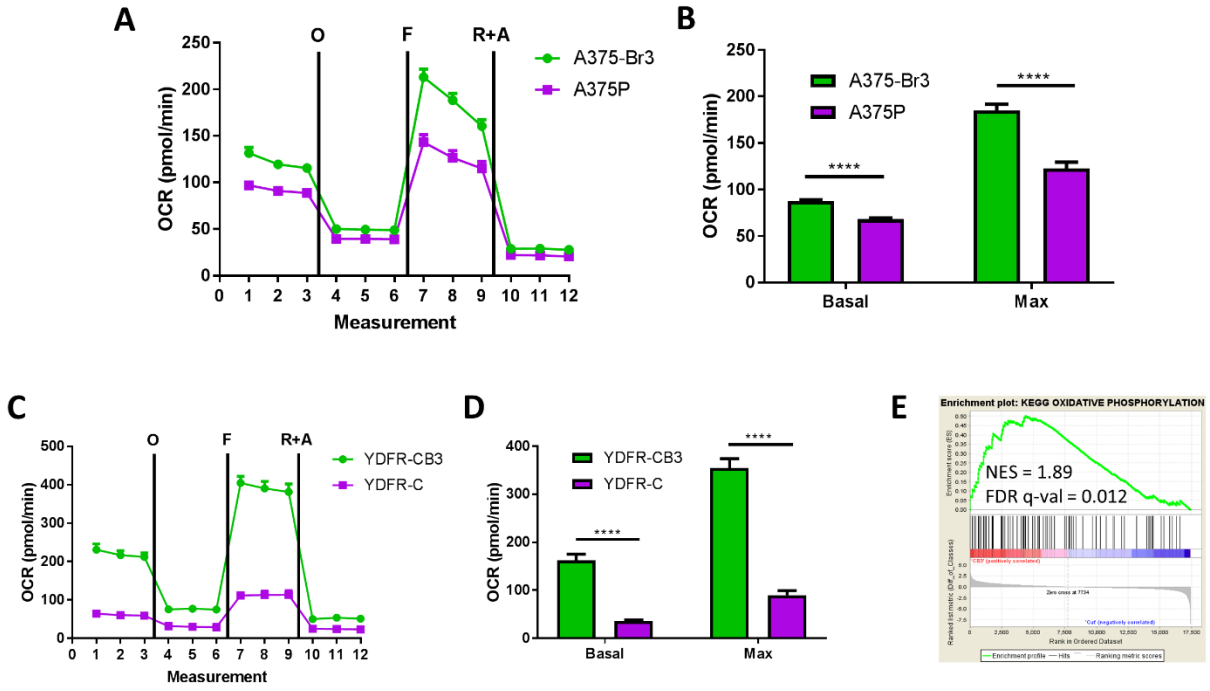

Figure 21: Oxidative phosphorylation is enriched in brain-metastatic melanoma cell lines. (A) Seahorse mitochondrial stress test was performed on A375P cells and their brain-metastatic variants (A375-Br3) derived through 3 rounds of *in vivo* selection. The figure shows basal, oligomycin-inhibited ("O"), FCCP-activated ("F") and Antimycin/Rotenone inhibited ("A&R") oxygen consumption rate (OCR) levels. (**B**) Basal and maximum OCR values for A375P and A375Br3 cells were calculated from (**A**); ****P<0.0001 by two-sided Student's t-test. (**C**) Seahorse mitochondrial stress test was performed on YDFR.C cells and their brain-metastatic variants (YDFR-CB3) derived through 3 rounds of *in vivo* selection. (**D**) Basal and maximum OCR values for YDFR.C and YDFR.CB3 cells were calculated from (**C**); ****P<0.0001 by two-sided Student's t-test. (**E**) GSEA enrichment plot demonstrating significant enrichment of the KEGG Oxidative Phosphorylation gene set in YDFR.CB3 cells vs. YDFR.C cells with available Affymetrix microarray data. Normalized enrichment score (NES) and FDR q-val are listed on the enrichment plot. Significance was set to FDR q-val < 0.05.

4.2.2 - OXPHOS Inhibition Prevents the Growth But Not Formation of Melanoma Brain Metastases

To functionally test the role of OXPHOS in MBM pathogenesis, newborn *Dct::TVA; Braf*^{CA};*Cdkn2a*$^{lox/lox}$;*Pten*$^{lox/lox}$ mice were injected subcutaneously with viruses encoding myr*Akt1* and *Cre* to induce brain-metastatic *Braf*^{V600E};*Cdkn2a*$^{-/-}$;*Pten*$^{-/-}$;myr*Akt1* primary tumors. Mice with palpable primary tumors were randomized to receive IACS-010759 (7.5 mg/kg p.o. once daily) or 0.5% methylcellulose treatment (**Figure 22A**). Treatment with IACS-010759 for 72 hours eliminated pimonidazole staining in primary tumors, confirming target inhibition (**Figure 22B**). Interestingly, IACS-010759 had no significant impact on Ki-67 staining in primary tumors (p=0.4336) nor did the treatment affect primary tumor growth (rate-based T/C=0.7002; p=0.543) (193) (**Figure 22C-D**). IACS-010759 also did not inhibit lung metastasis incidence (p=0.635), but it significantly decreased the incidence of detectable brain metastases (incidence 4/10 vs. 0/11, p=0.035) (**Figure 22E**).

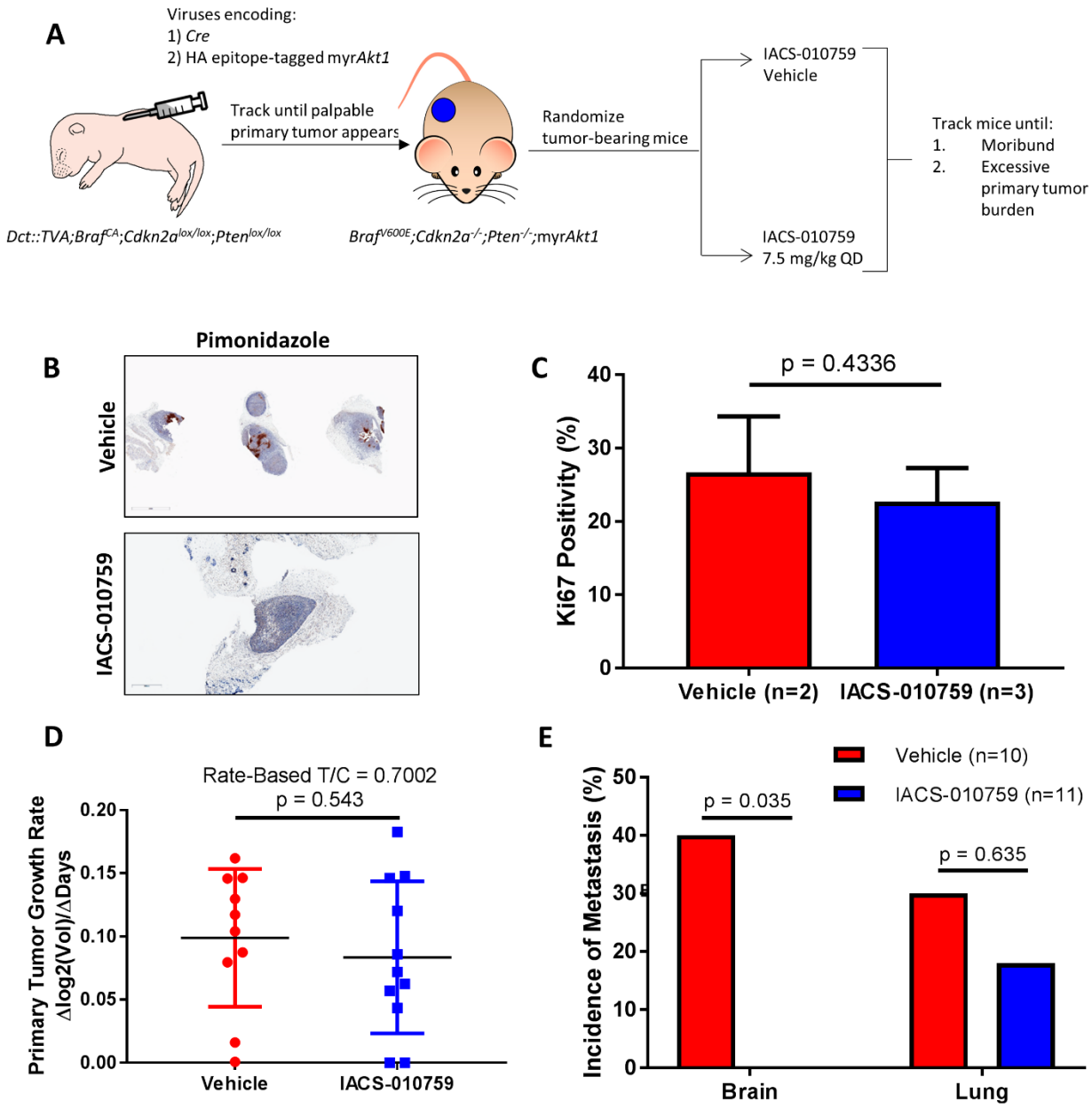

Figure 22: Oxidative phosphorylation is functionally significant for melanoma brain metastasis pathogenesis in an RCAS-TVA model of spontaneous murine melanoma brain metastasis. (**A**) Experimental design used to functionally validate the role of OXPHOS in MBM pathogenesis in the RCAS-TVA model. (**B**) Representative pimonidazole staining analysis results of *Braf*^{V600E}*;Cdkn2a*$^{-/-}$*;Pten*$^{-/-}$*;*myr*Akt1* primary tumors treated for 72 hours with IACS-010759 (7.5 mg/kg p.o. once daily) or vehicle. (**C**) Comparison of Ki67 positivity between *Braf*^{V600E}*;Cdkn2a*$^{-/-}$*;Pten*$^{-/-}$*;*myr*Akt1* primary tumors treated for 72 hours with IACS-010759 (7.5 mg/kg p.o. once daily) or vehicle. Significance determined via two-sided Student's *t*-test. **(D)** Comparison of *Braf*^{V600E}*;Cdkn2a*$^{-/-}$*;Pten*$^{-/-}$*;*myr*Akt1* primary tumor growth rates in mice treated with IACS-010759 (7.5 mg/kg p.o. once daily) or vehicle upon initial detection of palpable tumor. Rated-based T/C metric was used to reflect primary tumor growth rates. Significance determined via two-sided Student's *t*-test. (**E**) Incidence of brain and lung metastases in mice with *Braf*^{V600E}*;Cdkn2a*$^{-/-}$*;Pten*$^{-/-}$*;*myr*Akt1* primary tumors treated with IACS-010759 (7.5 mg/kg p.o. once daily) or vehicle. Systemic treatment was started upon initial detection of palpable primary tumor. Y-axis indicates tumor incidence, and x-axis indicates metastatic site. Significance determined via Fisher's exact test.

While highly novel, this model features two critical limitations. First, we did not know when cells metastasized from the primary tumor. Second, we had to rely exclusively on necropsy to identify MBMs. It is possible that OXPHOS inhibition primarily impeded the outgrowth of micrometastases as opposed to preventing their initial formation. To further investigate this topic, we established an immunocompetent experimental model of melanoma brain metastasis with duel luciferase/GFP-tagged YUMM5.2 cells. To increase the brain-seeking capacity of the brain-metastasizing variants, we used an approach undertaken previously (141). Cells were cycled through the brain for three successive passages yielding brain metastatic variants (Br1, Br2, and Br3—the numerals represent the number of selection cycles). Only the YUMM5.2-Br3 cells were used for subsequent analyses.

Figure 23 illustrates our experimental metastasis model. YUMM5.2-Br3 cells were treated *in vitro* with IACS-010759 (100 nM) or with vehicle control for 12 hours. This dose of IACS-010759 significantly inhibited OCR (**Figure 24A**) without affecting cell viability (data not shown). $2.5x10^6$ cells were then injected into the left cardiac ventricles of C57BL/6 mice. Mice injected with the cells treated *in vitro* with vehicle were randomized to receive either 0.5% methylcellulose vehicle control (once daily) or the maximum tolerated dose of IACS-010759 (7.5 mg/kg once daily) via oral gavage. In parallel, mice injected with cells treated *in vitro* with IACS-010759 were randomized to receive either 0.5% methylcellulose vehicle control (once daily) or IACS-010759 (7.5 mg/kg once daily) via oral gavage. After 14 days, mice were euthanized and *ex vivo* bioluminescence imaging (BLI) analysis was used to evaluate brain and lung involvement (**Figure 24B**). Harvested brains underwent histological examination by a pathologist.

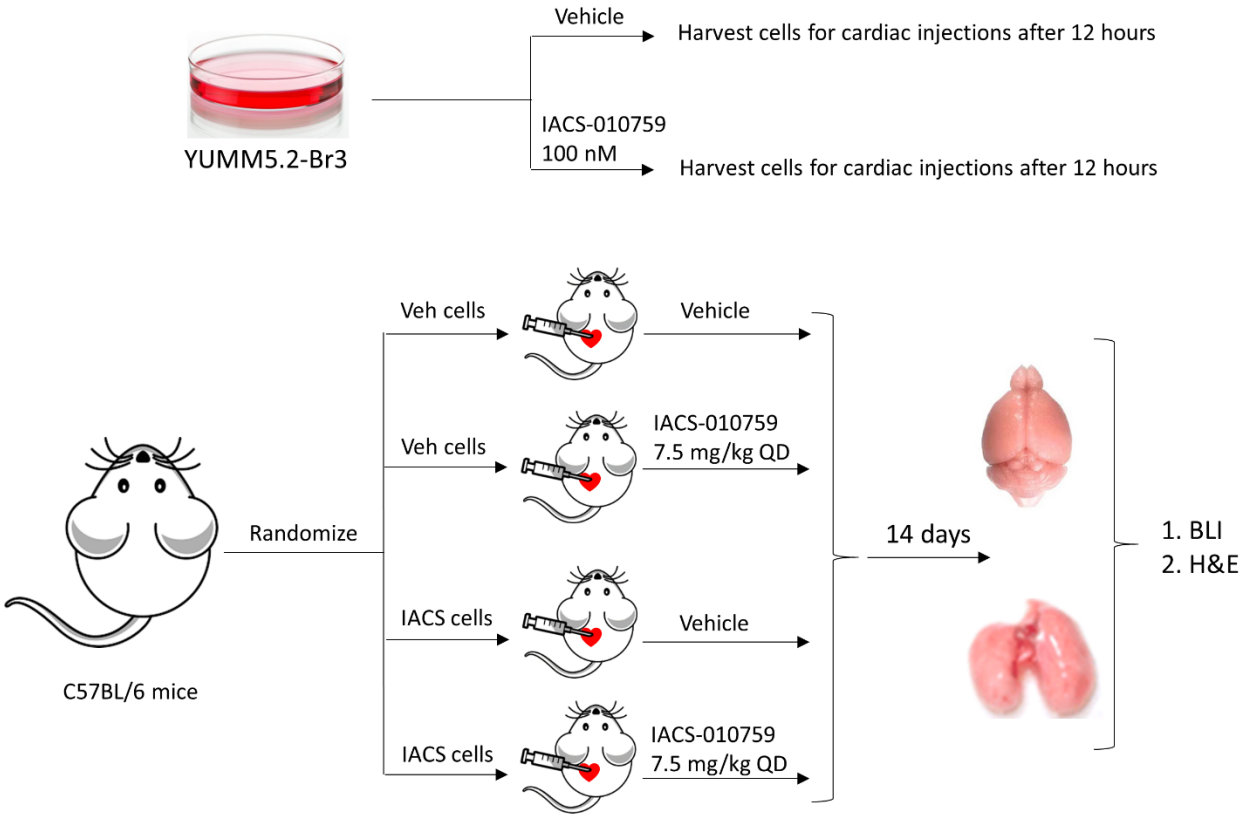

Figure 23: Experimental metastasis model used to assess the role of oxidative phosphorylation in melanoma brain metastasis pathogenesis. To determine if inhibition of OXPHOS decreases brain-metastatic potential, YUMM5.2-Br3 cells were treated *in vitro* with IACS-010759 (100 nM) or with vehicle control for 12 hours. $2.5x10^6$ cells were then injected into the left cardiac ventricles of C57BL/6 mice (female, 8 weeks of age). Mice injected with the cells treated *in vitro* with vehicle were randomized to receive either 0.5% methylcellulose vehicle control (once daily) or IACS-010759 (7.5 mg/kg once daily) via oral gavage. In parallel, mice injected with cells treated *in vitro* with IACS-010759 were randomized to receive either 0.5% methylcellulose vehicle control (once daily) or IACS-010759 (7.5 mg/kg once daily) via oral gavage. *In vivo* treatments began 3 hours after cardiac injections. After 14 days, mice were injected with 150 mg/kg D-luciferin salt and euthanized 10 minutes later for *ex vivo* bioluminescence imaging (BLI) analysis to evaluate organ involvement in detail. Brains were fixed in formalin overnight, dehydrated in 70% ethyl alcohol, and paraffin embedded. Sections were stained with H&E for review by a pathologist.

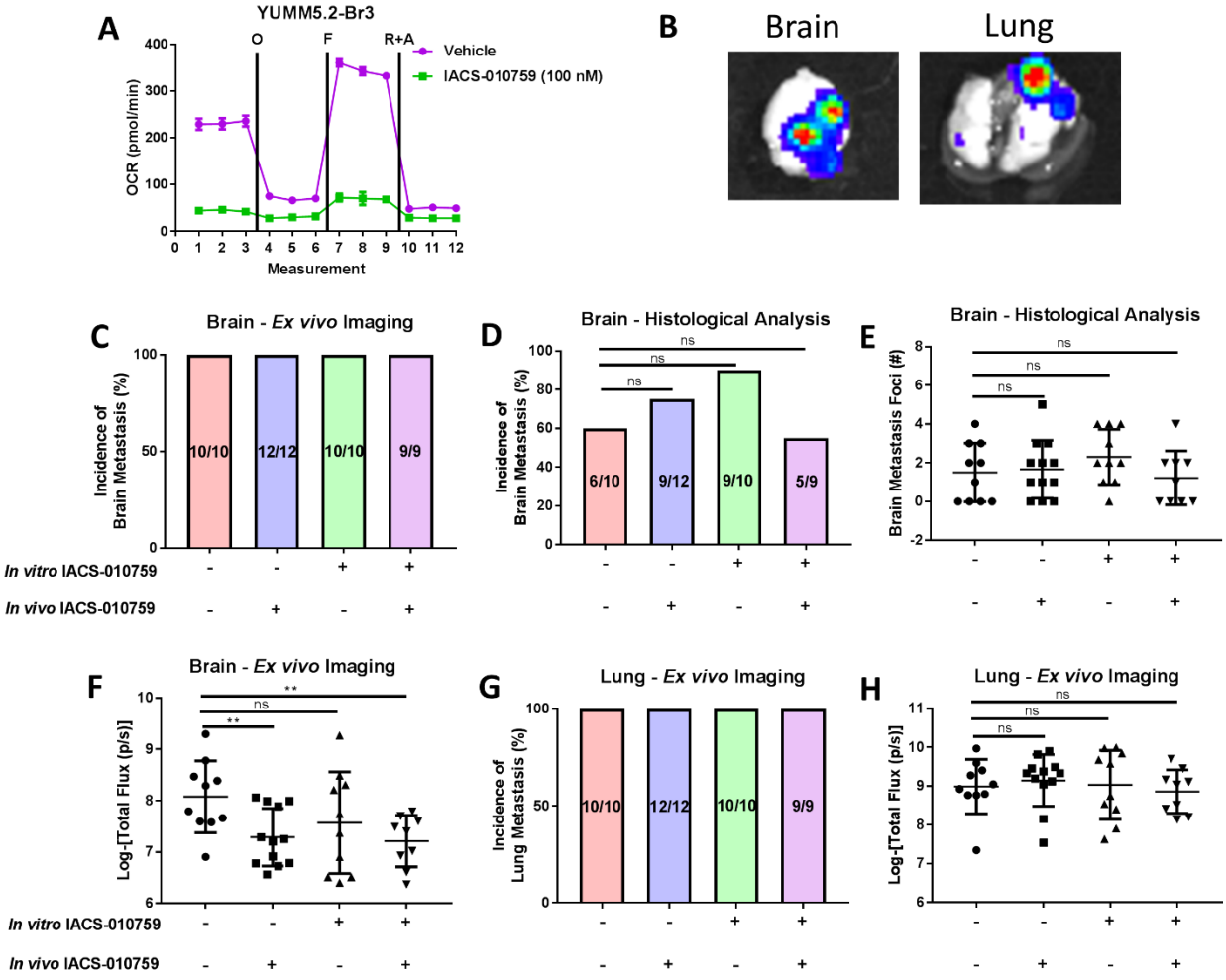

Figure 24: Oxidative phosphorylation is functionally significant for growth of melanoma brain metastases. (**A**) Seahorse mitochondrial stress test was performed on YUMM5.2-Br3 cells treated for 12 hours with vehicle or 100 nM of IACS-010759. The figure shows basal, oligomycin-inhibited ("O"), FCCP-activated ("F") and Antimycin/Rotenone inhibited ("A&R") oxygen consumption rate (OCR) levels. (**B**) Representative *ex vivo* bioluminescence imaging (BLI) of brain and lung tissue harvested from a moribund mouse that previously underwent an intracardiac injection of YUMM5.2-Br3 cells. (**C**) Incidence of brain metastasis determined via *ex vivo* BLI in mice that had undergone intracardiac injections with YUMM5.2-Br3 cells treated *in vitro* with IACS-010759 or vehicle and then underwent daily treatments with IACS-010759 or vehicle. (**D**) Incidence of brain metastasis determined via histological analysis in mice that had undergone intracardiac injections with YUMM5.2-Br3 cells treated *in vitro* with IACS-010759 or vehicle and then underwent daily treatments with IACS-010759 or vehicle. ns: not significant (P>0.05) by two-sided Fisher's exact test. (**E**) Histological quantification of brain metastatic foci in mice that had undergone intracardiac injections with YUMM5.2-Br3 cells treated *in vitro* with IACS-010759 or vehicle and then underwent daily treatment with IACS-010759 or vehicle. ns: not significant (P>0.05) by two-sided Student's *t*-test. (**F**) *Ex vivo* BLI quantification of tumor burden in brains of mice that had undergone intracardiac injections with YUMM5.2-Br3 cells treated *in vitro* with IACS-010759 or vehicle and then underwent daily treatment with IACS-010759 or vehicle. **P <0.01, ns: not significant (P>0.05) by two-sided Student's *t*-test. (**G**) Incidence of lung metastasis determined via *ex vivo* BLI in mice that had undergone intracardiac injections with YUMM5.2-Br3 cells treated *in vitro* with IACS-010759 or vehicle and then underwent daily treatments with IACS-010759 or vehicle. (**H**) *Ex vivo* BLI quantification of tumor burden in lungs of mice that had undergone intracardiac injections with YUMM5.2-Br3 cells treated *in vitro* with IACS-010759 or vehicle and then underwent daily treatment with IACS-010759 or vehicle. ns: not significant (P>0.05) by two-sided Student's *t*-test.

Interestingly, *ex vivo* BLI and histological analyses determined that the incidence of brain metastasis did not differ between any of the experimental groups (**Figure 24C-E**). However, *in vivo* IACS-010759 treatment significantly decreased MBM tumor burden compared to vehicle controls ($p<0.01$), regardless of whether or not the cells were previously treated with IACS-010759 prior to injection (**Figure 24F**). *In vitro* OXPHOS inhibition alone failed to significantly decrease MBM tumor burden compared to vehicle controls (**Figure 24F**). Together, these results indicate that OXPHOS plays a critical role in the growth of MBMs without affecting their initial formation. Finally, we observed no differences in lung metastasis incidence or tumor burden between experimental arms (**Figure 24G-H**).

Subsequently, we acquired previously characterized A375P and G361 melanoma cells stably transfected with shRNA targeting PGC1α (shPGC1α) and a scrambled control vector (shScr). Bioenergetics stress testing by Seahorse analyzer showed that PGC1α silencing significantly inhibited OXPHOS in both cell lines (**Figure 25A-D**). These cell lines were implanted into the brains and SQ tissue of CD-1 nude mice. Interestingly, PGC1α knockdown had no effect on the subcutaneous growth rates of either cell line compared to their scrambled controls (**Figure 25E-F**). In contrast, silencing of PGC1α significantly extended survival of mice bearing intracranial xenografts (**Figure 25G-H**).

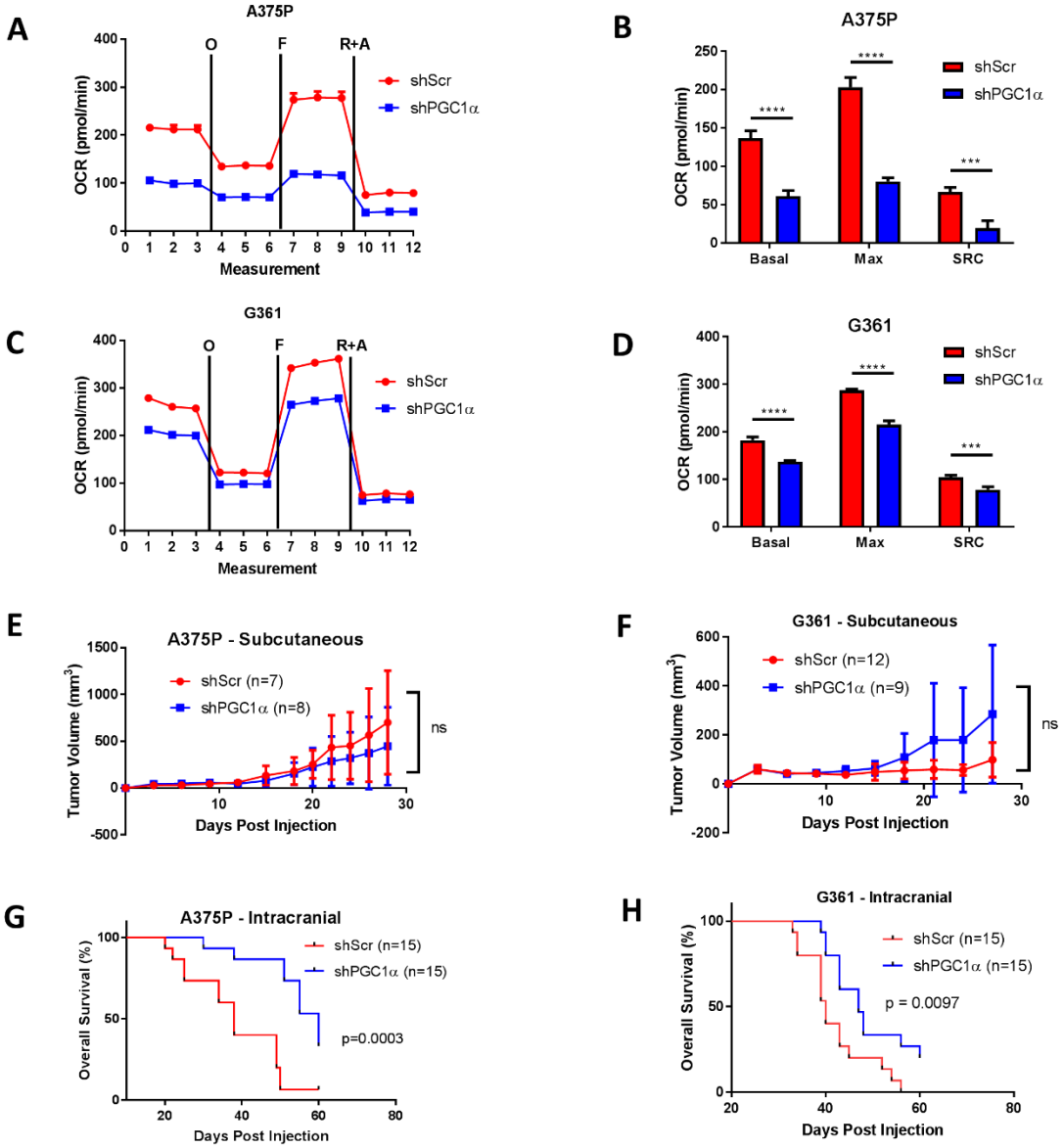

Figure 25: Oxidative phosphorylation is necessary for growth of melanoma cells in the brain but not subcutaneous tissue. (**A**) Seahorse mitochondrial stress test was performed on A375P cells stably transfected with shRNAs targeting PGC1α (shPGC1α) or scrambled control (shScr). The figure shows basal, oligomycin-inhibited ("O"), FCCP-activated ("F") and Antimycin/Rotenone inhibited ("A&R") oxygen consumption rate (OCR) levels. (**B**) Comparison of basal and maximum OCR values and spare respiratory capacity (SRC) for shPGC1α and shScr A375P cells calculated from (**A**). ****P<0.0001, ***P<0.001 by two-sided Student's t-test. (**C**) Seahorse mitochondrial stress test was performed on G361 cells stably transfected with shRNAs targeting PGC1α (shPGC1α) or scrambled control (shScr). (**D**) Comparison of basal and maximum OCR values and SRC for shPGC1α and shScr G361 cells calculated from (**C**). ****P<0.0001, ***P<0.001 by two-sided Student's t-test. (**E**) shPGC1α and shScr A375P cells were grown as subcutaneous xenograft tumors in CD-1 nude mice. Tumor volumes were recorded for the number of days shown. Error bars represent mean ± S.D. (**F**) shPGC1α and shScr G361 cells were grown as subcutaneous xenograft tumors in CD-1 nude mice. Tumor volumes were recorded for the number of days shown. Error bars represent mean ± S.D. (**G**) Kaplan-Meier overall survival (OS) analysis of mice bearing intracranial (ICr) shPGC1α and shScr A375P xenografts. Significance determined via log-rank test. (**H**) Kaplan-Meier OS analysis of mice bearing ICr shPGC1α and shScr G361 xenografts. Significance determined via log-rank test.

Because PGC1α has been implicated in mediating cellular programming beyond OXPHOS, we implanted A375-R1 cells into the brains of CD-1 nude mice and initiated treatment immediately following tumor cell injection (**Figure 26A**). BLI of tumor-bearing mice indicated that pharmacological inhibition of OXPHOS significantly lowered ($p<0.001$) total flux 14 days following treatment initiation (**Figure 26B**). Furthermore, IACS-010759 treatment significantly extended overall survival (**Figure 26C**). Together, these studies indicate that OXPHOS inhibition prevented growth of cells injected into the brains of mice.

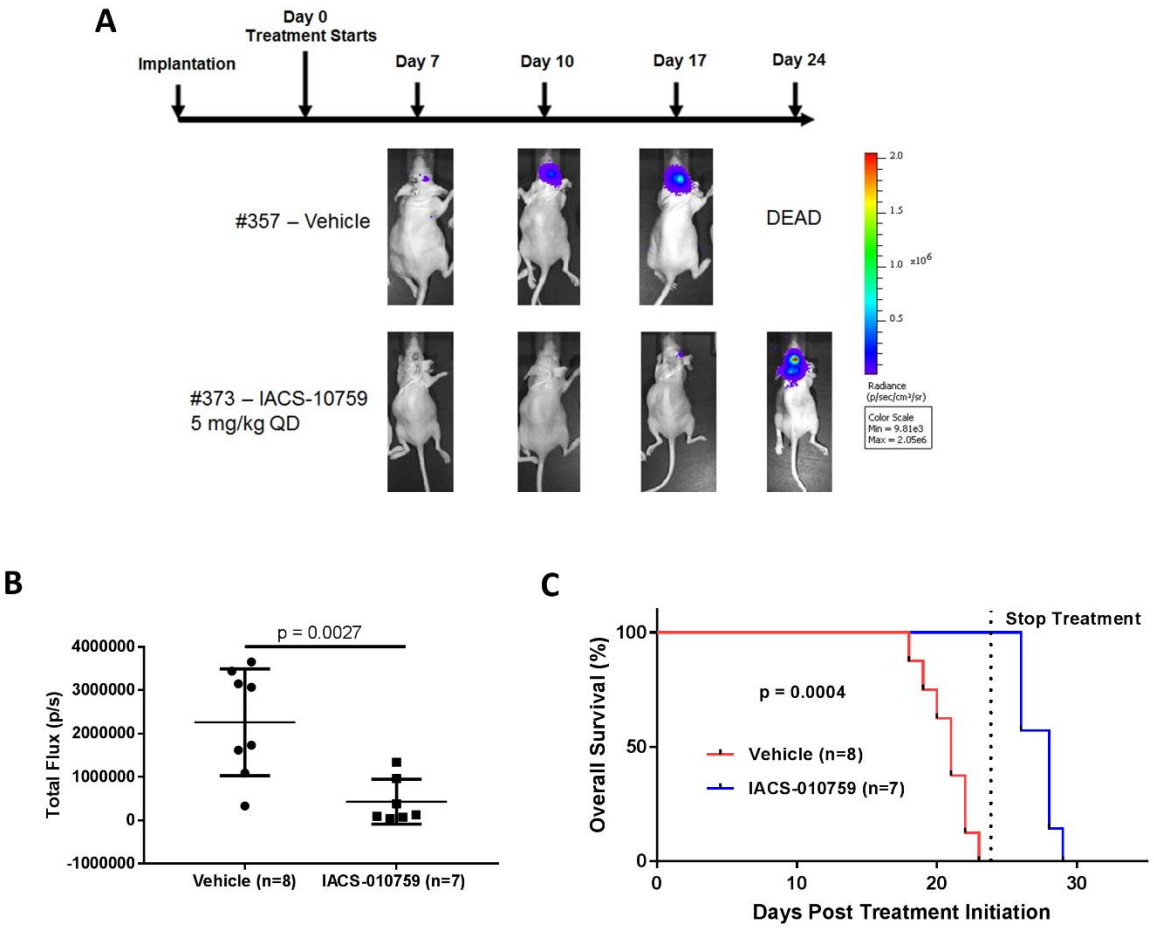

Figure 26: Oxidative phosphorylation inhibition prevents outgrowth of intracranial melanoma xenografts. (**A**) Representative bioluminescence imaging (BLI) of mice with intracranial A375-R1-F-Luc xenografts treated with vehicle or IACS-010759 (5 mg/kg p.o. once daily). Treatment was initiated 3 hours after tumor cell implantation and stopped after all vehicle mice had been euthanized. (**B**) BLI of tumor-bearing mice indicates significantly lower ($p<0.001$) total flux in IACS-010759-treated mice 14 days following treatment initiation. Significance determined via two-sided Student's *t*-test. (**C**) Log-rank analysis of Kaplan-Meier survival curves indicates significant survival benefit in IACS-010759-treated mice.

4.3 - DISCUSSION

In this study, we sought to functionally validate OXPHOS as a mediator of MBM pathogenesis. Based on our previous analysis of patient-matched MBMs and ECMs, **we hypothesized that OXPHOS promotes the formation and growth of MBMs.**

Using bulk RNA-seq methods and qRT-PCR, we confirmed OXPHOS gene set enrichment in MBMs formed in the RCAS-TVA mouse model compared to primary tumors and lung metastases. To define determinants of metastatic growth of melanoma cells in the brain, we compared primary tumors able to metastasize to the brain in this model with those unable to metastasize and demonstrated significant enrichment of OXPHOS gene set expression in the brain-metastatic primaries. Subsequently, we evaluated brain-metastatic variants of 2 different melanoma cell lines. Our Seahorse bioenergetics analyses demonstrated significantly higher basal/maximum OCR values in the brain-metastatic variants of both models. Additionally, microarray analysis of the YDFR model confirmed OXPHOS gene set enrichment in the YDFR.CB3 cells. Cumulatively, these studies characterize melanomas that metastasize to the brain as significantly enriched in OXPHOS vs. non-metastatic controls.

To functionally validate OXPHOS as a mediator of MBM pathogenesis, we treated mice bearing brain-metastatic primaries from the RCAS-TVA model with the novel OXPHOS inhibitor IACS-010759. Treatments did not affect primary tumor growth or cellular proliferation and did not significantly alter the incidence of lung metastasis. However, no mouse treated with IACS-010759 developed a detectable brain metastasis. While encouraging, we recognized two critical limitations of this model. First, we did not know when the primary tumors began to metastasize. We initiated treatments upon identification of palpable tumors, but it is possible that cells had already spread from the primary tumor site and seeded distant organs. In this case, we only

succeeded in impeding the outgrowth of brain micrometastases as opposed to preventing their initial formation. Second, this model relies exclusively on necropsy to identify distant metastases. This method might have failed to identify micrometastases in the brains of mice treated with IACS-010759 if the drug successfully prevented their outgrowth. To overcome these limitations, we utilized an immunocompetent experimental model of MBM that features a cell line expressing firefly luciferase. In this experiment, we pretreated cells with either vehicle or a concentration of IACS-010759 that inhibited the pathway without killing the cells and then injected these cells into the left cardiac ventricles of C57BL/6 mice, which then received either vehicle or IACS-010759 at a dose that potently inhibits the pathway *in vivo* (178). Lung metastases and brain metastases developed at similar incidences across all experimental groups. Interestingly, *in vivo* IACS-010759 treatment significantly decreased MBM tumor burden compared to vehicle controls, regardless of whether or not the cells were previously treated with IACS-010759 prior to injection. *In vitro* OXPHOS inhibition alone failed to significantly decrease MBM tumor burden compared to vehicle controls. Together, these results indicate that OXPHOS plays a critical role in the growth of MBMs without affecting their initial formation. Furthermore, the failure of the *in vitro*/*in vivo* IACS-010759 combination to affect lung metastasis formation and tumor burden indicates that OXPHOS plays no discernable role in the formation or growth of lung metastases. This finding corroborates our observations in the RCAS-TVA model and remains highly consistent with our previous profiling efforts that demonstrate OXPHOS enrichment in MBMs compared to metastases at other tumor sites.

To further validate our findings, we acquired two previously characterized cell lines stably transfected with shRNAs targeting PGC1α and a scrambled control. After confirming OXPHOS inhibition in the knockdown cells, we implanted these cells into the brains and SQ tissue of nude mice. Consistent with our experimental model of metastasis, we observed no differences in SQ

tumor growth between the shPGC1α and shScr lines while mice injected intracranially with shPGC1α cells lived significantly longer compared to shScr controls in both models. These results further indicate that OXPHOS preferentially promotes melanoma growth in the brain without affecting growth at other anatomical sites.

As a final means of validating the role of OXPHOS in MBM growth, we implanted MAPKi-resistant A375-R1 cells into the brains of nude mice and immediately began to treat them with either vehicle or IACS-010759 at a dose known to inhibit the pathway. We observed that OXPHOS inhibition significantly decreased tumor burden after 14 days and significantly extended the overall survival of the mice compared to vehicle controls.

This study is highly novel as it employed analysis of clinical samples and preclinical models to provide the first detailed assessment of the role of OXPHOS metabolism in MBM pathogenesis. We performed our functional studies in the first-ever RCAS-TVA model of melanoma that forms brain metastases from cutaneous primary tumors. Furthermore, we developed an experimental MBM model to validate our findings. Given the importance of immunotherapies in metastatic melanoma patients, we ensured that we performed as many studies as possible in models featuring functional immune systems. We utilized genetic and pharmacological approaches to achieve OXPHOS inhibition in our models. Our pharmacological studies employed a potent OXPHOS inhibitor (IACS-010759) that is currently in phase I clinical trials.

We could have made several improvements to the experiments in this study. First, we could have used patient-derived xenografts (PDXs) or PDX-derived cell lines capable of metastasizing to and/or growing in the brain. Compared to cell lines, PDXs more accurately model tumor cell biology *in vivo* and represent a potential improvement over standard cell lines. Ideally, we could have created a spontaneous or experimental metastasis model from PDXs or

PDX-derived cell lines. Further, we could have been more consistent with our use of cells between different experiments. For example, directly inhibiting OXPHOS in the RCAS-TVA via genetic manipulation would have circumvented the need to inhibit the pathway via pharmacological dosing and then confirm our findings in the unrelated YUMM5.2-Br3 model. Unfortunately, logistical issues prevented us from making this possible. While these limitations should be noted, they did not preclude us from making scientifically valid conclusions using the resources available.

Findings from this study are highly clinically relevant. Our experiments suggest that the use of IACS-010759 might impede brain metastasis development in metastatic melanoma patients. While IACS-010759 did not prevent the formation of MBMs, this study presents numerous lines of evidence that IACS-010759 treatment could keep lesions small and asymptomatic. Indeed, the ability of IACS-010759 to prevent the formation of detectable MBMs could significantly alter treatment options for metastatic melanoma patients. Other OXPHOS inhibitors effectively synergize with and prevent resistance to MAPKi therapy (26, 245). Thus, upfront treatment of *BRAF*-mutant melanoma patients with MAPKi therapy and IACS-010759 could effectively reduce tumor burden, prevent the onset of resistance, and decrease the incidence of escape to the brain.

CHAPTER 5: NOVEL THERAPEUTIC STRATEGIES OF OVERCOMING OXIDATIVE PHOSPHORYLATION IN MELANOMA BRAIN METASTASES

Copyright Disclosure:

This chapter is based upon:

1. **Fischer, G. M.**, Y. N. Vashisht Gopal, J. L. McQuade, W. Peng, R. J. DeBerardinis, and M. A. Davies. 2018. Metabolic strategies of melanoma cells: Mechanisms, interactions with the tumor microenvironment, and therapeutic implications. *Pigment Cell Melanoma Res* 31: 11-30.

2. **Fischer, G. M.**, A. Jalali, D. A. Kircher, W. C. Lee, J. L. McQuade, L. E. Haydu, A. Y. Joon, A. Reuben, M. P. de Macedo, F. C. L. Carapeto, C. Yang, A. Srivastava, C. R. Ambati, A. Sreekumar, C. W. Hudgens, B. Knighton, W. Deng, S. D. Ferguson, H. A. Tawbi, I. C. Glitza, J. E. Gershenwald, Y. N. Vashisht Gopal, P. Hwu, J. T. Huse, J. A. Wargo, P. A. Futreal, N. Putluri, A. J. Lazar, R. J. DeBerardinis, J. R. Marszalek, J. Zhang, S. L. Holmen, M. T. Tetzlaff, and M. A. Davies. 2019. Molecular Profiling Reveals Unique Immune and Metabolic Features of Melanoma Brain Metastases. *Cancer Discov.* 9: 628-645.

5.1 - INTRODUCTION

5.1.1 - Immune Effects of Metabolic Reprogramming

As immune cells compose a critical component of the tumor microenvironment (TME), there is an increasing interest in studying the metabolic interactions that occur between melanoma cells and immune cells. To fully understand the complexity of these dynamic interactions, it is necessary to review the typical metabolic statuses of the key immune cells present in the TME.

Neutrophils contain few mitochondria and therefore use glycolysis extensively to meet their bioenergetic demands. Upon activation, these cells consume large quantities of glucose to feed the pentose phosphate pathway (PPP) for production of NADPH, needed to activate NADPH oxidase, which in turn produces hydrogen peroxide, a bactericidal byproduct (246). Unlike neutrophils, dendritic cells are a highly complex group of cells responsible for connecting the innate and adaptive arms of the immune system by responding to pathogen associated molecular patterns (PAMPS) and subsequently controlling the fates of T cells. Naïve dendritic cells rely extensively on oxidative phosphorylation (OXPHOS) to produce ATP. Activation of dendritic cells stimulates the PI3K-AKT pathway and shifts the metabolic dependency to glycolysis (221). The two categories (M1 and M2) of macrophages differ in their preferred bioenergetic pathways. M1 macrophages, which have antimicrobial and antitumor functions, exhibit a glycolytic phenotype. In contrast, M2 macrophages, which are critical regulators of wound healing with minimal antitumor activity, utilize OXPHOS as their main source of ATP (246). T cells, the most researched component of the adaptive immune system, utilize a spectrum of metabolic phenotypes depending on their activation state and the subclass of T cells to which they belong. Activated $CD4^+$ and $CD8^+$ effector T cells adopt a glycolytic phenotype, upregulating glucose transporters

and glycolytic enzymes in the process (201). Unlike cells of the innate immune system, T cells produce memory cells, which catabolize fatty acids and utilize OXPHOS to produce ATP (221). Regulatory $CD4^+$ T cells (Tregs) are highly oxidative cells while regulatory T helper-17 (Th17) cells depend on glycolysis (246). While much work remains to full understand the metabolic dependencies of B lymphocytes, these cells appear to utilize both OXPHOS and glycolysis (221).

Tumor metabolism can suppress the function of nearby immune cells (**Figure 18**). As $CD8^+$ T cells are glycolytic, they must compete with highly glycolytic tumor cells for access to glucose (247). Without glucose, $CD8^+$ T cell activity is inhibited. Furthermore, high concentrations of lactate in the TME prevent adequate secretion of lactate out of T cells, again inhibiting their function (221, 248). By inducing P38 MAPK and c-Jun N-terminal kinase (JNK)/c-JUN signaling pathways, lactate-based immunosuppression has been demonstrated in numerous cancers, including melanoma (221, 249). Melanoma spheroids inhibit cytokine secretion from T cells by secreting lactate into the TME (221, 250). However, T cells can recover from this inhibition upon lactate clearance (248). Lactate can also suppress cells of the innate immune system. It converts M1 macrophages to M2 macrophages, promoting tumor progression (221). In addition, it prevents the maturation of dendritic cells, resulting in an increase in the immunosuppressive IL-10 cytokine in the TME (221).

Tumor cell metabolism can also profoundly impact the immune system via tryptophan metabolism. Once activated, effector T helper-1 (Th1) cells secrete interferon-γ (IFNγ), which stimulates indoleamine 2,3-dioxygenase (IDO) in tumor cells. In turn, IDO metabolizes tryptophan, producing kynurenine in the process. IDO promotes melanoma tumorigenesis and diminishes survival through two mechanisms (251, 252). First, IDO starves effector T cells of tryptophan, resulting in general control nonderepressible 2 (GCN2)-mediated suppression of proliferation and promotion of apoptosis (252-255). While a minimum level of tryptophan for T

cell maintenance has not been demonstrated, low serum tryptophan levels correlate with a poor prognosis in melanoma patients (252, 256). In addition, kynurenine binds to the aryl hydrocarbon receptor (AhR), inducing Treg differentiation and polarizing dendritic cells and macrophages to immunosuppressive phenotypes (255, 257). Moreno et al. demonstrated that targeting IDO with the competitive inhibitor 1-methyl-tryptophan (1-MT) retards the proliferation of melanoma cells *in vitro* (258). Furthermore, 1-MT treatment delays the outgrowth of Lewis lung cancer cells in syngeneic mice (259). Though monotherapy with 1-MT has little effect on the growth of subcutaneous B16-F10 tumors, 1-MT sensitizes the tumors to chemotherapy and whole-body radiation (260). While promising, additional exploration is required to further define how IDO mediates immunosuppression in melanoma and whether or not 1-MT can be combined with currently approved therapies.

5.1.2 - Therapeutic Implications of Melanoma Metabolism

The development of effective immune and targeted therapies has revolutionized the management of patients with metastatic melanoma. However, these treatments have metabolic implications that must be understood in order to identify potential mechanisms of resistance and novel treatment combinations.

5.1.2a - Immunotherapy

Metabolic reprogramming of tumor cells has significant implications for immunotherapy. Ipilimumab, an antibody that inhibits signaling by cytotoxic T-lymphocyte-associated protein (CTLA-4) on T cells, was approved by the US FDA in

2011 for the treatment of patients with metastatic melanoma. Three years later, the programmed cell death protein-1 (PD-1) blocking antibodies pembrolizumab and nivolumab were also approved. These three antibodies overcome inhibitory signals encountered by T cells in their attempt to locate and destroy tumor cells. Specifically, the expression of CTLA-4, also known as CD152, increases significantly following the activation of $CD4^+$ and $CD8^+$ T cells (261). This T cell surface molecule subsequently competes with CD28 for interactions with CD80 and CD86 (B7-1 and B7-2, respectively) on the surface of antigen presenting cells, such as dendritic cells and macrophages. The interactions between CTLA-4 and CD80 and CD86 are more favorable than those between CD28 and CD80 and CD86, resulting in CTLA-4 binding with these molecules in place of CD28. In response, inhibitory signals are transmitted to the effector $CD8^+$ T cells, resulting in suppression of the immune response (262, 263). Like CTLA-4, PD-1 is expressed on the surface of T cells. Its ligand, PD-L1, is expressed on the surface of dendritic cells, M2 macrophages, fibroblasts, and tumor cells (264). Activation of PD-1 following binding to PD-L1 inhibits effector $CD8^+$ T cells, suppressing the antitumor response (265). Mechanistically, CTLA-4 and PD-1 both inhibit the PI3K-AKT pathway in distinct yet synergistic ways, with CTLA-4 signaling inhibiting AKT through protein phosphatase 2A (PP2A) and PD-1 signaling inhibiting PI3K (266). Since this pathway promotes glycolysis, CTLA-4 and PD-1 signaling promote OXPHOS at the expense of glycolysis, and PD-1 signaling augments fatty acid oxidation (267). As activated effector T cells utilize glycolysis, these metabolic alterations provide a metabolic explanation for CTLA-4- and PD-1-mediated immunosuppression. Checkpoint inhibitors remove the suppression of the PI3K-AKT in effector T cells, allowing them to become active once again and adopt a glycolytic phenotype. Once this occurs, tumor cell death caused by

the checkpoint inhibitors results in the release of glucose into the TME, promoting further activation of effector $CD8^+$ T cells (247).

While naïve $CD4^+$ and $CD8^+$ T cells rely exclusively on OXPHOS to meet their bioenergetic demands, activation triggers a shift to a hypermetabolic phenotype characterized by increased glycolysis and OXPHOS (268). Interestingly, pharmacological suppression of OXPHOS does not appear to negatively impact effector T cell function. Treatment with the OXPHOS inhibitors metformin and phenformin improves the response of melanoma xenografts to anti-PD1 therapy (173, 269, 270). Metformin decreases intratumoral hypoxia that is highly detrimental to effector $CD8^+$ T cell function (173), and phenformin facilitates an increased response by preventing the immunosuppressive effects of myeloid derived suppressor cells (MDSCs) (270). Metformin monotherapy is sufficient to significantly increase intratumoral $CD8^+$ effector cells and protect them from apoptosis in the TME (271).

In addition to central carbon metabolism, tryptophan metabolism also appears to play a critical role in mediating response to immunotherapy. Holmgaard et al. demonstrated that treatment of IDO-knockout mice with anti-CTLA-4 and anti-PD-1 inhibited the growth of B16-F10 melanoma tumors compared to wild-type mice. Furthermore, IDO inhibitors synergized with anti-CTLA-4 treatment, promoting $CD8^+$ T cell recruitment and inhibiting tumor growth to a significantly greater extent than anti-CTLA-4 treatment alone (272). When given to 19 treatment-naïve metastatic melanoma patients participating in a phase I clinical trial (NCT02178722), the combination of pembrolizumab and the IDO inhibitor Epacadostat achieved complete responses in 4 patients, partial responses in 7 patients, and stable disease in 3 patients (273). Furthermore, the combination demonstrated an acceptable safety profile (273). Treatment-naive

metastatic melanoma patients are currently being enrolled in phase II and III clinical trials (NCT02752074) designed to evaluate this treatment strategy.

5.1.2b - Targeted Therapy

While the BRAF inhibitors dabrafenib and vemurafenib and the MEK inhibitors trametinib and cobimetinib are highly effective in metastatic melanoma patients with activating *BRAF* mutations, the depth and duration of clinical responses to these agents are variable, and the majority of patients will eventually develop resistance to them (3). As the MAPK pathway promotes aerobic glycolysis in tumor cells (**Figure 1**), inhibition of the pathway results in significant reduction in glucose utilization and glycolytic flux. This suppression results from modulation of the glycolytic regulators HIF1α and MYC and is necessary to achieve clinical responses to BRAF inhibitors (20). Studies have shown that glycolytic flux is restored in cells resistant to BRAF inhibition, and that combined inhibition of BRAF and glycolysis could overcome targeted therapy resistance (20). While those observations were based largely on experiments performed after 24-hour treatments, Haq et al. demonstrated increased PGC1α-driven OXPHOS in response to longer (i.e., ≥ 72 hours) treatments with MAPK inhibitors (26). Induction of OXPHOS has been identified in 30-50% of *BRAF*-mutant melanomas with both *de novo* and acquired resistance to MAPK pathway inhibitors (3). Enforced expression of PGC1α induces resistance in cells previously sensitive to MAPK inhibitors (26), while genetic knockdown of PGC1α results in synergistic growth inhibition and apoptosis induction with MAPK pathway therapies in PGC1α-mediated High-OXPHOS cells (3). In addition, studies by Herlyn and colleagues previously identified a population of slow-cycling, treatment-

resistant cells characterized by expression of the histone 3 K4 demethylase JARID1B. They further showed that these slow-cycling cells are characterized by High-OXPHOS. Interestingly, Transcription factor A, mitochondrial (TFAM), not PGC1α, facilitates the High-OXPHOS phenotype in these cells, indicating that some High-OXPHOS melanoma cells adopt this metabolic phenotype independent of the MITF-PGC1α signaling axis, (35, 274, 275). Combination treatments with vemurafenib and mitochondrial inhibitors overcame the multi-drug resistance of JARID1B^{high} cells *in vitro* (275). This strategy of targeting both the MAPK pathway and OXPHOS has been highly effective in other studies as well. For example, our lab determined that the High-OXPHOS phenotype predicts sensitivity to combination treatment with MAPK pathway inhibitors and mTORC1/2 inhibitors (3). Mechanistically, mTORC1/2 inhibitors prevented the nuclear translocation of MITF, thereby inhibiting PGC1α transcription (**Figure 2**) (3). Similarly, directly targeting mitochondrial biogenesis with the mitochondria-targeted, small-molecule HSP90 inhibitor gamitrinib, has also been shown to overcome MAPK pathway resistance in melanomas with the High-OXPHOS phenotype (35).

Numerous studies have also examined the effects of the biguanide metformin as a combinatorial strategy in melanoma. Commonly used for the treatment of diabetes mellitus type 2, metformin became the subject of extensive oncological research after an initial report indicated that diabetic patients treated with metformin had lower rates of cancer (276). As an inhibitor of complex I of the mitochondrial electron transport chain, metformin deprives cells of ATP, stimulating AMPK and resulting in mTOR inhibition, p53 activation, and apoptosis (277). Furthermore, metformin independently inhibits mTOR likely through a RAS-related GTPase and suppresses NFκB-STAT3 signaling (277). Experiments testing metformin as a single-agent therapy have produced mixed

results (277). While several studies demonstrated the anti-melanoma effect of metformin therapy *in vitro*, Martin et al. found that metformin treatments promoted the growth of $BRAF^{V600E}$-mutated melanomas *in vivo* by inducing angiogenesis (278-281). Despite this effect, metformin treatment also sensitized melanoma cells to treatment with angiogenesis inhibitors (279). Other combination studies have been very promising, with Niehr et al. demonstrating synergy between vemurafenib and metformin in $BRAF^{V600E}$-mutated melanomas (280). Currently, two phase I/II trials are enrolling patients to test combinations of vemurafenib and metformin (NCT01638676) and dabrafenib, trametinib, and metformin (NCT02143050) in metastatic melanoma patients.

Recent work also supports that BRAF inhibitor-resistant, High-OXPHOS melanomas prefer glutamine metabolism over glucose metabolism (282). This finding suggests a new therapeutic opportunity, and experiments demonstrated that the glutaminase inhibitor BPTES enhanced the antitumor effects of MAPK pathway inhibitors in the treatment of these High-OXPHOS melanomas (282). While promising, additional work remains to understand optimal dosing of treatment combinations with targeted therapies and metabolic inhibitors.

5.1.3 - Hypothesis Tested

While the treatments and outcomes for patients with advanced melanoma have improved dramatically over the last decade, MBMs remain a clinically significant challenge in this disease. Improving our understanding of the features of MBMs is a critical first step to facilitate the development of new, more effective therapeutic approaches to treat them. Our recent analysis of gene expression in the largest cohort of MBMs analyzed by RNA-seq to date, and the largest

cohort of patient-matched brain metastases and extracranial metastases from any tumor type, provided key new insights into the pathogenesis of these tumors (174). A number of these novel findings provide the rationale for the testing of new clinical strategies, including the targeting of OXPHOS, to improve the outcomes of MBM patients. Importantly, our profiling efforts also identified variability in OXPHOS levels between MBMs. Studies by our group and others previously demonstrated that increased OXPHOS in melanoma (High-OXPHOS phenotype) is associated with poor clinical outcomes, therapeutic resistance, oncogenic signaling pathways, and therapeutic vulnerabilities (7-9) (173). Thus, melanomas with the High-OXPHOS phenotype represent a clinically significant, metabolically-defined subgroup of this disease. Characterizing this metabolic phenotype in MBMs could facilitate the development of new treatments for patients with these tumors. **We tested the hypothesis that OXPHOS associates with distinct molecular, immunological, and metabolic features that, in addition to OXPHOS itself, could be exploited therapeutically in High-OXPHOS MBMs.**

5.2 - RESULTS

5.2.1 - Molecular, Immunological, and Metabolic Associations of Oxidative Phosphorylation in Melanoma Brain Metastases

5.2.1a - RNA-seq Identifies Clinically and Biologically Distinct Clusters of Melanoma Brain Metastases Defined by Differential Enrichment of Oxidative Phosphorylation

We calculated OXPHOS-Indices (OP-Indices) for all 88 MBMs with available RNA-seq data and performed hierarchical clustering to elucidate heterogeneity in

OXPHOS gene expression amongst the tumors. Three large clusters were observed, which we labeled as “High-OXPHOS,” “Intermediate-OXPHOS”, and “Low-OXPHOS” (**Figure 27A**). To confirm that the High-OXPHOS MBMs differed significantly from the other groups, we performed Preranked Gene Set Enrichment Analysis (GSEA-P) and determined that the KEGG OXPHOS gene set was significantly enriched in High- vs. Low-OXPHOS, High- vs. Intermediate-OXPHOS, and High- vs. Low- and Intermediate-OXPHOS MBMs (**Figure 27B-D**). Supporting the clinical significance of the observed heterogeneity of OXPHOS amongst MBMs, Kaplan-Meier analysis identified a significant decrease in overall survival (OS) from craniotomy for patients with High-OXPHOS MBMs vs. patients with Low-OXPHOS MBMs (HR 0.393, 95% CI 0.187-0.830, p=0.014) (**Figure 27E**).

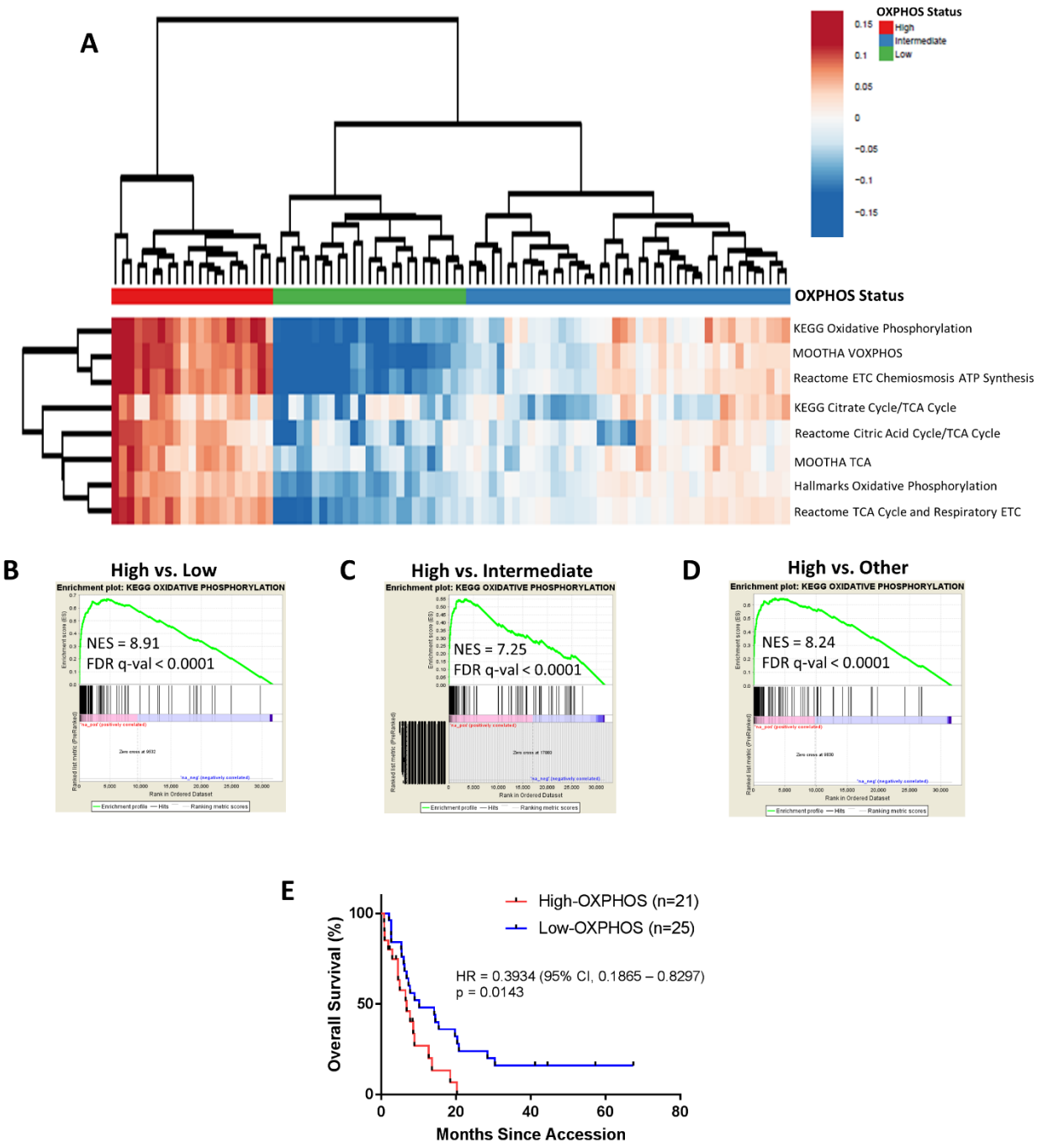

Figure 27: Identification of High-OXPHOS and Low-OXPHOS melanoma brain metastases. (**A**) Hierarchical clustering of the OXPHOS-Indices from 88 MBMs with available RNA-seq data resulted in the formation of 3 clusters: MBMs with significant enrichment (High-OXPHOS; n=21) and depletion (Low-OXPHOS; n=25) of OXPHOS gene sets and MBMs with intermediate OXPHOS gene set enrichment (n=42). Results are represented as a heatmap of median-centered values from each of the 8 components of the OXPHOS-Index. (**B**) Kaplan-Meier overall survival (OS) analysis from craniotomy of patients with High-OXPHOS MBMs (n=21) vs. patients with Low-OXPHOS MBMs (n=25). Hazard ratio determined via Mantel-Haenszel test and significance by log-rank test.

5.2.1b - Molecular and Metabolic Associations of Oxidative Phosphorylation in Melanoma Brain Metastases

As anticipated, High-OXPHOS MBMs express PGC1α and MITF - known mediators of OXPHOS in melanoma - at significantly higher levels (FDR q-val<0.05) than Low-OXPHOS MBMs (**Figure 28A**). Furthermore, GSEA-P analysis demonstrated significant enrichment (FDR q-val<0.0001) of genes regulated by the mTORC1 signaling pathway in High-OXPHOS MBMs (**Figure 28B**).

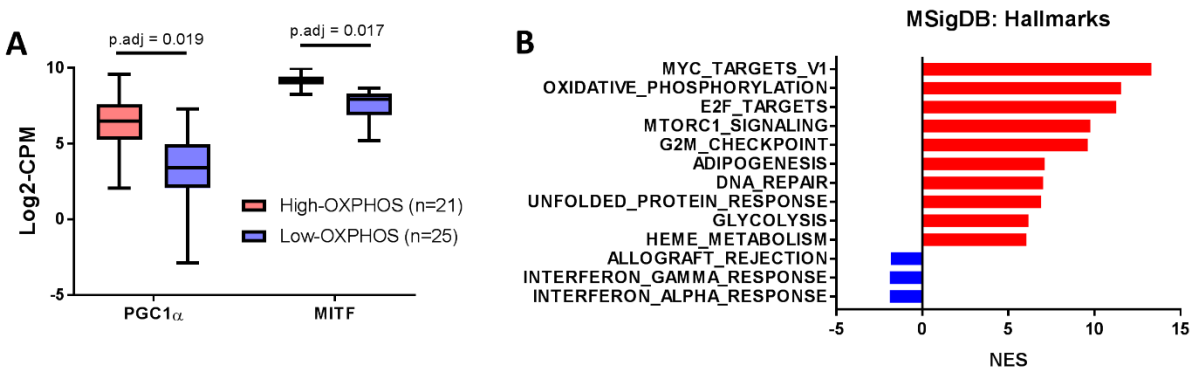

Figure 28: Transcriptomic analysis of High-OXPHOS and Low-OXPHOS melanoma brain metastases. (**A**) Gene expression analysis of PGC1α and MITF in High- and Low-OXPHOS MBMs identified via clustering analysis. Each plot is a simple box and whisker plot. Median values (lines) and interquartile range (whiskers) are indicated. Adjusted p values calculated via generalized linear model analysis are listed. (**B**) Cumulative GSEA-P enrichment plot demonstrating significant enrichment or depletion (FDR q-val < 0.0001) of MSigDB Hallmarks gene sets in High-OXPHOS vs. Low-OXPHOS MBMS identified via clustering methods. The 10 most up-regulated gene sets are shown in red. All down-regulated gene sets are shown in blue. The normalized enrichment score (NES) forms the x-axis.

To confirm the association between mTORC1 signaling and OXPHOS status in MBMs, we stained our High- and Low-OXPHOS MBMs for P-PRAS40 (marker of PI3K-AKT pathway activity), PTEN (complete loss promotes PI3K-AKT pathway hyperactivity), and P-S6 (marker of mTORC1 pathway activity). No significant difference in P-PRAS40 staining was observed between High- and Low-OXPHOS MBMs (p=0.4339) (**Figure 29A**). Additionally, prevalence of complete PTEN loss did not differ significantly between High- and Low-OXPHOS MBMs (p=0.6844) (**Figure 29B**). However, P-S6 stained significantly higher (p=0.0027) in High- vs. Low-OXPHOS MBMs (**Figure 29C**). Together, these findings implicate mTORC1 signaling in High-

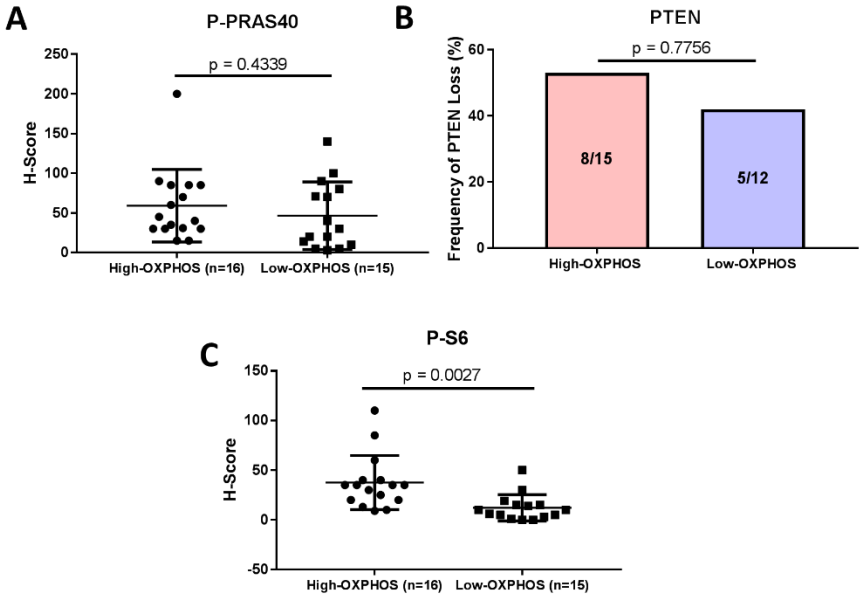

Figure 29: Molecular associations of High-OXPHOS and Low-OXPHOS melanoma brain metastases. (**A**) Comparison of P-PRAS40 H-scores between High-OXPHOS MBMs and Low-OXPHOS MBMs identified via hierarchical clustering with available tissue for IHC analysis. Lines represent mean ± S.D., and each dot represents a single sample. Significance determined via two-sided Student's *t*-test. (**B**) Comparison of the prevalence of complete PTEN loss between High-OXPHOS and Low-OXPHOS MBMs identified via hierarchical clustering with available tissue for IHC analysis**.** Y-axis represents the frequency (%) of MBMs with complete PTEN loss out of the MBMs from each OXPHOS category. Significance determined via two-sided Fisher's exact test. (**C**) Comparison of P-S6 H-scores between High-OXPHOS MBMs and Low-OXPHOS MBMs identified via hierarchical clustering with available tissue for IHC analysis. Lines represent mean ± S.D., and each dot represents a single sample. Significance determined via two-sided Student's *t*-test.

OXPHOS MBMs and that mTORC1 activation in these lesions occurs independently of input from the PI3K-AKT pathway.

We fully compared KEGG metabolism gene set enrichment between the High-and Low-OXPHOS MBMs. As expected, the KEGG OXPHOS gene set was the most enriched pathway in the High-OXPHOS MBMs (FDR q-val<0.0001) (**Figure 30A**). Interestingly, the next most enriched pathways included purine synthesis, pyrimidine synthesis, and aminoacyl tRNA biosynthesis (**Figure 30A**). Enrichment of these nucleic acid synthesis and protein synthesis pathways suggests increased growth potential in High-OXPHOS MBMs. Furthermore, all of these pathways require glutamine, which represents a potential therapeutic target.

These clinical MBMs were uniformly FFPE samples and could not be reliably subjected to direct metabolite analysis. To overcome this issue and further define the metabolic dependencies of High- and Low-OXPHOS MBMs, we performed a focused liquid chromatography-mass spectrometry (LC-MS) analysis of Low-OXPHOS A375 and High-OXPHOS A375-R1 (3) intracranial xenografts to identify differentially expressed glycolytic, tricarboxylic acid (TCA) cycle, and amino acid metabolites (FDR q-val<0.25). As expected, A375-R1 xenografts were characterized by significantly lower concentrations of the glycolytic metabolites pyruvate and 3-phosphoglycerate/2-phosphoglycerate and higher concentrations of the TCA cycle metabolites malate and fumarate (**Figure 30B**). Interestingly, we also observed evidence of increased glutaminolysis. Specifically, A375-R1 xenografts featured significantly increased concentrations of glutamic acid, threonine, and asparagine (**Figure 30B**). The presence of these metabolites suggests that catabolized glutamine was feeding the TCA cycle, which in turn produced the amino acids threonine and asparagine from oxaloacetate/aspartate.

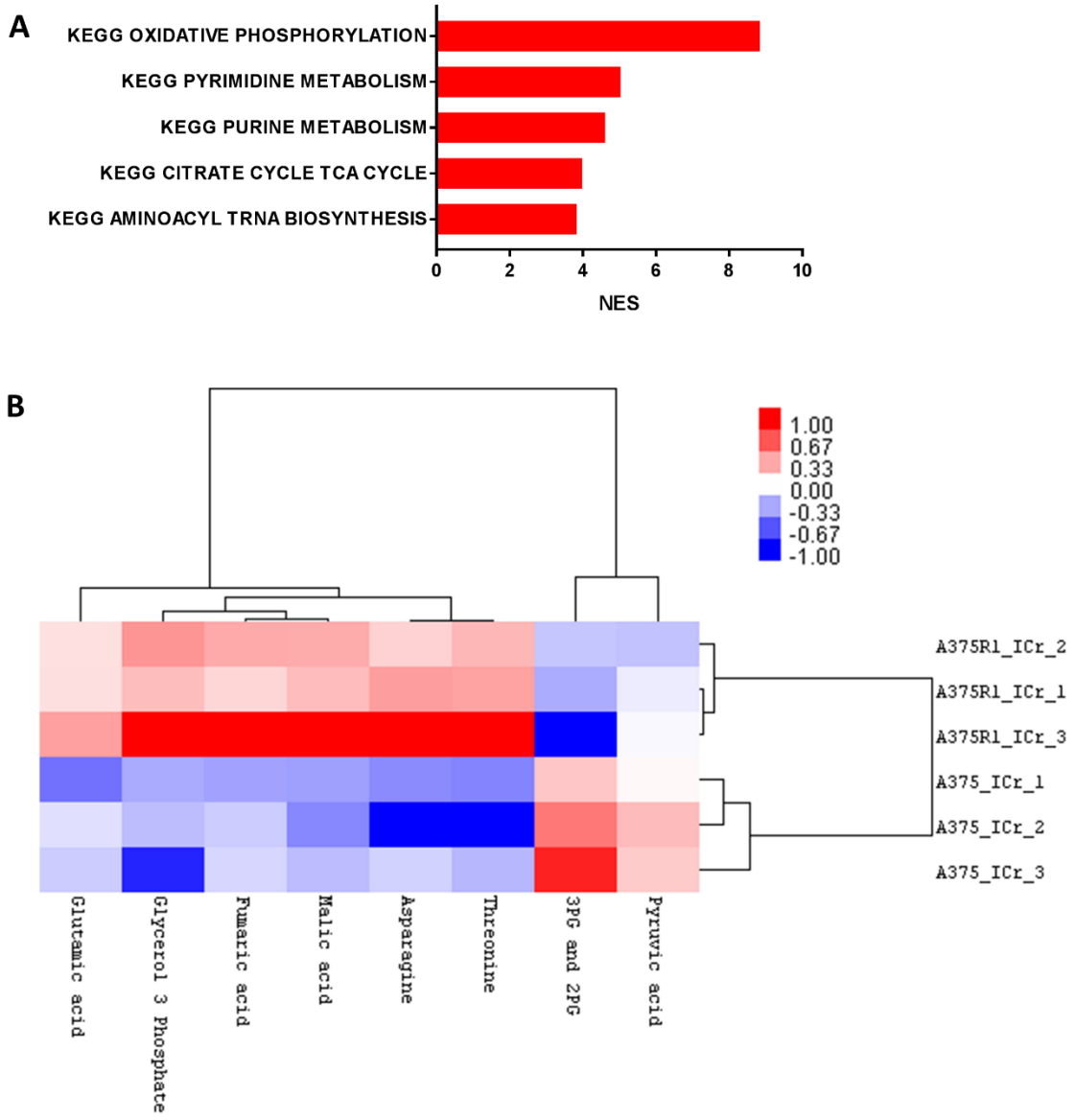

Figure 30: Metabolic associations of oxidative phosphorylation in melanoma brain metastases. (**A**) Cumulative GSEA-P enrichment plot demonstrating significant enrichment or depletion (FDR q-val < 0.0001) of KEGG metabolism gene sets in High-OXPHOS vs. Low-OXPHOS MBMS identified via clustering methods. Enriched gene sets are shown in red. No depleted gene sets met the criteria for significance. The normalized enrichment score (NES) forms the x-axis. (**B**) A focused liquid chromatography mass spectrometry (LC-MS) analysis of Low-OXPHOS A375 and High-OXPHOS A375-R1 intracranial xenografts identified differentially expressed tricarboxylic acid and amino acid metabolites (FDR q-val<0.25). Data are presented as a heatmap of median-centered log2-tranformed concentrations of these metabolites..

5.2.1c - Immunological Associations of Oxidative Phosphorylation in Melanoma Brain Metastases

We assessed if High- and Low-OXPHOS MBMs differ in immune infiltrates. Together, the ESTIMATE and MCP-Counter R packages identified significant decreases in the ImmuneScore ($p<0.0001$), T cells ($p<0.0001$), $CD8^+$ T cells ($p<0.001$), cytotoxic lymphocytes ($p<0.0001$), monocytic lineage cells ($p<0.0001$), and myeloid dendritic cells ($p<0.01$) in the High-OXPHOS MBMs (**Figure 31A-B**). Furthermore, High-OXPHOS MBMs were characterized by significantly lower expression ($p=0.0263$) of a 6-gene IFNγ mRNA signature previously demonstrated to correlate with response to anti-PD1 immunotherapy (283) (**Figure 31C**). Together, these findings indicate that OXPHOS associates with significant immunosuppression in MBMs.

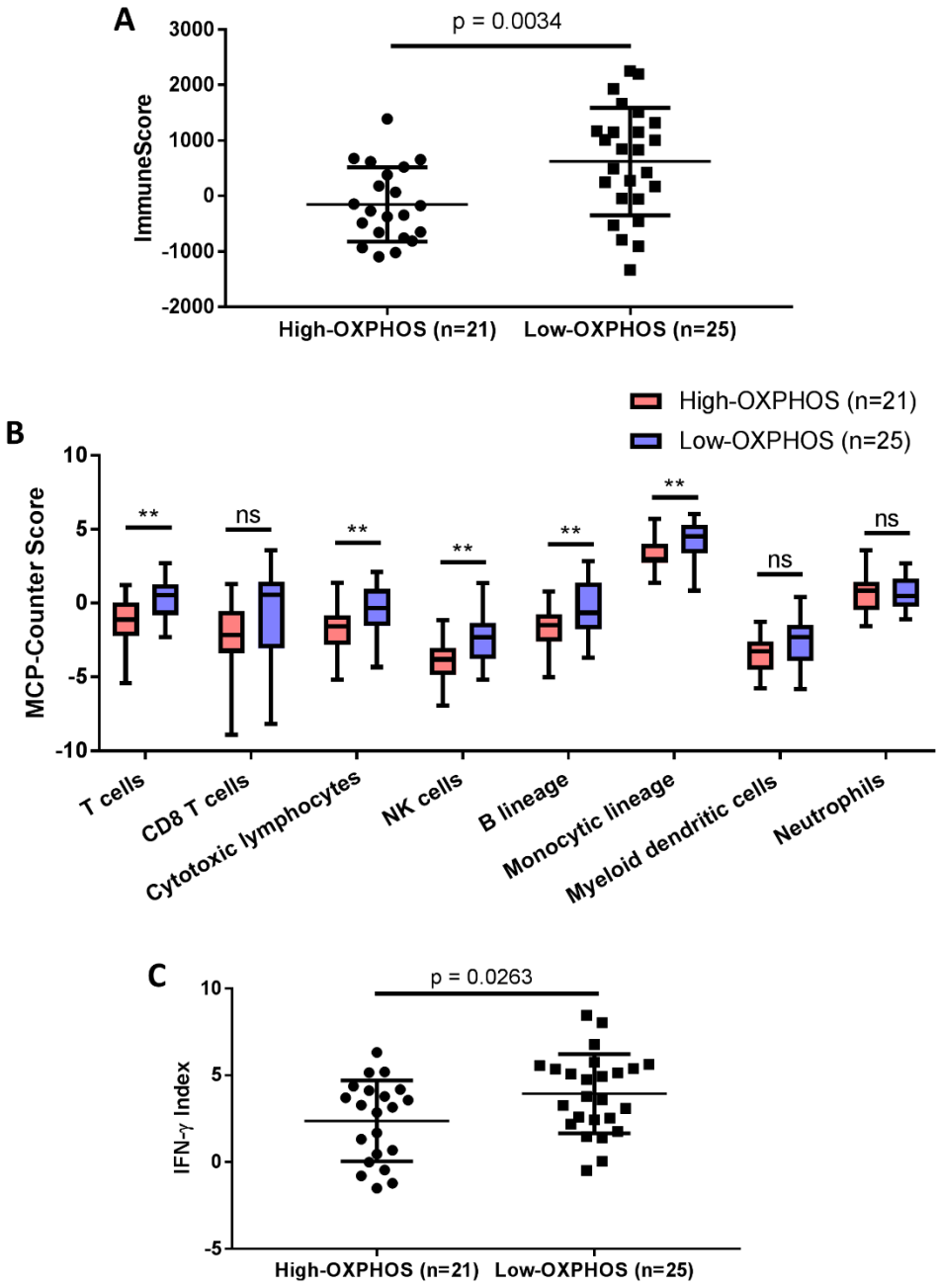

Figure 31: Oxidative phosphorylation associates with immunosuppression in melanoma brain metastases. (**A**) ESTIMATE ImmuneScore analysis of High-OXPHOS (n=21) and Low-OXPHOS (n=25) MBMs. Lines represent mean ± S.D., and each dot represents a single sample. Significance determined via two-sided Student's *t*-test. (**B**) MCP-Counter analysis of High-OXPHOS (n=21) and Low-OXPHOS (n=25) MBMs. Each plot is a simple box and whisker plot. Median values (lines) and interquartile range (whiskers) are indicated. $^{**}P < 0.01$, ns: not significant ($P > 0.05$) via two-sided Student's *t*-test. (**C**) Comparison of a 6-gene IFN-γ mRNA signature previously demonstrated to correlate with response to anti-PD1 immunotherapy. Lines represent mean ± S.D., and each dot represents a single sample. Significance determined via two-sided Student's *t*-test.

5.2.1d - Clinical Correlates of Oxidative Phosphorylation in Melanoma Brain Metastases

We accessed patient data archives maintained by the MD Anderson Cancer Center MelCore to identify clinical factors that associate with OXPHOS in MBMs. Patient age ($p=0.0661$), gender ($p=0.1328$), body mass index (BMI) ($p=0.2347$), serum lactate dehydrogenase (LDH) status ($p=0.1328$), and history of prior radiation therapy (XRT) ($p=0.2122$) do not significantly associate with MBM OXPHOS status (**Figure 32A-F**).

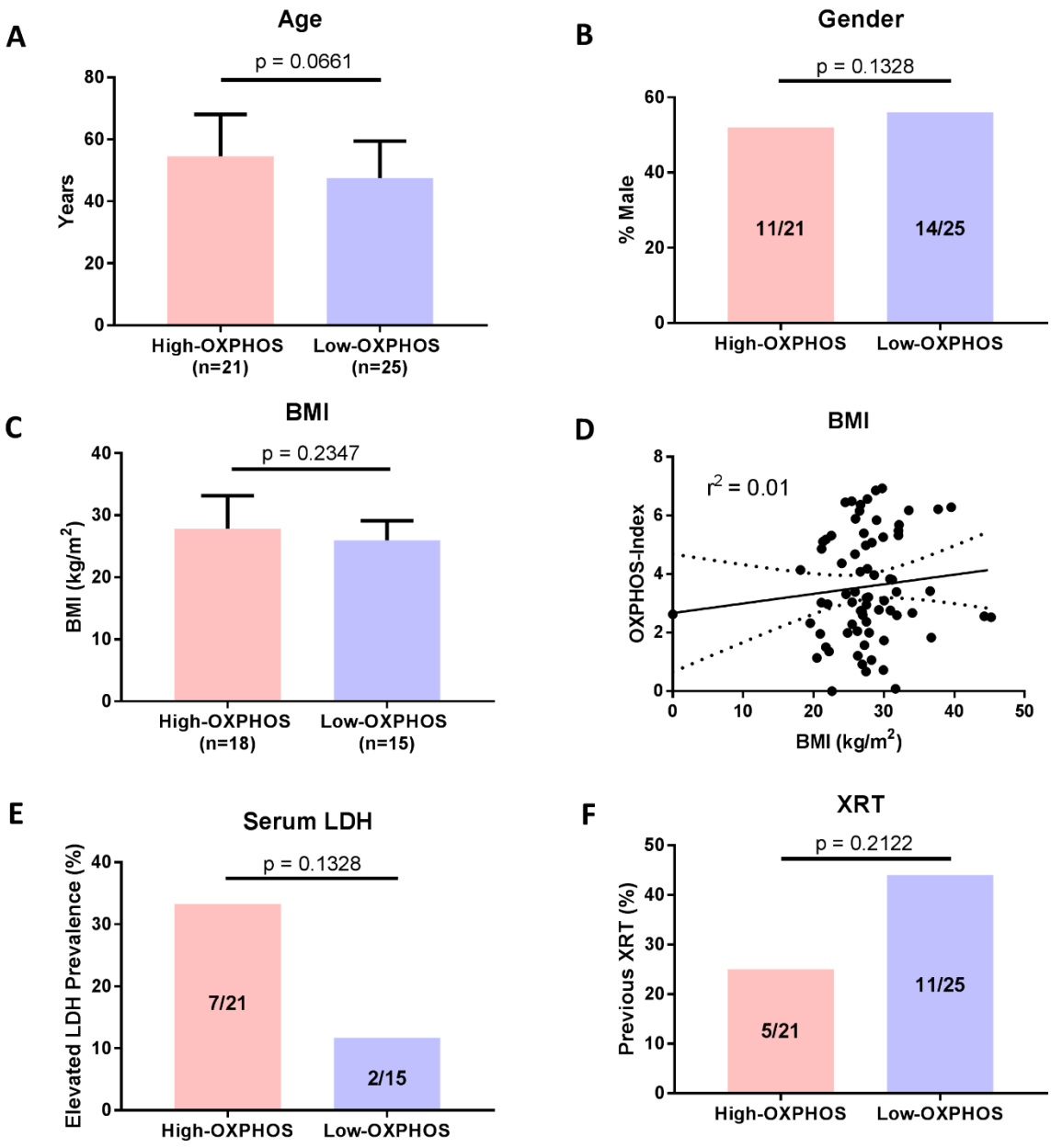

Figure 32: Clinical correlates of oxidative phosphorylation in melanoma brain metastases. (**A**) Comparison of the mean age of patients with High- and Low-OXPHOS MBMs. (**B**) Comparison of gender prevalence of patients with High- and Low-OXPHOS MBMs.. Y-axis indicates the % of High- and Low-OXPHOS MBMs that were resected from male patients. The total number of samples from each category is listed inside the bar graphs. (**C**) Comparison of mean body mass index (BMI) of patients with High- and Low-OXPHOS MBMs. (**D**) Correlation analysis between BMI and OP-Index in MBMs. Correlation coefficient is listed on the graph. (**E**) Comparison of the prevalence of elevated serum lactate dehydrogenase (LDH) between patients with High- and Low-OXPHOS MBMs. Y-axis indicates the % of High- and Low-OXPHOS MBMs that were resected from patients with elevated serum LDH recorded within 30 days of surgical accession. The total number of samples from each category is listed inside the bar graphs. (**F**) Comparison of prevalence of previous radiation therapy (XRT) between patients with High-and Low-OXPHOS MBMs.. Y-axis indicates the % of High- and Low-OXPHOS MBMs that were resected from patients previously treated with XRT. The total number of samples from each category is listed inside the bar graphs.

5.2.2 - Overcoming Oxidative Phosphorylation in the Treatment of Melanoma Brain Metastases

5.2.2a - Efficacy and Pharmacodynamic (PD) Effects of IACS-010759 in High-OXPHOS, MAPKi-Resistant Intracranial Human Melanoma Xenografts

We first evaluated the feasibility of indirectly targeting OXPHOS via mTORC1/2 inhibition in intracranial (ICr) xenografts of a human melanoma cell line with acquired (A375-R1) resistance to BRAF and MEK inhibitors (3). Mice were randomized to treatment with AZD2014 (20 mg/kg p.o. once daily) – an mTORC1/2 inhibitor previously shown to synergize with MEKi in subcutaneous High-OXPHOS melanoma xenografts (3) – or vehicle control. However, treatment for 7 days did not decrease P-S6 staining ($p=0.8623$), indicating that the drug failed to sustainably inhibit its target (**Figure 33A-B**). Thus, we focused our efforts on testing IACS-010759 (5 mg/kg p.o. once daily) – a novel mitochondrial complex I inhibitor currently in phase I clinical trials (NCT02882321 and NCT03291938) – against its 0.5% methylcellulose vehicle control in mice with ICr A375-R1 tumors (284). Treatment with IACS-010759 for 24 hours and 7 days eliminated pimonidazole staining, confirming sustained intracranial target inhibition (**Figure 33C-D**) (284). OXPHOS inhibition should silence mTORC1 pathway signaling by depriving cells of ATP and subsequently inducing increased phosphorylation and activation of AMPK (178). Consistent with this mechanism, IACS-010759 induced a significant decrease ($p=0.011$) in P-S6 staining after 7 days of treatment and an observable though insignificant decrease in P-S6 staining after only 24 hours of treatment (**Figure 33E**). Finally, IACS-010759 caused a significant increase in cleaved caspase-3 staining after 7 days of

treatment (p=0.0138), indicating that OXPHOS inhibition induced apoptosis in the intracranial A375-R1 tumors (**Figure 33F**). Consistent with these PD studies, IACS-010759 (5 mg/kg p.o. once daily) significantly decreased mean bioluminescence imaging (BLI) signal after 14 days of treatment and ultimately improved survival of mice bearing ICr A375-R1 tumors (HR 0.197, 95% CI 0.075 – 0.519, p=0.001) (**Figure 34A-B**).

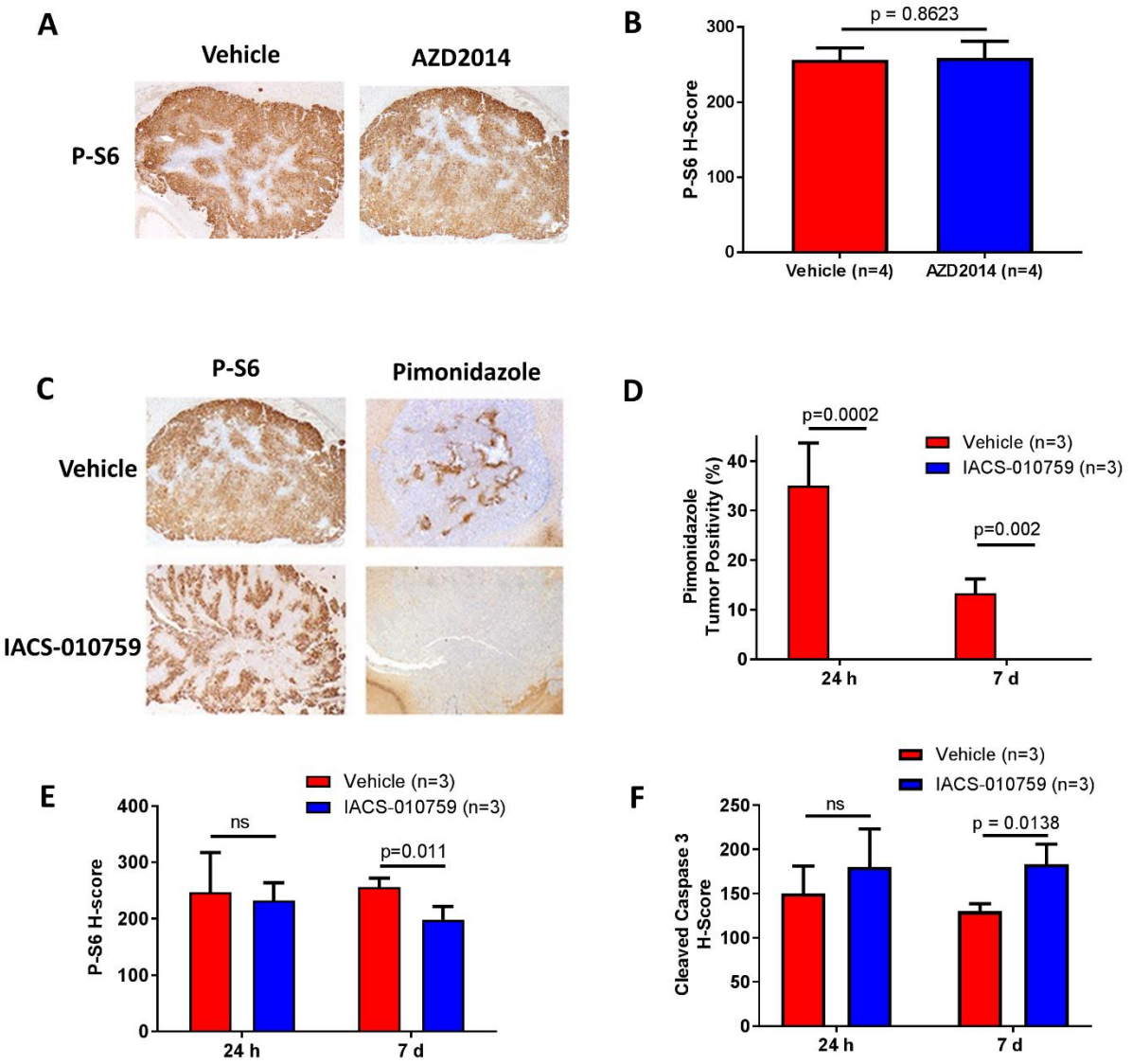

Figure 33: Pharmacodynamics of OXPHOS inhibitors in High-OXPHOS, MAPKi-resistant intracranial melanoma xenografts. (**A**) Representative P-S6 staining analysis results of intracranial (ICr) A375-R1 xenografts treated for 1 week with AZD2014 (20 mg/kg p.o. once daily) or vehicle. (**B**) P-S6 staining analysis of ICr A375-R1 xenografts treated for 1 week with either AZD2014 (20 mg/kg p.o. once daily) or vehicle. Y-axis indicates the H-score of tumor positivity and intensity. Average values and S.D. of three biological replicates per condition are displayed. Significance determined via two-sided Student's *t*-test. (**C**) Representative P-S6 and pimonidazole staining analysis results of ICr A375-R1 xenografts treated for 1 week with IACS-010759 (5 mg/kg p.o. once daily) or vehicle. (**D**) Pimonidazole staining analysis of ICr A375-R1 xenografts treated with either IACS-010759 (5 mg/kg p.o. once daily) or vehicle. Y-axis indicates percentage of total tumor positivity. Average values and S.D. of three biological replicates per condition are displayed. Significance determined via two-sided Student's *t*-test. (**E**) P-S6 staining analysis of ICr A375-R1 xenografts treated with either IACS-010759 (5 mg/kg p.o. once daily) or vehicle. Y-axis indicates the H-score of tumor positivity and intensity. Average values and S.D. of three biological replicates per condition are displayed. Significance determined via two-sided Student's *t*-test. (**F**) Cleaved caspase 3 staining analysis of ICr A375-R1 xenografts treated with either IACS-010759 (5 mg/kg p.o. once daily) or vehicle. Y-axis indicates the H-score of tumor positivity and intensity. Average values and S.D. of three biological replicates per condition are displayed. Significance determined via two-sided Student's *t*-test.

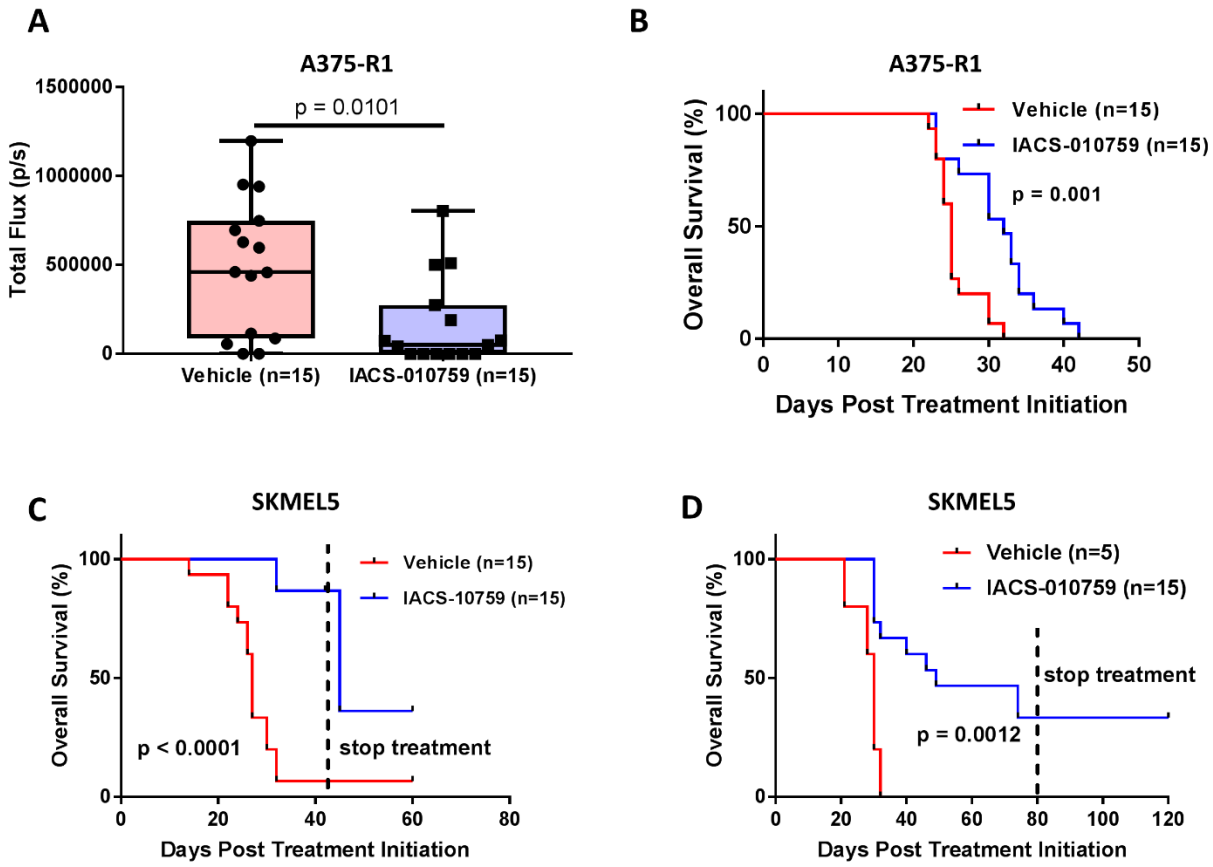

Figure 34: IACS-010759 monotherapy extends survival of mice bearing High-OXPHOS, MAPKi-resistant intracranial melanoma xenografts. (**A**) Bioluminescence imaging (BLI) of A375-R1 tumor-bearing mice indicates significantly lower (p=0.0101) total flux in IACS-010759-treated mice 14 days following treatment initiation. Significance determined via two-sided Student's *t*-test. (**B**) Kaplan-Meier overall survival (OS) analysis of mice bearing intracranial (ICr) A375-R1 xenografts and treated with either IACS-010759 (5 mg/kg p.o. once daily) or vehicle. Significance determined via log-rank test. (**C**) Kaplan-Meier OS analysis of mice bearing ICr SKMEL5 xenografts and treated with either IACS-010759 (5 mg/kg p.o. once daily) or vehicle. Treatments ended 42 days after randomization, and mice were tracked for an additional 18 days following cessation of treatments. Significance determined via log-rank test. (**D**) Kaplan-Meier OS analysis of mice bearing ICr SKMEL5 xenografts and treated with either IACS-010759 (5 mg/kg p.o. once daily) or vehicle. Treatments ended 80 days after randomization, and mice were tracked for an additional 40 days following cessation of treatments. Significance determined via log-rank test.

We confirmed these findings in a High-OXPHOS model characterized by *de novo* resistance to MAPKi (SKMEL5). Single-agent IACS-010759 (5 mg/kg p.o. once daily) significantly improved survival of mice with ICr xenografts of SKMEL5 cells (HR 0.072, 95% CI 0.024-0.214, p<0.0001) (**Figure 34C**). We stopped treatment after 42 days but continued to monitor mice for an additional 18 days. While the majority of IACS-010759-treated mice died immediately after cessation of treatment, 5 mice survived until the end of the 18-day monitoring period without treatment (**Figure 34C**). This suggests that IACS-010759 either cured these mice or ablated the tumor sufficiently to allow the mice to survive for a period of time without treatment. To validate this finding, we treated mice bearing ICr SKMEL5 tumors with IACS-010759 (5 mg/kg p.o. once daily) or vehicle control for a total of 80 days. Again, we observed significant improvement in survival in the IACS-010759-treated mice (HR 0.044, 95% CI 0.006-0.291, p=0.0012) (**Figure 34D**). Further, 5/15 IACS-010759-treated mice survived long-term (40 days) following cessation of treatment, confirming that the drug has a curative effect in approximately 33% of mice bearing ICr SKMEL5 tumors (**Figure 34D**).

5.2.2b - MAPKi Does Not Improve the Efficacy of IACS-010759 in High-OXPHOS, MAPKi-Resistant Intracranial Human Melanoma Xenografts

Previously, we and others have demonstrated that OXPHOS mediates resistance to MAPK pathway inhibitors in non-CNS melanomas and cell lines, and that inhibiting factors that promote this metabolic pathway sensitizes cell lines to MAPK pathway inhibitors (3, 26). Thus, we evaluated whether or not direct OXPHOS inhibition sensitizes A375-R1 and SKMEL5 intracranial xenografts to BRAF inhibition (3). In collaboration

with the Center for Co-Clinical Trials (CCCT) at MD Anderson, we established that IACS-010759 could be tolerated at doses of 5 mg/kg p.o. once daily in combination with dabrafenib at its optimal dose of 30 mg/kg p.o. once daily. We then evaluated the feasibility of targeting the MAPK pathway in ICr A375-R1 xenografts. Mice were randomized to treatment with dabrafenib (30 mg/kg p.o. once daily) or vehicle control for 72 hours. Dabrafenib ablated P-ERK staining (**Figure 35A**), indicating intracranial target inhibition. Mice with ICr xenografts of A375-R1 and SKMEL5 cells were then treated for up to 60 days with vehicle, dabrafenib, IACS-010759, or the combination of dabrafenib + IACS-010759. Both models demonstrated *in vivo* resistance to dabrafenib (**Figure 35B-C**). As expected, single-agent IACS-010759 significantly improved the survival of mice in both models (**Figure 35B-C**). However, combined treatment with dabrafenib did not increase the efficacy of IACS-010759 in either model (**Figure 35B-C**).

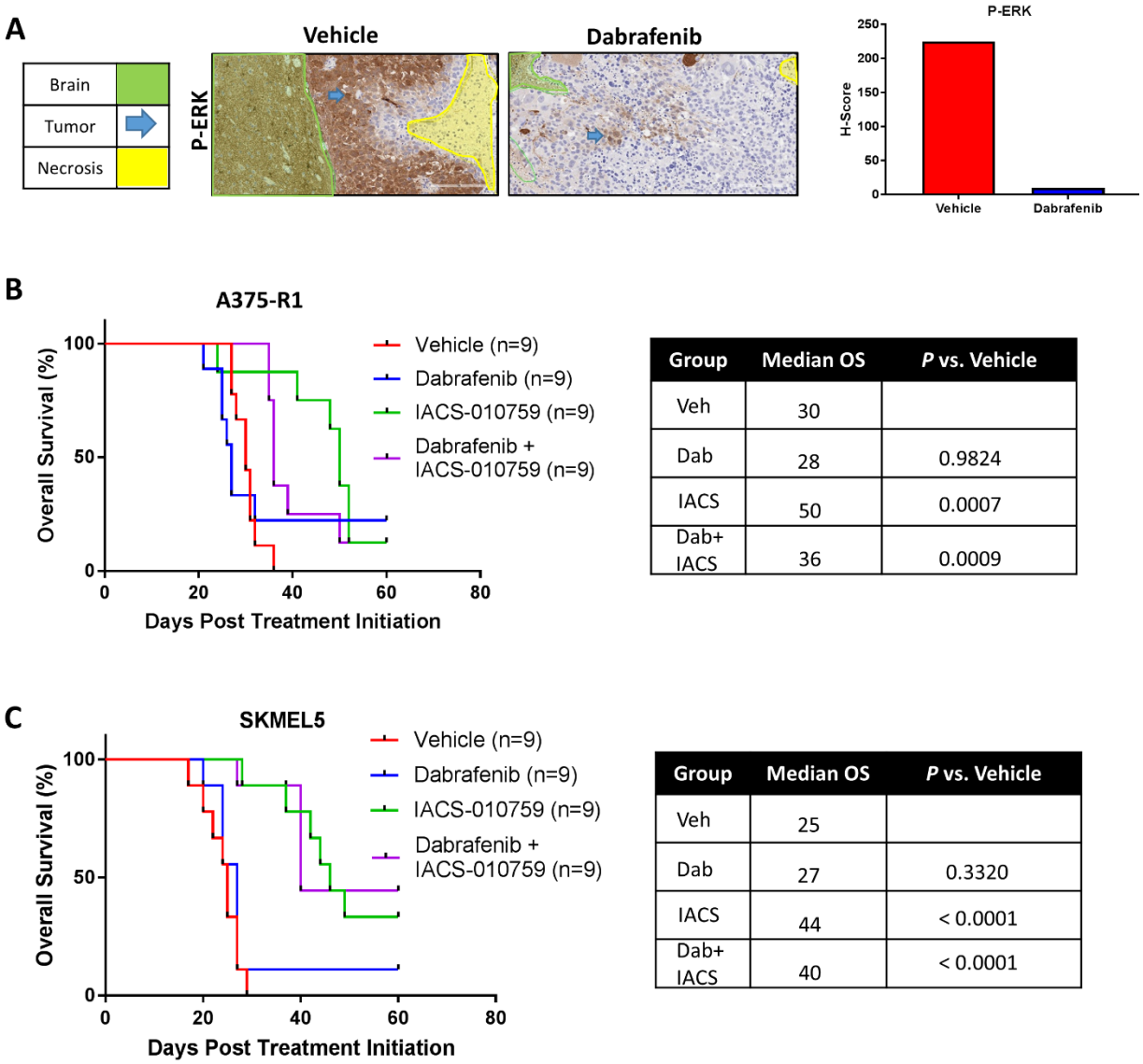

Group	Median OS	*P* vs. Vehicle
Veh	30	
Dab	28	0.9824
IACS	50	0.0007
Dab+ IACS	36	0.0009

Group	Median OS	*P* vs. Vehicle
Veh	25	
Dab	27	0.3320
IACS	44	< 0.0001
Dab+ IACS	40	< 0.0001

Figure 35: MAPKi did not improve the efficacy of IACS-010759 in the treatment of High-OXPHOS, MAPKi-resistant intracranial melanoma xenografts. (**A**) P-ERK staining of A375-R1 ICr xenografts treated with dabrafenib (30 mg/kg p.o. once daily) or vehicle for 72 hours. Regions of brain, tumor, and necrosis are delineated. Quantification of P-ERK staining was performed, and an H-score was calculated for vehicle- and dabrafenib-treated tissue. (**B**) Kaplan-Meier overall survival (OS) analysis of mice bearing ICr A375-R1 xenografts and treated with vehicle, dabrafenib (30 mg/kg p.o. once daily), IACS-010759 (5 mg/kg p.o. once daily), or dabrafenib (30 mg/kg p.o. once daily) + IACS-010759 (5 mg/kg p.o. once daily). Significance determined via log-rank test. (**C**) Kaplan-Meier OS analysis of mice bearing ICr SKMEL5 xenografts and treated with vehicle, dabrafenib (30 mg/kg p.o. once daily), IACS-010759 (5 mg/kg p.o. once daily), or dabrafenib (30 mg/kg p.o. once daily) + IACS-010759 (5 mg/kg p.o. once daily). Significance determined via log-rank test.

5.2.2c - The Combination of BRAFi + IACS-010759 Effectively Treats Intracranial Low-OXPHOS Human Melanoma Xenografts

Notably, previous studies have demonstrated that A375 subcutaneous xenografts respond to the BRAFi dabrafenib given orally at doses as low as 10 mg/kg once daily (285). In contrast, ICr xenografts of luciferase-tagged A375 cells demonstrated resistance to single-agent dabrafenib given at 30 mg/kg p.o. once daily (**Figure 36A**). Seahorse Bioanalyzer analysis of cell lines derived from mice progressing on dabrafenib and vehicle identified significantly greater basal and maximum oxygen consumption rates (OCRs) in tumors following treatment with dabrafenib vs. vehicle (**Figure 36B-C**). To determine if OXPHOS inhibition could overcome dabrafenib resistance in ICr A375 xenografts, we implanted luciferase-tagged A375 cells in the brains of CD-1 nude mice. Tumor-bearing mice did not respond to single-agent dabrafenib (30 mg/kg p.o. once daily) or IACS-010759 (5 mg/kg p.o. once daily) (**Figure 36D**). However, the combination of IACS-010759 and dabrafenib significantly improved survival of mice vs. vehicle controls ($p=0.0126$) (**Figure 36D**).

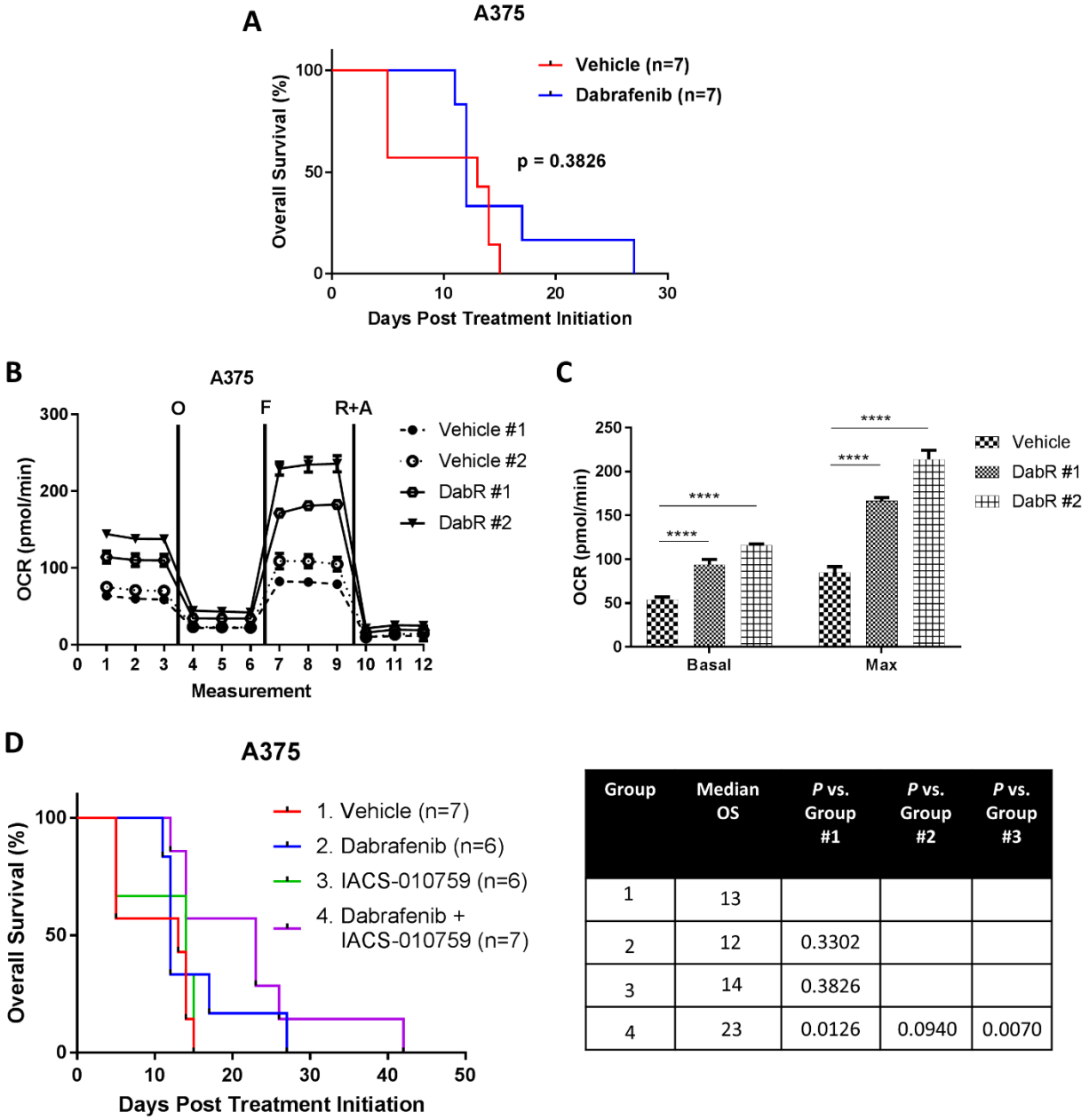

Group	Median OS	*P* vs. Group #1	*P* vs. Group #2	*P* vs. Group #3
1	13			
2	12	0.3302		
3	14	0.3826		
4	23	0.0126	0.0940	0.0070

Figure 36: The combination of IACS-010759 and dabrafenib improves survival in mice bearing intracranial melanoma xenografts with subcutaneous sensitivity to MAPKi. (**A**) Kaplan-Meier overall survival (OS) analysis of mice bearing intracranial (ICr) A375 xenografts and treated with vehicle or dabrafenib (30 mg/kg p.o. once daily). Significance determined via log-rank test. (**B**) Seahorse mitochondrial stress test was performed on cell lines derived from ICr A375 xenografts in mice progressing on vehicle (vehicle #1/2) or dabrafenib treatments (DabR #1/2). The figure shows basal, oligomycin-inhibited ("O"), FCCP-activated ("F") and Antimycin/Rotenone inhibited ("A&R") oxygen consumption rate (OCR) levels. (**C**) Comparison of basal and maximum OCR values for cells analyzed in (**B**). The two vehicle samples have been pooled and averaged. ****$P<0.0001$ by two-sided Student's *t*-test. (**D**) Kaplan-Meier OS analysis of mice bearing ICr A375 xenografts and treated with vehicle, dabrafenib (30 mg/kg p.o. once daily), IACS-010759 (5 mg/kg p.o. once daily), or dabrafenib (30 mg/kg p.o. once daily) + IACS-010759 (5 mg/kg p.o. once daily). Significance determined via log-rank test.

5.2.2d - OXPHOS Inhibition Improves Response of Intracranial B16-F10 Melanomas to Anti-PD1 Immunotherapy

Recently, investigators have implicated OXPHOS in mediating resistance to anti-PD1 immunotherapy in melanomas (173). Interestingly, low-dose treatment with metformin inhibits OXPHOS exclusively in tumor cells and improves response to anti-PD1 in subcutaneous xenografts of the High-OXPHOS B16-F10 melanoma cell line (173).

Our molecular profiling studies identified significant immunosuppression in High-OXPHOS MBMs and determined that these lesions were characterized by a gene signature predictive of anti-PD1 treatment failure (**Figure 31C**). To determine if OXPHOS inhibition could improve immunosuppression in High-OXPHOS MBMs, we implanted luciferase-tagged B16-F10 melanoma cells intracranially in C57BL/6 mice. Mice with 10% weight loss were randomized to receive 3 treatments of metformin at a dose previously shown to exclusively target tumor cells and promote immune cell function (50 mg/kg i.p. every other day) or PBS (10 ul/g body weight i.p. every other day) for 96 hours (173). RNA isolated from the tumors was subjected to qRT-PCR analysis of 2 different panels of genes: 1) a 5-gene signature indicative of activated $CD8^+$ cytotoxic T cells and 2) 5 genes from the aforementioned 6-gene IFNγ mRNA signature known to correlate with response to anti-PD1 (HLA-DRA from the original profile is only found in humans and was therefore excluded from the panel) (283, 286). qRT-PCR analysis of the tumors demonstrated significantly increased expression ($p<0.05$ – $p<0.0001$) of all genes in the metformin-treated tumors, indicating that metformin treatment profoundly altered the immune profile of the tumors (**Figure 37A-B**).

To determine if the immunological effects of metformin would translate to improved anti-PD1 response in High-OXPHOS MBMs, we implanted luciferase-tagged B16-F10 melanoma cells intracranially in C57BL/6 mice. After 5 days, tumor uptake was confirmed and mice were randomized into 4 treatment arms: isotype control (200 ug i.p. 3x/week) + PBS (10 ul/g body weight i.p. every other day), anti-PD1 (200 ug i.p. 3x/week) + PBS (10 ul/g body weight i.p. every other day), isotype control (200 ug i.p. 3x/week) + metformin (50 mg/kg i.p. every other day), and anti-PD1 (200 ug i.p. 3x/week) + metformin (50 mg/kg i.p. every other day). As expected, low-dose metformin demonstrated no single-agent efficacy compared to vehicle control mice (p=0.4533) (**Figure 37C**). Anti-PD1 monotherapy failed to improve survival compared to vehicle control mice (p=0.4361) (**Figure 37C**). Interestingly, only the mice treated with both metformin and anti-PD1 experienced a significant improvement in survival compared to vehicle control mice (p=0.013) (**Figure 37C**). Further, the combination regimen significantly improved survival vs. metformin monotherapy (p=0.0262). While the combination failed to statistically increase survival vs. anti-PD1 monotherapy (p=0.1972), a clear trend was observed and median survival improved from 11 days to 18 days.

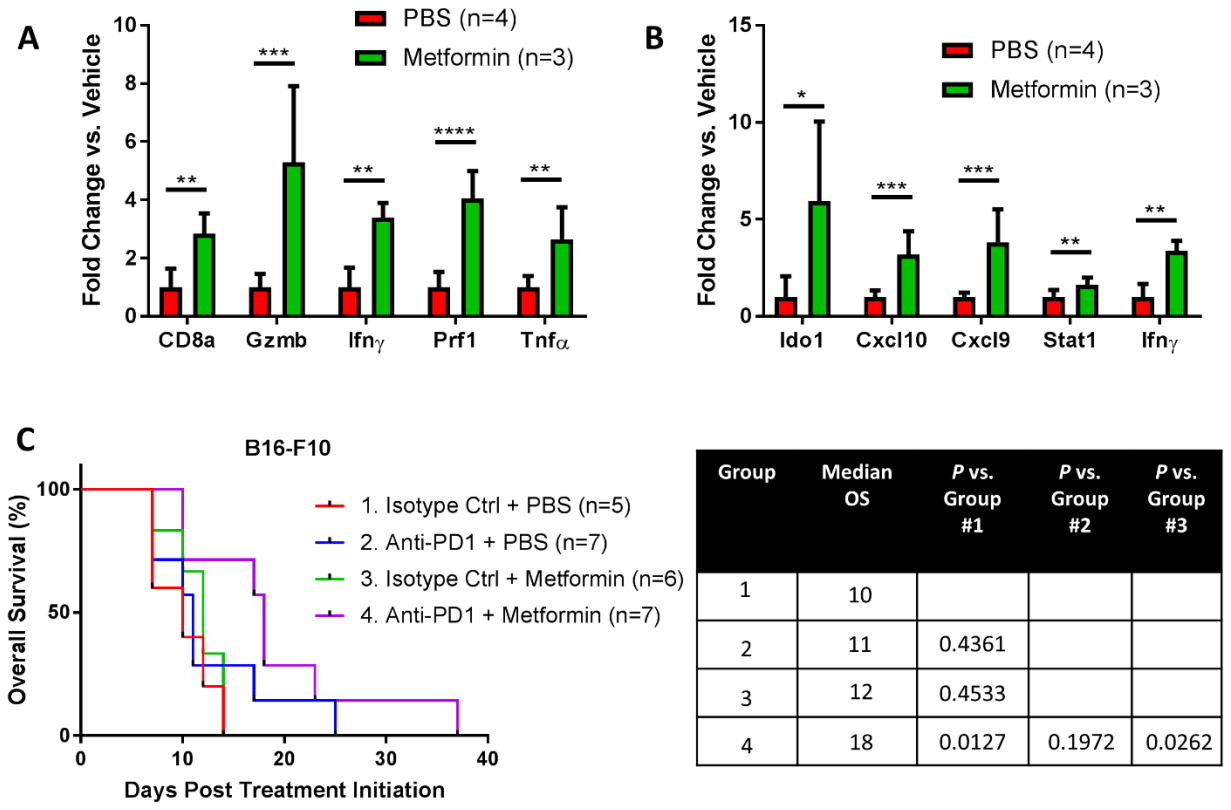

Group	Median OS	*P* vs. Group #1	*P* vs. Group #2	*P* vs. Group #3
1	10			
2	11	0.4361		
3	12	0.4533		
4	18	0.0127	0.1972	0.0262

Figure 37: Metformin improves the response of High-OXPHOS, syngeneic intracranial melanoma xenografts to anti-PD1 immunotherapy. B16-F10 cells were implanted in the brains of C57BL/6 mice and treated for 96 hours with low-dose metformin (50 mg/kg i.p. every other day) or PBS. qRT-PCR analysis was used to assess mRNA levels of (**A**) a panel of genes previously shown to predict the presence of activated $CD8^+$ T cells in melanomas and (**B**) a panel of IFNγ-related genes previously shown to predict response of melanomas to anti-PD1 immunotherapy. Values represent mean ± S.D. of indicated numbers of biological replicates analyzed as technical triplicates. $^{****}P < 0.0001$; $^{***}P < 0.001$; $^{**}P < 0.01$, $^{*}P < 0.05$ by two-sided Student's *t*-test. (**C**) Kaplan-Meier overall survival (OS) analysis of C57BL/6 mice bearing intracranial B16-F10 xenografts and treated with isotype control (200 ug i.p. 3x/week) + PBS (10 ul/g body weight i.p. every other day), anti-PD1 (200 ug i.p. 3x/week) + PBS (10 ul/g body weight i.p. every other day), isotype control (200 ug i.p. 3x/week) + metformin (50 mg/kg i.p. every other day), and anti-PD1 (200 ug i.p. 3x/week) + metformin (50 mg/kg i.p. every other day). Significance determined via log-rank test.

5.2.2e - The Glutaminase Inhibitor CB839 Improves Survival of Mice Bearing High-OXPHOS, MAPKi-Resistant Intracranial Human Melanoma Xenografts

Our IACS-010759 efficacy studies, gene expression studies, and LC-MS studies supported the rationale to investigate the efficacy of other metabolic inhibitors to treat High-OXPHOS, MAPKi-resistant MBMs. Specifically, our studies suggest that High-OXPHOS MBMs preferentially utilize pathways that require significant amounts of glutamine. Consistent with this finding, our direct metabolite analyses identified increased glutamine catabolism in High-OXPHOS brain xenografts. Based on these results, we evaluated the efficacy of CB839 – a small molecule glutaminase inhibitor currently being used in clinical trials (NCT02771626) – *in vitro* using Low-OXPHOS A375 and High-OXPHOS A375-R1 cells. As indicated in **Figure 38A-B**, CB839 significantly inhibited OCR in A375-R1 cells without affecting this metric in A375 cells. As expected, CB839 inhibited proliferation of A375-R1 cells significantly more than the parental cells (**Figure 38C**). The IC50 of A375-R1 cells (182 nM) was less than half of the IC50 of A375 cells (437 nM). Thus, we tested the response of mice bearing A375-R1 ICr xenografts to single-agent CB839. As anticipated, the drug significantly extended survival of these mice relative to vehicle controls (p=0.0292) (**Figure 38D**). To further confirm CB839 as a viable treatment for High-OXPHOS MBMs, we implanted luciferase-tagged High-OXPHOS, MAPKi-resistant MEL624 cells into the brains of mice. As observed in the A375-R1 model, CB839 significantly improved survival relative to vehicle controls in the MEL624 model (p=0.0266) (**Figure 38E**) and did so with minimal toxicity (**Figure 38F**).

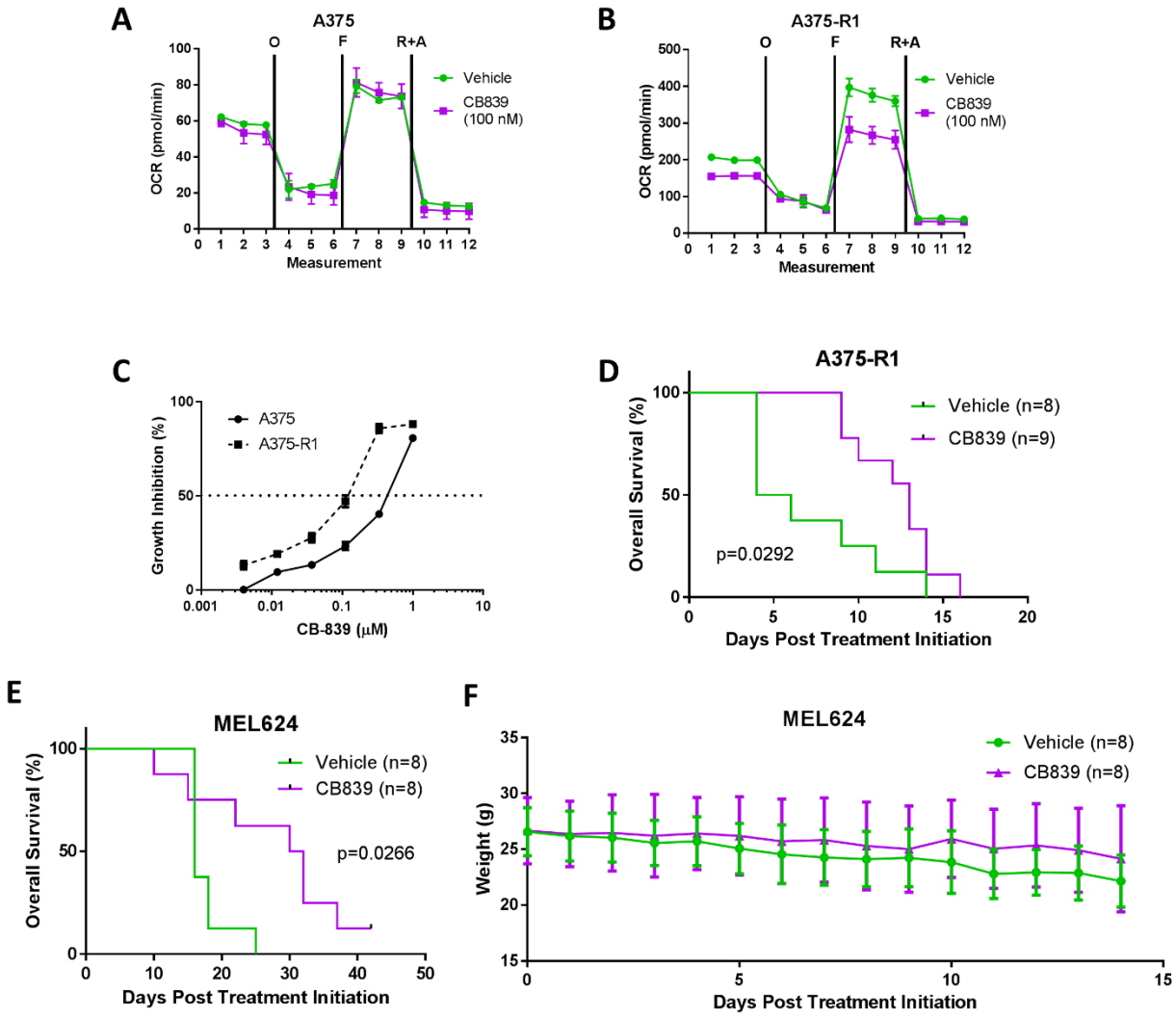

Figure 38: Glutaminase inhibition extends survival in mice bearing intracranial High-OXPHOS, MAPKi-resistant melanoma xenografts. (**A-B**) Seahorse mitochondrial stress test was performed on A375 and A375-R1 cells treated for 12 hours with vehicle or 100 nM of CB839. The figure shows basal, oligomycin-inhibited ("O"), FCCP-activated ("F") and Antimycin/Rotenone inhibited ("A&R") oxygen consumption rate (OCR) levels. (**C**) *In vitro* cell proliferation inhibition of A375 and A375-R1 cell lines treated with CB839 for 72 hours. Data is representative of triplicates and S.D. (**D**) Kaplan-Meier overall survival (OS) analysis of mice bearing intracranial (ICr) A375-R1 xenografts and treated with vehicle or CB839 (200 mg/kg p.o. twice daily). Significance determined via log-rank test. (**E**) Kaplan-Meier overall survival (OS) analysis of mice bearing ICr MEL624 xenografts and treated with vehicle or CB839 (200 mg/kg p.o. twice daily). Significance determined via log-rank test. (**F**) Assessment of body weight for mice bearing ICr MEL624 xenografts and treated with vehicle or CB839 (200 mg/kg p.o. twice daily) in (**E**). Values represent mean ± S.D.

5.3 - DISCUSSION

A metabolic phenotype defined by elevated oxidative phosphorylation (High-OXPHOS) has been identified in 30-50% of non-central nervous system (CNS) melanomas. This High-OXPHOS phenotype mediates *de novo* and acquired resistance to FDA-approved MAPK pathway inhibitors and anti-PD1 immunotherapy (7-9) (173). Thus, melanomas with increased OXPHOS represent a clinically significant subgroup of this disease. Prior to this study, we had observed significant heterogeneity of OXPHOS gene expression between our surgically resected MBMs, suggesting that these lesions could also be classified as "High-" or "Low-OXPHOS." In this study, we utilized our unique cohort of surgically resected tumors and preclinical models to improve our understanding of the High-OXPHOS phenotype in MBMs. **We tested the hypothesis that OXPHOS associates with distinct molecular, immunological, and metabolic features that, in addition to OXPHOS itself, could be exploited therapeutically in High-OXPHOS MBMs.**

Using bulk RNA-seq methods, we applied an OXPHOS transcriptomic signature (**Table 1**) to 88 surgically resected MBMs. Clustering by this signature identified MBMs with significant enrichment (High-OXPHOS) and depletion (Low-OXPHOS) of OXPHOS. Similar to non-CNS metastases, OXPHOS enrichment in MBMs correlated with poor clinical outcomes.

We observed significantly higher mTORC1 pathway activation in High-OXPHOS MBMs. However, OXPHOS did not associate with activation of the PI3K-AKT pathway. While mTORC1 can be activated independently of PI3K-AKT pathway input, all known mechanisms of mTORC1 activation require the small GTPase RAS homologue enriched in brain (RHEB) (287). PI3K-AKT pathway activation suppresses the tuberous sclerosis complex (TSC), which keeps RHEB in its active GTP-bound state and able to activate mTORC1 (287). Interestingly, the

MAPK pathway can also suppress TSC through p90 ribosomal S6 kinase (RSK), which promotes mTORC1 activation (288). The MAPK pathway is ubiquitously hyperactivated in cutaneous melanomas (70). Further, our previous studies demonstrated that OXPHOS status does not associate with *BRAF*/*NRAS* mutation status in cell lines or non-CNS metastases (3). Thus, differential input from the MAPK pathway is unlikely to explain our observations. Alternatively, exposure to amino acids can directly activate mTORC1 and is actually believed to be the most important input for mTORC1 activation (287). To date, the specific amino acids required to activate mTORC1 remain uncertain, though previous studies have implicated leucine, glutamine, and arginine (287). Thus, it is possible that the High-OXPHOS MBMs have better access to these amino acids compared to their Low-OXPHOS counterparts. Alternatively, increased P-AMPK signaling could suppress mTORC1 signaling in Low-OXPHOS MBMs without affecting P-PRAS40 staining (289).

Unfortunately, our attempts at directly targeting mTOR signaling failed due to AZD2014's inability to inhibit the pathway in High-OXPHOS MBMs, presumably due to poor penetration of the blood-brain barrier (BBB). Our future studies will focus on elucidating the mechanism underlying differential mTORC1 activation in High- and Low-OXPHOS MBMs. Further insights into how mTORC1 mediates OXPHOS heterogeneity in MBMs could elucidate additional pathways targetable via drugs known to pass the BBB. Additionally, we will continue to investigate the BBB penetrance of alternative mTOR inhibitors to identify a more suitable candidate for efficacy studies.

When our efforts to treat High-OXPHOS MBMs via the mTORC1/2 inhibitor failed, we proceeded to collaborate with the MD Anderson Institute for Applied Cancer Science (IACS), which recently developed and characterized a direct OXPHOS inhibitor (IACS-010759) able to exert antitumor effects in a variety of cancer cell types at tolerable doses (178). Our findings

demonstrate for the first time that single-agent OXPHOS inhibition with IACS-010759 can have beneficial effects in High-OXPHOS, MAPKi-resistant intracranial melanomas.

Previous studies have shown that *BRAF*-mutant extracranial melanoma metastases treated with BRAFi therapy can become addicted to OXPHOS and subsequently are highly sensitive to direct OXPHOSi. In addition, phenformin, which inhibits OXPHOS, delays the development of resistance to BRAFi treatment in human melanoma cell lines (26, 245). Thus, we reasoned that adding IACS-010759 to BRAFi therapy at the initiation of treatment of *BRAF*-mutant MBMs could increase the duration of tumor responses, which was the critical factor that limited the clinical benefit of treatment with dabrafenib and trametinib in the COMBI-MB study (171). Interestingly, we observed that the brain TME mediated resistance to dabrafenib treatment of intracranial A375 xenografts. Despite being given at doses known to inhibit tumor growth subcutaneously, single-agent dabrafenib failed to improve survival compared to vehicle controls. Our PD studies confirmed that dabrafenib suppressed P-ERK staining at the dose tested, which excludes the possibility that this observation occurred only because of dabrafenib's failure to achieve adequate on-target inhibition. Further, Seahorse Bioanalyzer analysis identified increased OCR (OXPHOS) in cell lines derived from ICr A375 xenografts progressing on dabrafenib, as compared to cell lines derived from ICr A375 xenografts progressing on vehicle. Excitingly, we showed that while ICr xenografts of A375 demonstrated resistance to single-agent dabrafenib and single-agent IACS-010759, the combination of these two treatments significantly improved survival compared to vehicle controls.

Previous studies have suggested that the combination of MAPKi and IACS-010759 could also yield synergistic effects in MBMs that have developed resistance to MAPKi therapies via increased dependence on OXPHOS. Specifically, combined targeting of the MAPK and mTOR pathways effectively treated MAPKi-resistant non-CNS melanomas dependent on OXPHOS (3).

mTORC1/2 inhibition triggered apoptosis by preventing these tumors from utilizing OXPHOS to meet their bioenergetic demands following MAPK pathway blockade (3). Interestingly, the addition of dabrafenib to IACS-010759 failed to improve survival of mice bearing intracranial A375-R1 and SKMEL5 xenografts compared to IACS-010759 monotherapy. While this observation was primarily due to the impressive efficacy of single-agent IACS-010759 in the treatment of these lesions, High-OXPHOS melanomas do not uniformly respond to single-agent IACS-010759 (290). A subset of High-OXPHOS melanoma cells resistant to IACS-010759 treatment respond to the combination of IACS-010759 and MAPKi, indicating a potential use for this combination in High-OXPHOS MBMs unresponsive to single-agent IACS-010759.

Our immunological analyses demonstrated that OXPHOS associates with features consistent with immunosuppression in MBMs. Additional studies are warranted to further characterize this apparent immunosuppressive factor in MBMs, but this finding is promising and clinically significant. Most importantly, High-OXPHOS MBMs were characterized by significantly lower expression of an IFN-γ gene signature known to predict response to anti-PD1 immunotherapy in non-CNS melanomas. These findings are consistent with previous studies that have shown that OXPHOS inhibitors can enhance response to anti-PD1 immunotherapy (291, 292), but to our knowledge this data is the first to implicate OXPHOS as a potential mediator of immunosuppression in MBMs. Notably, OXPHOS associated with decreased B cell infiltration, but not $CD8^+$ T cell density, in the MBMs. Numerous recent studies have highlighted the anti-tumor role of intratumoral B cells, and a potential link between baseline B cell infiltration and ipilimumab efficacy has been proposed (293-295). Recent data also implicate a possible important role for B cells in response to anti-PD1 (296) and thus our results support the rationale for investigating combinatorial approaches with these immunotherapies and OXPHOS inhibitors in MBM patients. As a first step in this effort, we demonstrated that low-dose metformin sensitized

intracranial High-OXPHOS B16-F10 melanoma xenografts to anti-PD1 treatment. Molecular studies demonstrated that metformin increased intratumoral expression of markers known to predict response to anti-PD1.

Our analysis of clinical and preclinical samples highlighted High-OXPHOS MBMs' dependence on glutamine metabolism. Profiling studies demonstrated increased activity of multiple glutamine-dependent metabolic pathways in these lesions. Direct metabolite analysis of High- and Low-OXPHOS intracranial xenografts confirmed increased glutamine metabolism in High-OXPHOS MBMs. Based on these results, we performed a pilot study to evaluate the safety and efficacy of CB839, a novel small molecule glutaminase inhibitor currently being used in clinical trials (NCT02771626), in mice with High-OXPHOS, MAPKi-resistant intracranial xenografts of A375-R1 and MEL624 cells. Excitingly, glutaminase inhibition significantly improved survival in both models.

This study is highly novel as it employed the largest available cohort of surgically resected MBMs with RNA-seq data and preclinical models to fully characterize the molecular, immunological, and metabolic associations of OXPHOS in MBMs. These analyses directly informed preclinical studies, which featured innovative strategies that overcame limitations in the treatment of High-OXPHOS MBMs. Further, this study extensively utilized novel metabolic inhibitors currently in clinical trials. Cumulatively, we verified our initial hypothesis and supported the rationale to improve our understanding of OXPHOS heterogeneity in MBMs.

CHAPTER 6: DISCUSSION

6.1 - SUMMARY / CONCLUSIONS

Melanoma is the cause of >80% of skin cancer-related deaths (1). Many of these deaths result from brain metastases, a devastating complication of melanoma that is diagnosed in up to 60% of patients with distant metastases (167). Surgery and radiation have historically been the predominant therapeutic modalities used to treat melanoma brain metastases (MBMs), but they have minimal impact on the long-term survival of patients (167). Targeted and immune therapies have activity for patients with MBMs but also significant shortcomings (154, 168-171). As patients with MBMs have a median survival of ~4 months, there is a critical unmet need to develop new, more effective therapeutic strategies for this disease. The development of such treatments will be facilitated by improving our understanding of the features, heterogeneity, and functional drivers of MBMs.

Prior to this dissertation research, I performed gene expression profiling which showed that OXPHOS was the most enriched metabolic pathway in MBMs compared to extracranial metastases (ECMs) from the same patients. Based on this preliminary data and previous studies, **the central hypothesis of this dissertation is that OXPHOS plays a critical role in the pathogenesis of MBMs.**

In this dissertation, I addressed the current gap in knowledge about the role of OXPHOS in MBM pathogenesis through the analysis of unique clinical specimens and functional testing of clinically relevant preclinical models. I showed that the experimental strategy of applying the Xenome pipeline to RNA-seq data from xenografts grown in distinct anatomical locations could characterize the gene expression profiles of melanoma cells in different metastatic sites by

discriminating signatures of cancer cells from stromal cells. This approach allowed me to demonstrate that the brain tumor microenvironment (TME) induces significant enrichment of OXPHOS gene set expression compared to subcutaneous (SQ) tissue. My analyses of brain and SQ xenografts via direct metabolite profiling and *in vivo* [U-^{13}C]-glucose tracing confirmed these findings. Interestingly, treating cutaneous variants of melanoma cells with brain-derived soluble factors significantly induced OXPHOS compared to untreated cells. RPPA analysis of brain and SQ xenografts demonstrated that the brain TME induced PI3K-AKT-mTOR signaling compared to the SQ tissue. Additionally, the brain TME upregulated mitochondrial biogenesis and downregulated production of glycolytic enzymes compared to the SQ tissue. I confirmed increased PI3K-AKT-mTOR signaling and OXPHOS enrichment in Tx-naïve MBMs vs. Tx-naïve, patient-matched ECMs. Importantly, I utilized multiple publicly available gene expression datasets to exclude the possibility that increased OXPHOS in MBMs results from increased efficiency of melanoma cells enriched in OXPHOS to form metastases at this site.

Next, I functionally validated OXPHOS as a mediator of MBM pathogenesis. Experiments in the RCAS-TVA model of spontaneous MBM and lung metastasis determined that pharmacological suppression of OXPHOS decreased the incidence of detectable MBMs without affecting the incidence of lung metastases or primary tumor growth. To clarify if OXPHOS promotes the formation of MBMs or the growth of established micrometastases, I used an imageable experimental model of MBM to determine that OXPHOS promotes the growth of MBMs without influencing their initial formation or the formation and growth of lung metastases. Knockdown of PGC1α/OXPHOS significantly extended the survival of mice challenged by intracranial (ICr) injection of melanoma cell lines but had no effect on subcutaneous tumor growth. Together these studies indicate that while OXPHOS does not affect the incidence of melanoma brain metastasis, it plays a crucial role in intracranial tumor growth.

Interestingly, molecular analyses identified a subset of MBMs particularly enriched for OXPHOS. These "High-OXPHOS" MBMs were characterized by the following: increased mTORC1 pathway activation independent of PI3K-AKT pathway input, overexpression of known mediators of OXPHOS in melanoma including MITF and PGC1α, enrichment of pathways known to consume glutamine, and significant immunosuppression. Analysis of High- and Low-OXPHOS brain xenografts confirmed increased glutamine metabolism in High-OXPHOS MBMs. Together, these observations determined that High-OXPHOS MBMs have unique and potentially targetable molecular, immunological, and metabolic features. Additionally, the identification of significant associations provided new insights into MBM biology and the interplay between prominent signaling and metabolic pathways. I utilized these insights to prioritize evaluation of novel metabolic inhibitors alone and in combination with approved therapies for metastatic melanoma. Single-agent treatment with IACS-010759 – a potent OXPHOS inhibitor currently in phase I clinical trials – significantly extended survival of mice bearing High-OXPHOS intracranial melanoma xenografts with acquired and *de novo* resistance to MAPKi. Importantly, I showed that the brain TME mediated resistance to MAPKi in a previously sensitive cell line via induction of OXPHOS and that the combination of IACS-010759 and dabrafenib significantly improved survival in mice bearing intracranial xenografts of this cell line. Additionally, I showed that OXPHOS inhibition overcame resistance to anti-PD1 immunotherapy in a High-OXPHOS syngeneic model of MBM. Finally, the novel glutaminase inhibitor CB839 induced significant responses in two High-OXPHOS, MAPKi-resistant models of MBM.

6.2 - NOVELTY

These studies employed the largest cohort of MBMs analyzed by RNA-seq to date, and the largest cohort of patient-matched brain metastases and extracranial metastases from any tumor type, to provide key new insights into the metabolic features and dependencies of MBMs. Analysis of these clinically-annotated, data-rich samples identified associations between OXPHOS and molecular, immune, and metabolic features. These findings supported the rationale for in-depth evaluation of novel therapeutic strategies designed to exploit these features in validated preclinical models. These novel therapeutic approaches included a potent OXPHOS inhibitor (IACS-010759) and glutaminase inhibitor (CB839) that are currently in clinical trials. Additionally, I integrated gene expression data and metabolomics data to determine that OXPHOS enrichment in MBMs vs. patient-matched ECMs occurred because the brain TME mediated significantly different metabolic reprogramming compared to the subcutaneous tissue and not because metastatic cells enriched in OXPHOS are inherently more capable of metastasizing to the brain. I utilized the first-ever RCAS-TVA model of melanoma that forms brain metastases from cutaneous primary tumors and numerous experimental models of metastasis and tumor growth to determine that OXPHOS plays a critical role in the growth of MBMs but not their initial formation.

6.3 - SIGNIFICANCE

My findings suggest that OXPHOSi may work better in MBMs than in metastases at other sites. This would be a revolutionary paradigm, as generally patients with MBMs have been excluded from clinical trials due to concerns about lack of efficacy in these lesions. My results not only have implications for the development of inhibitors that target OXPHOS, but for the design of future clinical trials and the preclinical evaluation of investigational agents.

The findings here support the rationale to see if there are unique dependencies of melanoma cells that have metastasized to organs besides the brain, particularly those associated with poor outcomes (i.e. the liver and bones). My data strongly supports that analyses should encompass immune, molecular, and metabolic features.

An obvious question is whether or not OXPHOS is only important for MBMs, or for brain metastases from other cancer types as well. Metabolic profiling of brain metastases from other cancer types remains limited to experimental models and small cohorts of clinical samples (211, 297). While these studies have implicated OXPHOS metabolism in brain metastasis pathogenesis, the results should be further validated in larger cohorts of patient-matched samples.

6.4 - FUTURE DIRECTIONS

6.4.1 - Providing Mechanistic Insight Into How the Brain Microenvironment Promotes Oxidative Phosphorylation Compared to Other Anatomical Locations

Despite the immense amount of molecular and metabolic profiling presented in this dissertation, the precise mechanism by which OXPHOS becomes preferentially activated in MBMs remains unclear. Given the role of this pathway in supporting MBM growth, providing mechanistic insight into how the brain TME promotes OXPHOS enrichment should be prioritized in future studies.

All cells respond to oxygen deprivation by inhibiting OXPHOS (298). Consequently, it might be tempting to blame the differential expression of OXPHOS genes on differences in oxygen tension between the brain and other anatomical sites. However, the oxygen concentration in the brain (0.5-8%) is comparable to the oxygen concentration in the lungs (4-14%), liver (4-

14%), and adipose tissue (2-8%) (299). Of course, it is possible that intratumoral oxygen tension differs significantly between MBMs and ECMs. However, my global analysis of brain and subcutaneous xenografts determined that hypoxia-associated gene sets were enriched in the brain xenografts (**Figure 15A**). Together, these findings exclude the possibility that ECMs inhibit OXPHOS in response to growing in a more hypoxic TME than the MBMs.

These studies identified enrichment of genes regulated by the mTORC1 and PI3K-AKT-mTOR signaling pathways in the brain xenografts. In addition, RPPA analysis identified increased concentrations of numerous proteins indicative of PI3K-AKT and mTORC1 pathway activation in the brain xenografts. I confirmed increased staining of activation markers for these pathways in surgically resected Tx-naive MBMs vs. Tx-naïve ECMs from the same patients. Importantly, I ruled out the possibility that the PI3K-AKT pathway was activated due to loss of PTEN. Instead, I demonstrated overexpression of IGF1R in brain xenografts. Previous studies have demonstrated that signaling through IGF1R drives the activation of mTOR and the High-OXPHOS phenotype in non-CNS melanomas (3, 215). Interestingly, specific factors within cerebrospinal fluid (CSF) activate the PI3K-AKT-mTOR signaling cascade in melanoma cells (105). High levels of IGF-1 have been reported in CSF (300). Thus, IGF-1 in the CSF could be mediating OXPHOS enrichment in MBMs by engaging IGF1R and activating the PI3K-AKT-mTOR pathway. Testing this hypothesis must be prioritized in the future.

Alternative hypotheses could be tested if future experiments exclude IGF-1/IGF1R signaling as a key mediator of MBM OXPHOS enrichment. First, additional brain-derived soluble factors could be responsible for activating the PI3K-AKT-mTOR signaling pathway. Alternatively, intercellular communication between tumor cells and surrounding stroma might be responsible for mediating the OXPHOS enrichment. The ability of astrocytes to alter tumor cell signaling has been extensively studied (101, 145). While none of these studies implicated

OXPHOS, it is possible that astrocytes somehow reprogram the tumor cells to increase mitochondrial biogenesis and utilize OXPHOS at significantly higher levels than cells metastasizing to other sites of the body.

Finally, it is worth noting that OXPHOS heterogeneity across the surgically resected MBMs associated significantly with mTORC1 signaling. These findings implicate mTORC1 as a critical mediator of OXPHOS in MBMs. As detailed in Chapter 5, PI3K-AKT pathway-independent activation of mTORC1 could occur via differential access to critical amino acids (287). In turn, mTORC1 could have then promoted MYC signaling, which also associated strongly with OXPHOS enrichment in MBMs in these studies and has been strongly implicated in OXPHOS signaling in independent studies (301).

Based on my findings, I now propose a schema in which melanoma cells growing in the brain parenchyma overexpress IGF1R, which ensures frequent engagement with IGF-1 that is present in high concentrations in the brain TME. This interaction hyperactivates the PI3K-AKT-mTOR signaling pathway, which induces mitochondrial biogenesis and OXPHOS. In parallel, MBMs from different patients differ in their access to critical amino acids and thus experience different degrees of mTORC1 signaling and OXPHOS enrichment.

6.4.2 - Understanding How Oxidative Phosphorylation Promotes the Growth of Melanoma Brain Metastases

6.4.2a - Metabolic Flexibility

The increased ability to perform OXPHOS could benefit melanoma cells growing in the brain parenchyma in a variety of ways. First, this pathway is able to metabolize

more than glucose. The brain utilizes over half of the glucose available in the body (302). For this reason, it appears as a saturated mass on whole body positron emission tomography-computed tomography (PET–CT) scans. However, competition for glucose in the brain is intense. Astrocytes in the brain avidly consume glucose and secrete lactate, which is consumed by neurons for OXPHOS. This "lactate shuttle" causes the levels of glucose available for MBMs to be highly variable (303, 304). OXPHOS would allow brain-metastatic cells to efficiently utilize glutamine and branch-chain amino acids richly available in the brain interstitium (244). Alternatively, OXPHOS would allow MBMs to scavenge acetate through its direct incorporation into the TCA cycle (297). This metabolic flexibility could provide a marked survival advantage for melanoma cells attempting to grow in the brain parenchyma. Testing this hypothesis could identify additional therapeutic targets. In addition, it could provide meaningful insights into a topic on the minds of many cancer patients – the effect of their diets on tumor growth. In general, the potential benefits of the ketogenic diet in metastatic melanoma remain unclear. For example, Xia et al. demonstrated that ketone bodies actually promoted the growth of *BRAF*-mutant xenografts and had no effect on *NRAS*-mutant and triple wild-type mutant melanoma xenografts (305). In contrast, several patients with metastatic melanoma appeared to benefit from the diet in a feasibility trial of multiple metastatic diseases (306). Regardless, this diet would significantly increase the circulating levels of acetate, which could feed MBMs attempting to survive in the hostile brain TME.

6.4.2b - Immune Evasion

Previously, I observed both enrichment of OXPHOS and depletion of immune cells in MBMs vs. patient-matched ECMs (174). This result suggests that OXPHOS enrichment in MBMs could mediate their immunosuppression. Consistent with this finding, I observed a significant association between OXPHOS and immunosuppression in MBMs. In addition to significant differences in B cell density between High- and Low-OXPHOS MBMs, I also observed significant alterations in IFNγ signaling. I demonstrated that High-OXPHOS MBMs were characterized by a signature previously shown to predict failure to anti-PD1 immunotherapy. OXPHOS could impact immune cell function in several ways. First, memory T cells rely significantly on OXPHOS to meet their bioenergetic needs (307). Intratumoral memory T cells have been identified in melanomas (308). Tumor cell OXPHOS could directly impede the ability of these cells to function and proliferate through direct competition for resources. Alternatively, OXPHOS facilitates intratumoral hypoxia. Hypoxia can negatively affect effector T cells by inducing detrimental epigenetic changes (309). In addition, effector T cells preferentially utilize glycolysis to meet their bioenergetic demands (307). As such, they rely significantly on glutamine to replenish their TCA cycles for production of biosynthetic precursors. Without oxygen available to act as an electron acceptor, the cycle ceases to operate efficiently and prevents the synthesis of intermediates. OXPHOS correlates significantly with glutamine consumption in melanomas (282). Thus, OXPHOS induction in MBMs might result in an intratumoral competition for glutamine that could be highly detrimental for effector T cells.

My findings pose many exciting questions. Future studies should assess if OXPHOS in MBMs inhibits the proliferation of immune cells after they successfully reach the tumor and/or if it somehow prevents their trafficking into the tumor. Second, it is

imperative to further investigate OXPHOS-mediated resistance to immunotherapies in MBMs and how we can overcome this resistance through combinations of immunotherapies and metabolic inhibitors such as IACS-010759, metformin, and CB839. The dosing and sequence of these combinations will certainly require an extensive amount of troubleshooting to ensure optimal response. Most importantly, we need to consider how to implement treatments in patients with metastases at multiple anatomical sites. A patient with a lung metastasis might require a combinatorial regimen that negatively affects MBM treatment or *vice versa*. Addressing these difficult issues must be a priority in the future to move the treatment of this deadly disease forward.

6.4.2c - Mitochondrial Signaling

Mitochondria are important stress sensors, and signaling by mitochondria allows the cell to adapt to its environment. For example, citrate produced in the TCA cycle can be transported to the cytosol, where ATP citrate lyase (ACL) cleaves it into acetyl-CoA and oxaloacetate. Acetyl-CoA can fuel acetylation of histones in epigenetic regulation reactions that could affect signaling pathways required for MBM growth (301). Likewise, α-ketoglutarate supports a range of chromatin-modifying reactions (301). Thus, TCA cycle function supported by mitochondrial biogenesis/OXPHOS enrichment could facilitate a range of beneficial intracellular epigenetic changes in MBMs.

6.4.2d - Mitigating Oxidative Stress

Studies have identified a subset of melanoma cell lines and surgically resected ECMs characterized by high expression of PGC1α and OXPHOS enrichment that are able to withstand significantly higher levels of oxidative stress (172). I analyzed the growth of two cell lines from this paper and found that silencing PGC1α inhibited the growth of these cells in the brains but not subcutaneous tissue of mice. This suggests that the brain TME induces particularly high levels of oxidative stress and that the knockdown cells could not detoxify reactive oxygen species (ROS) efficiently enough to survive. Further analyses should be prioritized to confirm this possibility.

6.4.3 - Translating Findings Into Novel Therapeutic Strategies

Treatment with the novel OXPHOS inhibitor IACS-010759 prolonged survival in mice with intracranial High-OXPHOS, MAPKi-resistant melanoma xenografts. While my results demonstrate that single-agent OXPHOS inhibition with IACS-010759 can have beneficial effects, the models I employed were selected due to their previously established *in vitro* sensitivity to the drug (290). Not all High-OXPHOS, MAPKi-resistant melanomas respond uniformly to this treatment (290). Furthermore, acquired resistance will likely be a barrier to overcome. Thus, it will be imperative to characterize predictive and prognostic markers of MBM response and to develop strategies to prevent and overcome resistance to feasibly utilize this drug in the treatment of MBMs.

One challenge in treating and studying brain metastases is the difficulty in routinely acquiring tissue. While these studies indicated that target inhibition by IACS-010759 significantly decreased pimonidazole and P-S6 staining, routinely acquiring biopsies of MBM patients treated with this drug would not be feasible. To benefit patients, we need a non-invasive way to assess

the extent of OXPHOS inhibition in MBMs following treatment. FAZA-PET analysis is a novel imaging technique that uses [^{18}F]-labeled FAZA (fluoroazomycin arabinoside) to assess OXPHOS inhibition following treatment with IACS-010759 (310). As this technique has been validated in orthotopic glioblastoma models, it could be used to confirm OXPHOS suppression in MBM patients treated with IACS-010759. Excitingly, CB839 inhibited OXPHOS in A375-R1 cells, indicating that this imaging modality could also be used to assess target inhibition in MBM patients treated with CB839. Future studies should assess the utility of this imaging modality in clinically relevant models of MBM treated with these inhibitors.

Ideally, we would want to be able to noninvasively identify High-OXPHOS MBMs as these lesions would be least likely to respond to MAPKi and anti-PD1 therapy and require alternative therapies such as IACS-010759 or CB839. Future studies should focus on establishing radiomic correlates for this metabolic phenotype in MBMs (311). My unique cohort of surgically resected High- and Low-OXPHOS MBMs with archived imaging makes this highly feasible. Preclinical models with pre-and post-treatment imaging could be used in parallel to validate radiomic markers predictive of response to IACS-010759 or CB839 and to identify prognostic radiomic markers for these treatments. Ultimately, these markers would need to be validated in patients.

6.4.4 - Obstacles to Translating Findings Into Novel Therapeutic Strategies

Resistance and/or toxicity will likely be critical challenges in the use of metabolic inhibitors in MBMs and will complicate efforts to move molecules such as IACS-010759 and CB839 into the clinic as single-agent therapies for MBMs. I observed significant survival benefit in mice treated with these two molecules. However, all mice eventually progressed on CB839

treatment, and the majority of mice eventually progressed on IACS-010759 treatment. Since these mice were injected with cells selected because of their *in vitro* sensitivities to these inhibitors, response rates could be worse in xenografts of other cell lines. IACS-010759 resistance would likely result from a switch from dependence on OXPHOS to glycolysis. Alternative mechanisms might include selection of rare subclones with mutated binding sites at complex I of the electron transport chain (ETC), which would inhibit the drug from effectively suppressing OXPHOS. Resistance to CB839 is well-documented in other cancer types and involves multiple compensatory pathways that alleviate cellular stress induced by disruption of glutamine metabolism (312).

I anticipate that metabolic inhibitors such as IACS-010759 and CB839 will be most useful in the treatment of MBMs by augmenting available targeted and immune therapies. IACS-010759 and dabrafenib provided a significant survival benefit in mice bearing intracranial A375 xenografts compared to either of these therapies alone. This finding is consistent with previous studies that have shown that *BRAF*-mutant extracranial melanoma metastases treated with BRAFi therapy can become addicted to OXPHOS and subsequently are highly sensitive to direct OXPHOSi. Phenformin, which inhibits OXPHOS, delays the development of resistance to BRAFi in human melanoma cell lines (26, 245). Thus, adding IACS-010759 to MAPKi therapies at the initiation of treatment of *BRAF*-mutant MBMs could increase the duration of tumor responses, which was the critical factor that limited the clinical benefit of treatment with dabrafenib and trametinib in the COMBI-MB study (171). Future studies should prioritize confirming these findings using relevant preclinical models. The combination of MAPKi and IACS-010759 could also yield synergistic effects in some MBMs that have already developed resistance to MAPKi therapies via increased dependence on OXPHOS. While my combination studies showed no benefit in the A375-R1 and SKMEL5 models, these observations were primarily due to the

impressive efficacy of single-agent IACS-010759 in the treatment of these lesions. Intracranial xenografts of other High-OXPHOS cell lines might not respond as well to single-agent IACS-010759, and the combination of MAPKi and IACS-010759 could be beneficial in this subset of tumors.

Immune therapies represent the other main category of front-line therapies for metastatic melanoma. Intracranial response rates (ICRR) observed with anti-PD1 (~20%) (153) (154) are significantly lower than response rates of ECMs, and promising results of combined immunotherapy with anti-CTLA4 and anti-PD1 have only been reported for patients with small, asymptomatic MBMs (155). Identifying ways to overcome MBM resistance to immune therapies remains a critical challenge. My findings demonstrated that OXPHOS inhibition can improve the response of MBMs to anti-PD1. I utilized metformin in these studies, but the effects of IACS-010759 on the immune system must be investigated. Also, future studies should investigate whether or not OXPHOS inhibition can improve MBM response to other single-agent immune therapies and if it can be added to the combination of anti-CTLA4 and anti-PD1 in the treatment of MBMs. Despite promising preclinical results, CB839 induced a response rate of only 19% in a cohort of 16 metastatic melanoma patients progressing on anti-PD1 therapy (313). However, this trial excluded patients with MBMs. My data identified enriched glutamine metabolism in MBMs compared to ECMs. Thus, MBMs might respond better to the combination of CB839 and anti-PD1 than ECMs. Future preclinical studies should prioritize testing this combination in immunocompetent models of MBM.

Finally, my data suggests that inhibition of OXPHOS could form part of a preventative strategy in the treatment of metastatic melanoma patients. OXPHOS inhibition significantly slowed the growth of MBMs in our experimental model and significantly decreased the incidence of detectable MBMs in the RCAS-TVA model. The ability of IACS-010759 to potentially keep

MBMs small and asymptomatic could significantly alter treatment options for metastatic melanoma patients. Excitingly, IACS-010759 could work regardless of tumor genotype, as my RNA-seq and LC-MS findings demonstrated enrichment of the OXPHOS pathway in ICr tumors, regardless of genotype. However, my findings suggest that OXPHOSi appears to be more important for inhibiting MBM growth than the growth of metastases at other sites. Thus, IACS-010759 would need to be combined with additional agents to form a comprehensive strategy able to prevent metastatic outgrowth at all sites of the body.

6.5 - CLOSING REMARKS

These studies represent a small fraction of my lab's efforts to perform the most comprehensive molecular profiling of patient-matched MBMs and ECMs reported to date. For the first time ever, I provide insights into the role of OXPHOS in MBM pathogenesis. Importantly, these studies suggest rational strategies to improve outcomes in patients. Together, the findings add to our understanding of the pathogenesis of MBMs, support the rationale for further dedicated analyses of these tumors, and provide new directions for interrogation in other diseases in which brain metastases remain a critical challenge.

BIBLIOGRAPHY

1. Siegel, R. L., K. D. Miller, and A. Jemal. 2017. Cancer statistics, 2017. *CA Cancer J. Clin.* 67: 7-30.
2. Luke, J. J., K. T. Flaherty, A. Ribas, and G. V. Long. 2017. Targeted agents and immunotherapies: optimizing outcomes in melanoma. *Nature Reviews.Clinical Oncology*.
3. Gopal, Y. N., H. Rizos, G. Chen, W. Deng, D. T. Frederick, Z. A. Cooper, R. A. Scolyer, G. Pupo, K. Komurov, V. Sehgal, J. Zhang, L. Patel, C. G. Pereira, B. M. Broom, G. B. Mills, P. Ram, P. D. Smith, J. A. Wargo, G. V. Long, and M. A. Davies. 2014. Inhibition of mTORC1/2 overcomes resistance to MAPK pathway inhibitors mediated by PGC1alpha and oxidative phosphorylation in melanoma. *Cancer Res.* 74: 7037-7047.
4. Hanahan, D., and R. A. Weinberg. 2011. Hallmarks of cancer: the next generation. *Cell* 144: 646-674.
5. Pavlova, N. N., and C. B. Thompson. 2016. The Emerging Hallmarks of Cancer Metabolism. *Cell Metab.* 23: 27-47.
6. Sudarsan, S., S. Dethlefsen, L. M. Blank, M. Siemann-Herzberg, and A. Schmid. 2014. The functional structure of central carbon metabolism in Pseudomonas putida KT2440. *Appl. Environ. Microbiol.* 80: 5292-5303.
7. Lehninger, A. L., D. L. Nelson, and M. M. Cox. 2013. *Lehninger principles of biochemistry*. W.H. Freeman, New York.
8. Lodish, H. F. 2000. *Molecular cell biology*. W.H. Freeman, New York.
9. Chatterjea, M. N., and R. Shinde. 2012. *Textbook of medical biochemistry*. Jaypee Brothers Medical Publications P Ltd., New Delhi.

10. Scott, D. A., A. D. Richardson, F. V. Filipp, C. A. Knutzen, G. G. Chiang, Z. A. Ronai, A. L. Osterman, and J. W. Smith. 2011. Comparative metabolic flux profiling of melanoma cell lines: beyond the Warburg effect. *The Journal of Biological Chemistry* 286: 42626-42634.

11. Jose, C., N. Bellance, and R. Rossignol. 2011. Choosing between glycolysis and oxidative phosphorylation: a tumor's dilemma? *Biochim. Biophys. Acta* 1807: 552-561.

12. DeBerardinis, R. J., and N. S. Chandel. 2016. Fundamentals of cancer metabolism. *Science Advances* 2: e1600200.

13. Ratnikov, B. I., D. A. Scott, A. L. Osterman, J. W. Smith, and Z. A. Ronai. 2017. Metabolic rewiring in melanoma. *Oncogene* 36: 147-157.

14. Porporato, P. E., V. L. Payen, J. Perez-Escuredo, C. J. De Saedeleer, P. Danhier, T. Copetti, S. Dhup, M. Tardy, T. Vazeille, C. Bouzin, O. Feron, C. Michiels, B. Gallez, and P. Sonveaux. 2014. A mitochondrial switch promotes tumor metastasis. *Cell Rep.* 8: 754-766.

15. Schwartz, L., M. Abolhassani, A. Guais, E. Sanders, J. M. Steyaert, F. Campion, and M. Israel. 2010. A combination of alpha lipoic acid and calcium hydroxycitrate is efficient against mouse cancer models: preliminary results. *Oncol. Rep.* 23: 1407-1416.

16. Cai, T., Y. Kuang, C. Zhang, Z. Zhang, L. Chen, B. Li, Y. Li, Y. Wang, H. Yang, Q. Han, and Y. Zhu. 2015. Glucose-6-phosphate dehydrogenase and NADPH oxidase 4 control STAT3 activity in melanoma cells through a pathway involving reactive oxygen species, c-SRC and SHP2. *Am. J. Cancer Res.* 5: 1610-1620.

17. Beroukhim, R., C. H. Mermel, D. Porter, G. Wei, S. Raychaudhuri, J. Donovan, J. Barretina, J. S. Boehm, J. Dobson, M. Urashima, K. T. Mc Henry, R. M. Pinchback, A. H. Ligon, Y. J. Cho, L. Haery, H. Greulich, M. Reich, W. Winckler, M. S. Lawrence, B.

A. Weir, K. E. Tanaka, D. Y. Chiang, A. J. Bass, A. Loo, C. Hoffman, J. Prensner, T. Liefeld, Q. Gao, D. Yecies, S. Signoretti, E. Maher, F. J. Kaye, H. Sasaki, J. E. Tepper, J. A. Fletcher, J. Tabernero, J. Baselga, M. S. Tsao, F. Demichelis, M. A. Rubin, P. A. Janne, M. J. Daly, C. Nucera, R. L. Levine, B. L. Ebert, S. Gabriel, A. K. Rustgi, C. R. Antonescu, M. Ladanyi, A. Letai, L. A. Garraway, M. Loda, D. G. Beer, L. D. True, A. Okamoto, S. L. Pomeroy, S. Singer, T. R. Golub, E. S. Lander, G. Getz, W. R. Sellers, and M. Meyerson. 2010. The landscape of somatic copy-number alteration across human cancers. *Nature* 463: 899-905.

18. Locasale, J. W., A. R. Grassian, T. Melman, C. A. Lyssiotis, K. R. Mattaini, A. J. Bass, G. Heffron, C. M. Metallo, T. Muranen, H. Sharfi, A. T. Sasaki, D. Anastasiou, E. Mullarky, N. I. Vokes, M. Sasaki, R. Beroukhim, G. Stephanopoulos, A. H. Ligon, M. Meyerson, A. L. Richardson, L. Chin, G. Wagner, J. M. Asara, J. S. Brugge, L. C. Cantley, and M. G. Vander Heiden. 2011. Phosphoglycerate dehydrogenase diverts glycolytic flux and contributes to oncogenesis. *Nat. Genet.* 43: 869-874.

19. Kumar, S. M., H. Yu, R. Edwards, L. Chen, S. Kazianis, P. Brafford, G. Acs, M. Herlyn, and X. Xu. 2007. Mutant V600E BRAF increases hypoxia inducible factor-1alpha expression in melanoma. *Cancer Res.* 67: 3177-3184.

20. Parmenter, T. J., M. Kleinschmidt, K. M. Kinross, S. T. Bond, J. Li, M. R. Kaadige, A. Rao, K. E. Sheppard, W. Hugo, G. M. Pupo, R. B. Pearson, S. L. McGee, G. V. Long, R. A. Scolyer, H. Rizos, R. S. Lo, C. Cullinane, D. E. Ayer, A. Ribas, R. W. Johnstone, R. J. Hicks, and G. A. McArthur. 2014. Response of BRAF-mutant melanoma to BRAF inhibition is mediated by a network of transcriptional regulators of glycolysis. *Cancer Discov.* 4: 423-433.

21. Semenza, G. L., B. H. Jiang, S. W. Leung, R. Passantino, J. P. Concordet, P. Maire, and A. Giallongo. 1996. Hypoxia response elements in the aldolase A, enolase 1, and lactate dehydrogenase A gene promoters contain essential binding sites for hypoxia-inducible factor 1. *The Journal of Biological Chemistry* 271: 32529-32537.

22. Kim, J. W., I. Tchernyshyov, G. L. Semenza, and C. V. Dang. 2006. HIF-1-mediated expression of pyruvate dehydrogenase kinase: a metabolic switch required for cellular adaptation to hypoxia. *Cell Metab.* 3: 177-185.

23. Kraehn, G. M., J. Utikal, M. Udart, K. M. Greulich, G. Bezold, P. Kaskel, U. Leiter, and R. U. Peter. 2001. Extra c-myc oncogene copies in high risk cutaneous malignant melanoma and melanoma metastases. *Br. J. Cancer* 84: 72-79.

24. Stine, Z. E., Z. E. Walton, B. J. Altman, A. L. Hsieh, and C. V. Dang. 2015. MYC, Metabolism, and Cancer. *Cancer Discov.* 5: 1024-1039.

25. Zeller, K. I., A. G. Jegga, B. J. Aronow, K. A. O'Donnell, and C. V. Dang. 2003. An integrated database of genes responsive to the Myc oncogenic transcription factor: identification of direct genomic targets. *Genome Biol.* 4: R69.

26. Haq, R., J. Shoag, P. Andreu-Perez, S. Yokoyama, H. Edelman, G. C. Rowe, D. T. Frederick, A. D. Hurley, A. Nellore, A. L. Kung, J. A. Wargo, J. S. Song, D. E. Fisher, Z. Arany, and H. R. Widlund. 2013. Oncogenic BRAF regulates oxidative metabolism via PGC1alpha and MITF. *Cancer Cell* 23: 302-315.

27. Davies, M. A., K. Stemke-Hale, C. Tellez, T. L. Calderone, W. Deng, V. G. Prieto, A. J. Lazar, J. E. Gershenwald, and G. B. Mills. 2008. A novel AKT3 mutation in melanoma tumours and cell lines. *Br. J. Cancer* 99: 1265-1268.

28. Guldberg, P., P. thor Straten, A. Birck, V. Ahrenkiel, A. F. Kirkin, and J. Zeuthen. 1997. Disruption of the MMAC1/PTEN gene by deletion or mutation is a frequent event in malignant melanoma. *Cancer Res.* 57: 3660-3663.

29. Kwong, L. N., and M. A. Davies. 2013. Navigating the therapeutic complexity of PI3K pathway inhibition in melanoma. *Clin. Cancer Res.* 19: 5310-5319.

30. Omholt, K., D. Krockel, U. Ringborg, and J. Hansson. 2006. Mutations of PIK3CA are rare in cutaneous melanoma. *Melanoma Res.* 16: 197-200.

31. Tsao, H., X. Zhang, E. Benoit, and F. G. Haluska. 1998. Identification of PTEN/MMAC1 alterations in uncultured melanomas and melanoma cell lines. *Oncogene* 16: 3397-3402.

32. Hudson, C. C., M. Liu, G. G. Chiang, D. M. Otterness, D. C. Loomis, F. Kaper, A. J. Giaccia, and R. T. Abraham. 2002. Regulation of hypoxia-inducible factor 1alpha expression and function by the mammalian target of rapamycin. *Mol. Cell. Biol.* 22: 7004-7014.

33. Land, S. C., and A. R. Tee. 2007. Hypoxia-inducible factor 1alpha is regulated by the mammalian target of rapamycin (mTOR) via an mTOR signaling motif. *The Journal of Biological Chemistry* 282: 20534-20543.

34. Zundel, W., C. Schindler, D. Haas-Kogan, A. Koong, F. Kaper, E. Chen, A. R. Gottschalk, H. E. Ryan, R. S. Johnson, A. B. Jefferson, D. Stokoe, and A. J. Giaccia. 2000. Loss of PTEN facilitates HIF-1-mediated gene expression. *Genes Dev.* 14: 391-396.

35. Zhang, G., D. T. Frederick, L. Wu, Z. Wei, C. Krepler, S. Srinivasan, Y. C. Chae, X. Xu, H. Choi, E. Dimwamwa, O. Ope, B. Shannan, D. Basu, D. Zhang, M. Guha, M. Xiao, S. Randell, K. Sproesser, W. Xu, J. Liu, G. C. Karakousis, L. M. Schuchter, T. C. Gangadhar, R. K. Amaravadi, M. Gu, C. Xu, A. Ghosh, T. Tian, J. Zhang, S. Zha, Q. Liu, P. Brafford, A. Weeraratna, M. A. Davies, J. A. Wargo, N. G. Avadhani, Y. Lu, G. B. Mills, D. C.

Altieri, K. T. Flaherty, and M. Herlyn. 2016. Targeting mitochondrial biogenesis to overcome drug resistance to MAPK inhibitors. *J. Clin. Investig.* 126: 1834-1856.

36. Abildgaard, C., and P. Guldberg. 2015. Molecular drivers of cellular metabolic reprogramming in melanoma. *Trends Mol. Med.* 21: 164-171.

37. Feige, E., S. Yokoyama, C. Levy, M. Khaled, V. Igras, R. J. Lin, S. Lee, H. R. Widlund, S. R. Granter, A. L. Kung, and D. E. Fisher. 2011. Hypoxia-induced transcriptional repression of the melanoma-associated oncogene MITF. *Proc. Natl. Acad. Sci. U. S. A.* 108: E924-933.

38. McQuade, J. L., and Y. Vashisht Gopal. 2015. Counteracting oxidative phosphorylation-mediated resistance of melanomas to MAPK pathway inhibition. *Molecular & Cellular Oncology* 2: e991610.

39. Shimobayashi, M., and M. N. Hall. 2014. Making new contacts: the mTOR network in metabolism and signalling crosstalk. *Nature Reviews.Molecular Cell Biology* 15: 155-162.

40. Cunningham, J. T., J. T. Rodgers, D. H. Arlow, F. Vazquez, V. K. Mootha, and P. Puigserver. 2007. mTOR controls mitochondrial oxidative function through a YY1-PGC-1alpha transcriptional complex. *Nature* 450: 736-740.

41. Shackelford, D. B., and R. J. Shaw. 2009. The LKB1-AMPK pathway: metabolism and growth control in tumour suppression. *Nature Reviews.Cancer* 9: 563-575.

42. Canto, C., Z. Gerhart-Hines, J. N. Feige, M. Lagouge, L. Noriega, J. C. Milne, P. J. Elliott, P. Puigserver, and J. Auwerx. 2009. AMPK regulates energy expenditure by modulating NAD+ metabolism and SIRT1 activity. *Nature* 458: 1056-1060.

43. Jager, S., C. Handschin, J. St-Pierre, and B. M. Spiegelman. 2007. AMP-activated protein kinase (AMPK) action in skeletal muscle via direct phosphorylation of PGC-1alpha. *Proc. Natl. Acad. Sci. U. S. A.* 104: 12017-12022.

44. Zheng, B., J. H. Jeong, J. M. Asara, Y. Y. Yuan, S. R. Granter, L. Chin, and L. C. Cantley. 2009. Oncogenic B-RAF negatively regulates the tumor suppressor LKB1 to promote melanoma cell proliferation. *Mol. Cell* 33: 237-247.

45. Wallace, D. C. 2012. Mitochondria and cancer. *Nature Reviews.Cancer* 12: 685-698.

46. Rabinovich, S., L. Adler, K. Yizhak, A. Sarver, A. Silberman, S. Agron, N. Stettner, Q. Sun, A. Brandis, D. Helbling, S. Korman, S. Itzkovitz, D. Dimmock, I. Ulitsky, S. C. Nagamani, E. Ruppin, and A. Erez. 2015. Diversion of aspartate in ASS1-deficient tumours fosters de novo pyrimidine synthesis. *Nature* 527: 379-383.

47. Owen, O. E., S. C. Kalhan, and R. W. Hanson. 2002. The key role of anaplerosis and cataplerosis for citric acid cycle function. *The Journal of Biological Chemistry* 277: 30409-30412.

48. Phannasil, P., C. Thuwajit, M. Warnnissorn, J. C. Wallace, M. J. MacDonald, and S. Jitrapakdee. 2015. Pyruvate Carboxylase Is Up-Regulated in Breast Cancer and Essential to Support Growth and Invasion of MDA-MB-231 Cells. *PLoS One* 10: e0129848.

49. Sellers, K., M. P. Fox, M. Bousamra, 2nd, S. P. Slone, R. M. Higashi, D. M. Miller, Y. Wang, J. Yan, M. O. Yuneva, R. Deshpande, A. N. Lane, and T. W. Fan. 2015. Pyruvate carboxylase is critical for non-small-cell lung cancer proliferation. *J. Clin. Investig.* 125: 687-698.

50. Ratnikov, B., P. Aza-Blanc, Z. A. Ronai, J. W. Smith, A. L. Osterman, and D. A. Scott. 2015. Glutamate and asparagine cataplerosis underlie glutamine addiction in melanoma. *Oncotarget* 6: 7379-7389.

51. Yang, C., J. Sudderth, T. Dang, R. M. Bachoo, J. G. McDonald, and R. J. DeBerardinis. 2009. Glioblastoma cells require glutamate dehydrogenase to survive impairments of glucose metabolism or Akt signaling. *Cancer Res.* 69: 7986-7993.

52. Hensley, C. T., A. T. Wasti, and R. J. DeBerardinis. 2013. Glutamine and cancer: cell biology, physiology, and clinical opportunities. *J. Clin. Investig.* 123: 3678-3684.

53. Filipp, F. V., D. A. Scott, Z. A. Ronai, A. L. Osterman, and J. W. Smith. 2012. Reverse TCA cycle flux through isocitrate dehydrogenases 1 and 2 is required for lipogenesis in hypoxic melanoma cells. *Pigment Cell Melanoma Res.* 25: 375-383.

54. Mullen, A. R., W. W. Wheaton, E. S. Jin, P. H. Chen, L. B. Sullivan, T. Cheng, Y. Yang, W. M. Linehan, N. S. Chandel, and R. J. DeBerardinis. 2011. Reductive carboxylation supports growth in tumour cells with defective mitochondria. *Nature* 481: 385-388.

55. Metallo, C. M., P. A. Gameiro, E. L. Bell, K. R. Mattaini, J. Yang, K. Hiller, C. M. Jewell, Z. R. Johnson, D. J. Irvine, L. Guarente, J. K. Kelleher, M. G. Vander Heiden, O. Iliopoulos, and G. Stephanopoulos. 2011. Reductive glutamine metabolism by IDH1 mediates lipogenesis under hypoxia. *Nature* 481: 380-384.

56. Jiang, L., A. A. Shestov, P. Swain, C. Yang, S. J. Parker, Q. A. Wang, L. S. Terada, N. D. Adams, M. T. McCabe, B. Pietrak, S. Schmidt, C. M. Metallo, B. P. Dranka, B. Schwartz, and R. J. DeBerardinis. 2016. Reductive carboxylation supports redox homeostasis during anchorage-independent growth. *Nature* 532: 255-258.

57. Abbas, S., S. Lugthart, F. G. Kavelaars, A. Schelen, J. E. Koenders, A. Zeilemaker, W. J. van Putten, A. W. Rijneveld, B. Lowenberg, and P. J. Valk. 2010. Acquired mutations in the genes encoding IDH1 and IDH2 both are recurrent aberrations in acute myeloid leukemia: prevalence and prognostic value. *Blood* 116: 2122-2126.

58. Mardis, E. R., L. Ding, D. J. Dooling, D. E. Larson, M. D. McLellan, K. Chen, D. C. Koboldt, R. S. Fulton, K. D. Delehaunty, S. D. McGrath, L. A. Fulton, D. P. Locke, V. J. Magrini, R. M. Abbott, T. L. Vickery, J. S. Reed, J. S. Robinson, T. Wylie, S. M. Smith, L. Carmichael, J. M. Eldred, C. C. Harris, J. Walker, J. B. Peck, F. Du, A. F. Dukes, G. E.

Sanderson, A. M. Brummett, E. Clark, J. F. McMichael, R. J. Meyer, J. K. Schindler, C. S. Pohl, J. W. Wallis, X. Shi, L. Lin, H. Schmidt, Y. Tang, C. Haipek, M. E. Wiechert, J. V. Ivy, J. Kalicki, G. Elliott, R. E. Ries, J. E. Payton, P. Westervelt, M. H. Tomasson, M. A. Watson, J. Baty, S. Heath, W. D. Shannon, R. Nagarajan, D. C. Link, M. J. Walter, T. A. Graubert, J. F. DiPersio, R. K. Wilson, and T. J. Ley. 2009. Recurring mutations found by sequencing an acute myeloid leukemia genome. *N. Engl. J. Med.* 361: 1058-1066.

59. Parsons, D. W., S. Jones, X. Zhang, J. C. Lin, R. J. Leary, P. Angenendt, P. Mankoo, H. Carter, I. M. Siu, G. L. Gallia, A. Olivi, R. McLendon, B. A. Rasheed, S. Keir, T. Nikolskaya, Y. Nikolsky, D. A. Busam, H. Tekleab, L. A. Diaz, Jr., J. Hartigan, D. R. Smith, R. L. Strausberg, S. K. Marie, S. M. Shinjo, H. Yan, G. J. Riggins, D. D. Bigner, R. Karchin, N. Papadopoulos, G. Parmigiani, B. Vogelstein, V. E. Velculescu, and K. W. Kinzler. 2008. An integrated genomic analysis of human glioblastoma multiforme. *Science (New York, N.Y.)* 321: 1807-1812.

60. Filipp, F. V., B. Ratnikov, J. De Ingeniis, J. W. Smith, A. L. Osterman, and D. A. Scott. 2012. Glutamine-fueled mitochondrial metabolism is decoupled from glycolysis in melanoma. *Pigment Cell Melanoma Res.* 25: 732-739.

61. Rakheja, D., L. J. Medeiros, S. Bevan, and W. Chen. 2013. The emerging role of d-2-hydroxyglutarate as an oncometabolite in hematolymphoid and central nervous system neoplasms. *Front. Oncol.* 3: 169.

62. Lopez, G. Y., Z. J. Reitman, D. Solomon, T. Waldman, D. D. Bigner, R. E. McLendon, S. A. Rosenberg, Y. Samuels, and H. Yan. 2010. IDH1(R132) mutation identified in one human melanoma metastasis, but not correlated with metastases to the brain. *Biochem. Biophys. Res. Commun.* 398: 585-587.

63. Shibata, T., A. Kokubu, M. Miyamoto, Y. Sasajima, and N. Yamazaki. 2011. Mutant IDH1 confers an in vivo growth in a melanoma cell line with BRAF mutation. *Am. J. Pathol.* 178: 1395-1402.

64. Dillon, B. J., V. G. Prieto, S. A. Curley, C. M. Ensor, F. W. Holtsberg, J. S. Bomalaski, and M. A. Clark. 2004. Incidence and distribution of argininosuccinate synthetase deficiency in human cancers: a method for identifying cancers sensitive to arginine deprivation. *Cancer* 100: 826-833.

65. Delage, B., D. A. Fennell, L. Nicholson, I. McNeish, N. R. Lemoine, T. Crook, and P. W. Szlosarek. 2010. Arginine deprivation and argininosuccinate synthetase expression in the treatment of cancer. *Int. J. Cancer* 126: 2762-2772.

66. Manca, A., M. C. Sini, F. Izzo, P. A. Ascierto, F. Tatangelo, G. Botti, G. Gentilcore, M. Capone, N. Mozzillo, C. Rozzo, A. Cossu, F. Tanda, and G. Palmieri. 2011. Induction of arginosuccinate synthetase (ASS) expression affects the antiproliferative activity of arginine deiminase (ADI) in melanoma cells. *Oncol. Rep.* 25: 1495-1502.

67. De Ingeniis, J., B. Ratnikov, A. D. Richardson, D. A. Scott, P. Aza-Blanc, S. K. De, M. Kazanov, M. Pellecchia, Z. Ronai, A. L. Osterman, and J. W. Smith. 2012. Functional specialization in proline biosynthesis of melanoma. *PLoS One* 7: e45190.

68. Healey, M., M. S. Crow, and C. A. Molina. 2013. Ras-induced melanoma transformation is associated with the proteasomal degradation of the transcriptional repressor ICER. *Mol. Carcinog.* 52: 692-704.

69. Albino, A. P., M. J. Vidal, N. S. McNutt, C. R. Shea, V. G. Prieto, D. M. Nanus, J. M. Palmer, and N. K. Hayward. 1994. Mutation and expression of the p53 gene in human malignant melanoma. *Melanoma Res.* 4: 35-45.

70. Cancer Genome Atlas, N. 2015. Genomic classification of cutaneous melanoma. *Cell* 161: 1681-1696.

71. Hodis, E., I. R. Watson, G. V. Kryukov, S. T. Arold, M. Imielinski, J. P. Theurillat, E. Nickerson, D. Auclair, L. Li, C. Place, D. Dicara, A. H. Ramos, M. S. Lawrence, K. Cibulskis, A. Sivachenko, D. Voet, G. Saksena, N. Stransky, R. C. Onofrio, W. Winckler, K. Ardlie, N. Wagle, J. Wargo, K. Chong, D. L. Morton, K. Stemke-Hale, G. Chen, M. Noble, M. Meyerson, J. E. Ladbury, M. A. Davies, J. E. Gershenwald, S. N. Wagner, D. S. Hoon, D. Schadendorf, E. S. Lander, S. B. Gabriel, G. Getz, L. A. Garraway, and L. Chin. 2012. A landscape of driver mutations in melanoma. *Cell* 150: 251-263.

72. Volkenandt, M., U. Schlegel, D. M. Nanus, and A. P. Albino. 1991. Mutational analysis of the human p53 gene in malignant melanoma. *Pigment Cell Melanoma Res.* 4: 35-40.

73. Weiss, J., K. Schwechheimer, W. K. Cavenee, M. Herlyn, and K. C. Arden. 1993. Mutation and expression of the p53 gene in malignant melanoma cell lines. *Int. J. Cancer* 54: 693-699.

74. Michael, D., and M. Oren. 2003. The p53-Mdm2 module and the ubiquitin system. *Semin. Cancer Biol.* 13: 49-58.

75. Anwar, A., D. A. Norris, and M. Fujita. 2011. Ubiquitin proteasomal pathway mediated degradation of p53 in melanoma. *Arch. Biochem. Biophys.* 508: 198-203.

76. Ji, Z., C. N. Njauw, M. Taylor, V. Neel, K. T. Flaherty, and H. Tsao. 2012. p53 rescue through HDM2 antagonism suppresses melanoma growth and potentiates MEK inhibition. *The Journal of Investigative Dermatology* 132: 356-364.

77. Worrall, C., N. Suleymanova, C. Crudden, I. Trocoli Drakensjo, E. Candrea, D. Nedelcu, S. I. Takahashi, L. Girnita, and A. Girnita. 2017. Unbalancing p53/Mdm2/IGF-1R axis by

Mdm2 activation restrains the IGF-1-dependent invasive phenotype of skin melanoma. *Oncogene* 36: 3274-3286.

78. Menendez, J. A., and R. Lupu. 2007. Fatty acid synthase and the lipogenic phenotype in cancer pathogenesis. *Nature Reviews.Cancer* 7: 763-777.

79. Kersten, S. 2001. Mechanisms of nutritional and hormonal regulation of lipogenesis. *EMBO Reports* 2: 282-286.

80. Kim, J. B., P. Sarraf, M. Wright, K. M. Yao, E. Mueller, G. Solanes, B. B. Lowell, and B. M. Spiegelman. 1998. Nutritional and insulin regulation of fatty acid synthetase and leptin gene expression through ADD1/SREBP1. *J. Clin. Investig.* 101: 1-9.

81. Saab, J., M. L. Santos-Zabala, M. Loda, E. C. Stack, and T. J. Hollmann. 2017. Fatty Acid Synthase and Acetyl-CoA Carboxylase Are Expressed in Nodal Metastatic Melanoma But Not in Benign Intracapsular Nodal Nevi. *The American Journal of Dermatopathology*.

82. Sumantran, V. N., P. Mishra, and N. Sudhakar. 2015. Microarray analysis of differentially expressed genes regulating lipid metabolism during melanoma progression. *Indian J. Biochem. Biophys.* 52: 125-131.

83. Thomas, C. P., A. Buronfosse, V. Combaret, S. Pedron, B. Fertil, and J. Portoukalian. 1996. Gangliosides protect human melanoma cells from ionizing radiation-induced clonogenic cell death. *Glycoconj. J.* 13: 377-384.

84. Hamamura, K., K. Furukawa, T. Hayashi, T. Hattori, J. Nakano, H. Nakashima, T. Okuda, H. Mizutani, H. Hattori, M. Ueda, T. Urano, and K. O. Lloyd. 2005. Ganglioside GD3 promotes cell growth and invasion through p130Cas and paxillin in malignant melanoma cells. *Proc. Natl. Acad. Sci. U. S. A.* 102: 11041-11046.

85. Rodrigues, M. F., E. Obre, F. H. de Melo, G. C. Santos, Jr., A. Galina, M. G. Jasiulionis, R. Rossignol, F. D. Rumjanek, and N. D. Amoedo. 2016. Enhanced OXPHOS,

glutaminolysis and beta-oxidation constitute the metastatic phenotype of melanoma cells. *The Biochemical Journal* 473: 703-715.

86. Carracedo, A., D. Weiss, A. K. Leliaert, M. Bhasin, V. C. de Boer, G. Laurent, A. C. Adams, M. Sundvall, S. J. Song, K. Ito, L. S. Finley, A. Egia, T. Libermann, Z. Gerhart-Hines, P. Puigserver, M. C. Haigis, E. Maratos-Flier, A. L. Richardson, Z. T. Schafer, and P. P. Pandolfi. 2012. A metabolic prosurvival role for PML in breast cancer. *J. Clin. Investig.* 122: 3088-3100.

87. Carracedo, A., L. C. Cantley, and P. P. Pandolfi. 2013. Cancer metabolism: fatty acid oxidation in the limelight. *Nature Reviews.Cancer* 13: 227-232.

88. Zaugg, K., Y. Yao, P. T. Reilly, K. Kannan, R. Kiarash, J. Mason, P. Huang, S. K. Sawyer, B. Fuerth, B. Faubert, T. Kalliomaki, A. Elia, X. Luo, V. Nadeem, D. Bungard, S. Yalavarthi, J. D. Growney, A. Wakeham, Y. Moolani, J. Silvester, A. Y. Ten, W. Bakker, K. Tsuchihara, S. L. Berger, R. P. Hill, R. G. Jones, M. Tsao, M. O. Robinson, C. B. Thompson, G. Pan, and T. W. Mak. 2011. Carnitine palmitoyltransferase 1C promotes cell survival and tumor growth under conditions of metabolic stress. *Genes Dev.* 25: 1041-1051.

89. Chen, G., N. Chakravarti, K. Aardalen, A. J. Lazar, M. Tetzlaff, B. Wubberhorst, S.-B. Kim, S. Kopetz, A. Ledoux, V. G. Yennu Nanda, C. Goncalves Pereira, W. Deng, J.-S. Lee, K. L. Nathanson, K. D. Aldape, V. G. Prieto, D. Stuart, and M. A. Davies. 2014. Molecular Profiling of Patient-Matched Brain and Extracranial Melanoma Metastases Implicates the PI3K Pathway as a Therapeutic Target. *Clinical Cancer Research* 20: 5337-5346.

90. Colombino, M., M. Capone, A. Lissia, A. Cossu, C. Rubino, V. De Giorgi, D. Massi, E. Fonsatti, S. Staibano, O. Nappi, E. Pagani, M. Casula, A. Manca, M. Sini, R. Franco, G.

Botti, C. Caraco, N. Mozzillo, P. A. Ascierto, and G. Palmieri. 2012. BRAF/NRAS mutation frequencies among primary tumors and metastases in patients with melanoma. *J. Clin. Oncol.* 30: 2522-2529.

91. Pollock, P. M., U. L. Harper, K. S. Hansen, L. M. Yudt, M. Stark, C. M. Robbins, T. Y. Moses, G. Hostetter, U. Wagner, J. Kakareka, G. Salem, T. Pohida, P. Heenan, P. Duray, O. Kallioniemi, N. K. Hayward, J. M. Trent, and P. S. Meltzer. 2003. High frequency of BRAF mutations in nevi. *Nat. Genet.* 33: 19-20.

92. Shain, A. H., I. Yeh, I. Kovalyshyn, A. Sriharan, E. Talevich, A. Gagnon, R. Dummer, J. North, L. Pincus, B. Ruben, W. Rickaby, C. D'Arrigo, A. Robson, and B. C. Bastian. 2015. The Genetic Evolution of Melanoma from Precursor Lesions. *N. Engl. J. Med.* 373: 1926-1936.

93. Davies, M. A. 2011. Regulation, Role, and Targeting of Akt in Cancer. *J Clin Oncol* 29: 4715-4717.

94. Kwong, L. N., and M. A. Davies. 2014. Targeted therapy for melanoma: rational combinatorial approaches. *Oncogene* 33: 1-9.

95. Omholt, K., D. Krockel, U. Ringborg, and J. Hansson. 2006. Mutations of PIK3CA are rare in cutaneous melanoma. *Melanoma Res.* 16: 197-200.

96. Davies, M. A., K. Stemke-Hale, C. Tellez, T. L. Calderone, W. Deng, V. G. Prieto, A. J. Lazar, J. E. Gershenwald, and G. B. Mills. 2008. A novel AKT3 mutation in melanoma tumours and cell lines. *Br J Cancer* 99: 1265-1268.

97. Bucheit, A. D., G. Chen, A. Siroy, M. Tetzlaff, R. Broaddus, D. Milton, P. Fox, R. Bassett, P. Hwu, J. E. Gershenwald, A. J. Lazar, and M. A. Davies. 2014. Complete loss of PTEN protein expression correlates with shorter time to brain metastasis and survival in stage IIIB/C melanoma patients with BRAFV600 mutations. *Clin Cancer Res* 20: 5527-5536.

98. Davies, M. A., K. Stemke-Hale, E. Lin, C. Tellez, W. Deng, Y. N. Gopal, S. E. Woodman, T. C. Calderone, Z. Ju, A. J. Lazar, V. G. Prieto, K. Aldape, G. B. Mills, and J. E. Gershenwald. 2009. Integrated Molecular and Clinical Analysis of AKT Activation in Metastatic Melanoma. *Clin Cancer Res* 15: 7538-7546.

99. Aguissa-Toure, A. H., and G. Li. 2012. Genetic alterations of PTEN in human melanoma. *Cell. Mol. Life Sci.* 69: 1475-1491.

100. Mirmohammadsadegh, A., A. Marini, S. Nambiar, M. Hassan, A. Tannapfel, T. Ruzicka, and U. R. Hengge. 2006. Epigenetic silencing of the PTEN gene in melanoma. *Cancer Res.* 66: 6546-6552.

101. Zhang, L., S. Zhang, J. Yao, F. J. Lowery, Q. Zhang, W. C. Huang, P. Li, M. Li, X. Wang, C. Zhang, H. Wang, K. Ellis, M. Cheerathodi, J. H. McCarty, D. Palmieri, J. Saunus, S. Lakhani, S. Huang, A. A. Sahin, K. D. Aldape, P. S. Steeg, and D. Yu. 2015. Microenvironment-induced PTEN loss by exosomal microRNA primes brain metastasis outgrowth. *Nature* 527: 100-104.

102. Roszik, J., C. J. Wu, A. E. Siroy, A. J. Lazar, M. A. Davies, S. E. Woodman, and L. N. Kwong. 2016. Somatic Copy Number Alterations at Oncogenic Loci Show Diverse Correlations with Gene Expression. *Sci. Rep.* 6: 19649.

103. Niessner, H., A. Forschner, B. Klumpp, J. B. Honegger, M. Witte, A. Bornemann, R. Dummer, A. Adam, J. Bauer, G. Tabatabai, K. Flaherty, T. Sinnberg, D. Beck, U. Leiter, C. Mauch, A. Roesch, B. Weide, T. Eigentler, D. Schadendorf, C. Garbe, D. Kulms, L. Quintanilla-Martinez, and F. Meier. 2013. Targeting hyperactivation of the AKT survival pathway to overcome therapy resistance of melanoma brain metastases. *Cancer Medicine* 2: 76-85.

104. Cho, J. H., J. P. Robinson, R. A. Arave, W. J. Burnett, D. A. Kircher, G. Chen, M. A. Davies, A. H. Grossmann, M. W. VanBrocklin, M. McMahon, and S. L. Holmen. 2015. AKT1 activation promotes the development of melanoma metastases. *Cell Reports* 13: 898-905.

105. Seifert, H., E. Hirata, M. Gore, K. Khabra, C. Messiou, J. Larkin, and E. Sahai. 2016. Extrinsic factors can mediate resistance to BRAF inhibition in central nervous system melanoma metastases. *Pigment Cell & Melanoma Research* 29: 92-100.

106. Jatiani, S. S., S. J. Baker, L. R. Silverman, and E. P. Reddy. 2010. Jak/STAT pathways in cytokine signaling and myeloproliferative disorders: approaches for targeted therapies. *Genes Cancer* 1: 979-993.

107. Yu, H., and R. Jove. 2004. The STATs of cancer--new molecular targets come of age. *Nat. Rev. Cancer* 4: 97-105.

108. Xie, T. X., F. J. Huang, K. D. Aldape, S. H. Kang, M. Liu, J. E. Gershenwald, K. Xie, R. Sawaya, and S. Huang. 2006. Activation of stat3 in human melanoma promotes brain metastasis. *Cancer Res.* 66: 3188-3196.

109. Huang, F. J., P. S. Steeg, J. E. Price, W. T. Chiu, P. C. Chou, K. Xie, R. Sawaya, and S. Huang. 2008. Molecular basis for the critical role of suppressor of cytokine signaling-1 in melanoma brain metastasis. *Cancer Res.* 68: 9634-9642.

110. Ferrara, N., H. P. Gerber, and J. LeCouter. 2003. The biology of VEGF and its receptors. *Nat. Med.* 9: 669-676.

111. Guo, D., Q. Jia, H. Y. Song, R. S. Warren, and D. B. Donner. 1995. Vascular endothelial cell growth factor promotes tyrosine phosphorylation of mediators of signal transduction that contain SH2 domains. Association with endothelial cell proliferation. *J. Biol. Chem.* 270: 6729-6733.

112. Eliceiri, B. P., R. Paul, P. L. Schwartzberg, J. D. Hood, J. Leng, and D. A. Cheresh. 1999. Selective requirement for Src kinases during VEGF-induced angiogenesis and vascular permeability. *Mol. Cell* 4: 915-924.

113. Yano, S., H. Shinohara, R. S. Herbst, H. Kuniyasu, C. D. Bucana, L. M. Ellis, D. W. Davis, D. J. McConkey, and I. J. Fidler. 2000. Expression of vascular endothelial growth factor is necessary but not sufficient for production and growth of brain metastasis. *Cancer Res.* 60: 4959-4967.

114. Kusters, B., W. P. Leenders, P. Wesseling, D. Smits, K. Verrijp, D. J. Ruiter, J. P. Peters, A. J. van Der Kogel, and R. M. de Waal. 2002. Vascular endothelial growth factor-A(165) induces progression of melanoma brain metastases without induction of sprouting angiogenesis. *Cancer Res.* 62: 341-345.

115. Berghoff, A. S., O. Rajky, F. Winkler, R. Bartsch, J. Furtner, J. A. Hainfellner, S. L. Goodman, M. Weller, J. Schittenhelm, and M. Preusser. 2013. Invasion patterns in brain metastases of solid cancers. *Neuro Oncol.* 15: 1664-1672.

116. Cruz-Munoz, W., M. L. Jaramillo, S. Man, P. Xu, M. Banville, C. Collins, A. Nantel, G. Francia, S. S. Morgan, L. D. Cranmer, M. D. O'Connor-McCourt, and R. S. Kerbel. 2012. Roles for endothelin receptor B and BCL2A1 in spontaneous CNS metastasis of melanoma. *Cancer Res.* 72: 4909-4919.

117. Daneman, R., and A. Prat. 2015. The blood-brain barrier. *Cold Spring Harb. Perspect. Biol.* 7: a020412.

118. Pardridge, W. M. 2003. Blood-brain barrier drug targeting: the future of brain drug development. *Mol. Interv.* 3: 90-105, 151.

119. Kircher, D. A., M. R. Silvis, J. H. Cho, and S. L. Holmen. 2016. Melanoma Brain Metastasis: Mechanisms, Models, and Medicine. *Int. J. Mol. Sci.* 17.

120. Chen, G., and M. A. Davies. 2012. Emerging insights into the molecular biology of brain metastases. *Biochemical Pharmacology* 83: 305-314.

121. Garcia-Martin, A. B., P. Zwicky, T. Gruber, C. Matti, F. Moalli, J. V. Stein, D. Francisco, G. Enzmann, M. P. Levesque, E. Hewer, and R. Lyck. 2018. VLA-4 mediated adhesion of melanoma cells on the blood-brain barrier is the critical cue for melanoma cell intercalation and barrier disruption. *J. Cereb. Blood Flow Metab.*: 271678X18775887.

122. Schlesinger, M., M. Roblek, K. Ortmann, A. Naggi, G. Torri, L. Borsig, and G. Bendas. 2014. The role of VLA-4 binding for experimental melanoma metastasis and its inhibition by heparin. *Thromb. Res.* 133: 855-862.

123. Fazakas, C., I. Wilhelm, P. Nagyoszi, A. E. Farkas, J. Hasko, J. Molnar, H. Bauer, H. C. Bauer, F. Ayaydin, N. T. Dung, L. Siklos, and I. A. Krizbai. 2011. Transmigration of melanoma cells through the blood-brain barrier: role of endothelial tight junctions and melanoma-released serine proteases. *PLoS One* 6: e20758.

124. Marchetti, D. 1997. Specific degradation of subendothelial matrix proteoglycans by brain-metastatic melanoma and brain endothelial cell heparanases. *J Cell Physiol* 172: 334-342.

125. Murry, B. P., B. E. Blust, A. Singh, T. P. Foster, and D. Marchetti. 2006. Heparanase mechanisms of melanoma metastasis to the brain: Development and use of a brain slice model. *J. Cell. Biochem.* 97: 217-225.

126. Marchetti, D., J. Li, and R. Shen. 2000. Astrocytes contribute to the brain-metastatic specificity of melanoma cells by producing heparanase. *Cancer Res.* 60: 4767-4770.

127. Marchetti, D., D. Menter, L. Jin, M. Nakajima, and G. L. Nicolson. 1993. Nerve growth factor effects on human and mouse melanoma cell invasion and heparanase production. *Int. J. Cancer* 55: 692-699.

128. Zhang, L., P. S. Sullivan, J. C. Goodman, P. H. Gunaratne, and D. Marchetti. 2011. MicroRNA-1258 suppresses breast cancer brain metastasis by targeting heparanase. *Cancer Res.* 71: 645-654.

129. Jilaveanu, L. B., F. Parisi, M. L. Barr, C. R. Zito, W. Cruz-Munoz, R. S. Kerbel, D. L. Rimm, M. W. Bosenberg, R. Halaban, Y. Kluger, and H. M. Kluger. 2015. PLEKHA5 as a Biomarker and Potential Mediator of Melanoma Brain Metastasis. *Clin. Cancer Res.* 21: 2138-2147.

130. Herwig, N., B. Belter, and J. Pietzsch. 2016. Extracellular S100A4 affects endothelial cell integrity and stimulates transmigration of A375 melanoma cells. *Biochem Biophys Res Commun* 477: 963-969.

131. Gialeli, C., A. D. Theocharis, and N. K. Karamanos. 2011. Roles of matrix metalloproteinases in cancer progression and their pharmacological targeting. *FEBS J* 278: 16-27.

132. Rotte, A., M. Martinka, and G. Li. 2012. MMP2 expression is a prognostic marker for primary melanoma patients. *Cell Oncol (Dordr)* 35: 207-216.

133. Rizzo, A., C. Vasco, V. Girgenti, V. Fugnanesi, C. Calatozzolo, A. Canazza, A. Salmaggi, L. Rivoltini, M. Morbin, and E. Ciusani. 2015. Melanoma cells homing to the brain: an in vitro model. *Biomed Res Int* 2015: 476069.

134. Klein, A., H. Schwartz, O. Sagi-Assif, T. Meshel, S. Izraely, S. Ben Menachem, R. Bengaiev, A. Ben-Shmuel, C. Nahmias, P. O. Couraud, I. P. Witz, and N. Erez. 2015. Astrocytes facilitate melanoma brain metastasis via secretion of IL-23. *J. Pathol.* 236: 116-127.

135. Tang, Q., J. Li, H. Zhu, P. Li, Z. Zou, and Y. Xiao. 2013. Hmgb1-IL-23-IL-17-IL-6-Stat3 axis promotes tumor growth in murine models of melanoma. *Mediators Inflamm.* 2013: 713859.

136. Kienast, Y., L. von Baumgarten, M. Fuhrmann, W. E. Klinkert, R. Goldbrunner, J. Herms, and F. Winkler. 2010. Real-time imaging reveals the single steps of brain metastasis formation. *Nat. Med.* 16: 116-122.

137. Hanniford, D., J. Zhong, L. Koetz, A. Gaziel-Sovran, D. J. Lackaye, S. Shang, A. Pavlick, R. Shapiro, R. Berman, F. Darvishian, Y. Shao, I. Osman, and E. Hernando. 2015. A miRNA-Based Signature Detected in Primary Melanoma Tissue Predicts Development of Brain Metastasis. *Clin. Cancer Res.* 21: 4903-4912.

138. Zhang, C., F. Zhang, R. Tsan, and I. J. Fidler. 2009. Transforming growth factor-beta2 is a molecular determinant for site-specific melanoma metastasis in the brain. *Cancer Res.* 69: 828-835.

139. Izraely, S., A. Klein, O. Sagi-Assif, T. Meshel, G. Tsarfaty, D. S. Hoon, and I. P. Witz. 2010. Chemokine-chemokine receptor axes in melanoma brain metastasis. *Immunol. Lett.* 130: 107-114.

140. Klein, A., O. Sagi-Assif, T. Meshel, A. Telerman, S. Izraely, S. Ben-Menachem, J. Bayry, D. M. Marzese, S. Ohe, D. S. B. Hoon, N. Erez, and I. P. Witz. 2017. CCR4 is a determinant of melanoma brain metastasis. *Oncotarget* 8: 31079-31091.

141. Izraely, S., O. Sagi-Assif, A. Klein, T. Meshel, G. Tsarfaty, M. Pasmanik-Chor, C. Nahmias, P. O. Couraud, E. Ateh, J. L. Bryant, D. S. Hoon, and I. P. Witz. 2012. The metastatic microenvironment: brain-residing melanoma metastasis and dormant micrometastasis. *Int. J. Cancer* 131: 1071-1082.

142. Izraely, S., O. Sagi-Assif, A. Klein, T. Meshel, S. Ben-Menachem, A. Zaritsky, M. Ehrlich, V. G. Prieto, M. Bar-Eli, C. Pirker, W. Berger, C. Nahmias, P. O. Couraud, D. S. Hoon, and I. P. Witz. 2015. The metastatic microenvironment: Claudin-1 suppresses the malignant phenotype of melanoma brain metastasis. *Int. J. Cancer* 136: 1296-1307.

143. Hamilton, R., M. Krauze, M. Romkes, B. Omolo, P. Konstantinopoulos, T. Reinhart, M. Harasymczuk, Y. Wang, Y. Lin, S. Ferrone, T. Whiteside, S. Bortoluzzi, J. Werley, T. Nukui, B. Fallert-Junecko, D. Kondziolka, J. Ibrahim, D. Becker, J. Kirkwood, and S. Moschos. 2013. Pathologic and gene expression features of metastatic melanomas to the brain. *Cancer* 119: 2737-2746.

144. Brastianos, P. K., S. L. Carter, S. Santagata, D. P. Cahill, A. Taylor-Weiner, R. T. Jones, E. M. Van Allen, M. S. Lawrence, P. M. Horowitz, K. Cibulskis, K. L. Ligon, J. Tabernero, J. Seoane, E. Martinez-Saez, W. T. Curry, I. F. Dunn, S. H. Paek, S. H. Park, A. McKenna, A. Chevalier, M. Rosenberg, F. G. Barker, 2nd, C. M. Gill, P. Van Hummelen, A. R. Thorner, B. E. Johnson, M. P. Hoang, T. K. Choueiri, S. Signoretti, C. Sougnez, M. S. Rabin, N. U. Lin, E. P. Winer, A. Stemmer-Rachamimov, M. Meyerson, L. Garraway, S. Gabriel, E. S. Lander, R. Beroukhim, T. T. Batchelor, J. Baselga, D. N. Louis, G. Getz, and W. C. Hahn. 2015. Genomic characterization of brain metastases reveals branched evolution and potential therapeutic targets. *Cancer Discov.* 5: 1164-1177.

145. Park, E. S., S. J. Kim, S. W. Kim, S. L. Yoon, S. H. Leem, S. B. Kim, S. M. Kim, Y. Y. Park, J. H. Cheong, H. G. Woo, G. B. Mills, I. J. Fidler, and J. S. Lee. 2011. Cross-species hybridization of microarrays for studying tumor transcriptome of brain metastasis. *Proc. Natl. Acad. Sci. U. S. A.* 108: 17456-17461.

146. Jonsson, G., C. Busch, S. Knappskog, J. Geisler, H. Miletic, M. Ringner, J. R. Lillehaug, A. Borg, and P. E. Lonning. 2010. Gene expression profiling-based identification of molecular subtypes in stage IV melanomas with different clinical outcome. *Clin. Cancer Res.* 16: 3356-3367.

147. Kluger, H. M., C. R. Zito, M. L. Barr, M. K. Baine, V. L. Chiang, M. Sznol, D. L. Rimm, L. Chen, and L. B. Jilaveanu. 2015. Characterization of PD-L1 Expression and Associated T-cell Infiltrates in Metastatic Melanoma Samples from Variable Anatomic Sites. *Clin. Cancer Res.* 21: 3052-3060.

148. Kwong, L. N., M. P. De Macedo, L. Haydu, A. Y. Joon, M. T. Tetzlaff, T. L. Calderone, and C. J. Wu. 2018. Biological validation of RNA sequencing data from formalin-fixed paraffin-embedded primary melanomas. *JCO Precision Oncology* 2: 1-19.

149. Chen, K., F. Meric-Bernstam, H. Zhao, Q. Zhang, N. Ezzeddine, L. Y. Tang, Y. Qi, Y. Mao, T. Chen, Z. Chong, W. Zhou, X. Zheng, A. Johnson, K. D. Aldape, M. J. Routbort, R. Luthra, S. Kopetz, M. A. Davies, J. de Groot, S. Moulder, R. Vinod, C. J. Farhangfar, K. M. Shaw, J. Mendelsohn, G. B. Mills, and A. K. Eterovic. 2015. Clinical actionability enhanced through deep targeted sequencing of solid tumors. *Clin. Chem.* 61: 544-553.

150. Reuben, A., R. Gittelman, J. Gao, J. Zhang, E. C. Yusko, C. J. Wu, R. Emerson, C. Tipton, J. Li, K. Quek, V. Gopalakrishnan, R. Chen, L. M. Vence, T. Cascone, M. Vignali, J. Fujimoto, J. Rodriguez-Canales, E. R. Parra, L. D. Little, C. Gumbs, M. A. Forget, L. Federico, C. Haymaker, C. Behrens, S. Benzeno, C. Bernatchez, B. Sepesi, D. L. Gibbons, J. A. Wargo, W. N. William, Jr., S. Swisher, J. V. Heymach, H. Robins, J. J. Lee, P. Sharma, J. P. Allison, P. A. Futreal, and I. I. Wistuba. 2017. TCR repertoire intratumor heterogeneity in localized lung adenocarcinomas: an association with predicted neoantigen heterogeneity and postsurgical recurrence. *Cancer Discov.* 7: 1088-1097.

151. Tumeh, P. C., C. L. Harview, J. H. Yearley, I. P. Shintaku, E. J. Taylor, L. Robert, B. Chmielowski, M. Spasic, G. Henry, V. Ciobanu, A. N. West, M. Carmona, C. Kivork, E. Seja, G. Cherry, A. J. Gutierrez, T. R. Grogan, C. Mateus, G. Tomasic, J. A. Glaspy, R. O. Emerson, H. Robins, R. H. Pierce, D. A. Elashoff, C. Robert, and A. Ribas. 2014. PD-1 blockade induces responses by inhibiting adaptive immune resistance. *Nature* 515: 568-571.

152. Chen, P. L., W. Roh, A. Reuben, Z. A. Cooper, C. N. Spencer, P. A. Prieto, J. P. Miller, R. L. Bassett, V. Gopalakrishnan, K. Wani, M. P. De Macedo, J. L. Austin-Breneman, H. Jiang, Q. Chang, S. M. Reddy, W. S. Chen, M. T. Tetzlaff, R. J. Broaddus, M. A. Davies, J. E. Gershenwald, L. Haydu, A. J. Lazar, S. P. Patel, P. Hwu, W. J. Hwu, A. Diab, I. C. Glitza, S. E. Woodman, L. M. Vence, I. I. Wistuba, R. N. Amaria, L. N. Kwong, V. Prieto, R. E. Davis, W. Ma, W. W. Overwijk, A. H. Sharpe, J. Hu, P. A. Futreal, J. Blando, P. Sharma, J. P. Allison, L. Chin, and J. A. Wargo. 2016. Analysis of immune signatures in longitudinal tumor samples yields insight into biomarkers of response and mechanisms of resistance to immune checkpoint blockade. *Cancer Discov.* 6: 827-837.

153. Goldberg, S. B., S. N. Gettinger, A. Mahajan, A. C. Chiang, R. S. Herbst, M. Sznol, A. J. Tsiouris, J. Cohen, A. Vortmeyer, L. Jilaveanu, J. Yu, U. Hegde, S. Speaker, M. Madura, A. Ralabate, A. Rivera, E. Rowen, H. Gerrish, X. Yao, V. Chiang, and H. M. Kluger. 2016. Pembrolizumab for patients with melanoma or non-small-cell lung cancer and untreated brain metastases: early analysis of a non-randomised, open-label, phase 2 trial. *Lancet Oncol.* 17: 976-983.

154. Long, G. V., V. Atkinson, A. M. Menzies, S. Lo, A. D. Guminski, M. P. Brown, M. M. Gonzalez, K. Diamante, S. K. Sandhu, R. A. Scolyer, L. Emmett, and G. A. McArthur. 2017. A randomized phase II study of nivolumab or nivolumab combined with ipilimumab

in patients (pts) with melanoma brain metastases (mets): The Anti-PD1 Brain Collaboration (ABC). *J. Clin. Oncol.* 35: 9508-9508.

155. Tawbi, H. A., P. A. Forsyth, A. Algazi, O. Hamid, F. S. Hodi, S. J. Moschos, N. I. Khushalani, K. Lewis, C. D. Lao, M. A. Postow, M. B. Atkins, M. S. Ernstoff, D. A. Reardon, I. Puzanov, R. R. Kudchadkar, R. P. Thomas, A. Tarhini, A. C. Pavlick, J. Jiang, A. Avila, S. Demelo, and K. Margolin. 2018. Combined nivolumab and ipilimumab in melanoma metastatic to the brain. *N. Engl. J. Med.* 379: 722-730.

156. Chen, W.-S., M. C. Andrews, C. Spencer, H. A.-H. Tawbi, A. Lazar, M. T. Tetzlaff, S. P. Patel, P. Hwu, W.-J. Hwu, A. Diab, I. C. Glitza, R. N. Amaria, E. M. Burton, S. E. Woodman, M. A. Davies, J. E. Gershenwald, P. Sharma, J. P. Allison, A. Futreal, and J. A. Wargo. 2017. Molecular and immune predictors of response and toxicity to combined CTLA-4 and PD-1 blockade in metastatic melanoma (MM) patients (pts). *J. Clin. Oncol.* 35: suppl; abstr 9579.

157. Obermeier, B., R. Daneman, and R. M. Ransohoff. 2013. Development, maintenance and disruption of the blood-brain barrier. *Nat. Med.* 19: 1584-1596.

158. Goldberg, S. B., S. N. Gettinger, A. Mahajan, A. C. Chiang, R. S. Herbst, M. Sznol, A. J. Tsiouris, J. Cohen, A. Vortmeyer, L. Jilaveanu, J. Yu, U. Hegde, S. Speaker, M. Madura, A. Ralabate, A. Rivera, E. Rowen, H. Gerrish, X. Yao, V. Chiang, and H. M. Kluger. 2016. Pembrolizumab for patients with melanoma or non-small-cell lung cancer and untreated brain metastases: early analysis of a non-randomised, open-label, phase 2 trial. *The Lancet Oncology* 17: 976-983.

159. Margolin, K., M. S. Ernstoff, O. Hamid, D. Lawrence, D. McDermott, I. Puzanov, J. D. Wolchok, J. I. Clark, M. Sznol, T. F. Logan, J. Richards, T. Michener, A. Balogh, K. N.

Heller, and F. S. Hodi. 2012. Ipilimumab in patients with melanoma and brain metastases: an open-label, phase 2 trial. *The Lancet Oncology* 13: 459-465.

160. Peng, W., J. Q. Chen, C. Liu, S. Malu, C. Creasy, M. T. Tetzlaff, C. Xu, J. A. McKenzie, C. Zhang, X. Liang, L. J. Williams, W. Deng, G. Chen, R. Mbofung, A. J. Lazar, C. A. Torres-Cabala, Z. A. Cooper, P. L. Chen, T. N. Tieu, S. Spranger, X. Yu, C. Bernatchez, M. A. Forget, C. Haymaker, R. Amaria, J. L. McQuade, I. C. Glitza, T. Cascone, H. S. Li, L. N. Kwong, T. P. Heffernan, J. Hu, R. L. Bassett, Jr., M. W. Bosenberg, S. E. Woodman, W. W. Overwijk, G. Lizee, J. Roszik, T. F. Gajewski, J. A. Wargo, J. E. Gershenwald, L. Radvanyi, M. A. Davies, and P. Hwu. 2016. Loss of PTEN promotes resistance to T cell-mediated immunotherapy. *Cancer Discov.* 6: 202-216.

161. Spranger, S., R. Bao, and T. F. Gajewski. 2015. Melanoma-intrinsic beta-catenin signalling prevents anti-tumour immunity. *Nature* 523: 231-235.

162. Van Allen, E. M., D. Miao, B. Schilling, S. A. Shukla, C. Blank, L. Zimmer, A. Sucker, U. Hillen, M. H. G. Foppen, S. M. Goldinger, J. Utikal, J. C. Hassel, B. Weide, K. C. Kaehler, C. Loquai, P. Mohr, R. Gutzmer, R. Dummer, S. Gabriel, C. J. Wu, D. Schadendorf, and L. A. Garraway. 2015. Genomic correlates of response to CTLA-4 blockade in metastatic melanoma. *Science* 350: 207-211.

163. Yang, L., Y. Pang, and H. L. Moses. 2010. TGF-beta and immune cells: an important regulatory axis in the tumor microenvironment and progression. *Trends Immunol.* 31: 220-227.

164. Gigante, M., L. Gesualdo, and E. Ranieri. 2012. TGF-beta: a master switch in tumor immunity. *Curr. Pharm. Des.* 18: 4126-4134.

165. Walentynowicz, K. A., N. Ochocka, M. Pasierbinska, K. Wojnicki, K. Stepniak, J. Mieczkowski, I. A. Ciechomska, and B. Kaminska. 2018. In Search for Reliable Markers of Glioma-Induced Polarization of Microglia. *Front. Immunol.* 9: 1329.

166. Priego, N., L. Zhu, C. Monteiro, M. Mulders, D. Wasilewski, W. Bindeman, L. Doglio, L. Martinez, E. Martinez-Saez, S. R. Y. Cajal, D. Megias, E. Hernandez-Encinas, C. Blanco-Aparicio, L. Martinez, E. Zarzuela, J. Munoz, C. Fustero-Torre, E. Pineiro-Yanez, A. Hernandez-Lain, L. Bertero, V. Poli, M. Sanchez-Martinez, J. A. Menendez, R. Soffietti, J. Bosch-Barrera, and M. Valiente. 2018. STAT3 labels a subpopulation of reactive astrocytes required for brain metastasis. *Nat. Med.* 24: 1024-1035.

167. Glitza, I. C., A. B. Heimberger, E. P. Sulman, M. A. Davies, and M. Hayat. 2016. Prognostic factors for survival in melanoma patients with brain metastases. In *Brain Metastases from Primary Tumors, Volume 3: Epidemiology, Biology, and Therapy of Melanoma and Other Cancers*. Academic Press, Boston, MA. 267-292.

168. Margolin, K., M. S. Ernstoff, O. Hamid, D. Lawrence, D. McDermott, I. Puzanov, J. D. Wolchok, J. I. Clark, M. Sznol, T. F. Logan, J. Richards, T. Michener, A. Balogh, K. N. Heller, and F. S. Hodi. 2012. Ipilimumab in patients with melanoma and brain metastases: an open-label, phase 2 trial. *Lancet Oncol.* 13: 459-465.

169. McArthur, G. A., M. Maio, A. Arance, P. Nathan, C. Blank, M. F. Avril, C. Garbe, A. Hauschild, D. Schadendorf, O. Hamid, M. Fluck, M. Thebeau, J. Schachter, R. Kefford, M. Chamberlain, M. Makrutzki, S. Robson, R. Gonzalez, and K. Margolin. 2017. Vemurafenib in metastatic melanoma patients with brain metastases: an open-label, single-arm, phase 2, multicentre study. *Ann. Oncol.* 28: 634-641.

170. Long, G. V., U. Trefzer, M. A. Davies, R. F. Kefford, P. A. Ascierto, P. B. Chapman, I. Puzanov, A. Hauschild, C. Robert, A. Algazi, L. Mortier, H. Tawbi, T. Wilhelm, L.

Zimmer, J. Switzky, S. Swann, A. M. Martin, M. Guckert, V. Goodman, M. Streit, J. M. Kirkwood, and D. Schadendorf. 2012. Dabrafenib in patients with Val600Glu or Val600Lys BRAF-mutant melanoma metastatic to the brain (BREAK-MB): a multicentre, open-label, phase 2 trial. *Lancet Oncol.* 13: 1087-1095.

171. Davies, M. A., P. Saiag, C. Robert, J. J. Grob, K. T. Flaherty, A. Arance, V. Chiarion-Sileni, L. Thomas, T. Lesimple, L. Mortier, S. J. Moschos, D. Hogg, I. Marquez-Rodas, M. Del Vecchio, C. Lebbe, N. Meyer, Y. Zhang, Y. Huang, B. Mookerjee, and G. V. Long. 2017. Dabrafenib plus trametinib in patients with BRAF(V600)-mutant melanoma brain metastases (COMBI-MB): a multicentre, multicohort, open-label, phase 2 trial. *Lancet Oncol.* 18: 863-873.

172. Vazquez, F., J. H. Lim, H. Chim, K. Bhalla, G. Girnun, K. Pierce, C. B. Clish, S. R. Granter, H. R. Widlund, B. M. Spiegelman, and P. Puigserver. 2013. PGC1alpha expression defines a subset of human melanoma tumors with increased mitochondrial capacity and resistance to oxidative stress. *Cancer Cell* 23: 287-301.

173. Scharping, N. E., A. V. Menk, R. D. Whetstone, X. Zeng, and G. M. Delgoffe. 2017. Efficacy of PD-1 Blockade Is Potentiated by Metformin-Induced Reduction of Tumor Hypoxia. *Cancer Immunol Res* 5: 9-16.

174. Fischer, G. M., A. Jalali, D. A. Kircher, W. C. Lee, J. L. McQuade, L. E. Haydu, A. Y. Joon, A. Reuben, M. P. de Macedo, F. C. L. Carapeto, C. Yang, A. Srivastava, C. R. Ambati, A. Sreekumar, C. W. Hudgens, B. Knighton, W. Deng, S. D. Ferguson, H. A. Tawbi, I. C. Glitza, J. E. Gershenwald, Y. N. Vashisht Gopal, P. Hwu, J. T. Huse, J. A. Wargo, P. A. Futreal, N. Putluri, A. J. Lazar, R. J. DeBerardinis, J. R. Marszalek, J. Zhang, S. L. Holmen, M. T. Tetzlaff, and M. A. Davies. 2019. Molecular Profiling Reveals

Unique Immune and Metabolic Features of Melanoma Brain Metastases. *Cancer Discov.* 9: 628-645.

175. Meeth, K., J. X. Wang, G. Micevic, W. Damsky, and M. W. Bosenberg. 2016. The YUMM lines: a series of congenic mouse melanoma cell lines with defined genetic alterations. *Pigment Cell Melanoma Res.* 29: 590-597.

176. Klein, A., O. Sagi-Assif, S. Izraely, T. Meshel, M. Pasmanik-Chor, C. Nahmias, P. O. Couraud, N. Erez, D. S. Hoon, and I. P. Witz. 2012. The metastatic microenvironment: Brain-derived soluble factors alter the malignant phenotype of cutaneous and brain-metastasizing melanoma cells. *Int. J. Cancer* 131: 2509-2518.

177. Davies, M. A., K. Stemke-Hale, E. Lin, C. Tellez, W. Deng, Y. N. Gopal, S. E. Woodman, T. C. Calderone, Z. Ju, A. J. Lazar, V. G. Prieto, K. Aldape, G. B. Mills, and J. E. Gershenwald. 2009. Integrated molecular and clinical analysis of AKT activation in metastatic melanoma. *Clin. Cancer Res.* 15: 7538-7546.

178. Molina, J. R., Y. Sun, M. Protopopova, S. Gera, M. Bandi, C. Bristow, T. McAfoos, P. Morlacchi, J. Ackroyd, A. A. Agip, G. Al-Atrash, J. Asara, J. Bardenhagen, C. C. Carrillo, C. Carroll, E. Chang, S. Ciurea, J. B. Cross, B. Czako, A. Deem, N. Daver, J. F. de Groot, J. W. Dong, N. Feng, G. Gao, J. Gay, M. G. Do, J. Greer, V. Giuliani, J. Han, L. Han, V. K. Henry, J. Hirst, S. Huang, Y. Jiang, Z. Kang, T. Khor, S. Konoplev, Y. H. Lin, G. Liu, A. Lodi, T. Lofton, H. Ma, M. Mahendra, P. Matre, R. Mullinax, M. Peoples, A. Petrocchi, J. Rodriguez-Canale, R. Serreli, T. Shi, M. Smith, Y. Tabe, J. Theroff, S. Tiziani, Q. Xu, Q. Zhang, F. Muller, R. A. DePinho, C. Toniatti, G. F. Draetta, T. P. Heffernan, M. Konopleva, P. Jones, M. E. Di Francesco, and J. R. Marszalek. 2018. An inhibitor of oxidative phosphorylation exploits cancer vulnerability. *Nat. Med.*

179. Cho, J. H., J. P. Robinson, R. A. Arave, W. J. Burnett, D. A. Kircher, G. Chen, M. A. Davies, A. H. Grossmann, M. W. VanBrocklin, M. McMahon, and S. L. Holmen. 2015. AKT1 activation promotes development of melanoma metastases. *Cell Rep.* 13: 898-905.

180. Dobin, A., C. A. Davis, F. Schlesinger, J. Drenkow, C. Zaleski, S. Jha, P. Batut, M. Chaisson, and T. R. Gingeras. 2013. STAR: ultrafast universal RNA-seq aligner. *Bioinformatics* 29: 15-21.

181. Anders, S., P. T. Pyl, and W. Huber. 2015. HTSeq--a Python framework to work with high-throughput sequencing data. *Bioinformatics* 31: 166-169.

182. Liao, Y., G. K. Smyth, and W. Shi. 2014. featureCounts: an efficient general purpose program for assigning sequence reads to genomic features. *Bioinformatics* 30: 923-930.

183. Conway, T., J. Wazny, A. Bromage, M. Tymms, D. Sooraj, E. D. Williams, and B. Beresford-Smith. 2012. Xenome--a tool for classifying reads from xenograft samples. *Bioinformatics* 28: i172-178.

184. Li, B., and C. N. Dewey. 2011. RSEM: accurate transcript quantification from RNA-Seq data with or without a reference genome. *BMC Bioinformatics* 12: 323.

185. Law, C. W., M. Alhamdoosh, S. Su, G. K. Smyth, and M. E. Ritchie. 2016. RNA-seq analysis is easy as 1-2-3 with limma, Glimma and edgeR. *F1000Research* 5: 1408.

186. Roh, W., P. L. Chen, A. Reuben, C. N. Spencer, P. A. Prieto, J. P. Miller, V. Gopalakrishnan, F. Wang, Z. A. Cooper, S. M. Reddy, C. Gumbs, L. Little, Q. Chang, W. S. Chen, K. Wani, M. P. De Macedo, E. Chen, J. L. Austin-Breneman, H. Jiang, J. Roszik, M. T. Tetzlaff, M. A. Davies, J. E. Gershenwald, H. Tawbi, A. J. Lazar, P. Hwu, W. J. Hwu, A. Diab, I. C. Glitza, S. P. Patel, S. E. Woodman, R. N. Amaria, V. G. Prieto, J. Hu, P. Sharma, J. P. Allison, L. Chin, J. Zhang, J. A. Wargo, and P. A. Futreal. 2017. Integrated

molecular analysis of tumor biopsies on sequential CTLA-4 and PD-1 blockade reveals markers of response and resistance. *Sci. Transl. Med.* 9: 10.1126/scitranslmed.aah3560.

187. Subramanian, A., P. Tamayo, V. K. Mootha, S. Mukherjee, B. L. Ebert, M. A. Gillette, A. Paulovich, S. L. Pomeroy, T. R. Golub, E. S. Lander, and J. P. Mesirov. 2005. Gene set enrichment analysis: a knowledge-based approach for interpreting genome-wide expression profiles. *Proc. Natl. Acad. Sci. U. S. A.* 102: 15545-15550.

188. Cascone, T., J. A. McKenzie, R. M. Mbofung, S. Punt, Z. Wang, C. Xu, L. J. Williams, Z. Wang, C. A. Bristow, A. Carugo, M. D. Peoples, L. Li, T. Karpinets, L. Huang, S. Malu, C. Creasy, S. E. Leahey, J. Chen, Y. Chen, H. Pelicano, C. Bernatchez, Y. N. V. Gopal, T. P. Heffernan, J. Hu, J. Wang, R. N. Amaria, L. A. Garraway, P. Huang, P. Yang, Wistuba, II, S. E. Woodman, J. Roszik, R. E. Davis, M. A. Davies, J. V. Heymach, P. Hwu, and W. Peng. 2018. Increased Tumor Glycolysis Characterizes Immune Resistance to Adoptive T Cell Therapy. *Cell Metab.* 27: 977-987 e974.

189. Yoshihara, K., M. Shahmoradgoli, E. Martinez, R. Vegesna, H. Kim, W. Torres-Garcia, V. Trevino, H. Shen, P. W. Laird, D. A. Levine, S. L. Carter, G. Getz, K. Stemke-Hale, G. B. Mills, and R. G. Verhaak. 2013. Inferring tumour purity and stromal and immune cell admixture from expression data. *Nat. Commun.* 4: 2612.

190. Becht, E., N. A. Giraldo, L. Lacroix, B. Buttard, N. Elarouci, F. Petitprez, J. Selves, P. Laurent-Puig, C. Sautes-Fridman, W. H. Fridman, and A. de Reynies. 2016. Estimating the population abundance of tissue-infiltrating immune and stromal cell populations using gene expression. *Genome Biol.* 17: 218-016-1070-1075.

191. Faubert, B., K. Y. Li, L. Cai, C. T. Hensley, J. Kim, L. G. Zacharias, C. Yang, Q. N. Do, S. Doucette, D. Burguete, H. Li, G. Huet, Q. Yuan, T. Wigal, Y. Butt, M. Ni, J. Torrealba, D. Oliver, R. E. Lenkinski, C. R. Malloy, J. W. Wachsmann, J. D. Young, K. Kernstine,

and R. J. DeBerardinis. 2017. Lactate Metabolism in Human Lung Tumors. *Cell* 171: 358-371.

192. Chong, J., O. Soufan, C. Li, I. Caraus, S. Li, G. Bourque, D. S. Wishart, and J. Xia. 2018. MetaboAnalyst 4.0: towards more transparent and integrative metabolomics analysis. *Nucleic Acids Res.* 46: W486-W494.

193. Hather, G., R. Liu, S. Bandi, J. Mettetal, M. Manfredi, W. C. Shyu, J. Donelan, and A. Chakravarty. 2014. Growth rate analysis and efficient experimental design for tumor xenograft studies. *Cancer Inform.* 13: 65-72.

194. Morikawa, K., S. M. Walker, J. M. Jessup, and I. J. Fidler. 1988. In vivo selection of highly metastatic cells from surgical specimens of different primary human colon carcinomas implanted into nude mice. *Cancer Res.* 48: 1943-1948.

195. Lazar, I., E. Clement, S. Dauvillier, D. Milhas, M. Ducoux-Petit, S. LeGonidec, C. Moro, V. Soldan, S. Dalle, S. Balor, M. Golzio, O. Burlet-Schiltz, P. Valet, C. Muller, and L. Nieto. 2016. Adipocyte Exosomes Promote Melanoma Aggressiveness through Fatty Acid Oxidation: A Novel Mechanism Linking Obesity and Cancer. *Cancer Res.* 76: 4051-4057.

196. Liu, Y. L., F. Lai, J. S. Wilmott, X. G. Yan, X. Y. Liu, Q. Luan, S. T. Guo, C. C. Jiang, H. Y. Tseng, R. A. Scolyer, L. Jin, and X. D. Zhang. 2014. Noxa upregulation by oncogenic activation of MEK/ERK through CREB promotes autophagy in human melanoma cells. *Oncotarget* 5: 11237-11251.

197. Ndoye, A., and A. T. Weeraratna. 2016. Autophagy- An emerging target for melanoma therapy. *F1000Research* 5: 10.12688/f11000research.18347.12681. eCollection 12016.

198. Marino, M. L., P. Pellegrini, G. Di Lernia, M. Djavaheri-Mergny, S. Brnjic, X. Zhang, M. Hagg, S. Linder, S. Fais, P. Codogno, and A. De Milito. 2012. Autophagy is a protective

mechanism for human melanoma cells under acidic stress. *The Journal of Biological Chemistry* 287: 30664-30676.

199. Commisso, C., S. M. Davidson, R. G. Soydaner-Azeloglu, S. J. Parker, J. J. Kamphorst, S. Hackett, E. Grabocka, M. Nofal, J. A. Drebin, C. B. Thompson, J. D. Rabinowitz, C. M. Metallo, M. G. Vander Heiden, and D. Bar-Sagi. 2013. Macropinocytosis of protein is an amino acid supply route in Ras-transformed cells. *Nature* 497: 633-637.

200. Alonso-Curbelo, D., L. Osterloh, E. Canon, T. G. Calvo, R. Martinez-Herranz, P. Karras, S. Martinez, E. Riveiro-Falkenbach, P. O. Romero, J. L. Rodriguez-Peralto, J. Pastor, and M. S. Soengas. 2015. RAB7 counteracts PI3K-driven macropinocytosis activated at early stages of melanoma development. *Oncotarget* 6: 11848-11862.

201. Gonzalez, C. D., S. Alvarez, A. Ropolo, C. Rosenzvit, M. F. Bagnes, and M. I. Vaccaro. 2014. Autophagy, Warburg, and Warburg reverse effects in human cancer. *BioMed Research International* 2014: 926729.

202. Pavlides, S., D. Whitaker-Menezes, R. Castello-Cros, N. Flomenberg, A. K. Witkiewicz, P. G. Frank, M. C. Casimiro, C. Wang, P. Fortina, S. Addya, R. G. Pestell, U. E. Martinez-Outschoorn, F. Sotgia, and M. P. Lisanti. 2009. The reverse Warburg effect: aerobic glycolysis in cancer associated fibroblasts and the tumor stroma. *Cell Cycle (Georgetown, Tex.)* 8: 3984-4001.

203. Pavlides, S., A. Tsirigos, I. Vera, N. Flomenberg, P. G. Frank, M. C. Casimiro, C. Wang, R. G. Pestell, U. E. Martinez-Outschoorn, A. Howell, F. Sotgia, and M. P. Lisanti. 2010. Transcriptional evidence for the "Reverse Warburg Effect" in human breast cancer tumor stroma and metastasis: similarities with oxidative stress, inflammation, Alzheimer's disease, and "Neuron-Glia Metabolic Coupling". *Aging* 2: 185-199.

204. Jensen, D. H., M. H. Therkildsen, and E. Dabelsteen. 2015. A reverse Warburg metabolism in oral squamous cell carcinoma is not dependent upon myofibroblasts. *Journal of Oral Pathology & Medicine: Official Publication of the International Association of Oral Pathologists and the American Academy of Oral Pathology* 44: 714-721.

205. Sotgia, F., U. E. Martinez-Outschoorn, and M. P. Lisanti. 2014. The reverse Warburg effect in osteosarcoma. *Oncotarget* 5: 7982-7983.

206. Ho, J., M. B. de Moura, Y. Lin, G. Vincent, S. Thorne, L. M. Duncan, L. Hui-Min, J. M. Kirkwood, D. Becker, B. Van Houten, and S. J. Moschos. 2012. Importance of glycolysis and oxidative phosphorylation in advanced melanoma. *Mol. Cancer* 11: 76-4598-4511-4576.

207. Sonveaux, P., F. Vegran, T. Schroeder, M. C. Wergin, J. Verrax, Z. N. Rabbani, C. J. De Saedeleer, K. M. Kennedy, C. Diepart, B. F. Jordan, M. J. Kelley, B. Gallez, M. L. Wahl, O. Feron, and M. W. Dewhirst. 2008. Targeting lactate-fueled respiration selectively kills hypoxic tumor cells in mice. *J. Clin. Investig.* 118: 3930-3942.

208. Smolkova, K., L. Plecita-Hlavata, N. Bellance, G. Benard, R. Rossignol, and P. Jezek. 2011. Waves of gene regulation suppress and then restore oxidative phosphorylation in cancer cells. *The International Journal of Biochemistry & Cell biology* 43: 950-968.

209. Rumsey, W. L., C. Schlosser, E. M. Nuutinen, M. Robiolio, and D. F. Wilson. 1990. Cellular energetics and the oxygen dependence of respiration in cardiac myocytes isolated from adult rat. *The Journal of Biological Chemistry* 265: 15392-15402.

210. Weinberg, S. E., and N. S. Chandel. 2015. Targeting mitochondria metabolism for cancer therapy. *Nat. Chem. Biol.* 11: 9-15.

211. Chen, E. I., J. Hewel, J. S. Krueger, C. Tiraby, M. R. Weber, A. Kralli, K. Becker, J. R. Yates, 3rd, and B. Felding-Habermann. 2007. Adaptation of energy metabolism in breast cancer brain metastases. *Cancer Res.* 67: 1472-1486.

212. Simoes, R. V., I. S. Serganova, N. Kruchevsky, A. Leftin, A. A. Shestov, H. T. Thaler, G. Sukenick, J. W. Locasale, R. G. Blasberg, J. A. Koutcher, and E. Ackerstaff. 2015. Metabolic plasticity of metastatic breast cancer cells: adaptation to changes in the microenvironment. *Neoplasia (New York, N.Y.)* 17: 671-684.

213. Chaube, B., P. Malvi, S. V. Singh, N. Mohammad, A. S. Meena, and M. K. Bhat. 2015. Targeting metabolic flexibility by simultaneously inhibiting respiratory complex I and lactate generation retards melanoma progression. *Oncotarget* 6: 37281-37299.

214. Marzese, D. M., J. L. Huynh, N. P. Kawas, and D. S. Hoon. 2014. Multi-platform Genome-wide Analysis of Melanoma Progression to Brain Metastasis. *Genom Data* 2: 150-152.

215. Gopal, Y. N., W. Deng, S. E. Woodman, K. Komurov, P. Ram, P. D. Smith, and M. A. Davies. 2010. Basal and treatment-induced activation of AKT mediates resistance to cell death by AZD6244 (ARRY-142886) in Braf-mutant human cutaneous melanoma cells. *Cancer Res.* 70: 8736-8747.

216. Long, G. V., J. J. Grob, P. Nathan, A. Ribas, C. Robert, D. Schadendorf, S. R. Lane, C. Mak, P. Legenne, K. T. Flaherty, and M. A. Davies. 2016. Factors predictive of response, disease progression, and overall survival after dabrafenib and trametinib combination treatment: a pooled analysis of individual patient data from randomised trials. *Lancet Oncol.* 17: 1743-1754.

217. Dimmer, K. S., B. Friedrich, F. Lang, J. W. Deitmer, and S. Broer. 2000. The low-affinity monocarboxylate transporter MCT4 is adapted to the export of lactate in highly glycolytic cells. *The Biochemical Journal* 350 Pt 1: 219-227.

218. Pinheiro, C., V. Miranda-Goncalves, A. Longatto-Filho, A. L. Vicente, G. N. Berardinelli, C. Scapulatempo-Neto, R. F. Costa, C. R. Viana, R. M. Reis, F. Baltazar, and V. L. Vazquez. 2016. The metabolic microenvironment of melanomas: Prognostic value of MCT1 and MCT4. *Cell Cycle (Georgetown, Tex.)* 15: 1462-1470.

219. Payen, V. L., P. E. Porporato, B. Baselet, and P. Sonveaux. 2016. Metabolic changes associated with tumor metastasis, part 1: tumor pH, glycolysis and the pentose phosphate pathway. *Cellular and Molecular Life Sciences : CMLS* 73: 1333-1348.

220. Ullah, M. S., A. J. Davies, and A. P. Halestrap. 2006. The plasma membrane lactate transporter MCT4, but not MCT1, is up-regulated by hypoxia through a HIF-1alpha-dependent mechanism. *The Journal of Biological Chemistry* 281: 9030-9037.

221. Romero-Garcia, S., M. M. Moreno-Altamirano, H. Prado-Garcia, and F. J. Sanchez-Garcia. 2016. Lactate Contribution to the Tumor Microenvironment: Mechanisms, Effects on Immune Cells and Therapeutic Relevance. *Front. Immunol.* 7: 52.

222. Sonveaux, P., T. Copetti, C. J. De Saedeleer, F. Vegran, J. Verrax, K. M. Kennedy, E. J. Moon, S. Dhup, P. Danhier, F. Frerart, B. Gallez, A. Ribeiro, C. Michiels, M. W. Dewhirst, and O. Feron. 2012. Targeting the lactate transporter MCT1 in endothelial cells inhibits lactate-induced HIF-1 activation and tumor angiogenesis. *PLoS One* 7: e33418.

223. Vegran, F., R. Boidot, C. Michiels, P. Sonveaux, and O. Feron. 2011. Lactate influx through the endothelial cell monocarboxylate transporter MCT1 supports an NF-kappaB/IL-8 pathway that drives tumor angiogenesis. *Cancer Res.* 71: 2550-2560.

224. Stuwe, L., M. Muller, A. Fabian, J. Waning, S. Mally, J. Noel, A. Schwab, and C. Stock. 2007. pH dependence of melanoma cell migration: protons extruded by NHE1 dominate protons of the bulk solution. *The Journal of Physiology* 585: 351-360.

225. Vahle, A. K., B. Domikowsky, C. Schwoppe, H. Krahling, S. Mally, M. Schafers, S. Hermann, V. Shahin, J. Haier, A. Schwab, and C. Stock. 2014. Extracellular matrix composition and interstitial pH modulate NHE1-mediated melanoma cell motility. *Int. J. Oncol.* 44: 78-90.

226. Alper, S. L., M. N. Chernova, and A. K. Stewart. 2002. How pH regulates a pH regulator: a regulatory hot spot in the N-terminal cytoplasmic domain of the AE2 anion exchanger. *Cell Biochem. Biophys.* 36: 123-136.

227. Benej, M., S. Pastorekova, and J. Pastorek. 2014. Carbonic anhydrase IX: regulation and role in cancer. *Subcell. Biochem.* 75: 199-219.

228. Donowitz, M., C. Ming Tse, and D. Fuster. 2013. SLC9/NHE gene family, a plasma membrane and organellar family of Na(+)/H(+) exchangers. *Mol. Aspects Med.* 34: 236-251.

229. Stock, C., B. Gassner, C. R. Hauck, H. Arnold, S. Mally, J. A. Eble, P. Dieterich, and A. Schwab. 2005. Migration of human melanoma cells depends on extracellular pH and Na+/H+ exchange. *The Journal of Physiology* 567: 225-238.

230. Rofstad, E. K., B. Mathiesen, K. Kindem, and K. Galappathi. 2006. Acidic extracellular pH promotes experimental metastasis of human melanoma cells in athymic nude mice. *Cancer Res.* 66: 6699-6707.

231. Klein, M., P. Seeger, B. Schuricht, S. L. Alper, and A. Schwab. 2000. Polarization of Na(+)/H(+) and Cl(-)/HCO (3)(-) exchangers in migrating renal epithelial cells. *The Journal of General Physiology* 115: 599-608.

232. Lagana, A., J. Vadnais, P. U. Le, T. N. Nguyen, R. Laprade, I. R. Nabi, and J. Noel. 2000. Regulation of the formation of tumor cell pseudopodia by the Na(+)/H(+) exchanger NHE1. *J. Cell Sci.* 113 (Pt 20): 3649-3662.

233. Svastova, E., W. Witarski, L. Csaderova, I. Kosik, L. Skvarkova, A. Hulikova, M. Zatovicova, M. Barathova, J. Kopacek, J. Pastorek, and S. Pastorekova. 2012. Carbonic anhydrase IX interacts with bicarbonate transporters in lamellipodia and increases cell migration via its catalytic domain. *The Journal of Biological Chemistry* 287: 3392-3402.

234. Gorrini, C., I. S. Harris, and T. W. Mak. 2013. Modulation of oxidative stress as an anticancer strategy. *Nature Reviews.Drug Discovery* 12: 931-947.

235. Jaramillo, M. C., and D. D. Zhang. 2013. The emerging role of the Nrf2-Keap1 signaling pathway in cancer. *Genes Dev.* 27: 2179-2191.

236. Piskounova, E., M. Agathocleous, M. M. Murphy, Z. Hu, S. E. Huddlestun, Z. Zhao, A. M. Leitch, T. M. Johnson, R. J. DeBerardinis, and S. J. Morrison. 2015. Oxidative stress inhibits distant metastasis by human melanoma cells. *Nature* 527: 186-191.

237. Innocenzi, D., P. L. Alo, A. Balzani, V. Sebastiani, V. Silipo, G. La Torre, G. Ricciardi, C. Bosman, and S. Calvieri. 2003. Fatty acid synthase expression in melanoma. *J. Cutan. Pathol.* 30: 23-28.

238. Zecchin, K. G., F. A. Rossato, H. F. Raposo, D. R. Melo, L. C. Alberici, H. C. Oliveira, R. F. Castilho, R. D. Coletta, A. E. Vercesi, and E. Graner. 2011. Inhibition of fatty acid synthase in melanoma cells activates the intrinsic pathway of apoptosis. *Laboratory Investigation; A Journal of Technical Methods and Pathology* 91: 232-240.

239. Carvalho, M. A., K. G. Zecchin, F. Seguin, D. C. Bastos, M. Agostini, A. L. Rangel, S. S. Veiga, H. F. Raposo, H. C. Oliveira, M. Loda, R. D. Coletta, and E. Graner. 2008. Fatty acid synthase inhibition with Orlistat promotes apoptosis and reduces cell growth and lymph node metastasis in a mouse melanoma model. *Int. J. Cancer* 123: 2557-2565.

240. Slipicevic, A., K. Jorgensen, M. Skrede, A. K. Rosnes, G. Troen, B. Davidson, and V. A. Florenes. 2008. The fatty acid binding protein 7 (FABP7) is involved in proliferation and invasion of melanoma cells. *BMC Cancer* 8: 276-2407-2408-2276.

241. Nath, A., and C. Chan. 2016. Genetic alterations in fatty acid transport and metabolism genes are associated with metastatic progression and poor prognosis of human cancers. *Sci. Rep.* 6: 18669.

242. Pascual, G., A. Avgustinova, S. Mejetta, M. Martin, A. Castellanos, C. S. Attolini, A. Berenguer, N. Prats, A. Toll, J. A. Hueto, C. Bescos, L. Di Croce, and S. A. Benitah. 2017. Targeting metastasis-initiating cells through the fatty acid receptor CD36. *Nature* 541: 41-45.

243. LeBleu, V. S., J. T. O'Connell, K. N. Gonzalez Herrera, H. Wikman, K. Pantel, M. C. Haigis, F. M. de Carvalho, A. Damascena, L. T. Domingos Chinen, R. M. Rocha, J. M. Asara, and R. Kalluri. 2014. PGC-1alpha mediates mitochondrial biogenesis and oxidative phosphorylation in cancer cells to promote metastasis. *Nat. Cell Biol.* 16: 992-1003, 1001-1015.

244. Chen, J., H. J. Lee, X. Wu, L. Huo, S. J. Kim, L. Xu, Y. Wang, J. He, L. R. Bollu, G. Gao, F. Su, J. Briggs, X. Liu, T. Melman, J. M. Asara, I. J. Fidler, L. C. Cantley, J. W. Locasale, and Z. Weihua. 2015. Gain of glucose-independent growth upon metastasis of breast cancer cells to the brain. *Cancer Res.* 75: 554-565.

245. Yuan, P., K. Ito, R. Perez-Lorenzo, C. Del Guzzo, J. H. Lee, C. H. Shen, M. W. Bosenberg, M. McMahon, L. C. Cantley, and B. Zheng. 2013. Phenformin enhances the therapeutic benefit of BRAF(V600E) inhibition in melanoma. *Proc. Natl. Acad. Sci. U. S. A.* 110: 18226-18231.

246. Pearce, E. L., and E. J. Pearce. 2013. Metabolic pathways in immune cell activation and quiescence. *Immunity* 38: 633-643.

247. Chang, C. H., J. Qiu, D. O'Sullivan, M. D. Buck, T. Noguchi, J. D. Curtis, Q. Chen, M. Gindin, M. M. Gubin, G. J. van der Windt, E. Tonc, R. D. Schreiber, E. J. Pearce, and E. L. Pearce. 2015. Metabolic Competition in the Tumor Microenvironment Is a Driver of Cancer Progression. *Cell* 162: 1229-1241.

248. Fischer, K., P. Hoffmann, S. Voelkl, N. Meidenbauer, J. Ammer, M. Edinger, E. Gottfried, S. Schwarz, G. Rothe, S. Hoves, K. Renner, B. Timischl, A. Mackensen, L. Kunz-Schughart, R. Andreesen, S. W. Krause, and M. Kreutz. 2007. Inhibitory effect of tumor cell-derived lactic acid on human T cells. *Blood* 109: 3812-3819.

249. Mendler, A. N., B. Hu, P. U. Prinz, M. Kreutz, E. Gottfried, and E. Noessner. 2012. Tumor lactic acidosis suppresses CTL function by inhibition of p38 and JNK/c-Jun activation. *Int. J. Cancer* 131: 633-640.

250. Feder-Mengus, C., S. Ghosh, W. P. Weber, S. Wyler, P. Zajac, L. Terracciano, D. Oertli, M. Heberer, I. Martin, G. C. Spagnoli, and A. Reschner. 2007. Multiple mechanisms underlie defective recognition of melanoma cells cultured in three-dimensional architectures by antigen-specific cytotoxic T lymphocytes. *Br. J. Cancer* 96: 1072-1082.

251. Brody, J. R., C. L. Costantino, A. C. Berger, T. Sato, M. P. Lisanti, C. J. Yeo, R. V. Emmons, and A. K. Witkiewicz. 2009. Expression of indoleamine 2,3-dioxygenase in metastatic malignant melanoma recruits regulatory T cells to avoid immune detection and affects survival. *Cell Cycle (Georgetown, Tex.)* 8: 1930-1934.

252. Sucher, R., K. Kurz, G. Weiss, R. Margreiter, D. Fuchs, and G. Brandacher. 2010. IDO-Mediated Tryptophan Degradation in the Pathogenesis of Malignant Tumor Disease. *International Journal of Tryptophan Research : IJTR* 3: 113-120.

253. Lee, G. K., H. J. Park, M. Macleod, P. Chandler, D. H. Munn, and A. L. Mellor. 2002. Tryptophan deprivation sensitizes activated T cells to apoptosis prior to cell division. *Immunology* 107: 452-460.

254. Munn, D. H., M. D. Sharma, B. Baban, H. P. Harding, Y. Zhang, D. Ron, and A. L. Mellor. 2005. GCN2 kinase in T cells mediates proliferative arrest and anergy induction in response to indoleamine 2,3-dioxygenase. *Immunity* 22: 633-642.

255. Munn, D. H., and A. L. Mellor. 2016. IDO in the Tumor Microenvironment: Inflammation, Counter-Regulation, and Tolerance. *Trends Immunol.* 37: 193-207.

256. Weinlich, G., C. Murr, L. Richardsen, C. Winkler, and D. Fuchs. 2007. Decreased serum tryptophan concentration predicts poor prognosis in malignant melanoma patients. *Dermatology (Basel, Switzerland)* 214: 8-14.

257. Mezrich, J. D., J. H. Fechner, X. Zhang, B. P. Johnson, W. J. Burlingham, and C. A. Bradfield. 2010. An interaction between kynurenine and the aryl hydrocarbon receptor can generate regulatory T cells. *Journal of Immunology (Baltimore, Md.: 1950)* 185: 3190-3198.

258. Moreno, A. C., R. O. Clara, J. B. Coimbra, A. R. Julio, R. C. Albuquerque, E. M. Oliveira, S. S. Maria-Engler, and A. Campa. 2013. The expanding roles of 1-methyl-tryptophan (1-MT): in addition to inhibiting kynurenine production, 1-MT activates the synthesis of melatonin in skin cells. *The FEBS Journal* 280: 4782-4792.

259. Friberg, M., R. Jennings, M. Alsarraj, S. Dessureault, A. Cantor, M. Extermann, A. L. Mellor, D. H. Munn, and S. J. Antonia. 2002. Indoleamine 2,3-dioxygenase contributes to tumor cell evasion of T cell-mediated rejection. *Int. J. Cancer* 101: 151-155.

260. Hou, D. Y., A. J. Muller, M. D. Sharma, J. DuHadaway, T. Banerjee, M. Johnson, A. L. Mellor, G. C. Prendergast, and D. H. Munn. 2007. Inhibition of indoleamine 2,3-

dioxygenase in dendritic cells by stereoisomers of 1-methyl-tryptophan correlates with antitumor responses. *Cancer Res.* 67: 792-801.

261. Alegre, M. L., K. A. Frauwirth, and C. B. Thompson. 2001. T-cell regulation by CD28 and CTLA-4. *Nature Reviews.Immunology* 1: 220-228.

262. Krummel, M. F., and J. P. Allison. 1995. CD28 and CTLA-4 have opposing effects on the response of T cells to stimulation. *The Journal of Experimental Medicine* 182: 459-465.

263. Walunas, T. L., C. Y. Bakker, and J. A. Bluestone. 1996. CTLA-4 ligation blocks CD28-dependent T cell activation. *The Journal of Experimental Medicine* 183: 2541-2550.

264. Pardoll, D. M. 2012. The blockade of immune checkpoints in cancer immunotherapy. *Nature Reviews.Cancer* 12: 252-264.

265. Lee, J., R. Kefford, and M. Carlino. 2016. PD-1 and PD-L1 inhibitors in melanoma treatment: past success, present application and future challenges. *Immunotherapy* 8: 733-746.

266. Parry, R. V., J. M. Chemnitz, K. A. Frauwirth, A. R. Lanfranco, I. Braunstein, S. V. Kobayashi, P. S. Linsley, C. B. Thompson, and J. L. Riley. 2005. CTLA-4 and PD-1 receptors inhibit T-cell activation by distinct mechanisms. *Mol. Cell. Biol.* 25: 9543-9553.

267. Patsoukis, N., K. Bardhan, P. Chatterjee, D. Sari, B. Liu, L. N. Bell, E. D. Karoly, G. J. Freeman, V. Petkova, P. Seth, L. Li, and V. A. Boussiotis. 2015. PD-1 alters T-cell metabolic reprogramming by inhibiting glycolysis and promoting lipolysis and fatty acid oxidation. *Nat. Commun.* 6: 6692.

268. Zhang, L., and P. Romero. 2018. Metabolic Control of CD8(+) T Cell Fate Decisions and Antitumor Immunity. *Trends Mol. Med.* 24: 30-48.

269. Afzal, M. Z., R. R. Mercado, and K. Shirai. 2018. Efficacy of metformin in combination with immune checkpoint inhibitors (anti-PD-1/anti-CTLA-4) in metastatic malignant melanoma. *J Immunother Cancer* 6: 64.

270. Kim, S. H., M. Li, S. Trousil, Y. Zhang, M. Pasca di Magliano, K. D. Swanson, and B. Zheng. 2017. Phenformin Inhibits Myeloid-Derived Suppressor Cells and Enhances the Anti-Tumor Activity of PD-1 Blockade in Melanoma. *J. Invest. Dermatol.* 137: 1740-1748.

271. Eikawa, S., M. Nishida, S. Mizukami, C. Yamazaki, E. Nakayama, and H. Udono. 2015. Immune-mediated antitumor effect by type 2 diabetes drug, metformin. *Proc. Natl. Acad. Sci. U. S. A.* 112: 1809-1814.

272. Holmgaard, R. B., D. Zamarin, D. H. Munn, J. D. Wolchok, and J. P. Allison. 2013. Indoleamine 2,3-dioxygenase is a critical resistance mechanism in antitumor T cell immunotherapy targeting CTLA-4. *The Journal of Experimental Medicine* 210: 1389-1402.

273. Gangadhar, T. C., O. Hamid, D. C. Smith, T. M. Bauer, J. S. Wasser, A. J. Olszanski, J. Luke, A. S. Balmanoukian, D. R. Kaufman, Y. Zhao, J. Maleski, M. J. Jones, L. Leopold, and T. F. Gajewski. 2016. Epacadostat plus pembrolizumab in patients with advanced melanoma and select solid tumors: Updated phase 1 results from ECHO-202/KEYNOTE-037. *Ann Onc* 27: 379-400.

274. Roesch, A., M. Fukunaga-Kalabis, E. C. Schmidt, S. E. Zabierowski, P. A. Brafford, A. Vultur, D. Basu, P. Gimotty, T. Vogt, and M. Herlyn. 2010. A temporarily distinct subpopulation of slow-cycling melanoma cells is required for continuous tumor growth. *Cell* 141: 583-594.

275. Roesch, A., A. Vultur, I. Bogeski, H. Wang, K. M. Zimmermann, D. Speicher, C. Korbel, M. W. Laschke, P. A. Gimotty, S. E. Philipp, E. Krause, S. Patzold, J. Villanueva, C. Krepler, M. Fukunaga-Kalabis, M. Hoth, B. C. Bastian, T. Vogt, and M. Herlyn. 2013. Overcoming intrinsic multidrug resistance in melanoma by blocking the mitochondrial respiratory chain of slow-cycling JARID1B(high) cells. *Cancer Cell* 23: 811-825.

276. Pulito, C., T. Sanli, P. Rana, P. Muti, G. Blandino, and S. Strano. 2013. Metformin: On Ongoing Journey across Diabetes, Cancer Therapy and Prevention. *Metabolites* 3: 1051-1075.

277. Cerezo, M., T. Tomic, R. Ballotti, and S. Rocchi. 2015. Is it time to test biguanide metformin in the treatment of melanoma? *Pigment Cell Melanoma Res.* 28: 8-20.

278. Janjetovic, K., L. Harhaji-Trajkovic, M. Misirkic-Marjanovic, L. Vucicevic, D. Stevanovic, N. Zogovic, M. Sumarac-Dumanovic, D. Micic, and V. Trajkovic. 2011. In vitro and in vivo anti-melanoma action of metformin. *Eur. J. Pharmacol.* 668: 373-382.

279. Martin, M. J., R. Hayward, A. Viros, and R. Marais. 2012. Metformin accelerates the growth of BRAF V600E-driven melanoma by upregulating VEGF-A. *Cancer Discov.* 2: 344-355.

280. Niehr, F., E. von Euw, N. Attar, D. Guo, D. Matsunaga, H. Sazegar, C. Ng, J. A. Glaspy, J. A. Recio, R. S. Lo, P. S. Mischel, B. Comin-Anduix, and A. Ribas. 2011. Combination therapy with vemurafenib (PLX4032/RG7204) and metformin in melanoma cell lines with distinct driver mutations. *J. Transl. Med.* 9: 76-5876-5879-5876.

281. Tomic, T., T. Botton, M. Cerezo, G. Robert, F. Luciano, A. Puissant, P. Gounon, M. Allegra, C. Bertolotto, J. M. Bereder, S. Tartare-Deckert, P. Bahadoran, P. Auberger, R. Ballotti, and S. Rocchi. 2011. Metformin inhibits melanoma development through autophagy and apoptosis mechanisms. *Cell Death Dis.* 2: e199.

282. Baenke, F., B. Chaneton, M. Smith, N. Van Den Broek, K. Hogan, H. Tang, A. Viros, M. Martin, L. Galbraith, M. R. Girotti, N. Dhomen, E. Gottlieb, and R. Marais. 2016. Resistance to BRAF inhibitors induces glutamine dependency in melanoma cells. *Mol. Oncol.* 10: 73-84.

283. Ayers, M., J. Lunceford, M. Nebozhyn, E. Murphy, A. Loboda, D. R. Kaufman, A. Albright, J. D. Cheng, S. P. Kang, V. Shankaran, S. A. Piha-Paul, J. Yearley, T. Y. Seiwert, A. Ribas, and T. K. McClanahan. 2017. IFN-gamma-related mRNA profile predicts clinical response to PD-1 blockade. *J. Clin. Invest.* 127: 2930-2940.

284. Molina, J. R., Y. Sun, M. Protopopova, S. Gera, M. Bandi, C. Bristow, T. McAfoos, P. Morlacchi, J. Ackroyd, A. A. Agip, G. Al-Atrash, J. Asara, J. Bardenhagen, C. C. Carrillo, C. Carroll, E. Chang, S. Ciurea, J. B. Cross, B. Czako, A. Deem, N. Daver, J. F. de Groot, J. W. Dong, N. Feng, G. Gao, J. Gay, M. G. Do, J. Greer, V. Giuliani, J. Han, L. Han, V. K. Henry, J. Hirst, S. Huang, Y. Jiang, Z. Kang, T. Khor, S. Konoplev, Y. H. Lin, G. Liu, A. Lodi, T. Lofton, H. Ma, M. Mahendra, P. Matre, R. Mullinax, M. Peoples, A. Petrocchi, J. Rodriguez-Canale, R. Serreli, T. Shi, M. Smith, Y. Tabe, J. Theroff, S. Tiziani, Q. Xu, Q. Zhang, F. Muller, R. A. DePinho, C. Toniatti, G. F. Draetta, T. P. Heffernan, M. Konopleva, P. Jones, M. E. Di Francesco, and J. R. Marszalek. 2018. An inhibitor of oxidative phosphorylation exploits cancer vulnerability. *Nat. Med.* 24: 1036-1046.

285. Rheault, T. R., J. C. Stellwagen, G. M. Adjabeng, K. R. Hornberger, K. G. Petrov, A. G. Waterson, S. H. Dickerson, R. A. Mook, Jr., S. G. Laquerre, A. J. King, O. W. Rossanese, M. R. Arnone, K. N. Smitheman, L. S. Kane-Carson, C. Han, G. S. Moorthy, K. G. Moss, and D. E. Uehling. 2013. Discovery of Dabrafenib: A Selective Inhibitor of Raf Kinases with Antitumor Activity against B-Raf-Driven Tumors. *ACS Med. Chem. Lett.* 4: 358-362.

286. Bommareddy, P. K., S. Aspromonte, A. Zloza, S. D. Rabkin, and H. L. Kaufman. 2018. MEK inhibition enhances oncolytic virus immunotherapy through increased tumor cell killing and T cell activation. *Sci. Transl. Med.* 10.

287. Jewell, J. L., R. C. Russell, and K. L. Guan. 2013. Amino acid signalling upstream of mTOR. *Nat. Rev. Mol. Cell Biol.* 14: 133-139.

288. Jegg, A. M., T. M. Ward, E. Iorns, N. Hoe, J. Zhou, X. Liu, S. Singh, R. Landgraf, and M. D. Pegram. 2012. PI3K independent activation of mTORC1 as a target in lapatinib-resistant ERBB2+ breast cancer cells. *Breast Cancer Res. Treat.* 136: 683-692.

289. Kim, J., M. Kundu, B. Viollet, and K. L. Guan. 2011. AMPK and mTOR regulate autophagy through direct phosphorylation of Ulk1. *Nat. Cell Biol.* 13: 132-141.

290. Yennu-Nanda, V. G., Z. Hu, V. M. Thiele, T. P. Heffernan, M. DiFrancesco, J. R. Marszalek, R. J. DeBerardinis, and M. A. Davies. 2016. Overcoming mitochondrial oxidative phosphorylation-mediated resistance to targeted therapies in melanoma. *Mol. Cancer Res.* 14: suppl; abstr 52.

291. Vanpouille-Box, C., A. Alard, M. J. Aryankalayil, Y. Sarfraz, J. M. Diamond, R. J. Schneider, G. Inghirami, C. N. Coleman, S. C. Formenti, and S. Demaria. 2017. DNA exonuclease Trex1 regulates radiotherapy-induced tumour immunogenicity. *Nat Commun* 8: 15618.

292. Gerber, S. A., A. L. Sedlacek, K. R. Cron, S. P. Murphy, J. G. Frelinger, and E. M. Lord. 2013. IFN-gamma mediates the antitumor effects of radiation therapy in a murine colon tumor. *Am. J. Pathol.* 182: 2345-2354.

293. DiLillo, D. J., K. Yanaba, and T. F. Tedder. 2010. B cells are required for optimal CD4+ and CD8+ T cell tumor immunity: therapeutic B cell depletion enhances B16 melanoma growth in mice. *J. Immunol.* 184: 4006-4016.

294. Kobayashi, T., Y. Hamaguchi, M. Hasegawa, M. Fujimoto, K. Takehara, and T. Matsushita. 2014. B cells promote tumor immunity against B16F10 melanoma. *Am. J. Pathol.* 184: 3120-3129.

295. Tarhini, A. A., H. Edington, L. H. Butterfield, Y. Lin, Y. Shuai, H. Tawbi, C. Sander, Y. Yin, M. Holtzman, J. Johnson, U. N. Rao, and J. M. Kirkwood. 2014. Immune monitoring of the circulation and the tumor microenvironment in patients with regionally advanced melanoma receiving neoadjuvant ipilimumab. *PLoS One* 9: e87705.

296. Reddy, S. M., B. A. Helmink, J. Gao, S. Zhang, K. Yizhak, M. Sade-Feldman, J. Blando, H. Guangchun, V. Gopalakrishnan, H. Zhao, W. Liu, H. Tawbi, R. Amaria, M. A. Davies, P. Hwu, J. Lee, J. E. Gershenwald, S. E. Woodman, E. Burton, L. Haydu, A. J. Lazar, C. W. Hudgens, A. P. Cogdill, O. Krijgsman, E. Rozeman, D. Peeper, C. Blank, T. Schumacher, E. Keung, P. O. Gaudreau, A. Reuben, C. Spencer, L. H. Butterfield, J. P. Allison, M. T. Tetzlaff, F. Petitprez, W. H. Fridman, C. Sautes-Fridman, N. Hacohen, P. Sharma, L. Wang, and J. A. Wargo. 2018. B-cells and tertiary lymphoid structures (TLS) predict response to immune checkpoint blockade (ICB). *J Immunother Cancer* 6: suppl 1; abstr O5.

297. Mashimo, T., K. Pichumani, V. Vemireddy, K. J. Hatanpaa, D. K. Singh, S. Sirasanagandla, S. Nannepaga, S. G. Piccirillo, Z. Kovacs, C. Foong, Z. Huang, S. Barnett, B. E. Mickey, R. J. DeBerardinis, B. P. Tu, E. A. Maher, and R. M. Bachoo. 2014. Acetate is a bioenergetic substrate for human glioblastoma and brain metastases. *Cell* 159: 1603-1614.

298. Fischer, G. M., Y. N. Vashisht Gopal, J. L. McQuade, W. Peng, R. J. DeBerardinis, and M. A. Davies. 2018. Metabolic strategies of melanoma cells: Mechanisms, interactions

with the tumor microenvironment, and therapeutic implications. *Pigment Cell Melanoma Res* 31: 11-30.

299. Haque, N., M. T. Rahman, N. H. Abu Kasim, and A. M. Alabsi. 2013. Hypoxic culture conditions as a solution for mesenchymal stem cell based regenerative therapy. *ScientificWorldJournal* 2013: 632972.

300. Salehi, Z., F. Mashayekhi, and M. Naji. 2008. Insulin like growth factor-1 and insulin like growth factor binding proteins in the cerebrospinal fluid and serum from patients with Alzheimer's disease. *Biofactors* 33: 99-106.

301. Vyas, S., E. Zaganjor, and M. C. Haigis. 2016. Mitochondria and Cancer. *Cell* 166: 555-566.

302. Fehm, H. L., W. Kern, and A. Peters. 2006. The selfish brain: competition for energy resources. *Prog. Brain Res.* 153: 129-140.

303. Belanger, M., I. Allaman, and P. J. Magistretti. 2011. Brain energy metabolism: focus on astrocyte-neuron metabolic cooperation. *Cell Metab.* 14: 724-738.

304. Mirzaei, R., S. Sarkar, and V. W. Yong. 2017. T Cell Exhaustion in Glioblastoma: Intricacies of Immune Checkpoints. *Trends Immunol.* 38: 104-115.

305. Xia, S., R. Lin, L. Jin, L. Zhao, H. B. Kang, Y. Pan, S. Liu, G. Qian, Z. Qian, E. Konstantakou, B. Zhang, J. T. Dong, Y. R. Chung, O. Abdel-Wahab, T. Merghoub, L. Zhou, R. R. Kudchadkar, D. H. Lawson, H. J. Khoury, F. R. Khuri, L. H. Boise, S. Lonial, B. H. Lee, B. P. Pollack, J. L. Arbiser, J. Fan, Q. Y. Lei, and J. Chen. 2017. Prevention of Dietary-Fat-Fueled Ketogenesis Attenuates BRAF V600E Tumor Growth. *Cell Metab.* 25: 358-373.

306. Weber, D. D., S. Aminazdeh-Gohari, and B. Kofler. 2018. Ketogenic diet in cancer therapy. *Aging (Albany NY)* 10: 164-165.

307. Buck, M. D., D. O'Sullivan, and E. L. Pearce. 2015. T cell metabolism drives immunity. *J. Exp. Med.* 212: 1345-1360.

308. Dumauthioz, N., S. Labiano, and P. Romero. 2018. Tumor Resident Memory T Cells: New Players in Immune Surveillance and Therapy. *Front. Immunol.* 9: 2076.

309. Najjar, Y. G., A. V. Menk, C. Sander, U. Rao, A. Karunamurthy, R. Bhatia, S. Zhai, J. M. Kirkwood, and G. M. Delgoffe. 2019. Tumor cell oxidative metabolism as a barrier to PD-1 blockade immunotherapy in melanoma. *JCI Insight* 4.

310. Gammon, S. T., F. Pisaneschi, M. Bandi, M. Smith, Y. Rao, V. G. Yennu-Nanda, Y. Sun, M. A. Davies, E. D. DiFrancesco, J. R. Marszalek, and D. Piwnica-Worms. 2018. [18F]FAZA PET imaging reveals precise pharmacodynamics in vivo of the novel chemotherapeutic IACS-010759. *Cancer Res.* 78: suppl; abstr LB-367.

311. Zinn, P. O., S. K. Singh, A. Kotrotsou, I. Hassan, G. Thomas, M. M. Luedi, A. Elakkad, N. Elshafeey, T. Idris, J. Mosley, J. Gumin, G. N. Fuller, J. F. de Groot, V. Baladandayuthapani, E. P. Sulman, A. J. Kumar, R. Sawaya, F. F. Lang, D. Piwnica-Worms, and R. R. Colen. 2018. A Coclinical Radiogenomic Validation Study: Conserved Magnetic Resonance Radiomic Appearance of Periostin-Expressing Glioblastoma in Patients and Xenograft Models. *Clin. Cancer Res.* 24: 6288-6299.

312. Biancur, D. E., J. A. Paulo, B. Malachowska, M. Quiles Del Rey, C. M. Sousa, X. Wang, A. S. W. Sohn, G. C. Chu, S. P. Gygi, J. W. Harper, W. Fendler, J. D. Mancias, and A. C. Kimmelman. 2017. Compensatory metabolic networks in pancreatic cancers upon perturbation of glutamine metabolism. *Nat Commun* 8: 15965.

313. Meric-Bernstam, F., M. Gordon, S. Tykodi, E. Lam, U. Vaishampayan, J. Chaves, P. Nikolinakos, A. Fan, R. Lee, D. McDermott, G. Shapiro, L. Gandhi, H. Tawbi, S. Bhatia, L. Muigai, Y. Jenkins, S. Whiting, and M. H. Voss. 2017. A phase 1/2 study of CB-839,

a first-in-class glutaminase inhibitor,combined with nivolumab in patients with advanced melanoma (MEL), renal cell carcinoma (RCC), or non-small cell lung cancer (NSCLC). *J Immunother Cancer* 5: suppl 2; abstr O16.

VITA

Grant Matthew Fischer was born in Collinsville, Illinois, the son of Gary and Rhonda Fischer. After graduating from Collinsville High School (Collinsville, Illinois) in 2008, he entered Rockhurst University in Kansas City, Missouri. He received the degree of Bachelor of Science with a major in biochemistry and minor in theology from Rockhurst University in May of 2012. In May of 2012, he entered The MD/PhD Program at the University of Texas at Houston, which is the result of a partnership between the McGovern Medical School and the University of Texas MD Anderson Cancer Center / UTHealth Graduate School of Biomedical Sciences.